



Technische Universität München

Fakultät für Maschinenwesen

Lehrstuhl für Windenergie

Wind sensing for wind farm control

Johannes Matthias Schreiber

Vollständiger Abdruck der von der Fakultät für Maschinenwesen der Technischen Universität München zur Erlangung des akademischen Grades eines

Doktor-Ingenieurs (Dr.-Ing.)

genehmigten Dissertation.

Vorsitzender:

Prof. Dr.-Ing. Manfred Hajek

Prüfer der Dissertation:

Prof. Dr. Carlo L. Bottasso

Prof. dr. ir. Jan-Willem van Wingerden

Die Dissertation wurde am 09.04.2020 bei der Technischen Universität München eingereicht und durch die Fakultät für Maschinenwesen am 12.08.2020 angenommen.

Technische Universität München
Fakultät für Maschinenwesen
Lehrstuhl für Windenergie
Boltzmannstraße 15
D-85748 Garching bei München
Germany
Tel.: +49 (0) 89 / 289 – 16681
Fax.: +49 (0) 89 / 289 – 16611
Email: info@wind.tum.de
Web: www.wind.mw.tum.de

ABSTRACT

The goal of this dissertation is the development and demonstration of methods to improve wind condition awareness on wind turbine and farm level to finally benefit wind farm control and other applications.

Currently, turbines are not fully aware of their wind inflow as typically only point measurements, taken at the turbine nacelle, are available. Within a wind farm also, it is unknown where and how wakes, characterized by reduced wind speed and increased turbulence, develop exactly. The interaction between wake and turbine leads to power loss and increased fatigue loading. During operation of wind farms today, this interaction is largely neglected, and therefore turbines are controlled individually to optimize their own performance, instead of the collective wind farm performance.

Within this dissertation, first a new method is presented that improves wind condition awareness on turbine level: By analysis of blade bending moments, which are available on many modern turbines, the detailed inflow within the rotor disc of a turbine is inferred. Second, it is shown that such information can be exploited to detect and measure the position of wakes within a wind farm. Additionally, a method to improve and correct wind farm models by learning from turbine measurements, that are today already available by default, is presented. Lastly, the wind and wake condition awareness is used for the collective optimization of turbines using wake steering wind farm control.

Numerical simulations have been used to develop, test and improve the various methods and models. The approaches have been validated and the technical feasibility has been confirmed in scaled wind tunnel tests, that provide measurable and repeatable conditions. Full-scale tests and real turbine data has been employed to prove and demonstrate the final applications.

The presented publications include practical examples of wind sensing and their applications. Results feature a field test on a multi-MW turbine demonstrating the improved wind condition awareness using the load-based inflow estimation method. On the same turbine, also the ability to detect an impinging wake of a neighboring turbine could be successfully tested. The improvement of wind farm models by learning from historical operating data has been demonstrated on a large 43-turbine wind farm. The collective optimization of a wind farm during operation has finally been shown in scaled wind farm experiments, rewarded by reduced loads and a significant increase in total wind farm energy capture.

Deploying the presented methods in real wind farms, significant reductions in the cost of energy are to be expected. But also further applications are possible, reaching from the assessment of historical wind conditions and predictive maintenance to wake detection triggered sector management.

ACKNOWLEDGMENTS

I would like to express my special gratitude to my supervisor Professor Carlo L. Bottasso. Your useful comments, assistance, guidance, and patience through the learning process of this thesis, together with your constant encouragement, was extremely valuable for me and also made the study very pleasant. Carlo, I thank you also for the opportunities and trust you offered during more than five years of professional work at the wind energy institute: it was a great time.

I also thank Stefano, my mentor. Your personal encouragement and support is warmly appreciated, especially during the time I decided to pursue this PhD project.

The work at TU Munich was always in close collaboration with my colleagues, Bastian, Bruno, Carlo S., Chengyu, Elli, Filippo, Franz, Helena, Jai, Jesse, Manos, Marta, Pietro, Stefan, Robin, Vlaho, and Wendy. I'm thankful of having been part of such a supportive and generally uncomplicated team. You made the big difference.

I also thank the students who I could work with during their thesis, internship or project work. Amr, Andi, Anil, Bastian, Daniel, Delphine, Erdal, Henry, Johannes, Matteo, Robert, Sivateja, Stefan, and Umut, your strong motivation and dedication made supervision and collaboration a pleasure.

I want to acknowledge the partners within the CompactWind and CL-Windcon projects. A special thanks belongs to Alexander Gerds and Stefan Kern who both supported my field data work.

Two organizations, the European Academy of Wind Energy and WindForS have been of great value for me. Through their successful networking efforts, I got connected to the local and global wind energy research community and found peers and many new friends.

Finally and most importantly, I thank my parents, my bothers, and Laura: Your endless love and unconditional support is invaluable.

Contents

1	Introduction	1
1.1	Research topics and innovative content	2
1.2	Publications	6
2	Methods	11
2.1	Wind sensing	11
2.2	Wake detection	14
2.3	Wind farm models	18
2.4	Wind farm control	21
3	Paper 1: Local wind speed estimation, with application to wake impingement detection	25
4	Paper 2: Wind Tunnel Validation of a Wind Observer for Wind Farm Control	41
5	Paper 3: Wake detection for wind farm control – formulation and validation	51
6	Paper 4: Field testing of a local wind inflow estimator and wake detector	63
7	Paper 5: Brief communication: A double Gaussian wake model	83
8	Paper 6: Verification and Calibration of a Reduced Order Wind Farm Model by Wind Tunnel Experiments	93
9	Paper 7: Comparison of Analytical Wake Models with Wind Tunnel Data	107
10	Paper 8: Wind shear estimation and wake detection by rotor loads – First wind tunnel verification	121
11	Paper 9: Improving wind farm flow models by learning from operational data	131
12	Paper 10: Wind tunnel testing of a closed-loop wake deflection controller for wind farm power maximization	161
13	Paper 11: Online model updating by a wake detector for wind farm control	171
14	Paper 12: Wind tunnel testing of wake steering with dynamic wind direction changes	179
15	Paper 13: Study of wind farm control potential based on SCADA data	205
16	Discussion and Conclusion	219
16.1	Outlook	220
	Bibliography	223

Introduction

It is extremely likely that the increase of greenhouse gases within the earth atmosphere and the subsequent global warming since the mid-20th century is caused by human [1]. Due to the expected devastating effects of future global warming, the Paris Agreement of 2015 formulated the goal of keeping the temperature increase below 2° Celsius compared to the pre-industrial level. Today, this agreement is signed or acceded by almost all countries [2] and many countries try to reduce their greenhouse gas emissions.

A large fraction of man-made greenhouse gas emissions can already be attributed to electricity generation and a further increase in the electricity demand due to the future electrification of other sectors is very likely. Therefore, the development of solutions reducing the emissions from electricity production are of huge importance. Apart from a more sensible and less lavish electricity consumption, technologies to generate electricity with significantly reduced emissions can support the accomplishment of the Paris Goals. Today, commercially available technologies include biomass, geothermal, hydropower, nuclear, concentrated solar power, photovoltaics, and wind energy – here sorted from high to low life-cycle equivalent CO₂ emissions per kWh produced [3]. Note that wind energy still has positive life-cycle emissions, which are however about 70 times smaller than for conventional coal-fired power plants.

Even though there is no single best technology, wind energy has experienced a tremendous growth during the last decades due to several reasons including policies, subsidies and significant technological improvements. Indeed, the electricity production from wind energy has increased globally from 104 TWh in 2005 to 1273 TWh in 2018, representing more than a twelve-fold in 13 years. In 2018, 4.8% of the global electricity production has been generated by wind energy [4]. In Germany, that number has already reached 24.6% in 2019 [5]. This electricity is produced by a globally installed wind power capacity of 591 GW at the end of 2018 [6], out of which 60 GW are installed in Germany. Forecasts predict a relentless growth in the coming decades. The *Stated Policies Scenario* of the International Energy Association predicts a globally installed wind energy capacity of 1856 GW in 2040, which is more than three times the installed capacity at the end of 2018 [7].

The future growth of wind energy cannot be taken for granted. Indeed, the past growth revealed some new problems that will become even more relevant in a widespread use of wind energy. Especially in Germany, a public resistance caused among others by the turbines impact on landscape, their noise, bird strikes, and psychological effects is becoming stronger. In fact, changed policies and other causes have already led to a drastic reduction in new installations in Germany [8], especially in Bavaria [9].

Developing solutions to reduce such negative impacts on society and environment is part of the agenda within industry and research, even though the core goal is typically a reduction of the cost of energy [10]. Such cost reduction directly promotes wind energy usage leading to less emissions from conventional power plants. Likewise within this dissertation: new methods and tools have been developed, implemented and tested with the goal of improving the operation of wind farms and thereby primarily decreasing their cost of energy. Indirectly, the developed methods can also help reducing the negative impact of wind energy on the environment. For example, the achieved wind farm efficiency improvement through wind farm control increases the energy capture per surface area.

Thereby less space is needed and even sites with less good wind conditions can be economically used for wind energy projects. Hence, ecologically or socially precious sites might be left untouched.

1.1 Research topics and innovative content

The goal of this dissertation is the development and demonstration of methods to improve wind condition awareness on wind turbine and farm level to finally benefit wind farm control and other applications. To structure the work, four main topics – wind sensing, wake detection, wind farm models, and wind farm control – have been defined. Therein, methods and models have been developed and tested based on numerical simulations; the technical feasibility and validation has been confirmed in scaled wind tunnel tests; and full-scale tests as well as real turbine data has been employed to prove and demonstrate some of the applications.

In the following, the four topics are highlighted, their background is discussed and the respective innovative content within this dissertation is stated. Note that the topics and respective publications are highly linked among each other, as also described later on. Some parts of the following text within this chapter are excerpts of the various publications presented within this dissertation.

Topic 1: Wind sensing

Background: Wind turbines are not fully aware of the wind conditions they operate in. Every turbine is equipped with wind sensors on top of the nacelle, which are typically used for aligning the turbine into the wind and to identify whether cut-in or cut-out wind speeds have been reached. Even though the complex turbine-flow interaction is typically anticipated, those measurements are only accurate enough for some tasks.

External measurement equipment, as met-masts, LiDAR (Light Detection And Ranging) systems and other remote sensing technologies are often costly and difficult to use and integrate. Therefore, such equipment is mainly used in applications as site assessment or research projects. In addition, external and nacelle-based sensors often provide point information only, however wind conditions show spatial variability within the rotor disc and also within the whole wind farm, especially in complex terrain [11], but also in large offshore wind farms [12].

The knowledge of the detailed wind turbine inflow during operation or even historically benefits many applications. For example, a turbine controller can be improved when scheduled as function of wind speed [13], consumed turbine lifetime depends on historic wind and environmental conditions [14], and for successful wind farm control it is crucial to know the atmospheric stability and wake positions within a farm [15]. Moreover, wind farm power and weather forecasting, site assessment for wind farm extensions, wake detection triggered sector management (shutdown for closely spaced turbines), estimation of available wind farm power, and many further applications can benefit from detailed information of the inflow on each turbine rotor.

Innovative content: A new method estimating the turbine inflow using the *rotor-as-a-sensor* concept has been developed, implemented and successfully tested within this doctoral project. The wind estimation method bases on the analysis of measured blade root bending moments. The key advantage of the method is that the implementation on a turbine is simple and cheap as it requires only a software update. The necessary load sensors are already available on many modern turbines, especially if individual-pitch-control or condition monitoring is installed.

In details, a new *cone* coefficient is defined and computed using a standard numerical turbine model. The coefficient relates blade bending loads to the local inflow at the blade, depending on the tip-speed-ratio, blade pitch and other parameters. Employing the coefficient or a respective

look-up-table during turbine operation or historically, the estimated blade inflow can be mapped to a part of the rotor disc given the known blade position. Thereby a local- or sector-effective wind speed in four different quadrants of the rotor is estimated, but also local turbulence or rotor-effective inflow shear, that can be used as rough proxy of the atmospheric stability, can be inferred.

The method is tested systematically within a simulation environment in **Paper 1**. First experimental tests in scaled wind tunnel experiments are described in **Papers 2** and **3**. Finally, a successful field test on a 3.5 MW wind turbine is presented in **Paper 4**.

Topic 2: Wake detection

Background: The exact wake positions within a wind farm are often unknown or only known with low accuracy. Modern wind farms may contain tens or hundreds of individual wind turbines. Each machine converts a part of the kinetic energy carried by the air stream into electrical energy. As a consequence of this energy conversion process, behind each wind turbine a complex wake structure develops, which is characterized by a slower wind speed and a higher turbulence intensity. Wakes undergo complicated phenomena, including the breakdown of near-rotor vortical structures, mixing, recovery, meandering and merging with other wakes. All such processes are strongly influenced by several parameters, including the operating conditions of the machines, the characteristics of the atmosphere, the orography and roughness of the terrain or the sea state, and the interactions among neighboring wakes. Wakes impinging on downstream wind turbines within a wind farm are a cause of significant power loss and increased fatigue loading [16]. Depending on the situation, the increased loading forces in some cases wind farm operators to completely switch off closely spaced turbines for large wind direction sectors (sector management) [17].

Several solutions to address the problem of wake interaction are currently being actively investigated, including the alleviation of loads on the affected downstream machines by active controls [18] and the idea of redirecting wakes away from downstream turbines as discussed in more detail in Topic 4. For developing such solutions, a precise knowledge of the wind inflow conditions at the rotor disk of each machine as well as the wake positions within the wind farm is essential. For example, when using wake redirection to alleviate a partial wake overlap, it is necessary to know with certainty which side of the downstream rotor is affected, in order to deflect the wake of the upstream machine in the correct direction.

The wakes within a wind farm can be predicted by wind farm models (see also Topic 3), for example used in wind farm layout planning for the estimation of the annual energy production. Some of those models show good long-term accuracy, however especially their short-term prediction quality and reliability is strongly affected by a number of factors, including the stability and characteristics of the atmosphere and the proper calibration of the model parameters, as well as a good knowledge of the ambient wind conditions. For instance, during wind farm operation even a small bias in the wind direction model input leads to a significant error in the predicted wake position at a turbine several diameters downstream. In addition to wind farm models, also LiDAR and other remote sensing devices have been proposed for measuring wake positions within a wind farm. Installations are either based on ground [19] or nacelle [20, 21]. Even though some methods promise low cost, additional hardware is necessary by definition and the integration might be difficult.

At present, wind turbines in wind farms do not operate based on a detailed understanding of the wind conditions that affect them. In fact, wind turbines typically use only nacelle or hub

mounted wind measurement devices, which can only provide information on wind speed and direction at the single point in space where these devices are installed (see also Topic 1). Wind turbines are therefore unaware of the presence of an impinging wake.

Innovative content: Different wake detection methods, employing the wind sensing methods (see innovative content of Topic 1 and **Papers 1-4**) have been developed, implemented and successfully tested within this doctoral project. Key advantages are the abundance of additional hardware compared to remote sensing solutions, and an improved accuracy with respect to wake models in case of uncertainties.

The first method bases almost purely on the wind sensing methods and does not require any wind farm or wake model. The result is an independent wake detection, that can still be compared to wind farm model predictions, for example to identify significant violations between model and reality. The method works as follows: The local wind estimation shows a distinct fingerprint of an impinging wake, which is characterized by a significantly reduced flow velocity and increased turbulence intensity in the part of the rotor disc that is mostly affected by the wake. A simple but efficient threshold comparison has been proposed to indicate whether a wake impinges on either side of a turbine rotor. The approach is tested within a simulation environment in **Paper 1**, within a scaled wind tunnel environment in **Papers 2 and 3**, as well as in full-scale in **Paper 4**.

A second method measures the exact position of an impinging wake on a turbine rotor. Thereby, a wake model is directly compared against the local flow velocity estimates, such that more detailed information, carrying the exact wake position with respect to the rotor disc, can be inferred. The method is tested in a scaled wind tunnel environment in **Paper 8**.

Finally, a sophisticated method has been developed that combines the wind sensing method with a wind farm model. This way, the wind farm model is improved online during operation of the wind farm, generating high quality predictions of the wake speed and position. Following the updated model, significant improvements in model predictions can be achieved especially during situations that are characterized by uncertain wind farm model inputs, as shown in wind tunnel experiments in **Paper 11**.

Topic 3: Wind farm models

Background: Wind farm models are used to simulate the performance of wind power systems. A wind farm model typically includes a model of the wind turbines and a model of the flow.

Various wind farm flow models have been developed and are described in the literature. While Direct Numerical Simulation (DNS) is still out of reach for practical applications due to its overwhelming computational cost, Large Eddy Simulation (LES) methods are now routinely used for the modeling of wind farm flows [22, 23]. Although invaluable for the understanding of the behavior of the atmospheric boundary layer and of wakes, LES is however still very expensive, so that its use outside of some specialized applications is limited. To reduce cost, one can resort to lower fidelity computational fluid dynamics (CFD) models [24], or to the extraction of reduced order models (ROMs) from higher fidelity ones [25]. Instead of deriving models from first principles, another widely adopted approach is to use engineering models, which are expressed in the form of parametric analytical formulas with a limited number of degrees of freedom and hence a much reduced numerical complexity [26–28].

Such analytical wake models, as opposed to high-fidelity CFD models, are usually simple, easy to implement and computationally inexpensive. In fact, they only simulate macroscopic average effects of wakes and not their small scales and turbulent fluctuations. Analytical wake models

find applicability in all those cases that do not need to resolve small spatial and fast temporal scales, such as the calculation of the power production of a wind plant over a sufficiently long time horizon. Such models are also extremely useful in optimization problems, where a large number of simulations might be required before a solution is reached, or where calculations need to be performed on the fly in real-time. Analytical wake models are thus often utilized in wind farm layout planning and in the emerging field of wind farm and wake control [24, 29, 30]. Even though such models are constantly improved and refined [31], they will most likely always exhibit only a limited accuracy in many practical applications, for example whenever an important role is played by effects such as orography, (seasonal) vegetation, spatial variability of the wind, sea state roughness, the erection of other neighboring wind turbines, the presence of obstacles, and others. In addition, low fidelity models often lack some physics, e.g. the flow acceleration caused by wake and rotor blockage, secondary steering or others.

However, because of their indisputable usefulness, analytical wake models have been extensively studied in the literature. The Jensen (PARK) formulation is one of the most widely used wake models, to the extent that it is sometimes considered as the industry standard [32]. The model was first introduced by Jensen [33], and later further developed by Katic [34]. Other widely used and cited wake models include the Frandsen model [26], the FLORIS model [27], and the EPFL Gaussian models [28, 35].

Innovative content: An analytical turbine wake model, previously published with errors, has been corrected and presented in **Paper 5**. Due to the models double Gaussian wake shape, the wake model features an improved accuracy with respect to state-of-the-art models within the turbine near wake.

In **Paper 6**, wind farm model parameters are identified based on wake velocity measurements at hub height of an isolated scaled turbine, followed by an analysis of the model predicted power production within a scaled 3-turbine wind farm. Similarly, several different wind farm models are tuned in **Paper 7** and a detailed analysis of their respective accuracy in velocity predictions is presented.

Papers 8 and **11** combine the wind sensing approach (see Topic 1) with a wake model to enable the quantitative position estimation of an impinging wake (see Topic 2) and an online correction of the wake model itself.

Focusing on the practical applicability, **Paper 9** describes a method to calibrate and correct a wind farm model using only available SCADA (Supervisory Control And Data Acquisition) measurements. The idea pursued takes a rather pragmatic approach: based on the realization that it will always be difficult—if not altogether impossible—to include all effects and all physics in a model of limited numerical complexity, a given model is corrected by unknown parametric terms, which are then learnt by using operational data.

The application of wind farm models for wind farm control is discussed in **Paper 13**, and a scaled wind tunnel experiment demonstrating model-based wind farm control using wake steering is described and presented in **Paper 12** (for both, see Topic 4).

Topic 4: Wind farm control

Background: In the past, most of the research in wind energy technology focused on the optimization of wind turbines. In recent years, interest has expanded from the level of the individual machines to the one of wind farms, or to emphasize its role as a production unit often also called *wind power plant* within this context.

Wind energy production is often organized in wind turbine clusters and farms rather than single isolated wind turbines, because of lower construction, maintenance and commissioning costs. Since the wakes of upwind turbines have a strong impact on the power and loading of downstream machines, the design and planning of a wind farm take already the complex interactions through the individual wakes partially into account [36].

Recently, interest has grown in the area of cooperative control of wind turbines during operation, with the goal of maximizing the total wind farm power output, minimizing fatigue loading, or achieving a given power setpoint [37]. To reach those or similar goals, some form of wake coordination and control among the wind turbines is required. Ideas include the redirection of wakes away from downstream machines [22, 38–40], the curtailment of upstream wind turbines [41] and the promotion of a faster wake recovery, for example by periodic pitching of the rotor blades [42].

Wake steering, a particularly promising approach, uses an intentional misalignment of the upstream turbine rotor with respect to the incoming wind vector. Thereby, a lateral force is induced on the flow, leading to a slight change in the local wind direction and to a deflection of the wake downstream. The loss in power production caused by the turbine misalignment, can be more than compensated for by the increased power production of a wake-free downstream turbine.

Today, various wake steering wind farm control algorithms have been tested in simulation environment [27, 43, 44] and first field tests are being conducted showing very promising results [45–47].

Innovative content: A closed-loop wind farm controller, with a model-free gradient based extremum seeking algorithm, has been tested in a scaled 3-turbine wind farm. The experiment presented in **Paper 10** shows significant power gains and is the first closed-loop wind farm control experiment within a scaled wind farm. The work was awarded the Energy Price by the State of Bavaria [48].

The use or inclusion of wind farm models can improve the control performance and **Paper 13** presents first a field validation of the model power predictions and second a model-based estimation of the potential increase of the annual energy production for a specific onshore wind farm assuming wake steering wind farm control.

Combining the wind sensing method with a wind farm model, improved predictions of the wake speed and position, can be achieved (see Topic 2). Accordingly, in **Paper 11**, the expected achievable power production of a scaled wind farm using wind farm control is predicted using a wind farm model that is corrected online using the wind sensing method. Results highlight an improved predictability, especially during situations that are characterized by uncertain model inputs.

In **Paper 12**, a model-based wind farm controller for power maximization is tested in a scaled wind farm with varying ambient wind conditions. The open-loop controller relies on look-up-tables computed using different wind farm models, storing the optimal turbine misalignments depending on ambient wind conditions. Even though dynamic effects as wake propagation are not taken into account by the controller, a significant increase in power production could be achieved, especially when using the method and wind farm model presented in **Paper 9** (see Topic 3).

1.2 Publications

Within this publication-based dissertation, thirteen publications are included and referred to. Figure 1.1 shows a schematic overview of all publications (**Papers 1-13**), and the respective references are

listed below in Section 1.2.1. For reasons of clarity and comprehensibility, a color bar is assigned to each paper in Fig. 1.1 showing the four main topics covered: wind sensing (light gray), wake detection (gray), wind farm model (blue) or wind farm control (green). The papers are categorized in simulation, wind tunnel and full-scale, see also the dashed lines. The publications led by the author of this dissertation are marked with superscript L, the remaining papers contain significant scientific contribution, but are not led by the author.

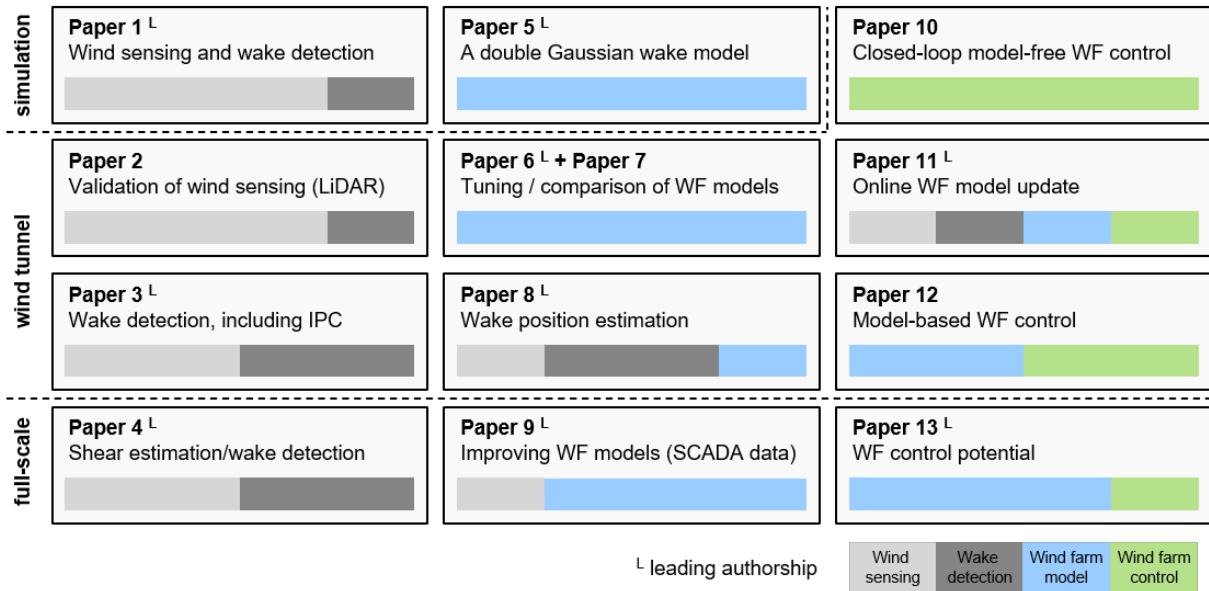


Figure 1.1: Schematic overview of publications presented within this thesis.

The first set of papers (first column in Fig. 1.1) focuses on topics of wind sensing and wake detection—starting at simulations, covering wind tunnel experiments and finally also full-scale experiments. In **Paper 1** the method of wind sensing and wake detection is described first and tested systematically within a simulation environment. An experimental test within a wind tunnel is conducted in **Paper 2**, including a validation using short-range LiDAR measurements of the turbine inflow. The applicability of the wake detection method, also during individual pitch control (IPC), is shown in **Paper 3**. **Paper 4** finally presents a test and validation of the wind estimation and wake detection methods on a multi-MW full-scale wind turbine.

The second set of papers (second column) focuses on wind farm models even though links to wind sensing and wake detection exist. **Paper 5** shows the development of a double Gaussian wake model for the near wake. **Papers 6** and **7** cover the tuning and comparison of wind farm (WF) models for scaled wind turbines. **Paper 8** combines the wind sensing approach with a wake model to enable the quantitative estimation of wake position. **Paper 9** describes a method to improve wind farm models using historical turbine measurements.

The last set of papers (third column) focuses on wind farm control, and includes links to wind sensing, wake detection, as well as wind farm models. In **Paper 10** a closed-loop model-free wind farm control algorithm is tested within the wind tunnel to maximize the total power. **Paper 11** combines wind sensing and wind farm models to online correct the modeled wake position and deficit, allowing an improved prediction of the maximum achievable power during farm operation and control. **Paper 12** presents model-based farm control during wind direction changes using different underlying wind farm models, again in wind tunnel experiments. **Paper 13** shows finally the application of a wind farm model on a full-scale plant to estimate wake losses and the potential increase in annual energy production using wake steering control.

1.2.1 List of publications

The following peer-reviewed, published and Scopus-listed publications have been included into this thesis. The respective chapter of each publication (Chapters 3 to 15) includes a summary and states the contribution of the author of this dissertation. As each publisher granted a reprint permit for this thesis, a copy of each paper is also included in each chapter.

Publications led by the author:

- **Paper 1:** C. L. Bottasso, S. Cacciola, and J. Schreiber, “Local wind speed estimation, with application to wake impingement detection,” *Renewable Energy*, vol. 116, pp. 155–168, 2018. doi: 10.1016/j.renene.2017.09.044
- **Paper 3:** C. L. Bottasso, S. Cacciola, F. Campagnolo, and J. Schreiber, “Wake detection for wind farm control – formulation and validation,” *34th Wind Energy Symposium, AIAA SciTech Forum*, 2016. doi: 10.2514/6.2016-1741
- **Paper 4:** J. Schreiber, C. L. Bottasso, and M. Bertelè, “Field testing of a local wind inflow estimator and wake detector,” *Wind Energy Science*, vol. 5, no. 3, pp. 867–884, 2020. doi: 10.5194/wes-5-867-2020
- **Paper 5:** J. Schreiber, A. Balbaa, and C. L. Bottasso, “Brief communication: A double-gaussian wake model,” *Wind Energy Science*, vol. 5, no. 1, pp. 237–244, 2020. doi: 10.5194/wes-5-237-2020
- **Paper 6:** J. Schreiber, E. M. Nanos, F. Campagnolo, and C. L. Bottasso, “Verification and calibration of a reduced order wind farm model by wind tunnel experiments,” *Journal of Physics: Conference Series*, vol. 854, p. 012041, 2017. doi: 10.1088/1742-6596/854/1/012041
- **Paper 8:** J. Schreiber, S. Cacciola, F. Campagnolo, V. Petrović, D. Mourembles, and C. L. Bottasso, “Wind shear estimation and wake detection by rotor loads — first wind tunnel verification,” *Journal of Physics: Conference Series*, vol. 753, p. 032027, 2016. doi: 10.1088/1742-6596/753/3/032027
- **Paper 9:** J. Schreiber, C. L. Bottasso, B. Salbert, and F. Campagnolo, “Improving wind farm flow models by learning from operational data,” *Wind Energy Science*, vol. 5, no. 2, pp. 647–673, 2020. doi: 10.5194/wes-5-647-2020
- **Paper 11:** C. L. Bottasso and J. Schreiber, “Online model updating by a wake detector for wind farm control,” in *2018 Annual American Control Conference (ACC)*. IEEE, 2018, pp. 676–681. doi: 10.23919/ACC.2018.8431626
- **Paper 13:** J. Schreiber, B. Salbert, and C. L. Bottasso, “Study of wind farm control potential based on SCADA data,” *Journal of Physics: Conference Series*, vol. 1037, p. 032012, 2018. doi: 10.1088/1742-6596/1037/3/032012 (publication led in equal amount by B. Salbert)

Publications with significant scientific contribution by the author:

- **Paper 2:** F. Campagnolo, J. Schreiber, A. M. Garcia, and C. L. Bottasso, “Wind tunnel validation of a wind observer for wind farm control,” *Proceedings of the International Offshore and Polar Engineering Conference*, 2017. [Online]. Available: <https://www.onepetro.org/conference-paper/ISOPE-I-17-410>
- **Paper 7:** F. Campagnolo, A. Molder, J. Schreiber, and C. L. Bottasso, “Comparison of analytical wake models with wind tunnel data,” *Journal of Physics: Conference Series*, vol. 1256, p. 012006, 2019. doi: 10.1088/1742-6596/1256/1/012006

-
- **Paper 10:** F. Campagnolo, V. Petrović, J. Schreiber, E. M. Nanos, A. Croce, and C. L. Bottasso, “Wind tunnel testing of a closed-loop wake deflection controller for wind farm power maximization,” *Journal of Physics: Conference Series*, vol. 753, p. 032006, 2016. doi: 10.1088/1742-6596/753/3/032006
 - **Paper 12:** F. Campagnolo, R. Weber, J. Schreiber, and C. L. Bottasso, “Wind tunnel testing of wake steering with dynamic wind direction changes,” *Wind Energy Science*, vol. 5, no. 4, pp. 1273–1295, 2020. doi: 10.5194/wes-5-1273-2020

Methods

Within this dissertation various new methods have been developed, but also existing methods have been implemented and integrated. As presented in Section 1.1, four main topics have been defined and the relevant methods are summarized in the following sections accordingly.

As this is a cumulative dissertation, the summarized methods have been published previously. Consequently, this chapter contains also excerpts of the various publications included within this dissertation.

2.1 Wind sensing

The concept of using the wind turbine rotor as a wind sensor has been proposed to improve wind condition awareness [62–64]. In a nutshell, wind sensing uses the response of the rotor—in the form of loads, accelerations and other operational data—to infer the characteristics of the wind blowing on the turbine. Therefore, wind sensing is a sort of model inversion, where the response of the system is used to estimate the disturbance (in this case, the wind).

The simplest and probably most widely used wind sensing technique is the torque-balance estimation [65, 66]. Thereby, turbine power or torque are used to estimate the rotor-effective wind speed by the power curve or power coefficient. The concept has been also extended to estimate other characteristics of the inflow, notably the wind directions and shears, as reviewed in [64].

Within this dissertation, a new method is developed that bases on an aerodynamic *cone* coefficient and uses the blade out-of-plane bending moment to estimate the local wind speed at the position occupied by a blade. The method is very similar to the torque-balance estimation of the wind speed, with the important difference that it produces a localized speed estimate instead of a rotor-effective one. The rotating blades therefore operate as scanning sensors that, travelling across the rotor disk, sample the local variability of the inflow. In turn, the local wind speed estimates are used for obtaining two key pieces of information on the inflow: the vertical shear, which is an important load-driver and an indicator of atmospheric stability, and the horizontal shear, which can be used to detect the presence and location of an impinging wake (methods are shown in Section 2.2). Today, only a scanning LiDAR would be able to provide similar information on the inflow, albeit not exactly at the rotor disk—as done here, as the rotor itself is the sensor in this case—and with a very different level of complexity and cost.

The present method has some very interesting features. First, it is model-based, and therefore it does not necessitate the use of extensive data sets for its training. Second, it is based on an extremely simple model of the rotor (expressed through the cone coefficient), which can be readily computed from a standard aeroelastic model of a wind turbine. Third, the resulting estimator is in the form of a simple look-up-table that is computed offline, resulting in an online on-board implementation of negligible computational cost. Fourth, when load sensors are already installed on the turbine for load-alleviating control or monitoring, this wind sensing technique requires no additional hardware, and therefore its implementation simply amounts to a software upgrade.

The remaining section is organized as follows. First, the basic method to estimate the standard rotor-effective and the novel blade-effective wind speed using the cone coefficient is presented in Section 2.1.1. Second, a simple procedure to derive a sector-effective wind speed from the blade-effective wind speed summarized in Section 2.1.2. Finally, it is shown in Section 2.1.3 how the effective vertical and horizontal wind shear can be estimated.

2.1.1 Rotor- and blade-effective wind speed estimation

Considering a steady and uniform wind speed V , the power C_p and cone C_m coefficients are defined as

$$C_p(\beta, \lambda, q) = \frac{T_{\text{aero}}\Omega}{0.5\rho AV^3}, \quad (2.1a)$$

$$C_m(\beta, \lambda, q, \psi_i) = \frac{m_i}{0.5\rho ARV^2}, \quad (2.1b)$$

where β is the blade pitch angle, $\lambda = \Omega R/V$ the tip speed ratio, Ω the rotor speed, R is the rotor radius and $A = \pi R^2$ the swept disk area, ρ is the air density and $q = 1/2\rho AV^2$ the dynamic pressure, while T_{aero} is the aerodynamic torque. The azimuthal position of the i th blade is given by ψ_i , while m_i is its out-of-plane root bending moment. Coefficients C_p and C_m are readily computed using an aeroelastic model of the turbine, today customarily based on a blade element momentum (BEM) method, for example the one implemented in the FAST code [67].

Different approaches to estimate wind speed from the power coefficient are reviewed in detail by Soltani et al. [66]. Here, both the power and the cone coefficients are used: while the former yields a rotor-effective wind speed (i.e., an average quantity over the entire rotor disk), the latter is used to sample the *local* wind speed at the azimuthal position occupied by a blade. Given coefficients C_p and C_m computed for a reference air density ρ_{ref} , look-up-tables (LUTs) are generated that return wind speeds given measured loads T_{aero} or m_i , blade pitch β , rotor speed Ω and air density ρ . Noting the rotor-effective wind speed estimated from the torque balance equilibrium as V_{TB} and the one from blade loads as V_i , the inversion of Eqs. (2.1) yields

$$V_{\text{TB}} = \text{LUT}_{C_p}(\beta, \Omega, T_{\text{aero}}, \frac{\rho}{\rho_{\text{ref}}}), \quad (2.2a)$$

$$V_i = \text{LUT}_{C_m}(\beta, \Omega, \psi, m_i, \frac{\rho}{\rho_{\text{ref}}}). \quad (2.2b)$$

Instead of the simple non-linear model inversion adopted here for simplicity, more sophisticated methods can be used, for example based on Kalman filters or input observers [66], which may slightly improve the results at the cost of an increased complexity. A rotor-effective wind speed can also be obtained from the blade-effective ones by simple averaging over all (three) blades:

$$V_B = 1/3 \sum_{i=1}^3 V_i. \quad (2.3)$$

Although in a non-uniform inflow the two rotor-effective speeds V_{TB} and V_B are not necessarily identical, they are in practice very similar. The redundancy offered by V_{TB} and V_B offers opportunities for sensor calibration, as shown in **Paper 4**.

In Eq. (2.2a), T_{aero} is computed from the dynamic torque balance equilibrium $J\dot{\Omega} = T_{\text{aero}} - T_{\text{meas}} - T_{\text{loss}}$, where J is the total rotor, drivetrain and generator rotational inertia, while $\dot{\Omega}$ is the rotor acceleration and T_{meas} is the measured torque at the generator. Mechanical losses in the whole drivetrain are taken into account by the term T_{loss} [66]. Here, for the accuracy of the wind speed estimate, a dynamic model is used to compute the aerodynamic torque. In fact, the energy converted into rotor acceleration or deceleration is typically large, given the large rotational inertia of the system.

A simpler approach is used for Eq. (2.2b), where the blade dynamic response is neglected. This way, the induced out-of-plane bending moment is directly set to the corresponding measured load, i.e. $m_i = m_{i,\text{meas}}$, where $m_{i,\text{meas}}$ is provided by blade-mounted strain gages, optical sensors or similar devices. Although even in this case one could include a dynamic model of the flapping motion, similarly to what is done for the torque balance case, the smaller inertia and high damping of this degree of freedom makes this more sophisticated approach superfluous.

The power and cone coefficients of Eqs. (2.1) are computed when the rotor axis is aligned with the ambient wind direction. Hence, strictly speaking, Eqs. (2.2) can be used to estimate wind speeds only in the same aligned conditions. However, this is typically not the case in practice, as turbines are often misaligned with respect to the wind by several degrees. It is shown in the results of **Paper 4** that moderate misalignments do not significantly affect the estimation of wind speeds, and that the effects of larger misalignments can be corrected for pragmatically.

2.1.2 Sector-effective wind speed estimation

An average wind speed over a rotor sector can be readily computed by averaging the blade-effective estimate V_i between two azimuthal angles ψ_a and ψ_b :

$$V_S = \int_{A_S} V_i(\psi) dA_S, \quad (2.4)$$

where $A_S = (\psi_b - \psi_a)R^2/2$ is the area of the sector. A new sector-effective speed estimate is generated as soon as a blade leaves the sector.

The sector width can be arbitrarily defined. Figure 2.1 shows the case of the four equally sized 90-degree-wide sectors, yielding the four sector-effective wind speed estimates $V_{S,\text{left}}$, $V_{S,\text{right}}$, $V_{S,\text{up}}$, and $V_{S,\text{down}}$. Clearly, a finer sampling of the inflow over the rotor disk can be achieved by using smaller sectors. With three blades, each of the sectors is updated three times per rotor revolution. With one single instrumented blade, the update frequency reduces to once per revolution.

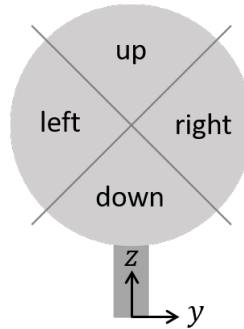


Figure 2.1: Wind turbine rotor disk with sectors and inflow coordinate system. This naming convention is in the downstream viewing direction.

It is shown in **Paper 1** that, for a linear inflow shear and a 90-degree-wide sector, the sector-effective wind speed corresponds to the inflow speed at a distance of approximately $2/3R$ from the hub center.

2.1.3 Shear estimation

The vertical wind shear can be modeled as a power law profile with exponent α , while the horizontal shear is assumed to be linear with coefficient κ . The inflow wind speed V can therefore be written as

$$V(z, y) = V_H \left(\left(\frac{z}{z_H} \right)^\alpha + \kappa \frac{y}{R} \right), \quad (2.5)$$

where z and y are the vertical and lateral coordinates, respectively, with origin at the turbine foundation, as shown in Fig. 2.1. Furthermore, V_H is the speed at the hub center, which is located at $z = z_H$ and $y = 0$.

Assuming that the sector-effective speed samples the inflow profile at $\pm 2/3R$ along the z and y axes, according to **Paper 1**, the shear coefficients can be estimated from the sector-effective wind speeds by using Eq. (2.5), which yields

$$\alpha_B = \ln \left(\frac{V_{S,\text{up}}}{V_{S,\text{down}}} \right) \left(\ln \left(\frac{z_H + 2/3R}{z_H - 2/3R} \right) \right)^{-1}, \quad (2.6a)$$

$$\kappa_B = \frac{3}{2} \frac{V_{S,\text{right}} - V_{S,\text{left}}}{V_{S,\text{right}} + V_{S,\text{left}}}. \quad (2.6b)$$

This way, the vertical shear is estimated using the top and bottom sectors, while the horizontal shear using the two lateral sectors. One could also use all four sectors together, and solve Eq. (2.5) simultaneously in a least squares sense for both α_B and κ_B .

2.2 Wake detection

The first part of this section, Section 2.2.1, includes the description of a model-free wake detection method that almost purely bases on the wind sensing methods without the use of any wake model. The second part, Section 2.2.2, describes methods to include a wake or wind farm model, such that more detailed wake information can be obtained.

2.2.1 Model-free

The model-free wake detection method has been formulated exploiting the distinct fingerprint that a wake causes on a downstream turbine when it is impinging on the rotor. The method's key feature is its simplicity. Successful experimental tests have been conducted in wind tunnel experiments presented in **Papers 2** and **3**, as well as in full-scale presented in **Paper 4**.

As a turbine wake can always be characterized by a reduced flow velocity, the sector-effective wind speed estimates, see Section 2.1.2, of a turbine operating in the proximity or within a wake of an upstream turbine, provides a variation, especially in the horizontal turbine rotor sectors. Without wake interaction, the wind speed within the left and right sectors, see Fig. 2.1, are expected equal, if averaged over a long enough time horizon to remove turbulent fluctuations. Note that a moderate turbine misalignment, that generally occurs during normal turbine operation, is not affecting the estimates significantly and that a larger known misalignment, used for wake steering, can be corrected for. On the other hand, the vertical sectors (up and down) are not equal and vary depending on the amount of vertical inflow shear caused mainly by the atmospheric stability and surface roughness.

A significant horizontally sheared inflow can be expected in case of larger obstacles blocking the inflow, which are typically not within the proximity of wind turbines. Importantly, also a neighboring wind turbine can be seen as obstacle, as due to the energy conversion process the flow velocity is reduced.

Assuming a similar hub height of the upstream turbine and its wake following approximately the surface of the terrain, the shed wake affects the downstream turbine horizontal sector-effective wind speed estimates qualitatively as a function of wind direction as illustrated in Fig. 2.2. In the lower part of the figure, different exemplary wake interference scenarios, indicated by letters A-E, are shown for a wind farm of two wind turbines from top-view. The upstream turbine rotor is shown by the gray bar and for the downstream turbine rotor the black and red bars indicate the left and right (downstream viewing) rotor disc sectors respectively. The wake of the upstream turbine is depicted in blue and

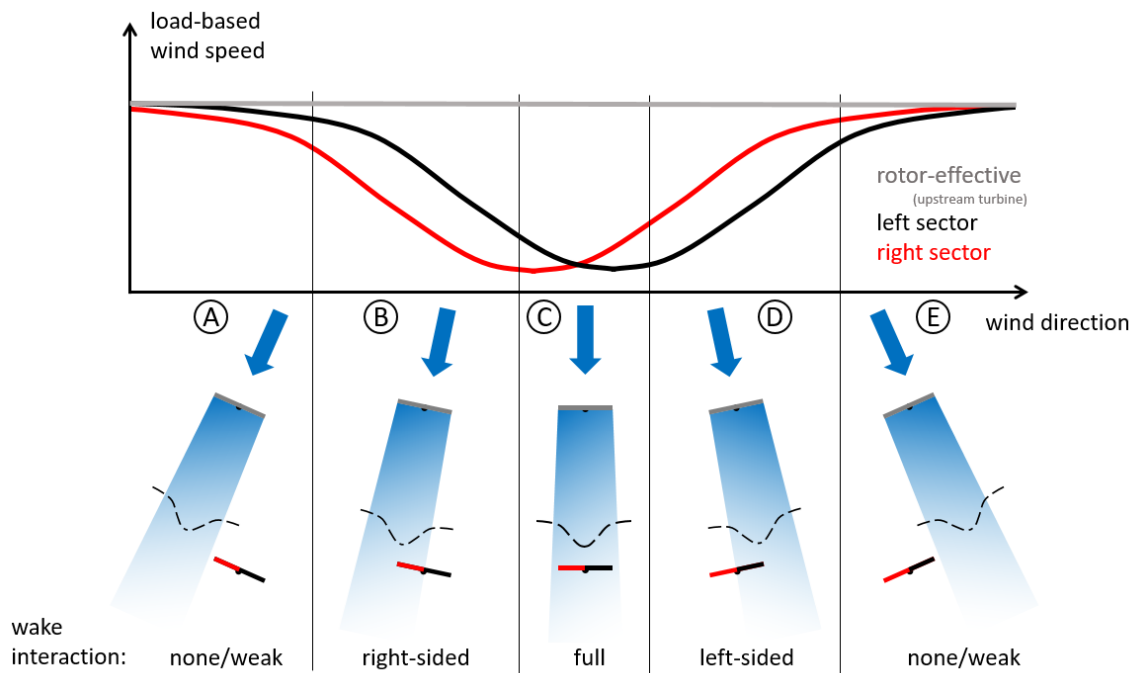


Figure 2.2: Illustration of the model-free wake detection concept.

the wake profile is sketched using dashed lines therein. The wake of the downstream turbine is not included. The ambient wind direction is shown by the blue thick arrow and, as in conventional wind farm operation, both turbine rotors are oriented to face the incoming wind. The upper part of Fig. 2.2 shows the velocity estimate or fingerprint in the left and right sectors as a function of wind direction. For low wind directions corresponding to scenario A, the wake of the upstream turbine is not or only very weakly affecting the downstream turbine. Still, depending on the wake expansion and wake meandering a slightly reduced velocity may be estimated within the right sector, as it is closer to the wake center. In scenario B the wind direction has increased, and the right sector is significantly affected by the upstream turbine wake. The left sector is also partially affected and, depending on the wake overlap a smaller or larger reduction can be observed. Note that this right sided wake impingement is always characterized by a significantly lower velocity in the right sector compared to the left. Scenario C shows the situation that the upstream turbine wake is fully impinging on the downstream turbine. This full wake scenario shows significant reductions in both sector velocities. As no significant delta between the two sector velocities can be identified, the scenario can be distinguished from a weak or absent wake interaction (scenario A and E) by a comparison of the absolute flow velocity, for example given by the rotor-effective wind speed estimate of the upstream turbine, indicated in gray. Scenarios D, showing a left-sided wake impingement, and E are symmetric to scenario B and A.

Based on these observations, a simple approach to detect a wake interference condition is to calculate the relative wind speed difference δ_V between the two rotor sides, by using a filtered sector-effective and rotor-effective wind speed

$$\delta_V = \frac{\overline{V_{S,\text{right}}} - \overline{V_{S,\text{left}}}}{\overline{V_B}} \quad (2.7)$$

where $\overline{(\cdot)}$ indicates a low-pass filtered value. An indication of a left- or right-sided wake impingement may now be obtained by evaluating the sign of δ_V and comparing its absolute value with a threshold. Clearly, the choice of threshold and also low-pass filter cut-off frequency during implementation, see **Papers 3** and **4**, is delicate and needs special attention as both depend, among other factors, on the

turbine distance, the wake recovery in the given ambient wind conditions and of course the application that is supposed to use the obtained wake detector information.

Note that this method can be used as trigger for wind farm sector management or similarly for a gradient based wind farm control algorithm as presented in **Paper 10**.

2.2.2 Model-based

Wake position estimation

Based on the knowledge of wind conditions as the ambient turbulence intensity and wind speed, analytical wake models, see also Section 2.3, can be used to estimate the wake shape and its speed deficit. By evaluating the model at the downstream distance where the sensing turbine is located, a model-based wake profile can be generated specific to the upstream turbine operation and current ambient conditions.

In turn, one can calculate the wake model expected horizontal shear $\kappa_M(d)$ and expected rotor-effective wind speed $V_M(d)$ that a turbine operating within the wake at a given lateral distance d to the wake center should be exposed to. The idea is then to match expected and load based observed shear and as well as rotor-effective wind speed, in order to estimate the lateral distance d to the wake center. This can be obtained by solving the following optimization problem

$$d = \operatorname{argmin}_d \left(\begin{bmatrix} V_B - V_M(d) \\ \kappa_B - \kappa_M(d) \end{bmatrix}^T \begin{bmatrix} \frac{c}{V_\infty^2} & 0 \\ 0 & \frac{1-c}{\kappa_{\text{ref}}^2} \end{bmatrix} \begin{bmatrix} V_B - V_M(d) \\ \kappa_B - \kappa_M(d) \end{bmatrix} \right), \quad (2.8)$$

where scaling is performed by weights based on the mean ambient wind speed V_∞ and a reference shear κ_{ref} , while $c \in [0, 1]$ allows one to give more emphasis to one term or the other. For example, the actual value of V_∞ can be set to the low pass filtered rotor-effective wind speed estimation of the first row of wind turbines, while κ_{ref} can be set to the maximum expected shear.

Clearly, instead of the horizontal shear κ also the relative wind speed difference δ_V can be used. It is similarly possible to use the individual sector-effective wind speeds, or other turbine estimated quantities as turbulence intensity, as long as the wake model shows a distinct dependency with respect to the lateral wake position d .

The method is demonstrated in detail in **Paper 8** by application on a scaled wind farm operated within a wind tunnel.

Integrated wind farm model update

This section extends the above presented idea of the wake position estimation. Here however, the corrections are fed back to the wind farm model itself. Thereby, based on the measurements made on the plant, the model can be corrected at run-time and consequently also the model predictions can be improved.

To correct model predictions, one might think of using standard and already available measurements of power and hub-height wind speed, for example using a Kalman filter. Unfortunately, this might not work in general because power and rotor speed might not carry enough informational content to correct for some model errors, as shown in **Paper 11**. In fact, in the case of a biased power prediction at a downstream wind turbine, one cannot distinguish whether the error is caused by a wrong wind speed in the wake (for example, due to an inaccurate modeling of wake recovery) or by a wrong location of the wake with respect to the impinged rotor disk.

This impasse is solved using the load based local wind speed estimates. This way, a wake model can be improved online during operation of the wind farm, generating high quality predictions of the wake speed and position within the farm. Depending on the application, the corrected model

can be used for example to improve the model-based control action. The idea is presented here with reference to a static wind farm flow model, although nothing in this approach prevents its extension to the dynamic case.

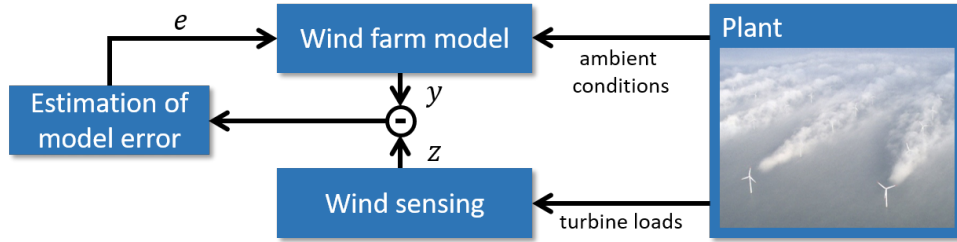


Figure 2.3: Wind farm model update scheme.

Figure 2.3 illustrates the concept, highlighting the main components. In general, the plant provides measurements of the ambient conditions to the wind farm model, such that it can be used for a specific purpose, for example wind farm control. For wind sensing, the specific turbine loads are employed as described in Section 2.1. By comparing the model outputs with the wind sensing estimates, the model error is estimated and the correction is fed back to the wind farm model.

In the following, the model update method is formulated based on a generic non-linear static wind farm model. A similar formulation could also be derived for a dynamic model, leading in that case to a standard Kalman filtering problem. The static model is written as

$$x = f(m, p), \quad (2.9a)$$

$$y = g(x), \quad (2.9b)$$

where f is a non-linear static function, which depends on the model formulation. Measurements of ambient conditions are noted m , and include air density and free stream wind speed as well as direction (typically estimated by the upstream wind turbines). Physical tunable coefficients of the model and the wind farm layout are represented by the vector of parameters p . The model states are indicated as x , and in the present work they include the velocity and lateral position of the wake of each turbine. A set of outputs y is defined by function g . The outputs may be represented by the turbine power of the downstream turbines, but they also include estimated sector-effective flow velocities at the downstream rotors.

In general, the predictions of the model states will be in error, due to a lack of model fidelity, mistuning of the parameters or inaccuracies in ambient conditions. This can be corrected by introducing a state error e . The corresponding corrected state \hat{x} becomes

$$\hat{x} = x + e. \quad (2.10)$$

A maximum likelihood estimate of the state error can be readily obtained by solving the following problem

$$\min_e (z - \hat{y})^T R^{-1} (z - \hat{y}) \quad (2.11)$$

where z are measurements and \hat{y} the corresponding updated model outputs ($y = g(\hat{x})$). For a given fixed covariance R , this procedure corresponds to the method of least squares.

Note that, as ambient wind conditions are often uncertain, the presented formulation could be extended by including these within the list of states. However, it is also clearly necessary to ensure the observability of all chosen states. For example, a wrong wind direction might not be distinguishable from a wrong wake location. The development of a general formulation for the estimation of wind farm flow model states is a problem of great interest, which has been however outside of the scope of this thesis.

The method is demonstrated in detail in **Paper 8** by application on a scaled wind farm operated within a wind tunnel.

2.3 Wind farm models

Within this section first, in Section 2.3.1, a double Gaussian wake model is described that models especially the near wake of an individual turbine. Second, in Section 2.3.2, it is shown how such a wake model can be extended and integrated to model the flow velocities and turbine power within a wind farm. Finally, in Section 2.3.3, a method to parameterize and improve a wind farm model by learning from operational data is presented.

2.3.1 Wake model

The double Gaussian wake model is derived similar to the Frandsen [26] and EPFL single Gaussian models [35]. Following their approach, the conservation of momentum principle is applied on an ansatz velocity deficit distribution, which includes an amplitude function. Thereby, an expression for the amplitude is obtained that assures conservation of momentum.

At the downstream distance x from the wind turbine rotor and at the radial distance r from the wake centerline, the wake velocity deficit $U_\infty - U(x, r)$ is modeled as the product of the normalized double Gaussian function $g(r, \sigma(x))$, which dictates the spatial shape of the deficit, with the amplitude function $C(\sigma(x))$. This yields

$$\frac{U_\infty - U(x, r)}{U_\infty} = C(\sigma(x))g(r, \sigma(x)), \quad (2.12)$$

where U_∞ represents the ambient wind speed and $U(x, r)$ the local flow velocity in the wake. The double Gaussian wake shape function, which is symmetric with respect to the wake center, is defined as

$$g(r, \sigma(x)) = \frac{1}{2} (e^{D^+} + e^{D^-}), \quad D_\pm = \frac{-(r \pm r_0)^2}{2\sigma^2(x)}, \quad (2.13)$$

where r_0 is the radial position of the Gaussian extrema. The standard deviation of the Gaussian function, noted $\sigma(x)$, represents the width (cross-section) of each of the two single Gaussian profiles. The wake expands with downstream distance x , causing the transformation of the initial double Gaussian profile in the near wake, through a flat-peak transition region, into a nearly single Gaussian profile in the far wake. As in [35] the wake expansion function is modeled as a linear function with respect to the downstream distance x

$$\sigma(x) = k^*(x - x_0) + \epsilon, \quad (2.14)$$

where parameter k^* controls the rate of expansion, while ϵ represents the wake expansion at x_0 , which is the downstream position of the stream tube outlet. A detailed discussion on the derivation of the parameters and x_0 , using a mass conservation between the Betz stream tube and the wake model can be found in **Paper 5**.

The conservation of momentum principle is now applied on the ansatz velocity deficit distribution, using the amplitude function $C(\sigma(x))$ as a degree of freedom. Accordingly, the axial thrust force T is related to the rate of change of momentum p of the flow throughout the stream tube (see Fig. 2.4), i.e.

$$T = \frac{dp}{dt} = \dot{m}\Delta\tilde{U} = \rho \int_{A_W} U(x, r) (U_\infty - U(x, r)) dA_W, \quad (2.15)$$

where \dot{m} is the mass flow rate through the stream tube, $\Delta\tilde{U}$ an effective wake velocity deficit, ρ the air density and A_W a planar cross-section at least large enough to contain the wake deficit. Equation (2.15)

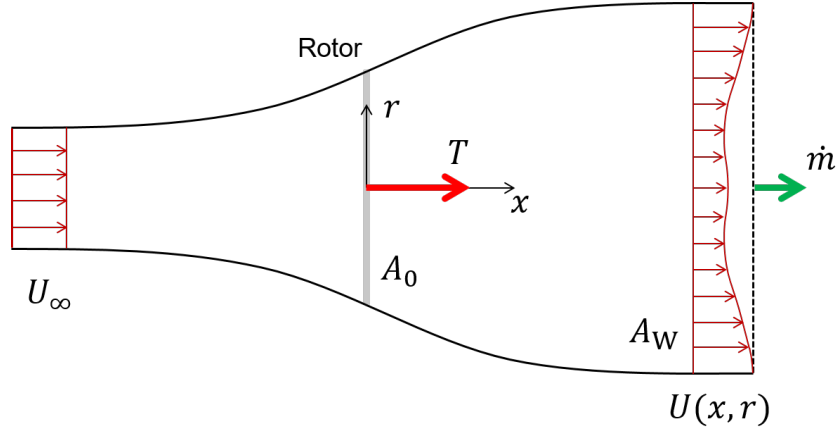


Figure 2.4: Stream tube with nomenclature: U_∞ is the ambient wind speed; $U(x, r)$ is the local flow velocity in the wake at the downstream position x and radial distance r from the wake centerline; \dot{m} is the mass flow rate through the stream tube; A_W is a planar cross-sectional area large enough to contain the wake deficit, and A_0 is the rotor disk area; T is the thrust force (by the principle of action and reaction, an equal and opposite force is applied by the rotor onto the flow).

is only valid if there is an equal pressure and negligible flow acceleration at the inlet and outlet sections of the stream tube and, additionally, if shear forces on the control volume can be neglected. The thrust force T is customarily expressed through the non-dimensional thrust coefficient C_T as

$$T = \frac{1}{2} \rho A_0 U_\infty^2 C_T, \quad (2.16)$$

where A_0 is the rotor swept area.

If the wake velocity, defined in Eqs. (2.12) and (2.13), is substituted into the Eq. (2.15), one obtains

$$T = \rho \pi U_\infty^2 C(\sigma) \int_0^\infty \left(e^{D^+} + e^{D^-} - \frac{C(\sigma)}{2} (e^{2D^+} + e^{2D^-} + 2e^{D^++D^-}) \right) r dr. \quad (2.17)$$

Note that, as the double Gaussian wake expands all the way to infinity, the integral boundary is set accordingly. The integration of Eq. (2.17), whose details are provided in **Paper 5**, yields

$$T = \rho \pi U_\infty^2 C(\sigma) (M - C(\sigma)N), \quad (2.18)$$

where

$$M = 2\sigma^2 e^{-\frac{r_0^2}{2\sigma^2}} + \sqrt{2\pi} r_0 \sigma \operatorname{erf}\left(\frac{r_0}{\sqrt{2}\sigma}\right), \quad (2.19a)$$

$$N = \sigma^2 e^{-\frac{r_0^2}{\sigma^2}} + \frac{\sqrt{\pi}}{2} r_0 \sigma \operatorname{erf}\left(\frac{r_0}{\sigma}\right). \quad (2.19b)$$

By substituting the thrust given by Eq. (2.16) into Eq. (2.18), and solving the resulting quadratic equation for the amplitude function $C(\sigma)$, one obtains

$$C_\pm(\sigma(x)) = \frac{M \pm \sqrt{M^2 - \frac{1}{2} N C_T d_0^2}}{2N}, \quad (2.20)$$

where $d_0 = \sqrt{4A_0/\pi}$ is the rotor diameter. Both solutions of the amplitude function $C(\sigma)$ would theoretically lead to the conservation of momentum at all downstream distances. However, the velocity profiles obtained by using $C_+(\sigma)$ are characterized by a negative speed (i.e., in the direction opposite

to the ambient flow), and thus $C_+(\sigma)$ is deemed to be a nonphysical solution. Therefore, the true solution for the amplitude function is $C_-(\sigma)$. In addition, a momentum-conserving solution exists only if $M^2 - 1/2 NC_T d_0^2 \geq 0$, which might not always be the case for large values of C_T .

The derived expressions for M and N presented in this thesis differ from the results reported in the original publication [32], even though all assumptions are identical. The expressions reported in the original paper were also evaluated numerically, yielding nonphysical results that violate the conservation of mass and momentum underlying the formulation.

In **Paper 5** the wake model is calibrated and validated using large eddy simulations replicating scaled wind turbine experiments.

2.3.2 Farm model

Using a static wake model, for example the double Gaussian model described in Section 2.3.1 and **Paper 5**, the steady state velocities within a wind farm together with the corresponding operating states and power outputs of all turbines can be computed using a farm model. As a basis, the ambient conditions need to be known. A procedure to estimate those from un-waked machines operating in free stream is described in **Paper 13**.

The algorithmic procedure which is typically followed in such wind farm models [27, 44] is summarized in the following steps:

1. The power and thrust of the upstream turbines are computed based on the turbine aerodynamic characteristics, the alignment with the local wind direction and the regulation strategy. In practice the power and thrust versus wind speed curves are typically employed, and a cosine-law is followed to model the power and thrust reduction due to turbine yaw misalignment.
2. The wakes shed by these turbines are calculated in terms of their speed deficit, see Section 2.3.1, and trajectory. Depending on the wake model, a separate wake deflection model [38] can be integrated in this step.
3. The velocity at the rotor disks of the turbines immediately downstream are now computed. In case of multiple wake impingements on a rotor, a combination model is used to superimpose multiple wake deficits.
4. Similarly, an added turbulence model [68] is used to estimate the turbulence intensity at a downstream turbine rotor disk, as this local ambient parameter affects the expansion rate of the turbine wake.
5. Steps 1-4 can be repeated marching downstream throughout the wind farm until the last downstream turbine is reached.

Different implementations of such wind farm models have been presented in literature and some are open-source [69, 70].

2.3.3 Model augmentation

Within this subsection a method to improve and correct an engineering wind farm flow model by using operational data is summarized. A detailed derivation is given in **Paper 9**.

The idea pursued takes a rather pragmatic approach: based on the realization that it will always be difficult—if not altogether impossible—to include all effects and all physics in a model of limited numerical complexity, the given model is corrected by unknown parametric terms, which are then learnt by using operational data.

In details, a reference baseline model is augmented with parametric error terms, which are identified using data. The baseline model already includes prior knowledge based on physics, empirical observations and experience. Therefore, even prior to the use of data, a minimum performance can be guaranteed. The choice of parametric error terms is driven by physics and the knowledge of the limitations of the baseline model. Once the errors are identified using operational data, their inspection can help clarify the causes of discrepancy between model and measurements. Eventually, this can be used to improve the underlying baseline model. Furthermore, by looking at the magnitude of the identified errors, significant deviations from the baseline model can be flagged to highlight issues with the model itself, the data or the training process.

Finally, it should be noted that the identification of the error terms can be combined with the tuning of the parameters of the baseline model. This addresses yet another problem: tuning the parameters of a model that lacks some physics may lead to unreasonable values for the parameters, as the model is stretched to represent phenomena that it does not contain. The proposed hybrid approach, the simultaneous identification of the parameters of the baseline model together with the ones of the error terms eases this problem, as unmodeled phenomena can be captured by the model-augmenting terms, thereby reducing the chances of nonphysical tuning of the baseline parameters.

As for many identification problems, it is in general not possible to guarantee that all unknown parameters are observable and non-collinear given a set of measurements and, hence, given a certain informational content. To address this problem, the method proposed in [71] can be used, where the original unknown parameters are recast into a new set of statistically uncorrelated variables by using the Singular Value Decomposition (SVD) of the inverse Fisher information matrix. Once the problem has been solved in the space of the orthogonal uncorrelated parameters, the solution is mapped back into the original physical space. This approach not only avoids the ill-posedness of the original problem, but also allows one to clarify which physical parameters are visible given a certain data set.

The method is applied and tested on a scaled wind farm as well as historical measurements of a full-scale 43-turbine wind farm in **Paper 9**.

2.4 Wind farm control

The wind farm control strategy presented in this section targets the maximization of the wind farm power output by redirecting, through yawing, the wakes shed by the upstream wind turbines. Part of this section are excerpts of a CL-Windcon project deliverable report [72], written by the author of this dissertation. Note that a very similar strategy could be followed with the objective of minimizing or redistributing fatigue loads assuming the wind farm model is able to describe those. However, by following the here described method, that is only targeting an optimization of the power production, also beneficial effects on the fatigue load distribution can be observed: Due to misalignment, small increases in the upstream turbine damage equivalent loads, which are in absolute terms still smaller than those measured at the downstream turbines due to the wake induced inhomogeneity and turbulence there, and a significant reduction at the downstream turbines, as they are less affected due to the deflected wakes, could be observed in **Paper 12**.

The overall methodology is sketched in Fig. 2.5, which is split into two parts separated by the dashed line. The upper part contains the modelling and optimization which can be done offline, and the lower one contains the wind farm control method that runs online at plant level. By this separation, the wind farm control algorithm does not require the execution of time demanding wind farm simulations or optimizations during operation, which significantly simplifies its deployment in industry.

The modeling and optimization parts rely on a static wind farm model, which eases the use of offline computed look-up tables of turbine set-points. First, historic SCADA (Supervisory Control and

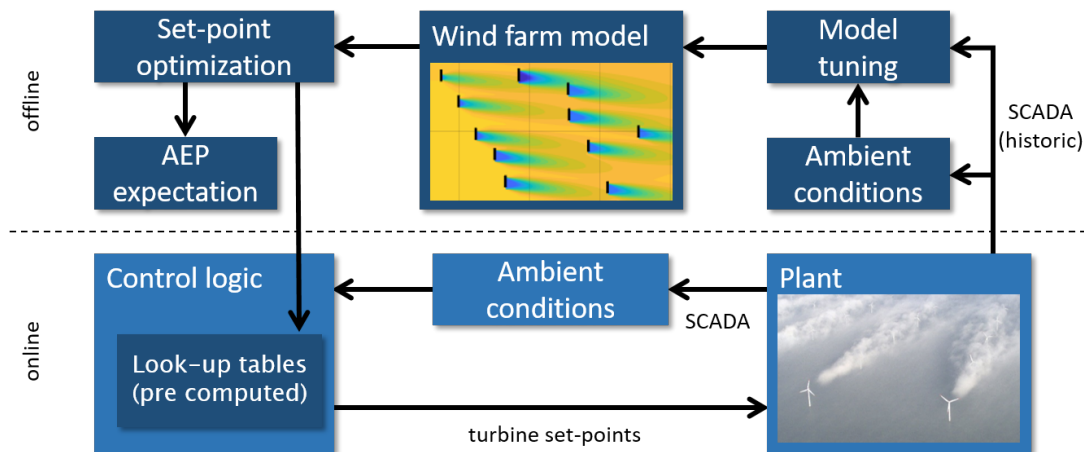


Figure 2.5: Wind farm control scheme.

Data Acquisition) measurements of the wind turbines are used to estimate the historic ambient wind conditions, for example following the approach presented in **Paper 13**, that bases on turbine power and yaw orientation. If available, also historic loads can be used, employing the *rotor-as-a-sensor* concept. Second a model tuning can be performed, following for example the approach presented in **Paper 9**, where even unmodeled effects are learned. Even though a traditionally parametrized baseline model leads to significant gains in power production, such learning increases the achieved gains further as shown in **Paper 12**. Note that it is also possible to base the parameterization on other field measurements or CFD simulations.

Once an accurate wind farm model is available, a look-up table of turbine set-points, i.e. the set of yaw misalignments that maximize the wind farm power output, for a grid of ambient wind conditions can be computed through optimization. In this regard, the most important inputs to such look-up tables are

- the wind direction, which mainly affects the direction followed by the wakes during their downstream propagation;
- the wind speed, that mainly defines whether turbines are operated below or at rated power;
- the turbulence intensity, which mainly affects the wake recovery.

In addition, uncertainties can be taken into account by the optimizer. For example, an approach can be followed that involves a robust optimization [43] or uncertainties can be accounted for employing the detector as presented in **Paper 11**. The most important sources of uncertainties include

- uncertainties in the measurement of ambient conditions, which can normally not be avoided. For example, if the wind direction is, due to turbulence, post-processed with low-pass filters, the induced phase delay could be a significant source of measurement or input error;
- model-plant mismatch: due to limited fidelity or wrong parametrization, the control-oriented wind farm model cannot exactly replicate the real plant in all possible operating conditions. Note that the work on model improvements presented in **Paper 9** effectively reduces model-plant mismatch;
- unmodeled dynamic effects: if the control-oriented wind farm model is, as in the present case, a static model, dynamic effects, like wake advection or wind farm actuation delays (e.g. due to a limited yaw rate), are not properly modeled. These effects generate uncertainties, which should

be considered. For example, the effect of delays associated to wake propagation during changing wind conditions can be partially cast into wind direction uncertainties;

- change of ambient conditions during control cycle: depending on the wind farm control frequency, i.e. how often the turbine set-points are updated, the ambient conditions might change during the cycle time. In case of large control cycles (e.g. every 10 minutes) the expected change in wind direction within that time window should be accounted for.

The lower part of Fig. 2.5 shows the wind farm control logic which has to be executed online. The approach allows a rather simple implementation in real plants [45–47]. First the ambient wind conditions are estimated following the same or similar procedure as used for the historic SCADA data. The control logic receives as input those ambient wind conditions, including wind direction, wind speed and turbulence intensity. Filtering might be used to remove fast fluctuations, obtaining a control behavior that only reacts to low-frequency changes [46, 73].

The core of the control logic is a simple interpolation within the look-up tables already computed offline. In addition, some sort of logic needs to be included ensuring a safe and reliable operation even during unexpected events. Finally, the turbine set-points are dispatched to each individual turbine. For each machine, the yaw misalignment can be applied as an offset to the current set point of the turbine yaw controller. In this sense, the original yaw control logic of the turbine is unaffected, which eases the implementation of wake deflection on existing turbines.

According to the presented method, the wind farm control potential of a specific wind farm has been computed in **Paper 13**: By evaluating the wind farm model on historic wind conditions, simulating the normal wind farm operation as well as the optimal one by employing identified optimal turbine set-points, the expected increase in annual energy production (AEP) has been quantified. The wind farm control method has been deployed in scaled wind farm experiments in **Paper 12**.

Paper 1: Local wind speed estimation, with application to wake impingement detection

3.1 Summary

First, a new method to estimate the rotor-effective wind speed (REWS) is presented. The method bases on the definition of an out-of-plane bending coefficient, correlating the turbine loads to wind speed. The coefficient can be computed using a blade element momentum based turbine simulation tool and, if blade bending sensors are available at the given turbine, employed for wind estimation during turbine operation. Based on dynamic turbine simulations, the new method is compared, also in terms of rotor-effective turbulence intensity and integral length scale estimates, to a state-of-the-art torque balance based estimator.

Second, the new method is further extended to estimate the local blade-effective wind speed and a sector-effective wind speed (SEWS), which describes the wind speed of only a part of the rotor disc. The later can be used for wind shear estimation and wake detection.

Simulations of a turbine operating within the wake of an upstream turbine are conducted, highlighting the ability to estimate the SEWS and turbulence intensity in highly non-uniform inflow. A wake detector, that bases on a simple comparison of the estimated local wind speed in the left and right part of the rotor disc, is tested in different wind conditions, including a meandering wake, and during turbine misalignment with respect to ambient wind.

Demonstrations on NREL CART3 turbine measurements confirm, that the REWS estimation is in good agreement with the state-of-the-art method and that the SEWS estimation correlates well with met-mast reference measurements. A validation of the wind sensing methods on a multi-MW wind turbine is presented in **Paper 4**.

3.2 Contribution

Within this peer-reviewed publication, the author of this dissertation has conducted the implementation, simulations and experimental analysis, which have been supervised by Stefano Cacciola. Carlo L. Bottasso developed the core idea of load-based wind sensing and all authors provided important input through discussions feedback and by writing the paper.

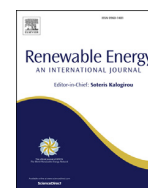
3.3 Reference

C. L. Bottasso, S. Cacciola, and J. Schreiber, "Local wind speed estimation, with application to wake impingement detection," *Renewable Energy*, vol. 116, pp. 155–168, 2018. doi: 10.1016/j.renene.2017.09.044



Contents lists available at ScienceDirect

Renewable Energy

journal homepage: www.elsevier.com/locate/renene

Local wind speed estimation, with application to wake impingement detection

C.L. Bottasso ^{a, b, *}, S. Cacciola ^b, J. Schreiber ^a^a Wind Energy Institute, Technische Universität München, Boltzmannstraße 15, D-85748 Garching bei München, Germany^b Dipartimento di Scienze e Tecnologie Aerospaziali, Politecnico di Milano, Via La Masa 34, I-20156, Milano, Italy

ARTICLE INFO

Article history:

Received 25 February 2016
 Received in revised form
 13 August 2017
 Accepted 12 September 2017
 Available online 21 September 2017

Keywords:

Rotor-effective wind speed
 Wind speed estimation
 Wakes
 Wake detection
 Wind farm control

ABSTRACT

Wind condition awareness is an important factor to maximize power extraction, reduce fatigue loading and increase the power quality of wind turbines and wind power plants. This paper presents a new method for wind speed estimation based on blade load measurements. Starting from the definition of a cone coefficient, which captures the collective zeroth-harmonic of the out-of-plane blade bending moment, a rotor-effective wind speed estimator is introduced. The proposed observer exhibits a performance similar to the well known torque balance estimator. However, while the latter only measures the average wind speed over the whole rotor disk, the proposed approach can also be applied locally, resulting in estimates of the wind speed in different regions of the rotor disk. In the present work, the proposed method is used to estimate the average wind speed over four rotor quadrants. The top and bottom quadrants are used for estimating the vertical shear profile, while the two lateral ones for detecting the presence of a wake shed by an upstream wind turbine. The resulting wake detector can find applicability in wind farm control, by indicating on which side of the rotor the upstream wake is impinging. The new approach is demonstrated with the help of field test data, as well as simulations performed with high-fidelity aeroservoelastic models.

© 2017 Elsevier Ltd. All rights reserved.

1. Introduction

Modern wind power plants may contain tens or hundreds of individual wind turbines. Each machine converts into electrical energy a part of the kinetic energy carried by an air stream tube interacting with its rotor disk. As a consequence of this energy conversion process, behind each wind turbine a complex wake structure develops, which is characterized by a slower wind speed and a higher turbulence intensity. Wakes undergo complicated phenomena, including the breakdown of near-rotor vortical structures, mixing, recovery, meandering and merging with other wakes. All such processes are strongly influenced by several parameters, including the operating conditions of the machines, the characteristics of the atmosphere, the orography and roughness of the terrain or the sea state, and the interactions among neighboring wakes.

Wakes impinging on downstream wind turbines within a wind

farm are a cause of significant power losses and increased fatigue loading. Several solutions to address this problem are currently being actively investigated [1], including the idea of redirecting wakes away from downstream machines [2,3,4,5], the curtailment of power of upstream wind turbines [6], the promotion of a faster wake recovery—for example by pitching the rotor blades [7]—, and the alleviation of loads on the affected downstream machines by active controls [8].

For developing effective solutions that are capable of actively changing the wind farm flow, a precise knowledge of the wind inflow conditions at the rotor disk of each machine is essential. For example, when using wake redirection to alleviate a partial wake overlap, it is necessary to know with certainty which side of the downstream rotor is affected, in order to deflect the wake of the upstream machine in the correct direction.

Unfortunately, at present wind turbines do not operate based on a detailed understanding of the wind conditions that affect them. In fact, wind turbines typically use nacelle or hub mounted wind measurement devices, which can only provide information on wind speed and direction at the single point in space where these devices are installed. Therefore, wind turbines are unaware of the presence

* Corresponding author. Wind Energy Institute, Technische Universität München, Boltzmannstraße 15, D-85748 Garching bei München, Germany.

E-mail address: carlo.bottasso@tum.de (C.L. Bottasso).

Notation			
A	Rotor disk area	γ	Horizontal wind misalignment
A_B	Planform area of the rotor blade	κ	Vertical power-law shear exponent
A_S	Area of a rotor sector	κ_{lin}	Vertical linear shear coefficient
B	Number of blades	λ	Tip speed ratio
C_{m_0}	Cone coefficient	ψ	Azimuth angle
C_p	Power coefficient	ρ	Air density
D	Rotor diameter	σ	Standard deviation
$E[\cdot]$	Expected value	ξ	Non-dimensional spanwise radial coordinate
J	Rotor inertia	$\overline{(\cdot)}$	Average quantity
P	Measurement noise variance	$\dot{(\cdot)}$	Time derivative, $d\cdot/dt$
Q	Process noise variance	$\overline{(\cdot)}$	Measured quantity
R	Rotor radius	$\overline{(\cdot)}_{BE}$	Blade-effective quantity
T_{aero}	Aerodynamic torque	$\overline{(\cdot)}_{RE}$	Rotor-effective quantity
$T_{friction}$	Friction torque	$\overline{(\cdot)}_{SE}$	Sector-effective quantity
T_{gen}	Generator torque	$\overline{(\cdot)}_h$	Quantity referred to the hub
V	Wind speed	$\overline{(\cdot)}_i$	Quantity referred to the i th blade
m	Out-of-plane bending moment	$\overline{(\cdot)}_k$	Quantity referred to the k th time step
n	Gearbox ratio	BEM	Blade Element Momentum
q	Dynamic pressure	BLE	Blade Load Estimator
r	Spanwise radial coordinate	HAWT	Horizontal Axis Wind Turbine
t	Time	ILS	Integral Length Scale
u	Longitudinal wind speed	LiDAR	Light Detection And Ranging
v	Measurement noise	REILS	Rotor-Effective Integral Length Scale
w	Process noise	RETI	Rotor-Effective Turbulence Intensity
z	Kalman filter output	REWS	Rotor-Effective Wind Speed
Ω	Rotor speed	SETI	Sector-Effective Turbulence Intensity
β	Blade pitch angle	SEWS	Sector-Effective Wind Speed
δ_{TI}	Left-right relative turbulence intensity difference	TBE	Torque Balance Estimator
δ_V	Left-right relative wind speed difference	TI	Turbulence Intensity
ϵ	Error	TSR	Tip Speed Ratio

of an impinging wake and of many other important inflow parameters, as for example vertical shear and veer. Clearly, this lack of situation awareness severely limits the application of sophisticated wind turbine and wind farm control approaches.

Reduced wind farm models [9,10], often based on engineering wake models or model-compression techniques, are able to represent to a certain extent the wind farm flow conditions and wake interactions at a moderate computational complexity. Given their limited computational cost, such models are also good candidates for the synthesis of model-based controllers. However, the quality and reliability of the predictions provided by these models are typically affected by a number of factors, including the stability and characteristics of the atmosphere and the proper calibration of the model parameters. Even in this case, a more sophisticated awareness of the flow conditions than it is currently available would prove very valuable. If one could measure the wind conditions at the rotor disk of each machine, this information could be used to improve/correct the predictions of the reduced order models, in turn providing higher quality information for advanced control applications.

LiDARs (Light Detection And Ranging) are remote sensing devices that are able to measure wind conditions and to detect wakes and their locations [11]. Both ground-based and nacelle-mounted LiDARs, possibly used in synergy, can provide a fairly complete description of the flow at the sampling rates necessary for wind turbine and wind farm control. Unfortunately, however, the use of LiDARs is still confined to research applications, and they are not yet routinely deployed in the field on production machines because of cost, availability, reliability and technological limits of the

measurements. These include spatio-temporal averaging, complexity of multi-component measurements of the wind vector, effects of turbulence convection and interaction with the rotor induction zone.

In summary, there is a need to develop alternative methods for wind flow measurement that can improve the situation awareness of wind turbines. Such methods should be simple and reliable, and they should be able to provide detailed information on the flow characteristics at each wind turbine rotor disk in real time during operation. The availability of such new methods would facilitate the development of modern smart control approaches, to improve power capture and reduce loading for wind turbines operating within power plants.

To address these needs, the concept of using the rotor as a generalized anemometer has been recently proposed [12,13,14,15]. In a nutshell, the idea of *wind sensing* is that any change in the wind conditions at the inflow will be reflected in a corresponding change in the response of the rotor. In other words, there is in general a well defined map between some wind parameters and some specific features of the rotor response. By measuring such response—for example in terms of blade loads or accelerations, torque, rotor speed, blade pitch, etc.—one may invert the map, under suitable hypotheses and conditions, to estimate the wind characteristics. Recent results (see Ref. [15] and references therein) indicate that several wind states can be reliably observed using blade loads, including wind speed, vertical and horizontal shears, lateral misalignment and upflow. As many modern machines are already equipped with load sensors, typically for enabling load-alleviating feedback control laws, the implementation of such approaches

may not require any additional hardware, and therefore may come at the cost of a simple software upgrade.

The current paper falls within the new field of wind sensing. Within the general idea of using the rotor as a wind sensor, the present work proposes a new and simple method to estimate some wind characteristics that imply non-uniform wind conditions at the rotor disk. Relevant examples are vertical shear and the impingement of a wake shed by an upstream machine.

The method is based on the estimation of the wind speed by the out-of-plane blade bending moment, as explained in more detail in Section 2. Similarly to the thrust coefficient, one may define a cone bending coefficient, which depends on the tip speed ratio (TSR) and blade pitch. The cone coefficient captures the (collective) zeroth-harmonic of the blade loads, and it can be interpreted as the constant term produced by Coleman—transforming the individual loads of each blade. Using the three blades together, knowledge of the loads in addition to rotor speed and blade pitch allows one to estimate a rotor-equivalent wind speed from the cone coefficient. The estimate is obtained by the use of a Kalman filter, which enhances the robustness of the approach in the face of noise and disturbances, always present in practical applications in the field.

A similar rotor-equivalent estimate of the wind speed may be obtained by the well known torque balance estimator [12]. In that case, one uses the power coefficient and, based on measured shaft torque together with rotor speed and blade pitch, wind speed is obtained by filtering. A comparison between the two approaches shows results of similar quality. It is speculated that the present approach might yield better estimates in the high frequency spectrum, especially on machines with particularly large diameters. In fact, the flap response of the rotor is not slowed by its large rotary inertia, as it is on the other hand the case for the torque balance estimator. Results shown in this paper indicate that the method has sufficient temporal resolution for estimating with good accuracy even the Turbulence Intensity (TI), and in turn the Integral Length Scale (ILS) of the flow.

However, a crucial difference of the proposed approach with respect to the torque balance method is that the former can be specialized to the observation of *local* flow conditions on different parts of the rotor; this is in contrast to the exclusively *global* estimates provided by the latter. Specifically, by using the load information for each single blade independently, one may sense the wind at the azimuthal location occupied by that blade, as explained in Section 3. Averaging over an azimuthal interval, an estimate of the local wind speed in a rotor sector can be readily obtained. In turn, from the local wind speed one may also easily derive an estimate of the corresponding local TI.

This new idea is here developed by subdividing the rotor into four quadrants, although other choices are clearly possible. The local speed estimates obtained by the proposed method may be used to detect speed differences over the rotor disk. At first, the idea of detecting the effects of the vertical shear is investigated by using field test data. Experiments conducted with different data sets show that the vertical distribution of wind speed detected over the top and bottom rotor quadrants correlates well with the one measured by a met-mast equipped with anemometers.

In Section 4, the new proposed concept is finally applied to the observation of waked conditions. A simulation environment is used in this case. Although any model cannot clearly be perfectly faithful to reality, the use of simulations has the advantage that one has a complete knowledge of the situation. In the present case, this means that one knows exactly the ground truth wind speeds in the various areas of interest. In addition, it is easier within a simulation environment to try and determine the effects of various disturbing effects. The study considers various waked conditions, which differ in the degree of overlap with the affected rotor disk. Extensive

simulations and comparisons of the results of the observations with respect to the reference exact solutions demonstrate the general ability of the proposed formulation of distinguishing between waked and unwaked conditions, indicating the affected rotor side of the interaction. Other recent related papers [16,17,18] present studies of the performance of the same method with reference to experimental data measured on a scaled wind farm facility. The papers also show how to estimate the wake position based on the local wind speed estimates developed in the present work.

Finally, the present work is terminated by Section 5, where conclusion are drawn and plans for future work are sketched.

2. Estimation of rotor-effective wind parameters

2.1. A novel formulation for wind speed estimation based on the cone coefficient

In this work, the Rotor-Effective Wind Speed (REWS) is obtained by a Blade-Load-based Estimator (BLE), which makes use of the zeroth harmonic (or cone) of the out-of-plane bending rotor loads. Considering a steady wind condition, the cone coefficient is defined as

$$C_{m_0}(\lambda_{RE}, \beta, q_{RE}) = \frac{\frac{1}{2\pi} \int_0^{2\pi} \sum_{i=0}^B m_i(\psi_i) d\psi}{\frac{1}{2} \rho A R V_{RE}^2}, \quad (1)$$

where $\lambda_{RE} = \Omega R / V_{RE}$ is the rotor-effective TSR, Ω the rotor speed, R the rotor radius, V_{RE} the REWS, β the blade pitch angle, B the number of blades, m_i the out-of-plane root bending moment of blade i (which occupies the azimuthal position ψ_i over the rotor disk), ρ the density of air, A the rotor disk area and finally $q_{RE} = 1/2 \rho V_{RE}^2$ the rotor-effective dynamic pressure. The numerator of the right hand side represents the average over a rotor revolution of the sum of the out-of-plane blade bending moments, $m_0 = \sum_{i=1}^B m_i$. In the terminology of the Coleman transformation, m_0 represents the collective, cone or zeroth harmonic of the loads, while the higher harmonics would be given by appropriate sine and cosine combinations of the same loads [19].

As in the case of the familiar power and thrust coefficients, also the cone coefficient depends on the operating condition through TSR and blade pitch. In addition, as indicated on the left hand side of the previous expression, the cone coefficient also depends on dynamic pressure. In fact, rotor and tower deform under loading, so that the same TSR and blade pitch at two different wind and/or density conditions may in principle correspond to slightly different non-dimensional cone (but also power and thrust) coefficients.

Once the cone coefficient has been computed for all operating conditions of interest, Eq. (1) can be used to estimate V_{RE} . To this end, the equation is rewritten for the generic time instant t as

$$\hat{m}_0(t) = \frac{1}{2} \rho A R V_{RE}^2(t) C_{m_0}(\lambda_{RE}(t), \beta(t), \bar{q}_{RE}(t)), \quad (2)$$

where \hat{m}_0 is computed based on the measurements provided at that instant of time by blade load sensors. The rotor-effective dynamic pressure \bar{q}_{RE} is computed by a moving average looking backward in time over a suitable time window, to capture the working point about which the machine is operating. Since also the rotor speed Ω can be easily measured together with the blade pitch angle β , the sole unknown in the equation is the REWS V_{RE} , which can therefore be readily computed.

The contribution of the gravitational loads are assumed to have been eliminated from the blade bending moments. In fact, not

having an aerodynamic origin, gravitational loads cannot be non-dimensionalized by the denominator of Eq. (1). In turn, this prevents the correction of the coefficient for density, which is on the other hand important for the practical application of the method in realistic conditions. The elimination of the effects of gravity is achieved by first pre-computing the corresponding bending moments for preselected values of the azimuthal blade position, at each time step interpolating these values to get the one corresponding to the actual position, and finally subtracting the interpolated value from the currently measured bending moment. As previously noted, to account for the deformation of the machine at different operating points, such procedure can be scheduled in terms of the current mean dynamic pressure.

To increase the robustness of the estimates in the face of measurement and process noise, an Extended Kalman filter is used for the computation of V_{RE} . The wind speed update at the generic time step k is defined as

$$V_{RE_k} = V_{RE_{k-1}} + w_{k-1}, \quad (3)$$

w_k being the process noise with covariance Q . The very simple model used here has the advantage of depending on the single tuning parameter Q , and it performed reasonably well in the experiments reported later on. Nonetheless, it is clear that a more sophisticated model of the wind dynamics might be considered, for example in order to ensure specific characteristics to the wind spectrum. Finally, the non-linear output equation of the filter is defined as

$$z_k = \frac{1}{2} \rho A R V_{RE_k}^2 C_{m_0}(\lambda_{RE}, \beta, \bar{q}_{RE_k}) - m_0 + v_k, \quad (4)$$

where v_k is the measurement noise with covariance P , while the output z_k is set to 0 to enforce Eq. (2) at each step. The filter parameters Q and P should be tuned in order to obtain good quality estimates in different wind conditions, as shown later on in the results section.

2.2. Estimation of wind speed by the power coefficient

A dynamic Torque Balance Estimator (TBE) [12,20,21,22,23] of the REWS is described next. The well known TBE is introduced to provide a reference performance in the estimation of the wind speed, to be used for comparison and validation of the previously described cone-coefficient-based estimator. The TBE uses a dynamic model of the rotor torque balance, which writes

$$J\dot{\Omega} = T_{aero} - nT_{gen} - T_{friction}, \quad (5)$$

where J is the moment of inertia of the rotor-generator-drive-train assembly referred to the low speed shaft, $\dot{\Omega}$ the rotor acceleration, T_{aero} the aerodynamic torque, n the gearbox ratio, T_{gen} the generator torque and $T_{friction}(\Omega)$ a mechanical loss term accounting for friction in the bearings and drive-train. The aerodynamic torque can be expressed as a function of the power coefficient C_p as

$$T_{aero} = \frac{1}{2\Omega} \rho A V_{RE}^3 C_p(\lambda_{RE}, \beta, q_{RE}). \quad (6)$$

Note that the power coefficient, similarly to the cone coefficient, is a function of the dynamic pressure as it may be influenced by aeroelastic effects. Here again, as all quantities appearing in the equation are either measured or can be estimated, the sole remaining unknown is the REWS V_{RE} for which the equation can be solved.

Even in this case, to hedge against disturbances and noise the Extended Kalman filter is used, resulting in the following non-linear output equation

$$z_k = \frac{1}{2\Omega} \rho A V_{RE_k}^3 C_p(\lambda_{RE}, \beta, \bar{q}_{RE_k}) - nT_{gen} - T_{friction} - J\dot{\Omega} + v_k. \quad (7)$$

2.3. Estimation of turbulence intensity and integral length scale

The Rotor-Effective Turbulence Intensity (RETI, noted TI_{RE}) is directly obtained by the 10-min REWS mean \bar{V}_{RE} and standard deviation $\sigma_{V_{RE}}$:

$$TI_{RE} = \frac{\sigma_{V_{RE}}}{\bar{V}_{RE}}. \quad (8)$$

Clearly, for the RETI to be a good quality estimate of the real flow turbulence intensity interacting with the rotor disk, the REWS should approximate the real wind speed in a sufficiently ample bandwidth, typically up to 0.2 Hz. In this sense, REWS estimators that perform an excessive filtering effect might not provide for suitable estimates of the RETI.

The Rotor-Effective Integral Length Scale (REILS) is readily obtained based on the 10-min auto-correlation of the REWS, as for example described in Ref. [24].

2.4. Comparison of the two methods

Before moving on to the estimation of local wind speeds, estimates of rotor-equivalent wind quantities based on blade loads are compared to the ones obtained with the use of the well known TBE, with the purpose of establishing the performance characteristics of the new method.

At first, a simulation study was conducted by using the high-fidelity aeroservoelastic model of a 3 MW wind turbine, implemented with the modeling environment Cp-Lambda [25]. The machine is an upwind three-bladed variable-speed HAWT, representative of current wind turbine designs, with a rotor diameter of 93 m and a hub height of 80 m. The wind turbine is modeled as a flexible multibody system expressed in Cartesian coordinates, whose blades and tower are rendered using geometrically exact beam models, which are in turn discretized in space using the isoparametric finite element method. Lagrange multipliers are used for enforcing mechanical constraints, resulting in a high-index differential algebraic formulation, which is marched in time by a preconditioned energy decaying integration scheme [26]. The aerodynamic model is based on the coupling of lifting lines with the classical Blade Element Momentum (BEM) theory. The model operates in closed-loop with a collective blade pitch and torque controller. Turbulent wind fields were obtained with the TurbSim code [27]. At each instant of time, sensors within the model, including strain sensors at the blade roots emulating strain-gages, gather the necessary information that is in turn fed to the estimators.

At each time instant, a reference “ground-truth” REWS was calculated from the wind grid as

$$V_{RE,grid} = \frac{1}{A} \int_0^R \int_0^{2\pi} u(r, \psi) r \, dr \, d\psi, \quad (9)$$

where u is the wind speed in the longitudinal direction, similarly to what done by Østergaard et al. [20]. Other definitions are possible, as the one used by Soltani et al. [12], where wind speed is weighted

by the local power coefficient. Based on this reference REWS, reference RETI and REILS were readily obtained, as previously described.

Fig. 1a shows at top the reference REWS (at left) and RETI (at right), for parts of one turbulent wind realization characterized by an ambient wind speed of 20 m/s with a TI of 5% and a vertical layer with shear exponent equal to 0.2, based on the Kaimal turbulence model. The bottom part of the figure shows the corresponding errors between estimate and reference, for both the REWS (at left, in meters per second) and the RETI (at right, in percentage points).

For different average wind speeds and TIs, the estimation error mean $E[\varepsilon]$ and standard deviation σ_ε are shown in Table 1a. These quantities are computed on one realization of the turbulent wind time history of 40 min of length, which are enough to bring the statistics to convergence. Results indicate that both methods produce similarly good estimates.

For the same wind conditions, Table 2 reports the statistical properties of the estimation error for the REILS, in percentage. Again both estimators yield reliable results, although the TBE appears to be slightly more accurate.

Next, field measurements were used to characterize the quality of the BLE, again in comparison with the TBE. Measurements were obtained on the CART3 (Controls Advanced Research Turbine, 3-bladed) [28], operated by the National Wind Technology Center (NWTC) of the National Renewable Energy Laboratory (NREL). This 600 kW wind turbine has a rotor radius of 20 m and a hub-height of 40 m.

A met-mast is located 85 m from the wind turbine, and it is equipped with three anemometers and wind vanes located at 15, 36 and 55 m above ground. Wind recordings sampled at 400 Hz were selected for wind directions aligned with the met-mast and wind turbine axis. To account for the time delay between met-mast and wind turbine, the three anemometer measurements were first averaged at each time instant to give a rotor mean wind speed, and then time-shifted based on the 1500-s averaged mean wind speed.

The wind turbine cone and power coefficients were based on a previously validated aeroelastic model of the wind turbine,

Table 1
REWS and RETI estimation error means $E[\varepsilon]$ and standard deviations σ_ε for the BLE and TBE estimators, for multiple realizations of different wind conditions.

(a) REWS					
ambient		$E[\varepsilon]$ in m/s		σ_ε in m/s	
V	TI	BLE	TBE	BLE	TBE
5 m/s	2%	-0.03	-0.03	0.02	0.01
5 m/s	5%	-0.04	-0.03	0.03	0.02
5 m/s	10%	-0.05	-0.02	0.05	0.05
20 m/s	2%	0.02	0.07	0.06	0.07
20 m/s	5%	0.02	0.08	0.13	0.14
20 m/s	10%	-0.09	0.02	0.25	0.25

(b) RETI					
ambient		$E[\varepsilon]$ in pps		σ_ε in pps	
V	TI	BLE	TBE	BLE	TBE
5 m/s	2%	0.14	-0.02	0.07	0.01
5 m/s	5%	0.12	-0.04	0.17	0.03
5 m/s	10%	0.10	-0.10	0.28	0.05
20 m/s	2%	0.06	0.13	0.01	0.01
20 m/s	5%	-0.01	0.11	0.01	0.03
20 m/s	10%	-0.03	0.05	0.03	0.04

Table 2
REILS estimation error means $E[\varepsilon]$ and standard deviations σ_ε for the BLE and TBE estimators, for multiple realizations of different wind conditions.

ambient					
		$E[\varepsilon]$ in %		σ_ε in %	
V	TI	BLE	TBE	BLE	TBE
5 m/s	2%	0.94	3.82	5.29	3.10
5 m/s	5%	5.49	5.08	5.36	5.21
5 m/s	10%	5.56	5.12	4.66	4.58
20 m/s	2%	0.16	-0.82	9.96	6.00
20 m/s	5%	2.56	0.33	6.51	5.93
20 m/s	10%	1.81	0.47	5.79	4.72

implemented with the simulation tool FAST [29,30]. The coefficients were obtained by averaging the machine relevant

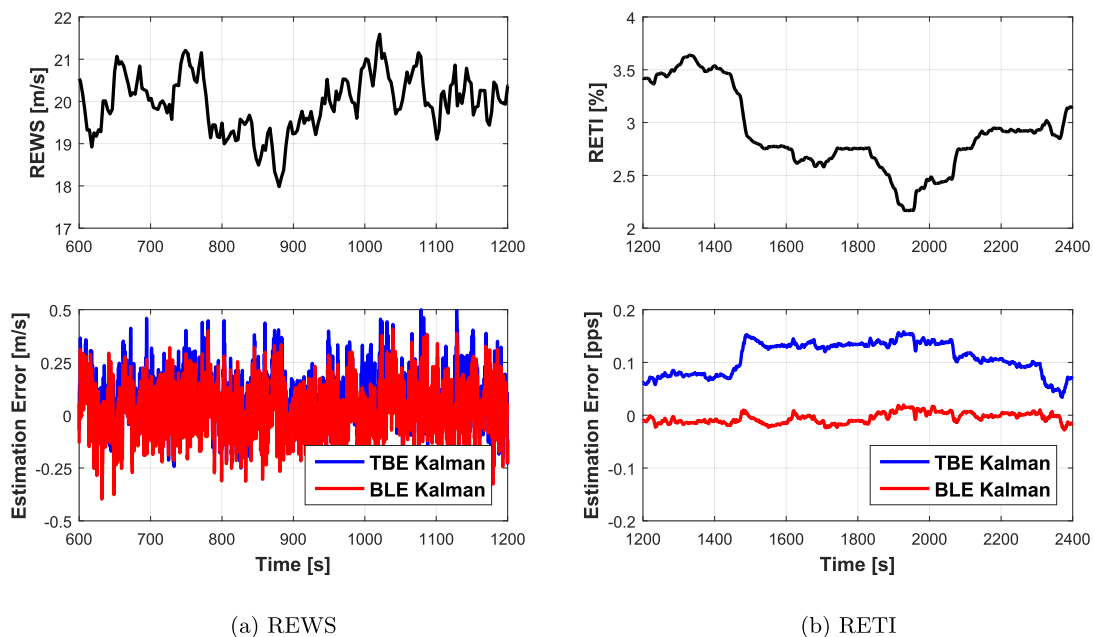


Fig. 1. Top: reference REWS (at left) and RETI (at right). Bottom: estimation errors for REWS (at left) and RETI (at right).

response obtained with dynamic simulations in steady-state winds at various TSR and blade pitch settings, once the solution had settled onto a periodic orbit. Given its small size and robust construction, for this machine the dependency of the coefficients on the dynamic pressure is negligible, and therefore it was not taken into account.

For one specific representative time history of 600 s of duration, Fig. 2 shows the met-mast average, as well as the REWS computed by the BLE and the TBE. For completeness, the plot also reports the wind speed measured by the nacelle-mounted anemometer, which however is a point measurement (as opposed to a rotor-equivalent quantity) and also exhibits a significant offset. It should be mentioned that in this case the met-mast-measured wind can hardly be considered as a “ground truth”, as it is only based on three point measurements and it neglects the evolution of the flow from the met-mast to the wind turbine rotor (Taylor’s frozen hypothesis). Nonetheless, the plot shows that the BLE and TBE are in good agreement between themselves and in a reasonable one with the met-mast-provided information. Similar results were obtained with the use of different time histories from this same machine and experimental setup.

3. Estimation of local-effective wind parameters

The BLE method can be finally specialized to estimate the wind speed experienced in different parts of the rotor disk. The basic idea is to use each blade as a moving sensor whose out-of-plane bending load is strictly connected to the local wind speed at the blade position.

To this end, Eq. (2) is modified as

$$\hat{m}_i(t) = \frac{1}{2B} \rho AR V_{BE}(\psi_i(t))^2 C_{m_0}(\lambda_{BE}(\psi_i(t)), \beta_i, q_{BE}), \quad (10)$$

where $(\cdot)_i$ indicates quantities pertaining to the i th blade. As in the previous case, this expression is used to define the output equation of an Extended Kalman filter (cf. Eq. (4)), which yields an estimate of the blade local-effective wind speed $V_{BE}(\psi_i(t_k))$ at the azimuthal location ψ_i occupied by the blade at time instant t_k .

From the blade local-effective wind speed, a Sector-Effective Wind Speed (SEWS), noted V_{SE} , is obtained by averaging over an azimuthal interval of interest, as

$$V_{SE}(t) = \frac{1}{A_S} \int_{A_S} V_{BE}(\psi(t)) dA_S. \quad (11)$$

The SEWS estimate can be updated every time a blade leaves the sector, i.e. with a frequency equal to $B \times \text{Rev}$, while the zero-order hold can be employed in between two updates. This concept is symbolically illustrated in Fig. 3.

A Sector-Effective Turbulence Intensity (SETI), noted T_{SE} , is readily computed from the SEWS as

$$T_{SE} = \frac{\sigma_{V_{SE}}}{V_{SE}}, \quad (12)$$

being $\sigma_{V_{SE}}$ the standard deviation of the SEWS.

The SEWS has the meaning of an average velocity over the disk sector. Hence, the question arises: what is the spanwise location of such an average along the disk radius? In fact, this information may be useful for the validation and interpretation of the results. For example, later on the estimated SEWS will be compared to measurements obtained with a met-mast, and therefore it is necessary to know at which height along the met mast the comparison should be performed.

The blade root bending moment on a sector S occupying the azimuthal span $\Delta\psi = \psi_2 - \psi_1$ with area $A_S = \Delta\psi R^2/2$ can be written as

$$m_S = \frac{1}{2B} \rho R^3 \int_0^1 \int_{\psi_1}^{\psi_2} V(\xi, \psi)^2 C_T(\xi, \psi) \xi^2 d\psi d\xi, \quad (13)$$

where $\xi = r/R$ is the nondimensional radial position, r the dimensional one, and C_T the local thrust coefficient. According to stream-tube theory, $C_T(\xi) = 4a(\xi)(1 - a(\xi))$, where $a(\xi)$ is the axial induction factor. As $a(\xi) \approx 1/3$ for a well designed blade, then C_T can be assumed to be roughly constant over the rotor disk. Therefore, introducing the constant equivalent wind speed V_{SE} over the sector, one readily finds

$$m_S = \frac{1}{2B} \rho V_{SE}^2 A_S \frac{2}{3} R C_T. \quad (14)$$

This expression indicates that the blade bending moment can be interpreted as being produced by the thrust applied at $2R/3$ span. In this sense, V_{SE} can be interpreted as the wind velocity sampled at that same location.

A more refined analysis can be developed by assuming a linear vertical wind shear, which can be expressed as

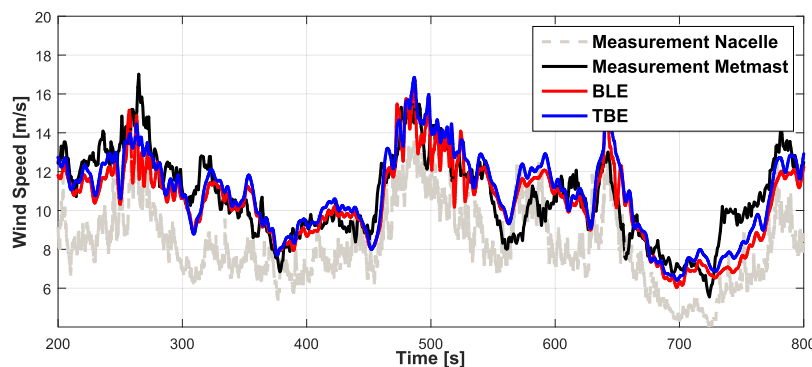


Fig. 2. REWS BLE (red line) and TBE (blue line) estimates, averaged time-shifted met-mast wind speed (black line), and onboard nacelle-mounted anemometer wind speed (gray dashed line), for field measurements obtained with the NREL CART3 wind turbine. (For interpretation of the references to colour in this figure legend, the reader is referred to the web version of this article.)

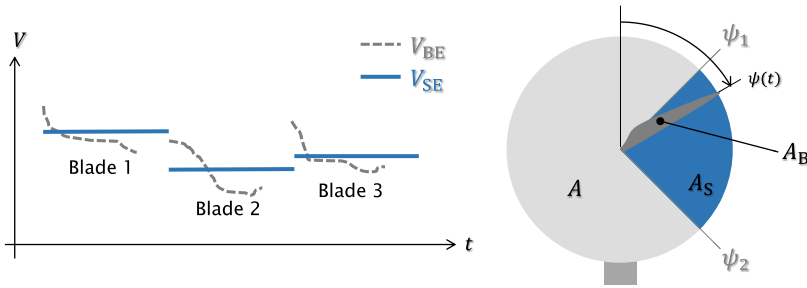


Fig. 3. Estimation of blade-effective and sector-effective wind speeds, from the loads of a blade passing through a rotor disk sector.

$$V(\xi, \psi) = V_h \left(1 + \kappa_{lin} \frac{z - z_h}{R} \right), \quad (15a)$$

$$= V_h (1 + \kappa_{lin} \xi \cos \psi), \quad (15b)$$

where V_h is the hub height, κ_{lin} the linear shear coefficient, and z a vertical coordinate pointing upwards, z_h being the hub height. In this case, one would like to find the equivalent height \tilde{z} where V is sampled by the estimator. Using both expressions (15a) and (15b) in Eq. (13), considering a constant C_T , solving for z and simplifying the result, one finds the following expression for the effective height \tilde{z} :

$$\frac{\tilde{z} - z_h}{R} = \frac{1}{\kappa_{lin}} \left(\sqrt{\frac{\int_0^1 \int_{\psi_1}^{\psi_2} (1 + \kappa_{lin} \xi \cos \psi)^2 \xi^2 d\psi d\xi}{\Delta\psi/3}} - 1 \right) \quad (16)$$

Even though the effective height is a function of the shear coefficient κ_{lin} , one may safely assume $(\tilde{z} - z_h)/R \approx \pm 2/3$ for the upper and lower sectors. Indeed, the variation of this quantity with κ_{lin} is very small, being for the upper sector $(\tilde{z} - z_h)/R|_{\kappa_{lin}=-0.5} = 0.662$ and $(\tilde{z} - z_h)/R|_{\kappa_{lin}=+0.5} = 0.682$.

3.1. Use of local-effective wind parameters

The concept of SEWS can be used for detecting areas of different wind speeds over the rotor disk. For example, consider the four quadrants depicted in Fig. 4.

A partial wake impingement, whereby the wake shed by an upstream wind turbine has a partial overlap with the rotor disk, will create different wind speeds on the right and left sectors of the

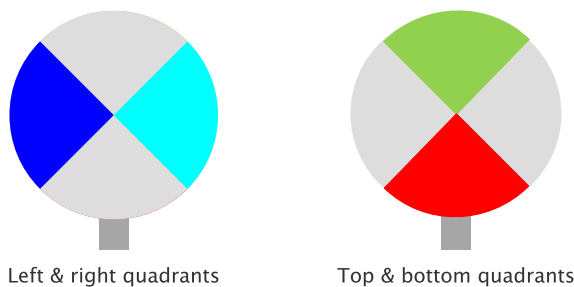


Fig. 4. Rotor disk partitioned into four quadrants, noted left and right, and top and bottom. Naming of the quadrants considers an upwind view direction.

rotor. Therefore, by looking at the difference of the SEWS between the right and left quadrants, one may be able to detect a wake interference condition, information that can be exploited for wind farm control. This information can also help distinguish whether the wake is impinging over one or the other side of the rotor disk, which is again useful for wake redirection control purposes.

Since a wake is characterized not only by a speed deficit but also by a higher TI than the ambient flow, a partial wake condition will also typically imply different TI levels on the two sides of the rotor. As the proposed formulation is also capable of estimating local TI values over the different quadrants, this information can in principle be used in conjunction with the local speed to increase the confidence level of a correct wake interference detection.

Similarly, a vertical wind shear will imply different wind speeds on the top and bottom quadrants. Here again, the SEWS on these two rotor sectors may be used for estimating this wind parameter, which in turn may find applicability in wind turbine and wind farm control (for example, by correlating wind shear and atmospheric stability, which has strong effects on the behavior of wakes). Additionally, by averaging over the left and right quadrants, one may have an indication of the wind speed at hub height. This, together with the SEWS of the top and bottom quadrants, produces a three-point estimate of the wind speed in the vertical direction, which can in principle be used for estimating an inverted wind profile, typical of conditions characterized by low level jets. In this case, the use of a higher number of sectors than the four used here might provide for an even better vertical resolution.

The use of SEWS for estimating shear and wake impingement is demonstrated in the following pages by the use of several examples, which make use of synthetic simulation data as well as field tests. A validation performed with scaled experiments conducted with wind turbine models in a boundary layer wind tunnel is described in a different publication [16].

4. Results

4.1. Vertical shear estimation from field test data

At first, the proposed formulation was verified with respect to its ability in estimating the vertical wind shear, again with reference to field test data gathered on the NREL CART3 wind turbine. Although the primary goal of this work is the development of a wake state estimator, both vertical shear and wake interference are characterized by different average wind speeds on different rotor quadrants. Therefore, this test still gives relevant information on the general ability of the formulation of detecting wind speed variations over the rotor disk.

Based on the previously illustrated analysis, wind velocity estimates can be interpreted as flow samples at $2/3R$. Therefore, for the lower sector, estimates are compared to the time-shifted and

linearly interpolated anemometer measurements at $2/3R$ below hub height (i.e., 27 m from the ground). Similarly, the upper sector reference is obtained by interpolating the measurements at $2/3R$ above hub height (i.e., 53 m from the ground).

Fig. 5 shows a time history of the estimated SEWS for a period of 100 s. It should be noted that the distance between met-mast and wind turbine clearly implies an approximation due to the adoption of Taylor's frozen turbulence hypothesis. In addition, it should also be remarked that the SEWS represents a spatial mean wind speed, while anemometers only provide point-wise measurements. Nonetheless, considering these two limitations of the present comparison, the estimates follow reasonably well the trend of the met-mast anemometers. In particular, it appears that the estimates are capable of consistently detecting the right sign of the shear (in other words, whether the speed in the top quadrant is higher or not than in the lower one), and the correct overall behavior of this quantity.

4.2. Wake state estimation

The simple wind farm layout depicted in Fig. 6 was used for studying the ability of the proposed formulation in detecting the impingement on a rotor of the wake shed by an upstream wind turbine. Both machines are 3 MW HAWTs, identical to the ones used in the previous numerical study.

The longitudinal distance between the two wind turbines is four times the diameter of the rotor ($4D$), which is a closely spaced configuration that might be representative of compact wind farms designed to reduce land occupation in onshore sites located in geographical areas of relatively high population density. The lateral distance of the two wind turbines is taken as a parameter, which is varied in order to realize different wake overlaps for a given fixed wind direction. When noted, the downstream wind turbine operates with a given misalignment angle γ with respect to the wind vector, which will probably be a relatively common mode of operation in the future within closely spaced wind farms. In fact, deliberate wind misalignment can be used for deflecting the wake away from downstream machines, thereby reducing interferences to the benefit of power output and loading. Tests conducted herein with a misaligned machine are meant to verify whether the wake state observer works also in this operating condition.

The wake of the upwind turbine is modeled by the superposition of a turbulent wind grid generated with TurbSim, and the first order solution of the wind speed deficit of the Larsen model

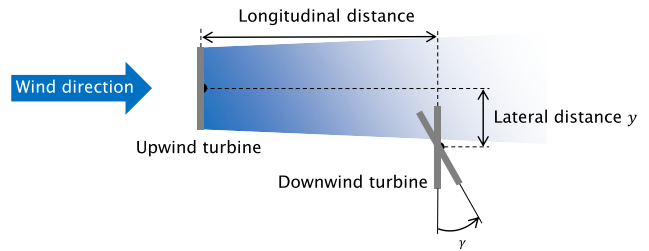


Fig. 6. Configuration of the two wind turbines for the wake detection simulation study.

(EWTSSII model) [31]. Although this is only a rather crude and idealized behavior of a wind turbine wake, it still serves the purpose of generating a wind field that has different wind speed values and TIs over the rotor of the affected downstream wind turbine.

As an example of the wind fields generated this way, Fig. 7a shows for a random time instant the TurbSim wind grid obtained for a mean wind speed of 8 m/s, a 5% TI and a shear layer with exponent equal to 0.2. For the same instant of time, Fig. 7b shows the superposition of the turbulent wind with the Larsen model, for a lateral distance between the two machines of $0.5D$.

Due to the wind speed deficit characterizing the wake core, turbulence inside the wake is increased, as shown in Fig. 8. Fig. 8a shows the 10-min TI in percentage at each grid point without wake superposition, whereas Fig. 8b shows the same quantity for the two superimposed wind fields. Clearly, this is only a very crude model of the actual turbulent behavior of a wake, although here again it serves the purpose of creating areas of different TI over the rotor disk.

4.3. Wake interference detection

There may be multiple ways of detecting a wake impingement by analyzing the turbine response. For a reliable wake detection a combination of various methods may be advisable, including geometric information on the wind farm layout and the wind direction in addition to wind speed. While the general problem of wake detection is very interesting and also quite important for wind farm control purposes, the attention is restricted in this work to the sole use of the information obtained by the proposed estimation technique.

A detection based on SEWS is investigated first. To this end,

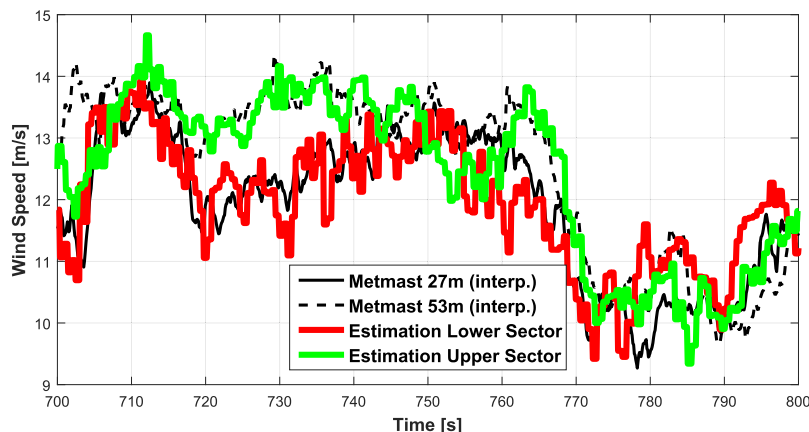


Fig. 5. SEWS estimation based on NREL CART3 measurements of the bottom (red) and top (green) sectors. Interpolated and time-shifted met-mast measurements are shown as reference in black. (For interpretation of the references to colour in this figure legend, the reader is referred to the web version of this article.)

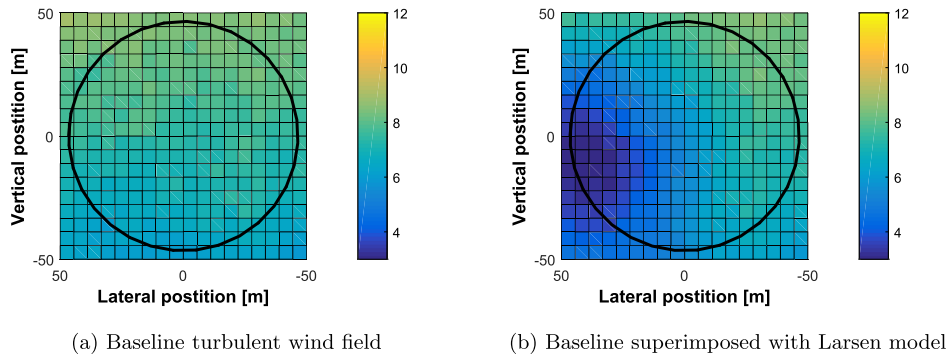


Fig. 7. Turbulent wake model obtained by the superposition of Kaimal turbulence with Larsen model. Color bar in m/s; the downstream rotor circumference is indicated by a black circle. (For interpretation of the references to colour in this figure legend, the reader is referred to the web version of this article.)

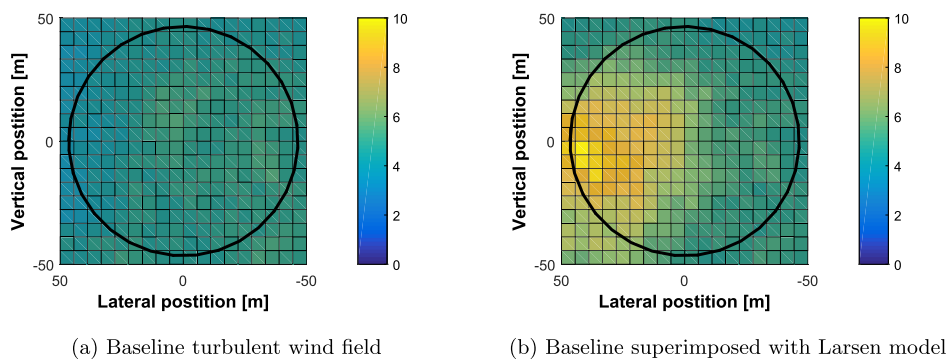


Fig. 8. TI for the turbulent wake model obtained by the superposition of Kaimal turbulence with Larsen model. Color bar in percentage; the downstream rotor circumference is indicated by a black circle. (For interpretation of the references to colour in this figure legend, the reader is referred to the web version of this article.)

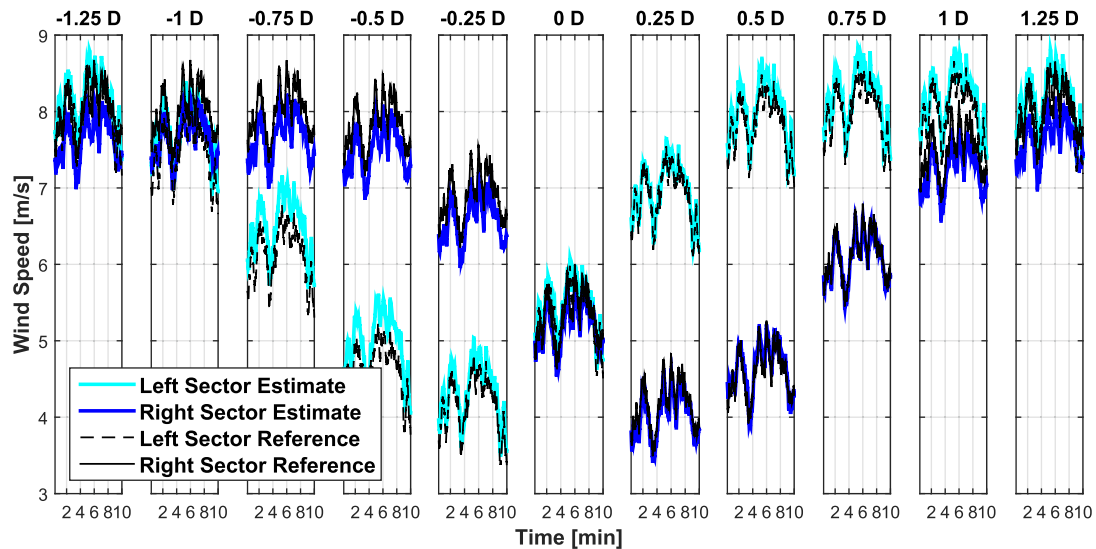


Fig. 9. Estimated and reference (ground truth) sector wind speeds vs. time. Each column plot represents a different wake overlap, characterized by a different lateral distance between upstream and downstream rotor centers. Left sector SEWS: reference speeds shown in black dashed lines, estimates in cyan; right sector SEWS: reference speeds in black solid lines, estimates in blue. (For interpretation of the references to colour in this figure legend, the reader is referred to the web version of this article.)

Fig. 9 shows various wake interference scenarios, defined by the lateral distance between the rotor centers of the upstream and downstream wind turbines, for an ambient mean wind speed of 8 m/s, a TI of 5% and a shear layer with exponent equal to 0.2. For

each scenario, corresponding to a column subplot of the overall figure, the left and right sector wind speed estimates are displayed as functions of time. Each column subplot also reports reference values computed by spatially averaging the wind speed at each

instant of time from the synthetic turbulent wind field. Such reference values represent a ground truth with respect to which the estimates should be compared.

The figure clearly shows that in partial wake conditions ($\pm 0.75D$, $\pm 0.5D$ and $\pm 0.25D$) the SEWS is, as expected, smaller on the side of the rotor disk affected by the wake. This difference increases for increasing overlap, suddenly dropping to zero when the downstream rotor is in full wake condition. Clearly, any wind speed estimator can not readily distinguish between a full waked and a completely unwaked condition, although wind direction and wind farm layout may come to the help in such a case. Interestingly, the plot also shows that the estimates seem to follow quite well the ground truth, correctly identifying both the sign and the magnitude of the wind speed imbalance over the two rotor sides.

Based on these observations, a simple approach to detect a wake interference condition is to calculate the relative wind speed difference δ_V between the two rotor sides, by using a moving averaged SEWS calculated on the left and right quadrants:

$$\delta_V = \frac{\bar{V}_{SE, \text{left}} - \bar{V}_{SE, \text{right}}}{\bar{V}_{RE}} \quad (17)$$

An indication of a left or right-sided wake impingement may be obtained by checking the sign of δ_V and comparing its absolute value with a threshold. It was observed that slightly different left and right thresholds could be used for better detection performance, on account of the non-symmetric lateral behavior of the rotor, due to its spin direction.

In turbulent unwaked wind conditions, speed fluctuations due to the passage of large eddies will generate significant lateral shears, which may be wrongly interpreted as the presence of a wake by the impingement detector. Similarly, in waked conditions, large turbulent fluctuations may temporarily hide the presence of the wake speed deficit. These problems may be alleviated by computing δ_V not with the instantaneous SEWS values, but with moving averages computed on a sufficiently long window of time to filter out the effects of turbulent fluctuations. Clearly, excessively long time windows would have the effect of inducing long delays and missing wake motions due to meandering.

In support of the information coming from wind speed imbalances, also TI can be used as an additional indicator of wake interference. Similarly to the previous plot, Fig. 10 shows the

ground truth and estimated SETI values for different degrees of overlap between the two machines. Here again it appears that the proposed estimator is capable of appreciating the differences in TI over the two sides of the rotor. In addition, these estimates correlate quite well with their reference values. Consequently, one could here again define a relative TI difference δ_{TI} , exactly as done for the wind speed. Checking the value and magnitude of this additional indicator could be used for reinforcing the information obtained by computing the wind speed imbalance, in the interest of a hopefully more robust and reliable indicator.

4.4. Simulation studies

In the following, several wake interference scenarios were realized with the wind and turbine models described above. Wake detection was based in all cases on the δ_V parameter, therefore looking for an imbalance of the SEWS on the right and left quadrants of the rotor. The threshold in δ_V used for discriminating a wake interference from a non-interference case was set to 0.12, while the time span of the moving average window to 60 s. Wind conditions also included a power-law vertical wind shear κ and downwind turbine yaw misalignment γ , to investigate the effects of these parameters on the detection quality.

Fig. 11 shows results obtained for four different shear and turbulence intensity combinations. For different overlaps, each plot displays the detection ratio on the right quadrant (dark blue bars pointing upwards), and on the left one (light blue bars pointing downwards). The detection ratio is defined as the ratio of the number of time instants when the wake is detected, divided by the total number of time instant in a sequence of a given length (here chosen to be 10 min). For each combination of parameters, one single 10-min sequence was used, as additional realizations lead only to marginal changes in the results.

For the cases of low ambient turbulence (TI = 5%) with two different vertical shear layers, results show that a wake can be always detected for overlaps between around $0.25D$ and $0.75D$ on either side of the disk. For the cases characterized by higher ambient turbulence (TI = 10%), the wake is not always perfectly detected due to a faster wake recovery, which in turn leads to a smaller wake deficit. In fact, the wake model predicts a maximum deficit in the wake center of around only 2.5 m/s. That deficit is not as large as in the low turbulence case, where the maximum deficit

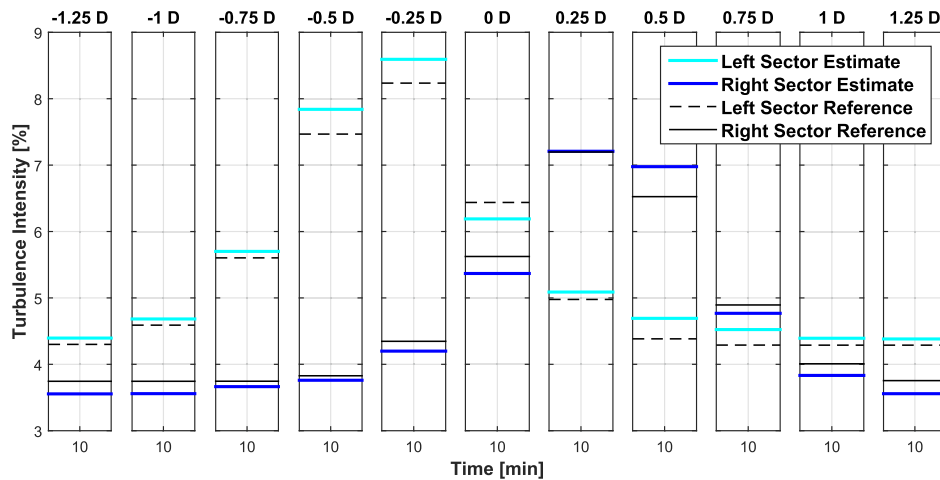


Fig. 10. Estimated and reference (ground truth) sector TIs vs. time. Each column plot represents a different wake overlap, characterized by a different lateral distance between upstream and downstream rotor centers. Left sector SETI: reference TIs shown in black dashed lines, estimates in cyan; right sector SETI: reference TIs in black solid lines, estimates in blue. (For interpretation of the references to colour in this figure legend, the reader is referred to the web version of this article.)

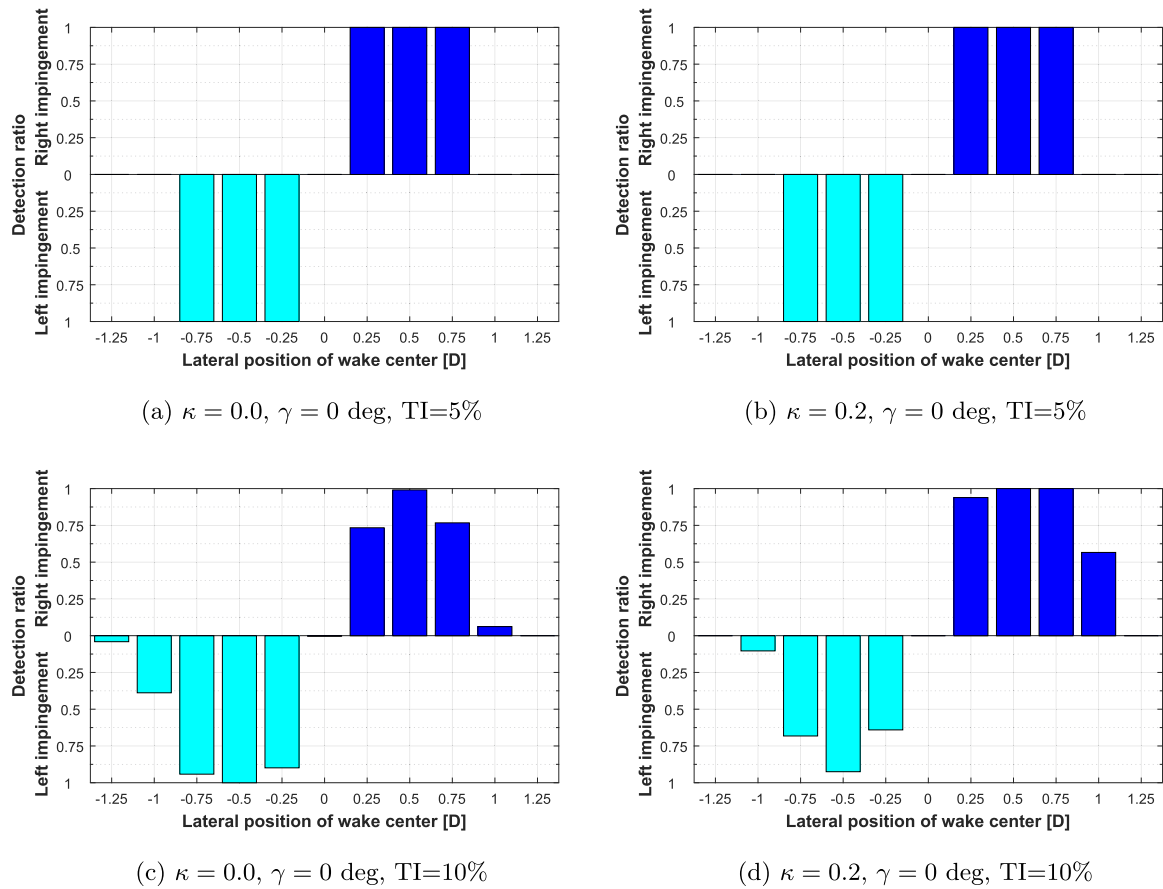


Fig. 11. Wake state detection based on SEWS estimation for varying wake overlap, for an 8 m/s ambient wind speed and different vertical shear and ambient TI.

is about 4.5 m/s. This smaller deficit creates a smaller difference between SEWS on the two rotor sides, in turn decreasing the detection quality. However, the detection ratio remains sufficiently high for all conditions between $0.25D$ and $0.75D$. It also appears that, although false negatives are clearly present, false positives are typically not. Improvement are foreseeable by scheduling both threshold and moving average window size as functions of ambient parameters, at the expense of an increased overall complexity of the algorithm implementation and use.

Fig. 12 shows results for one single wind condition (vertical shear exponent equal to 0.2, TI = 5%), but for four different yaw misalignment angles of the downstream wind turbine ($\gamma = \pm 10$ deg and ± 20 deg). These conditions are meant to represent situations when the downstream wind turbine is actively redirecting its wake away from a machine located further downstream, using some suitable control strategy. In all cases the detection quality is similar to the non-misaligned case reported previously. This can be explained by the fact that the SEWS of the two lateral sectors are little affected by wind direction.

Next, a case characterized by a meandering wake was considered. In order to approximate such a case, the lateral distance y between wake and turbine center was varied in time according to the following expression:

$$y = 1D(\sin(2\pi ft) - 1), \quad (18)$$

where f is the meandering frequency. Accordingly, the resulting wake will oscillate between an unwaked state ($y = -2D$) to a fully

waked one ($y = 0D$). In total, 28 wake oscillations with a frequency of $f = 0.05$ Hz were analyzed, for an ambient mean wind speed of 8 m/s, TI of 5% and a vertical shear layer exponent $\kappa = 0.1$. In this scenario, it is important to ensure a fast detection in order to capture wake motions. To this end, the detection threshold was raised to 0.2 and the moving average filter was eliminated. This same combination of parameters yields good results also in the low turbulence conditions analyzed earlier. The resulting detection ratio is displayed in Fig. 13.

The lower subplot shows the oscillating wake center. Positions between $-0.75D$ and $-0.25D$ are marked in red, since within that range a correct wake state detection is typically possible, as previously shown. The upper subplot shows the scaled mean REWS, using a dashed red line. This quantity was computed on the wind grid, and clearly exhibits a drop when a significant wake overlap is present.

The same upper plot also shows the detection ratio, using a solid blue line, which indicates that a left-sided wake impingement is detected twice throughout a full meandering cycle. When the wake center is far outside of the rotor disk, a wake impingement is never detected, so that there are no false positives. The first detection peak refers to the entrance of the wake on the rotor disk, while the second one to its exit, both times on the left side of the rotor disk. The gap between these two peaks corresponds to the full wake condition, realized when the wake is exactly aligned in front of the downstream wind turbine. This situation could be perhaps detected by comparing the REWS on the upstream and downstream wind turbines, as well as considering the alignment of their

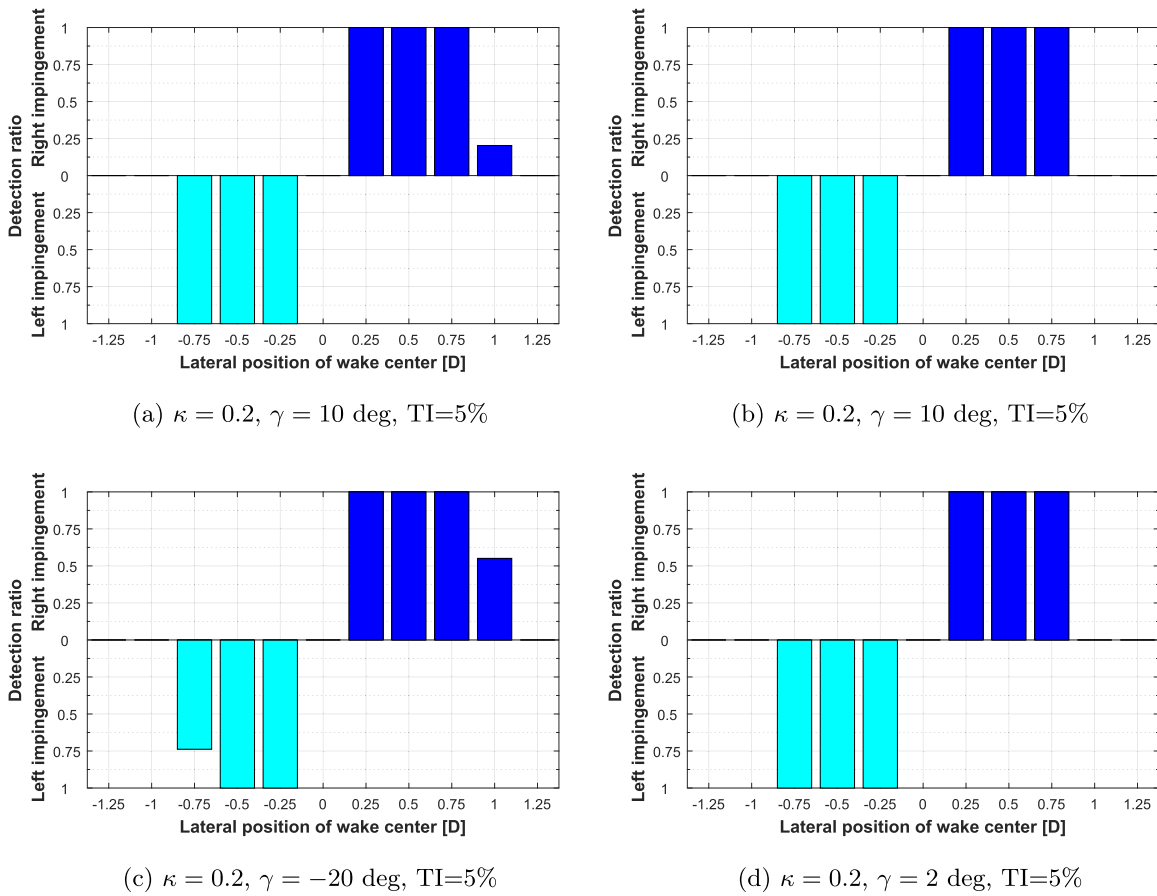


Fig. 12. Wake state detection based on SEWS estimation for varying wake overlap and different misalignment of the downstream wind turbine, for an 8 m/s ambient wind speed, vertical shear exponent equal to 0.2 and TI = 5%.

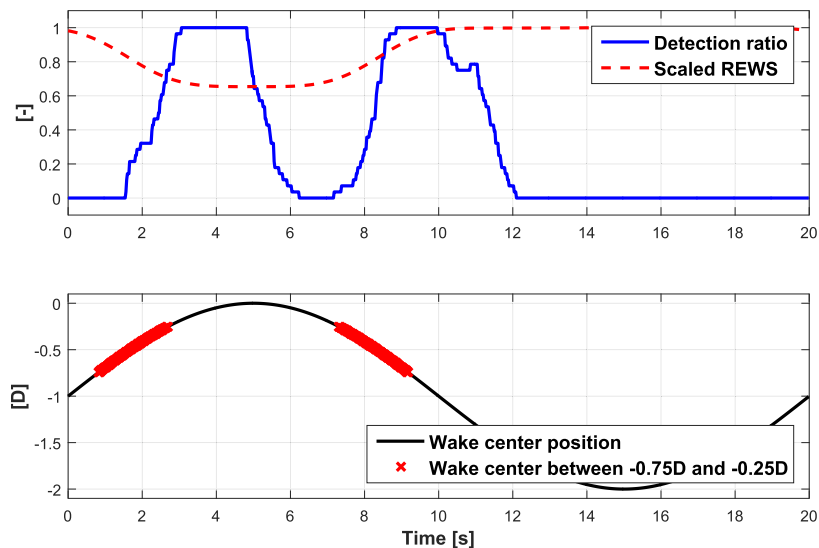


Fig. 13. Upper subplot: detection ratio (blue line) for the meandering wake problem, and scaled REWS (dashed red line), as an average over 28 cycles. Lower subplot: wake center positions vs. time over one cycle. (For interpretation of the references to colour in this figure legend, the reader is referred to the web version of this article.)

connecting line with the wind direction. Comparing the detection rate with the wake center position, a delay of about 2 s can be

observed. This time delay corresponds to approximately 1/3 of a rotor revolution, and it is due to the fact that a new estimate of the

SEWS is realized only once a blade leaves a sector.

5. Conclusions and outlook

This work has presented the formulation of a new method to estimate the wind speed inflow at the rotor disk of a wind turbine. The proposed method falls within the general area of wind sensing, where the whole rotor is turned into a sensor. By using measurements of the rotor response, in this case in the form of blade loads, the response is inverted to estimate the wind conditions. If load sensors are available on a wind turbine, for example to enable load-driven control, the present method does not require any additional hardware and it amounts to a simple software upgrade.

The proposed approach uses the cone coefficient, which captures the zeroth-harmonic bending of the blades, to infer the wind speed by means of a Kalman filter. When loads from all rotor blades are used together, a rotor-equivalent wind speed can be estimated. Simulation and experimental results shown here indicate that this method compares favourably with the well known approach based on the power coefficient. Furthermore, it also appears that the time resolution is sufficient to successfully estimate the associated RETI and REILS.

However, differently from other wind sensing approaches, the proposed formulation has also the ability of sensing variations of the wind speed over the rotor disk. In fact, by using the bending moment measured on each blade individually, one can obtain local estimates of the wind speed. These estimates were here averaged over four rotor quadrants, to yield sector-equivalent wind speed measurements.

The knowledge of areas of different local wind speeds over the rotor disk can be used to infer a lack of uniformity of the wind field. In particular, it was shown with the help of experimental field test data that the method is capable of observing the different wind speeds that characterize the top and bottom quadrants of the rotor, on account of the vertical shear profile.

As an even more interesting application, the paper considered also the detection of the impingement of the wake shed by an upstream wind turbine. Since a wake is characterized by a speed deficit and an increased TI, a partial wake overlap can in principle be detected by measuring speed and TI on the left and right quadrants of the rotor. Simulation results indicate that this is indeed possible with the proposed approach. In fact, studies conducted with a high-fidelity aeroservoelastic model of a wind turbine interacting with a turbulent wake model have shown the general ability of the present method in detecting the presence of a partial wake overlap, even in the presence of wake meandering.

The proposed idea is being further investigated along different lines of research. From a validation point of view, the method is being demonstrated with the help of wind tunnel tests conducted with aeroelastically scaled models. Full-scale experiments with LiDAR measurements of waked conditions should become available soon, hopefully enabling a first verification in the field. Additionally, the scaled experimental facility is being used for exploiting the proposed method at the wind farm control level, where it is being used to trigger a left or right deflection of the upstream wake, based on where the wake impingement is detected. The method is also being used to improve the quality of the estimates produced by a reduced order flow model, used for closed-loop model-based wind farm control. Finally, the vertical resolution provided by the use of sectors is being exploited for the identification of the presence of low level jets in the atmosphere.

Acknowledgements

The authors gratefully acknowledge Dr. Paul Fleming (NWT,

NREL) for having provided the CART3 experimental data.

References

- [1] T. Knudsen, T. Bak, M. Svenstrup, Survey of wind farm control-power and fatigue optimization, *Wind Energy* 18 (8) (2015) 1333–1351, <https://doi.org/10.1002/we.1760>.
- [2] P.A. Fleming, P.M.O. Gebraad, S. Lee, J.-W. van Wingerden, K. Johnson, M. Churchfield, J. Michalakes, P. Spalart, P. Moriarty, Evaluating techniques for redirecting turbine wakes using SOWFA, *Renew. Energy* 70 (2014) 211–218, <https://doi.org/10.1016/j.renene.2014.02.015>.
- [3] A. Jiménez, A. Crespo, E. Migoya, Application of a LES technique to characterize the wake deflection of a wind turbine in yaw, *Wind Energy* 13 (6) (2010) 559–572, <https://doi.org/10.1002/we.380>.
- [4] J. Wang, S. Foley, E.M. Nanos, T. Yu, F. Campagnolo, C.L. Bottasso, A. Zanotti, A. Croce, Numerical and experimental study of wake redirection techniques in a boundary layer wind tunnel, in: *Wake Conference*, Visby, Sweden, 2017, <https://doi.org/10.1109/acc.2011.5991022>.
- [5] F. Campagnolo, V. Petrovic, J. Schreiber, E. M. Nanos, A. Croce, C. L. Bottasso, Wind tunnel testing of a closed-loop wake deflection controller for wind farm power maximization, *J. Phys. Conf. Ser.* 753(032006), <https://doi.org/10.1088/17426596/753/3/032006>.
- [6] P.M.O. Gebraad, F.C. van Dam, J.-W. van Wingerden, A model-free distributed approach for wind plant control, in: *American Control Conference (ACC)*, Washington, DC, USA, 2013, pp. 628–633, <https://doi.org/10.1109/acc.2013.6579907>.
- [7] J. Annoni, P. M. O. Gebraad, A. K. Scholbrock, P. A. Fleming, J.-W. van Wingerden, Analysis of axial-induction-based wind plant control using an engineering and a high-order wind plant model, *Wind Energy*, <https://doi.org/10.1002/we.1891>.
- [8] Z. Yang, Y. Li, J. Seem, Individual pitch control for wind turbine load reduction including wake interaction, in: *American Control Conference (ACC)*, Washington, DC, USA, 2011, pp. 5207–5212, <https://doi.org/10.1109/acc.2011.5991022>.
- [9] P.M.O. Gebraad, F.W. Teeuwisse, J.W. van Wingerden, P.A. Fleming, S.D. Ruben, J.R. Marden, L.Y. Pao, Wind plant power optimization through yaw control using a parametric model for wake effects – a CFD simulation study, *Wind Energy* 19 (1) (2016) 95–114, <https://doi.org/10.1002/we.1822>.
- [10] N. S. Ghaisas, C. L. Archer, Geometry-based models for studying the effects of wind farm layout, *J. Atmos. Ocean. Technol.* <https://doi.org/10.1175/jtech-d-14-00199.1>.
- [11] H. Wang, R.J. Barthelmie, Wind turbine wake detection with a single Doppler wind LiDAR, *J. Phys. Conf. Ser.* 625 (1) (2015) 012017, <https://doi.org/10.1088/1742-6596/625/1/012017>.
- [12] M. Soltani, T. Knudsen, M. Svenstrup, R. Wisniewski, P. Brath, R. Ortega, K. Johnson, Estimation of rotor effective wind speed: a comparison, *IEEE Trans. Control Syst. Technol.* 21 (4) (2013) 1155–1167, <https://doi.org/10.1109/tcst.2013.2260751>.
- [13] C.L. Bottasso, C.E.D. Riboldi, Estimation of wind misalignment and vertical shear from blade loads, *Renew. Energy* 62 (2014) 293–302, <https://doi.org/10.1016/j.renene.2013.07.021>.
- [14] C.L. Bottasso, C.E.D. Riboldi, Validation of a wind misalignment observer using field test data, *Renew. Energy* 74 (2015) 298–306, <https://doi.org/10.1016/j.renene.2014.07.048>.
- [15] M. Bertelè, C. L. Bottasso, S. Cacciola, F. D. Adegas, S. Delport, Wind inflow observation from load harmonics, *Wind Energy Sci.* under review.
- [16] C.L. Bottasso, S. Cacciola, F. Campagnolo, J. Schreiber, Wake detection for wind farm control – formulation and validation, in: *AIAA Scitech*, San Diego, CA, USA, 2016, p. 1741, <https://doi.org/10.2514/6.2016-1741>.
- [17] S. Cacciola, M. Bertelè, J. Schreiber, C. Bottasso, Wake center position tracking using downstream wind turbine hub loads, *J. Phys. Conf. Ser.* 753(032036), <https://doi.org/10.1088/1742-6596/753/3/032036>.
- [18] J. Schreiber, S. Cacciola, F. Campagnolo, V. Petrovic, D. Mourembles, C. L. Bottasso, Wind shear estimation and wake detection by rotor loads – first wind tunnel verification, *J. Phys. Conf. Ser.* 753(032027), <https://doi.org/10.1088/1742-6596/753/3/032027>.
- [19] R.P. Coleman, A.M. Feingold, *Theory of Self-excited Mechanical Oscillations of Helicopter Rotors with Hinged Blades*, Tech. Rep. TN 1351, NACA, 1958.
- [20] K.Z. Østergaard, P. Brath, J. Stoustrup, Estimation of effective wind speed, *J. Phys. Conf. Ser.* 75 (2007) 012082, IOP Publishing.
- [21] X. Ma, N. Poulsen, H. Bindner, *Estimation of Wind Speed in Connection to a Wind Turbine*, Tech. rep., Informatics and Mathematical Modelling, Technical University of Denmark, 1995.
- [22] C.L. Bottasso, A. Croce, *Advanced Control Laws for Variable-speed Wind Turbines and Supporting Enabling Technologies*, Tech. rep., Dipartimento di Ingegneria Aerospaziale, Politecnico di Milano, January 2009.
- [23] I. Munteanu, G. Besançon, Control-based strategy for effective wind speed estimation in wind turbines, in: *IFAC'14, 19th World Congress of the International Federation of Automatic Control*, Cape Town, South Africa, 2014, pp. 6776–6781, <https://doi.org/10.3182/20140824-6-ZA-1003.01952>.
- [24] J.F. Manwell, J.G. McGowan, A.L. Rogers, *Wind Energy Explained*, John Wiley & Sons, Ltd, 2009, <https://doi.org/10.1002/9781119994367>.
- [25] C. L. Bottasso, A. Croce, *Cp-lambda Users's Manual*, Tech. rep., Dipartimento di Scienze e Tecnologie Aerospaziali, Politecnico di Milano (2006–2016).

- 168 *C.L. Bottasso et al. / Renewable Energy 116 (2018) 155–168*
- [26] O.A. Bauchau, C.L. Bottasso, L. Trainelli, Robust integration schemes for flexible multibody systems, *Comput. Methods Appl. Mech. Eng.* 192 (34) (2003) 395–420, [https://doi.org/10.1016/S0045-7825\(02\)00519-4](https://doi.org/10.1016/S0045-7825(02)00519-4).
- [27] N.D. Kelley, B.J. Jonkman, *Overview of the TurbSim Stochastic Inflow Turbulence Simulator*, Tech. rep., National Renewable Energy Laboratory, February 2007.
- [28] P.A. Fleming, A.D. Wright, L.J. Fingersh, J.-W. van Wingerden, Resonant vibrations resulting from the re-engineering of a constant-speed 2-bladed turbine to a variable-speed 3-bladed turbine, in: 49th AIAA Aerospace Sciences Meeting, Orlando, FL, USA, 2011, pp. 4–7, <https://doi.org/10.2514/6.2011-634>.
- [29] J.M. Jonkman, An Aeroelastic Computer-aided Engineering (CAE) Tool for Horizontal axis Wind Turbines, 2015. NWTC Information Portal (FAST), <https://nwtc.nrel.gov/FAST>. (Accessed 2 February 2016). Last modified 19-March-2015.
- [30] J.M. Jonkman, M.L. Buhl, *FAST User's Guide*. 6.0, 2005.
- [31] D.J. Renkema, *Validation of Wind Turbine Wake Models (Master's thesis)*, Delft University of Technology, 2007.

Paper 2: Wind Tunnel Validation of a Wind Observer for Wind Farm Control

4.1 Summary

Within this paper, an experimental wind tunnel validation of the wind observer described in **Paper 1** is conducted. A scaled wind turbine of type G1 is used and described in detail. As the scaled turbine is not equipped with blade root bending sensors, a method using the Coleman transformation is used, which estimates the blade root bending moments from low-speed shaft loads. The experimental setup includes a second turbine, that is located 4 diameters upstream. It is laterally displaced by 0.5 diameters and generates a wake that impinges on the sensing downstream turbine. Two synchronized short-range LiDARs (Light Detection And Ranging) are located further upstream, scanning a defined circular trajectory in variable distances upstream the sensing wind turbine, providing a reference velocity measurement.

Within the first experiment, the upstream turbine is not operating and the load-based velocity estimates of the sensing turbine within the four rotor disc sectors is compared to the LiDAR reference. As the LiDAR measurements are conducted within the turbine induction zone and the load-based estimates represent ambient velocities, the LiDAR measurements are corrected using an induction model. Within the second experiment, the upstream turbine is operating and the LiDAR reference velocity within the most wake affected sector is corrected for the effect of wake recovery in addition. Results show the estimators capability of accurately detecting wind speed in free-stream, even though some small estimation bias could be identified. During waked turbine operation, the most affected sector shows a larger velocity estimate than the LiDAR reference, probably due to a variety of causes. The part of the rotor disc where the wake center is located, shows the smallest velocity estimates proving the capability of qualitatively detecting the wake.

4.2 Contribution

Within this peer-reviewed publication, the author of this dissertation has implemented the wind estimator for the experimental test. The design and conduction of the experiments has been shared equally with Filippo Campagnolo, who also led the analysis. The discussion of results and the writing of the publication was shared in equal parts among all authors.

4.3 Reference

F. Campagnolo, J. Schreiber, A. M. Garcia, and C. L. Bottasso, "Wind tunnel validation of a wind observer for wind farm control," *Proceedings of the International Offshore and Polar Engineering Conference*, 2017. [Online]. Available: <https://www.onepetro.org/conference-paper/ISOPE-I-17-410>

Wind Tunnel Validation of a Wind Observer for Wind Farm Control

Filippo Campagnolo*, Johannes Schreiber*, Andrea Martínez García*, Carlo L. Bottasso*†

*Wind Energy Institute, Technische Universität München, Garching b. München, Germany

†Department of Aerospace Science and Technology, Politecnico di Milano, Milano, Italy

ABSTRACT

This paper describes the validation of a wind observer using LiDAR measurements obtained during a wind tunnel experiment. The setup represents a scaled wind farm composed of three actuated and sensorized wind turbine models operating in a turbulent boundary layer. Rotor loads and other wind turbine response data are used to estimate in real time during operation the local wind speed experienced by each wind turbine. The estimates of the rotor inflow produced by the wind observer are compared with flow data measured by two short-range LiDARs. These devices provide fully synchronized scans of the flow along given trajectories. The paper compares the observed and measured wind conditions, demonstrating a good match between these two independent flow measurement techniques.

KEY WORDS: wind observers; wind farm; wakes; LiDAR; scaled wind turbine models; wind tunnel testing

INTRODUCTION

Wakes shed by wind turbines exhibit a lower wind speed and higher turbulence intensity than the free stream, leading to reduced power output and increased fatigue loads for downwind turbines within wind farms. Knudsen et al. (2014) suggested that there is a large potential in wind farm control (WFC) by means of active wake deflection or wake management. This technology, if brought to maturity and deployed in the field, might lead to significant increases in energy capture and reduced loading for wake-affected turbines.

Independently from the use of a specific WFC algorithm, it is clear that both a detailed knowledge of the wind conditions within a wind farm and of the effects of control actions on the behavior

of wakes, play a key role. Indeed, wakes can be managed effectively only if one can estimate with sufficient accuracy their characteristics –including trajectory, speed deficit, turbulence intensity, and others–, as well as the response of wakes to changes in wind turbine operational conditions and environmental effects. In fact, wake characteristics are affected by ambient wind direction, atmospheric stability, neighboring orography of the terrain, the possible misalignment of the turbine with the wind vector and other factors. Given the complexity of the involved physics, it is generally difficult to predict the behavior of wakes and their evolution purely by means of numerical tools. In this sense, the estimation and/or measurement of wind characteristics in the field may come to the help.

Some of such methods, like nacelle-mounted anemometers or met-masts, might not be sufficient for enabling sophisticated wind farm control, since they provide only point-wise measurements. Scanning LiDAR systems, despite being very effective, are still not widely available due to their cost. Instead of using devices that directly measure the wind flow, wind properties can be estimated directly from the operational response of wind turbines, as it is the case for the rotor effective wind speed computed by means of turbine power or torque (Soltani et al., 2013), or wind shears and misalignments obtained from rotor load harmonics (see Cacciola et al., 2016 and references therein).

Recently, Bottasso et al. (2016) proposed a method for estimating the local wind speed, using measured blade root bending moments. This method, once applied to downwind wind turbines impinged by wakes, has been used by Schreiber et al. (2016) to estimate the wake deficit and the wake position. The same authors also experimentally demonstrated some capabilities of the method by using scaled wind turbines operated in a large boundary layer wind tunnel.

This paper aims at expanding the work done so far. At first the method is briefly described. Next, an experimental facility is de-

scribed that is used to simulate wind farms, and therefore wake-to-turbine and wake-to-wake interactions, within the boundary layer wind tunnel of the Politecnico di Milano. Results concerning the experimental validation of the full capabilities of the wind observer are then discussed, followed by conclusions and future activities.

WIND SECTOR OBSERVER

The observer, whose capabilities are discussed and validated in the following, is the one described in Schreiber et al. (2016) and Bottasso et al. (2016). As specified in greater detail therein, measured blade root bending moments are correlated with the local effective (LE) wind speed felt by the blade through a cone coefficient defined as

$$C_{m_0}(\lambda_{LE}, \beta, q) = \frac{m(\psi)}{\frac{1}{2} \rho A R V_{LE}^2}, \quad (1)$$

where λ_{LE} is the local effective tip speed ratio (TSR), β the blade pitch angle, q the dynamic pressure, m the measured out-of-plane root bending moment of the blade located at the azimuthal position ψ , V_{LE} the local effective wind speed, ρ the density of air, A the rotor disk area and R the rotor radius. Equation 1 makes use of cone coefficients –stored in look-up tables and obtained through a BEM-based simulation tool–, which are functions of TSR, β and q . Since both the TSR and the dynamic pressure are functions of the unknown local effective wind speed, the equation can be solved numerically for each of the rotating blades by using, as inputs, the rotor speed, the blade pitch, the bending moment and, of course, the cone coefficients.

The LE wind speed can then be used to compute, through simple averaging, the velocities in non-rotating sectors of the rotor disk. Choosing four equally sized sectors, as shown in Fig. 1, the sector effective (SE) wind speed can be readily inferred.

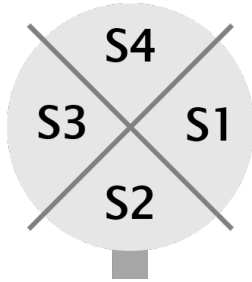


Fig. 1: Wind turbine rotor with four sectors (S1, S2, S3, S4).

The scaled wind turbines used within this research are currently not equipped with blade load sensors, but rather by strain gages mounted on the rotating shaft. However, the out-of-plane root bending moment m_i of blade i can be readily reconstructed by employing the Coleman transformation

$$\begin{bmatrix} m_1 \\ m_2 \\ m_3 \end{bmatrix} = \begin{bmatrix} 0.5 & \cos(\psi_1) & \sin(\psi_1) \\ 0.5 & \cos(\psi_2) & \sin(\psi_2) \\ 0.5 & \cos(\psi_3) & \sin(\psi_3) \end{bmatrix} \begin{bmatrix} m_0 \\ N \\ Y \end{bmatrix}, \quad (2)$$

where ψ_i is the azimuth position of blade i .

To obtain the collective or mean out-of-plane root bending moment m_0 , the rotor effective wind speed V_{RE} is estimated first by solving the torque balance equation

$$J\dot{\Omega} = \frac{\rho A V_{RE}^3 C_P(\lambda, \beta)}{2\Omega} - T_{\text{shaft}}, \quad (3)$$

where J is the rotor inertia, Ω the rotor speed, T_{shaft} the measured torque at the shaft, while $\dot{(\cdot)}$ indicates a derivative with respect to time. Next, m_0 can be obtained solving Eqn. 1 by setting $V_{RE} = V_{LE}$.

To obtain the fixed frame aerodynamic nodding and yawing moments (noted N and Y , respectively) the measured rotating shaft bending loads (N_{rot} and Y_{rot}) are first high-pass (HP) filtered to remove a possible zero drift. This does not lead to a loss of information as long as the assumption of a steady inflow is fulfilled. Next, loads are transformed into the fixed frame of reference through a rotation matrix. The constant gravitational nodding moment $N_G = Md$, where M is the rotor mass and d the sensor distance to the rotor plane, is also considered. The fixed frame nodding and yawing moments become

$$\begin{bmatrix} N \\ Y \end{bmatrix} = \begin{bmatrix} \cos(\psi) & \sin(\psi) \\ -\sin(\psi) & \cos(\psi) \end{bmatrix} \begin{bmatrix} N_{\text{rot,HP}} \\ Y_{\text{rot,HP}} \end{bmatrix} - \begin{bmatrix} N_G \\ 0 \end{bmatrix}, \quad (4)$$

and Eqn. 2 can finally be solved.

EXPERIMENTAL SETUP

Experiments were conducted in the boundary-layer (BL) test section of the wind tunnel of the Politecnico di Milano, which has a cross-sectional area of 13.84 m by 3.84 m and a length of 36 m. The experimental setup included scaled wind turbine models, designed for wind farm control research applications, as well as two short-range WindScanners, developed by the Department of Wind Energy of the Technical University of Denmark (DTU). Atmospheric boundary-layer (ABL) conditions were simulated by the use of spires placed at the chamber inlet. The vertical profile of the longitudinal wind speed was measured prior to testing, resulting in the following best-fitted exponential law

$$U(z) = U_H \left(\frac{z}{z_H} \right)^{0.088}, \quad (5)$$

where $U_H \approx 5.7$ m/s and $z_H = 0.825$ m are the free-stream wind speed at hub height and the elevation of the rotor axis from the ground, respectively. The turbulence intensity at hub height was circa 5%.

The G1 wind turbine models

Tests were conducted with scaled wind turbine models whose rotor diameter D is 1.1 m (in the following named G1s, for Generic

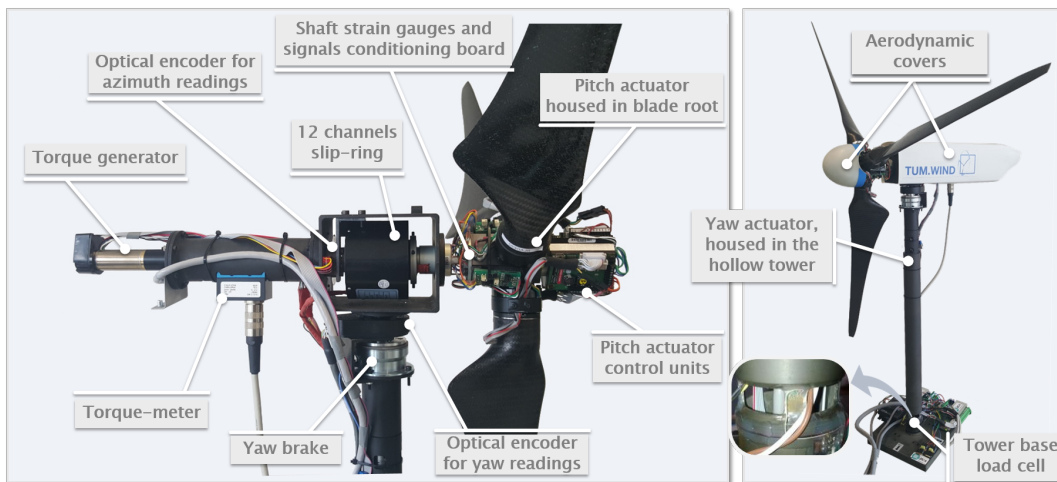


Fig. 2: G1 rotor-nacelle assembly (left) and overall model layout (right).

1 meter diameter rotor), which have been used within other research projects (Campagnolo et al., 2016a, 2016b, 2016c).

The model (see Fig. 2) has dimensions that seek for a compromise among the need for miniaturization, wind tunnel blockage, Reynolds effects and the need to realize multiple wind turbine interference conditions typical of wind farm operations. The scaled wind turbine was designed to enable a realistic energy conversion process. This means that it exhibits good aerodynamic performance both at the airfoil and rotor levels, while its wake is characterized by realistic shape, deficit and recovery when compared to full scale machines. Moreover, the model features active individual pitch, torque and yaw control that, together with a comprehensive onboard sensorization of the machine (including measures of shaft and tower loads), enables the testing of modern control strategies.

The G1 turbine rotor has an angular speed up to 850 rpm (clockwise rotation) and it is equipped with three blades, whose individual pitch angle can be varied by means of a small brushed motor equipped with a gearhead and built-in relative encoder. The three motors, housed in the hollow root of the blades, are each controlled by an electronic board placed within the hub spinner. Between the hub and the front bearings, strain gages glued on four small bridges provide measurements of the aerodynamic torque and of the bending loads. Three miniaturized electronic boards, fixed to the hub, provide for the power supply and conditioning of the shaft strain gages, while a 12-channels slip-ring, located within the rectangular carrying box that holds the main shaft by means of two bearings, is used to transmit signals from the rotating system to the fixed one, and vice versa. A torque-meter measures the torque provided by a brushless motor operated as a generator, located in the rear part of the nacelle. At tower base, a custom made load cell measures fore-aft and side-side bending moments. The entire nacelle can be yawed by means of a brushed motor located within the hollow tower, while an optical encoder provides the necessary feedback to an electronic device that con-

trols both the yaw actuator and a magnetic brake, which is enabled only when no yaw actuation is required.

Each model is controlled by a M1 Bachmann hard-real-time module that real-time executes, similarly to what is done on real wind turbines, collective or individual pitch-torque control laws similar to the ones described in Bossanyi (2000) and references therein. The wind farm layout, consisting of 3 G1s longitudinally spaced of 4D and laterally shifted by 0.5D, is shown in Fig. 3, together with two short-range WindScanners, labelled LiDAR1 and LiDAR2.

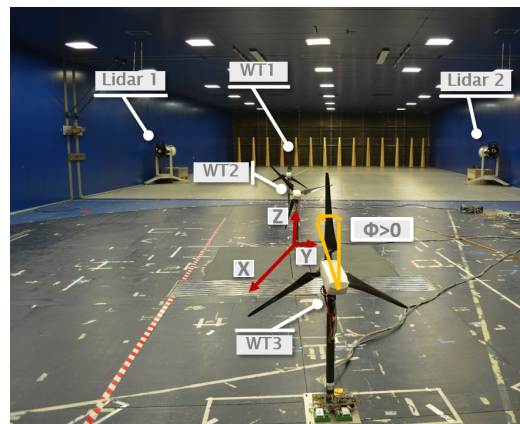


Fig. 3: Wind farm layout in the wind tunnel, showing also reference frame (centered at the tower base of WT2) and direction of positive yaw misalignment Φ .

The performance of the G1 rotor, whose blades are equipped with the low-Reynolds airfoil RG14 (Lyon et al., 1998), was measured for different values of the airfoil Reynolds numbers (between 50-90000) and at several combinations of TSR and collective pitch settings.

Nominal airfoil polars were obtained with XFOIL. Parameter n_{crit} , which governs flow transition (Drela and Youngren, 2001), was set to a value that is typical of the turbulent flow conditions experienced in the Politecnico di Milano wind tunnel. However, significant differences were noticed between the measured and theoretical Blade Element Momentum (BEM)-based aerodynamic performance computed using nominal polars. This problem is probably due to inaccuracies in the airfoil performance computation, in turn due to the challenges associated with the prediction of the laminar bubble separation at very-low Reynolds number. To correct for this, an identification procedure (Bottasso et al., 2014) was used to calibrate the polars, leading to the satisfactory agreement shown in Fig. 4.

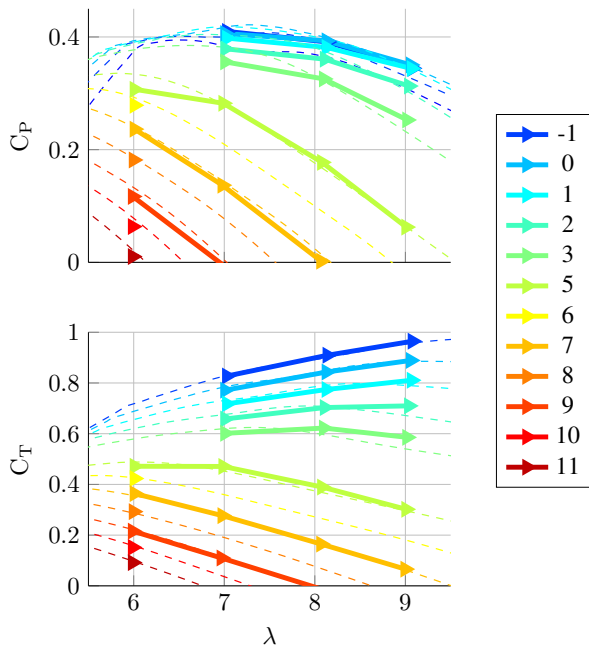


Fig. 4: G1 power (top) and thrust (bottom) experimental (solid lines) and BEM (dashed lines) coefficients, as function of TSR and blade pitch.

The short-range LiDARs

Each of the two short-range LiDARs was installed near the walls of the tunnel, approximately 7D upwind of the turbine models. The LiDARs provide averaged wind speeds at rates up to 390 Hz. They are both equipped with two prism motors and a focus motor, steering the laser beam within a cone of 120 deg of aperture. A common central motion controller ensures that the two focused laser beams are synchronously following a common scanning trajectory. A complete description of the system, as well as the demonstration of its potential when applied to the measurement of small scale flow structures in a wind tunnel, is given in Floris van Dooren et al. (2017).

Three LiDAR systems with three linearly independent beam di-

rections would be necessary to measure the three-dimensional flow velocity vector. Given the distance from the LiDARs and the points of measurement, as well as considering that LiDAR heads are located slightly above the turbine hub height, the plane created by the LiDAR beams is mostly horizontal (± 3 deg). It can therefore be assumed that, from two temporally and spatially synchronised line-of-sight measurements, one can derive the components of the flow speed along (v) and laterally (u) to the main wind direction, with an insignificant contamination of the result by the vertical wind speed component (w) (Floris van Dooren et al., 2017).

Measurement campaign

The measurement campaign aimed at demonstrating the capabilities of the developed wind sector observer described in a previous section. More specifically, the following scenarios were tested.

Measurement of wake profiles along a line

The LiDARs performed measurements along crosswind lines at 1D distance upstream of WT2 and at hub height, spanning approximately 6D around the rotor axis of WT1. The complete line, covered every 1 s with equally sampled measurements, was measured for 30 s and for different settings of the WT1 yaw misalignment angle Φ^{WT1} . Goal of this test was to prove the ability of the wind sector observer to detect, in the sector impinged by the wake of WT1, wind speed changes due to yaw-based wake steering. In order to compute, from measured data, the sector effective wind speeds in the four sectors of Fig. 1, it is necessary to know the flow speed on the overall rotor disk, starting from the available data measured along a crosswind line at hub height. To this end, the wake profile, obtained by bin averaging the LiDAR data, is first best-fitted with a Gaussian function, modeling the wake deficit. In addition, a first-order polynomial is used to account for a possibly non-uniform flow speed along the crosswind direction. This results in the wake profile shown in Fig. 5.

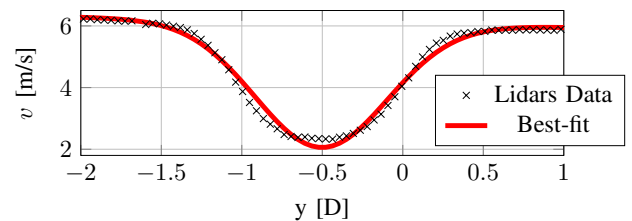


Fig. 5: LiDAR measured wake profile and its best-fit.

The Gaussian function is then rotated around the wake center and superimposed with the free-stream vertical shear and horizontal profiles, resulting in the longitudinal flow speed distribution $v_{LP}(y,z)$ shown in Fig. 6. The sector effective wind speeds can

then be computed as:

$$V_{LP-SE,i} = \frac{1}{A_i} \iint_{A_i} v_{LP}(y,z) dy dz, \quad (6)$$

where A_i is the i th non-rotating sector area of the WT2 rotor disk.

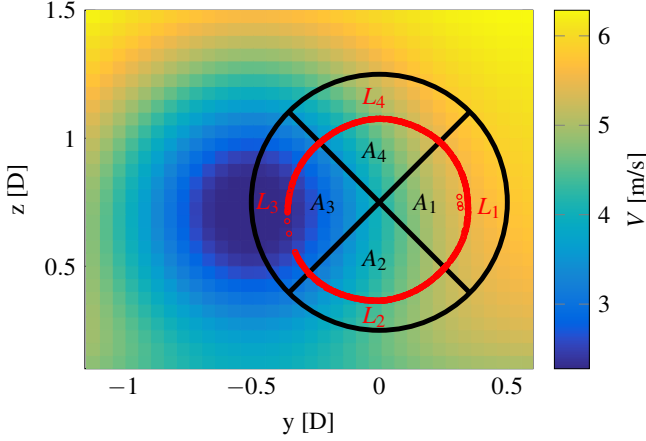


Fig. 6: Reconstruction of the longitudinal flow speed distribution from LiDAR crosswind measurements. The non-rotating sectors of the WT2 rotor disk and the LiDAR closed –nearly circular– path (red dots) are also depicted in the figure.

Measurement of flow profiles along a circular pattern

The LiDARs performed measurements, along the closed –nearly circular– path shown in Fig. 6, at three distances upstream of WT2 ($\xi = x/D = -0.5; -1; -2$). The diameter of the closed path was set equal to approximately $2/3D$, since it has been shown that, for linear horizontal shear profiles of the longitudinal wind speed, the wind speed sampled at this point represents the sector effective wind speed (Bottasso et al., 2016).

Tests were carried out under two different operating conditions. In the first case, WT1 is standing still, which means that WT2 was impinged by the vertical wind profile simulated within the wind tunnel; this condition is referred in the following as the **No-Wake** case. In the second case, WT1 operates in region II and with its rotor exactly aligned with the wind direction, which means that WT2 was partially impinged by the wake produced by the upstream wind turbine; this condition is termed the **Wake** case.

A set of longitudinal wind speed measurements $\{v_{CP}\}$ was acquired for a duration of 60 s, for each combination of operating conditions and measuring planes. This set can be mapped into a set of times $\{t\}$ and a set of in-plane coordinates $\{(y,z)\}$, which collects the positions the lasers beams focused on during the test. The whole closed path was covered in approximately 0.16 s, which yields the average speed along the four paths L_i shown in Fig. 6, sampled at a frequency of approximately 6.25 Hz. At first,

the set of wind speed measurements was split into the following sets

$$\{v_{CP,i}\} = \{v_{CP} | (y,z) \in A_i\}, \quad (7)$$

each associated to a set of times

$$\{t_i\} = \{t | (y,z) \in A_i\}. \quad (8)$$

Four sets $\{V_{CP-L,i}\}$ of average speeds along L_i can therefore be obtained, where the k th element of each set is defined as

$$V_{CP-L,i}^{(k)} = \left\langle \left\{ v_{CP,i} | t_{in,i}^{(k)} \leq t \leq t_{out,i}^{(k)} \right\} \right\rangle, \quad (9)$$

where $t_{in,i}^{(k)}$ and $t_{out,i}^{(k)}$ are the instants when the focus of the LiDAR beams respectively entered and left, for the k th time, the i th rotor disk sector. Four sets of times $\{T_{CP,i}\}$ are then associated to the average speeds, where the k th element of each set is defined as

$$T_{CP,i}^{(k)} = \frac{t_{in,i}^{(k)} + t_{out,i}^{(k)}}{2}. \quad (10)$$

In order to use this data sets for validating the wind sector observer, it is necessary to account for the fact that the average speeds $\{V_{CP-L,i}\}$ may differ from the mean of the flow speed within the i th rotor disk sector, especially for the **Wake** case. Therefore, the longitudinal flow speed distribution $v_{LP}(y,z)$, obtained by measuring along crosswind lines and with the models operating as in the **Wake** case, was used to compute the expected average speeds along the four paths L_i :

$$V_{LP-L,i} = \frac{\int_{L_i} v_{LP}(y,z) ds}{\int_{L_i} ds}, \quad (11)$$

which allows one to compute the ratio $r_i = \frac{V_{LP-SE,i}}{V_{LP-L,i}}$. In turn, this is used to obtain the following set of average speeds:

$$\{V_{CP-SE,i}\} = r_i \{V_{CP-L,i}\}. \quad (12)$$

Table 1, which reports the ratio for the four rotor disk sectors, shows that substantial differences are observed when one looks at the 3rd rotor disk sector, which is fully immersed into the wake produced by WT1. However, almost negligible differences are observed for the 1st one, which is almost out of the wake produced by WT1. Therefore, correcting the average speeds along L_i for the **No-Wake** case appears not to be necessary.

Sector	V_{LP-SE} [m/s]	V_{LP-L} [m/s]	r_i
1	5.441	5.412	1.005
2	4.308	4.234	1.017
3	2.798	2.626	1.065
4	4.814	4.683	1.028

Table 1: Comparison between average speeds along paths L_i and average speeds within the rotor disk sector A_i .

RESULTS

At first, we focused on the comparison between the average of the sets $\langle\{V_{CP-SE,i}\}\rangle$ with the average of speeds observed by the wind sector observer for the **No-Wake** case. The results, reported in Fig. 7, show that the 4th (upper) sector experiences the highest speed and the 2nd (bottom) the lowest one. On the other hand, wind flows through the 1st and 3rd sectors feature speeds that are between these two extreme values. This is indeed the expected behavior due to vertical shear. It can be also appreciated that the closer to the turbine the LiDAR beams are focused, the lower the measured velocity is, which agrees with the expected effect of the rotor induction on the upstream flow (Burton et al., 2001).

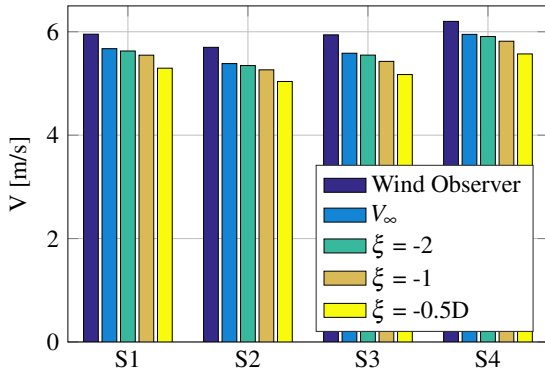


Fig. 7: **No-Wake** case: comparison between the average of the sets $\langle\{V_{CP-SE}\}\rangle$, computed at different $\xi = x/D$, and the undisturbed velocity V_∞ with the wind sector observer predictions.

Given that the wind speeds predicted by the observer are the ones of the undisturbed flow (Schreiber et al., 2016), one must correct the measured speed data by the effect produced by the rotor induction in order to properly validate the observer. The approach of Medici et al. (2011) has been used for this purpose. Specifically, the undisturbed velocity $V_{\infty,i}$ of each sector, as well as the axial induction factor a , are the ones that best-fit the following set of equations to the measured data:

$$\langle\{V_{CP-SE,i}\}\rangle(\xi) = V_{\infty,i} \left[1 - a - \frac{2a\xi}{\sqrt{1+4\xi^2}} \right]. \quad (13)$$

The rotor axial induction factor was included within the parameters that the fitting algorithm estimates, instead of using the BEM-based value. In fact, Eqn. 13 proved to overestimate the predicted velocity deficits when the BEM-based axial induction factor is used (Simley et al., 2016).

Table 2 reports a comparison between the sector undisturbed velocity $V_{\infty,i}$ and the wind speeds $V_{WO,i}$ predicted by the observer, together with the relative errors. Results show that the wind observer slightly overestimates, by approximately 5%, the wind speeds on all four rotor disk sectors, probably due to uncertainties in the BEM-based cone coefficients. Indeed, such coefficients could be further tuned to lead to a better agreement between measurements and observations. However, the observer appears to

be clearly capable of properly detecting the effect of the vertical shear on the wind speed experienced by each sector.

Sector	V_{WO} [m/s]	V_∞ [m/s]	Err. [%]
1	5.95	5.67	+4.70
2	5.70	5.38	+5.52
3	5.94	5.60	+5.98
4	6.20	5.95	+4.06

Table 2: **No-Wake** case: comparison between the sector undisturbed velocity V_∞ and the wind speeds V_{WO} predicted by the observer.

Results for the **Wake** case, are reported in Fig. 8. It can be noticed that the 3rd sector, being fully impinged by the wake of WT1, experiences a very low velocity. On the other hand, the 1st sector, being almost out of the wake, experiences nearly the same speed as in the **No-Wake** case. Meanwhile, sector 4, as expected, is crossed by a flow whose speed is higher than the one experienced by sector 2, due to the vertical shear. However, both sectors, being partially in the wake, experience speeds in between the ones of the left and right sectors, as expected.

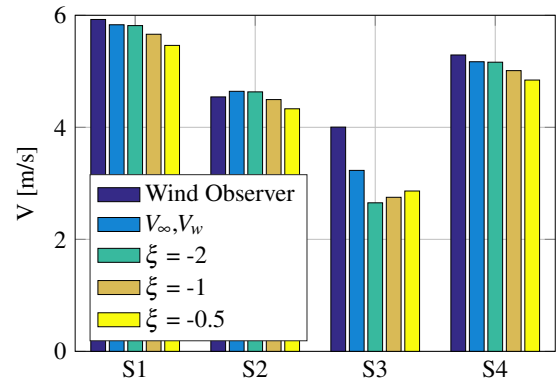


Fig. 8: **Wake** case: comparison between the average of the sets $\langle\{V_{CP-SE,i}\}\rangle$, computed at different $\xi = x/D$, and the undisturbed velocity V_∞ or wake speed V_w with the observer wind predictions.

As for the **No-Wake** case, measured data needs to be corrected by the effect of the rotor induction, which reduces the speed the closer one gets to the disk. However, for the sectors that are highly impinged by the wake of WT1, it is also necessary to account for wake recovery. Indeed, LiDAR beams are not focused at the rotor disk location; the speeds they measure would be therefore lower, even if corrected by rotor induction, than the speeds of the wind flows that cross the rotor sectors. As a result, they could not be compared to wind observations. Wake recovery plays, then, an opposite effect than rotor induction, since it accelerates the flow velocity as the wake moves further downstream, i.e. the closer to WT2 one looks. The combination of these two opposite effects is clearly visible if one observes the trend of $\langle\{V_{CP-SE,3}\}\rangle$, evaluated with respect to ξ . For the 3rd sector, indeed, the measured wind speed increases closer to the rotor disk, while the other sectors are characterized by behaviors similar to those observed for

the **No-Wake** case. The two effects can be modeled by combining the Jensen model equation (Katic et al., 1986)

$$V_w(\xi) = V_\infty \left[1 - \frac{2a^{WT1}}{[1 + 2k(4 + \xi)]^2} \right], \quad (14)$$

to Eqn. 13. The distance from WT1, expressed as $4 + \xi$, accounts for the longitudinal distance between the wind turbines, which is $4D$, and negative values of ξ . This way, one can obtain the undisturbed velocity $V_{\infty,i}$ of each sector, as well as the axial induction factor a of WT2, by best-fitting the following set of equations to the measured data:

$$\langle \{V_{CP-SE,i}\} \rangle (\xi) = V_{\infty,i} \left[1 - a - \frac{2a\xi}{\sqrt{1 + 4\xi^2}} \right], \quad \text{for } i = 1, 2, 4, \quad (15a)$$

$$\langle \{V_{CP-SE,3}\} \rangle (\xi) = V_{\infty,3} \left[1 - a - \frac{2a\xi}{\sqrt{1 + 4\xi^2}} \right] \left[1 - \frac{2a^{WT1}}{[1 + 2k(4 + \xi)]^2} \right]. \quad (15b)$$

A wake expansion coefficient $k = 0.046$, calibrated by previous wind tunnel tests (Campagnolo et al., 2016a), and a BEM-based axial induction factor $a^{WT1} = 0.4$ were used as parameters of the fitting.

By this approach, one can:

- compare wind speeds predicted by the observer to the undisturbed velocity V_∞ for sectors that are out or partially in the wake of WT1, thus neglecting the effects of wake recovery;
- for sector 3, which is fully impinged by the wake of WT1, compare the observer prediction to the wake speed V_w evaluated at $\xi = 0$.

The comparison, reported in Table 3, is satisfactory for sectors that are out or partially in the wake of WT1. On the other hand, the observer performance is poor in predicting the speed of the flow crossing a fully wake-impinged sector. The mismatch could be due to uncertainties in the measurements. In fact, the ability of short-range WindScanners of measuring wind speeds lower than 2 m/s along their line of sight is questionable (Floris van Dooren et al., 2017). An additional reason might be an inappropriate modeling of the wake recovery and/or rotor induction effects, or the detection accuracy of wind sector speeds by means of hub loads.

CONCLUSIONS

The paper has presented experimental results obtained in a large boundary layer wind tunnel, which were used to characterize the performance of a local wind observer based on rotor loads.

The observer proved to be capable of accurately detecting the sector effective wind speed for a wind turbine operating in free stream conditions, i.e. not impinged by wakes. In particular,

Sector	V_{WO} [m/s]	V_∞ [m/s]	$V_w(0)$ [m/s]	Err. [%]
1	5.92	5.83	-	+1.59
2	4.54	4.64	-	-2.20
3	4.00	-	3.23	+19.3
4	5.29	5.17	-	+2.28

Table 3: **Wake** case: comparison between the sectors undisturbed velocity V_∞ or wake speed V_w and the wind speeds V_{WO} predicted by the observer.

it has been shown that the observer can properly detect the effect of the vertical shear on the wind speed experienced by each sector. This could be exploited for estimating the vertical shear, which is known to be strictly related to the stability of the atmosphere. Since atmospheric stability plays a major role in determining wake behavior, which may significantly affect wake management techniques (Vollmer et al., 2016), it is clear that knowledge of vertical shear at each turbine location within a wind power plant could lead to potential benefits at the level of wind farm control.

The observer also proved to be capable of accurately detecting the speed of wind flows crossing sectors that are partially impinged by wakes. The comparison, in terms of mean values, between LiDAR and observer measurements proved to be unsatisfactory for sectors completely immersed in the wake shed by upstream machines. Possible explanations for this inconsistency have been proposed, but deeper analyses are required to fully explain these results. However, the velocity deficit is qualitatively detected by the wind observer. Such information will be exploited by wake management strategies, currently under development, which aim at steering wakes away from downstream turbines.

Further work will aim at characterizing the time it takes for the observer to detect changes of the SE wind speeds, due to the turbulent nature of the wind and time-varying wind directions. Moreover, further analyses will be performed to characterize the quality of the estimations for significant yaw misalignment angles, e.g. if the waked turbine itself is intentionally yawed to redirect its own wake.

ACKNOWLEDGEMENTS

This research was supported by the German Federal Ministry for Economic Affairs and Energy (BMWi) within the CompactWind project. The authors wish to thank M. Sjöholm, N. Angelou, T. Mikkelsen (Technical University of Denmark), and A. Croce (Politecnico di Milano), for the precious collaboration in the conduction of the experiments. S. Cacciola (Politecnico di Milano) is also acknowledged for his contribution concerning the development of the wind observers.

REFERENCES

Bossanyi, E (2000). "The design of closed loop controllers for wind turbines," *Wind Energy*, 3, 149-163.

- Bottasso, CL, Cacciola, S, and Iriarte, X (2014). "Calibration of wind turbine lifting line models from rotor loads," *Journal of Wind Engineering and Industrial Aerodynamics*, 124, 29-45.
- Bottasso, CL, Cacciola, S and Schreiber, J (2016). "Wind speed sensing and wake detection from rotor loads," *Renewable Energy*, under review
- Burton, T, Sharpe, D, Jenkins, N, and Bossanyi, E (2001). "Wind energy handbook," Wiley
- Cacciola, S, Bottasso, C L and Bertelè, M (2016). "Simultaneous observation of wind shears and misalignments from rotor loads," *Journal of Physics: Conference Series*, 753
- Campagnolo, F, Petrović, V, Bottasso, CL and Croce, A (2016a). "Wind tunnel testing of wake control strategies," *Conference proceedings of the 2016 American Control Conference*, Boston, ACC16.
- Campagnolo F, Petrović V, Schreiber J, Nanos EM, Croce A and Bottasso CL (2016b). "Wind tunnel testing of a closed-loop wake deflection controller for wind farm power maximization," *Journal of Physics: Conference Series*, 753.
- Campagnolo F, Petrović V, Nanos EM, Tan C W, Bottasso CL, Paek I, Kim H and Kim K (2016c). "Wind tunnel testing of power maximization control strategies applied to a multi-turbine floating wind power platform," *Proceedings of the International Offshore and Polar Engineering Conference*, Rodos, Greece, ISOPE, Vol 2.
- Drela, M and Youngren, H (2001). "XFOIL 6.94 User Guide"
- Floris van Dooren, M, Campagnolo, F, Sjöholm, M, Angelou, N, Mikkelsen,., Kühn, M (2017). "Demonstration and uncertainty analysis of synchronised scanning lidar measurements of 2D velocity fields in a boundary-layer wind tunnel," *Wind Energy Science*, under review
- Medici, D, Ivanell, S, Dahlberg, J-A, and Alfredsson, PH (2011). "The upstream flow of a wind turbine: blockage effect," *Wind Energy* 14
- Katic, I, Højstrup, J and Jensen, NO (1986). "A Simple Model for Cluster Efficiency," *Proceedings of EWEC 1986*.
- Knudsen, T, Bak, T, and Svenstrup, M (2014). "Survey of wind farm control-power and fatigue optimization," *Wind Energy*.
- Lyon, C, Broeren, A, Giguère, P, Gopalathnam, A, and Selig, M (1998). "Summary of Low-Speed Airfoil Data," *SoarTech Publications* 3.
- Schreiber, J, Cacciola, S, Campagnolo, F, Petrović, V, Mourembles, D and Bottasso, CL (2016). "Wind shear estimation and wake detection by rotor loads — First wind tunnel verification," *Journal of Physics: Conference Series*, 753
- Simley, E, Angelou, N, Mikkelsen, T, Sjöholm, M, Mann, J and Pao, LY (2016). "Characterization of wind velocities in the upstream induction zone of a wind turbine using scanning continuous-wave lidars," *Journal of Renewable and Sustainable Energy*, 8
- Soltani, MN, Knudsen, T, Svenstrup, M, Wisniewski, R, Brath, P, Ortega, R and Johnson, K (2013). "Estimation of Rotor Effective Wind Speed: A Comparison," *IEEE Transactions on control systems technology*, 21
- Vollmer, L, Steinfeld, G, Heinemann, D und Kühn, M (2016). "Estimating the wake deflection downstream of a wind turbine in different atmospheric stabilities: An LES study," *Wind Energy Science*, 1

Paper 3: Wake detection for wind farm control – formulation and validation

5.1 Summary

Within this work a method to detect an impinging wake on a turbine rotor is described. The underlying methods, which base on the sector-effective wind speed (SEWS) estimates and their variations within the turbine rotor disc, are described corresponding to the work within **Paper 1**.

An experimental validation is presented using scaled wind farm experiments within a boundary layer wind tunnel. The two scaled turbines of type G2 are equipped with blade root bending sensors (different to the models used in **Paper 2**) and the downstream turbine is installed at varying lateral positions with respect to the upstream turbine. Thereby, different amounts of wake impingement could be simulated to validate the wake detector. The SEWS within the part of the rotor disc that is affected most by the upstream turbine wake, shows significantly reduced velocity, confirming the general applicability of the wake detector. The wake detector, which bases on the comparison between the left and right sector-effective wind speed estimates, finally shows large wake detection ratios for lateral turbine displacements between $\pm(0.3$ up to $0.6)$ rotor diameters. Thereby, the wake detector identifies whether the wake impinges on the left or on the right part of the rotor disc, which is of importance especially if the specific location of a wake needs to be known, i.e. for wake steering wind farm control. The method does not identify very weak or full wake impingements, the latter however can be identified by power or rotor-effective wind speed comparisons. In experiments at different ambient wind speeds and without wake impingement, the wake detector shows now false positives.

The paper shows that the developed method for local wind estimation and wake detection also works when individual pitch control (IPC) is used at the sensing turbine.

5.2 Contribution

Within this peer-reviewed publication, the author of this dissertation has conducted all simulations and technical analysis of the wind speed estimator and wake detector. The wind tunnel experiments have been conducted by Filippo Campagnolo. The discussion of results and the writing of the publication was shared in equal parts among all authors.

5.3 Reference

C. L. Bottasso, S. Cacciola, F. Campagnolo, and J. Schreiber, “Wake detection for wind farm control – formulation and validation,” *34th Wind Energy Symposium, AIAA SciTech Forum*, 2016. doi: 10.2514/6.2016-1741



Wake detection for wind farm control – Formulation and validation

C.L. Bottasso^{1,2}, S. Cacciola¹, F. Campagnolo¹ and J. Schreiber¹

¹ Technische Universität München, München, Germany

² Politecnico di Milano, Milano, Italy

E-mail: carlo.bottasso@tum.de

Abstract. A method to detect wake impingement on a wind turbine is described. The wake detector, which uses rotor loads as measured by on-board sensors, can then be used for implementing wind farm control strategies, for example in the form of wake redirection. The method is verified and validated by using field test data, aeroservoelastic simulations and by experimental data obtained with scaled wind turbine models tested in a large boundary layer wind tunnel.

1. Introduction and motivation

In the past, most of the research in wind energy technology focused on the optimization of wind turbines. In recent years, interest has expanded from the level of the individual machines to the one of wind farms. Optimal site selection, layout and control of wind farms are extremely complex tasks that require an understanding of the aerodynamic interactions among the various machines and with the environment. These are all problems that are not yet fully understood and that are still challenging to model in an accurate way.

In this contribution, we describe our ongoing work on wind farm control. Ad hoc observers are used for detecting wake interaction conditions, in turn enabling cooperative control strategies for power maximization and load mitigation by active wake deflection. Our research program includes a scaled experimental facility for the simulation of wind farms in a boundary layer wind tunnel, which is used for the validation of simulation tools and the verification of control strategies.

A wind turbine extracts energy out of the wind flow and thereby sheds a wake characterized by a reduced wind speed and an increased turbulence intensity, as shown in Fig. 1. In certain conditions within a wind farm environment, turbines may be affected by the wake of upstream machines, an interaction that typically results in reduced power output and increased fatigue loads. Wake mitigation or redirection performed by a wind farm controller may reduce these undesired effects [1-3].



Figure 1. At left, wake and turbulence effects in a wind farm; at right: power curtailment and wake deflection strategies for wind farm cooperative control.

For any such control logic to be effective, it is crucial to know the flow conditions within the wind farm. A main objective of the present research project is to develop techniques for utilizing the rotor of each turbine as a wind sensor, by measuring wind characteristics as well as detecting potential wake impingements. Together with flow and wake models, these measurements can then be exploited by a closed loop wind farm controller for better energy capture and reduced fatigue loading. LiDARs (Light Detection and Ranging) may also be able to detect the location of a wind turbine wake [4], and therefore in principle they could be used to achieve such a goal. However, their use is still confined to research applications, and they are not yet routinely deployed in the field on production machines. The approach described herein represents an alternative method for wake detection that may be implemented at no cost on existing wind turbines equipped with load sensors.

In the present work, an estimation of the mean wind speed at the position occupied by each blade is obtained based on measurements of blade root bending moments. Those estimates are then used to detect a wake impingement condition on either side of the rotor disk. This new approach is demonstrated and validated with the help of aeroservoelastic simulations in a high-fidelity environment, using field test data, and also by wind tunnel tests of a scaled wind farm model. The use of rotor loads for the detection of wind conditions is a technology that was first proposed in [5] and further developed in [6-11].

2. Methods

At first, a rotor-effective wind speed estimator is developed, based on the out-of-plane cone (i.e. averaged over the number of blades) bending rotor loads. The cone coefficient is defined as

$$C_{m_0}(\lambda_{RE}, \beta, V_{RE}) = \frac{\frac{1}{2\pi} \int_{\psi=0}^{2\pi} \sum_{i=1}^B m_i(\psi_i) d\psi}{\frac{1}{2} \rho A R V_{RE}^2}, \quad (1)$$

where λ_{RE} is the rotor-effective tip speed ratio, β the pitch angle, m_i the out-of-plane bending moment of blade i occupying the azimuthal position ψ_i , ρ is the density of air, A the rotor disc area, R the rotor radius and V_{RE} the unknown rotor-effective wind speed. With this definition, the blade collective bending moment $m_0 = \sum_{i=1}^B m_i/B$ is computed as

$$m_0(t) = \frac{1}{2B} \rho A R V_{RE}^2(t) C_{m_0}(\lambda_{RE}(t), \beta(t), V_{RE}(t)), \quad (2)$$

where B is the number of blades. At each instant of time, m_0 is measured by blade load sensors. As also the rotor speed Ω can be easily measured together with the blade pitch angle β , the sole unknown in the equation is the effective wind speed V_{RE} , which can therefore be readily computed.

To increase robustness of the estimates in the face of measurement and process noise, an Extended Kalman filter is used for the computation of V_{RE} . The wind speed update is defined as

$$V_{REk} = V_{REk-1} + w_{k-1}, \quad (3)$$

w_k being the process noise with covariance \mathbf{Q} , while the non-linear output equation is defined as

$$z_k = \frac{1}{2} \rho A R V_{REk}^2 C_{m0}(\lambda_{RE}, \beta) - \hat{m}_0 + v_k, \quad (4)$$

where v_k is the zero-mean measurement noise with covariance \mathbf{R} , \hat{m}_0 are the measured loads, while the output z_k is set to 0 to enforce the desired equation at each step.

Such a method delivers estimates of the wind speed and turbulence intensity that are similar, if not slightly superior, to the classical rotor-effective wind speed estimators based on the torque balance equation using the power coefficient C_p [12]. In fact, the present approach may be somewhat less limited in frequency than the classical one, which is slowed by the significant inertia of the rotor. An example of the quality of the resulting estimates of the wind speed in the time domain is shown in Fig. 2. The effective wind speed reference, shown in the figure using a black solid line, was computed from the simulation input as the spatial mean of the longitudinal wind speed within the rotor disk area, as already done in Østergaard et al. [13]. The estimates provided by the present method are of good accuracy and robustness with respect to the tuning parameters of the filter.

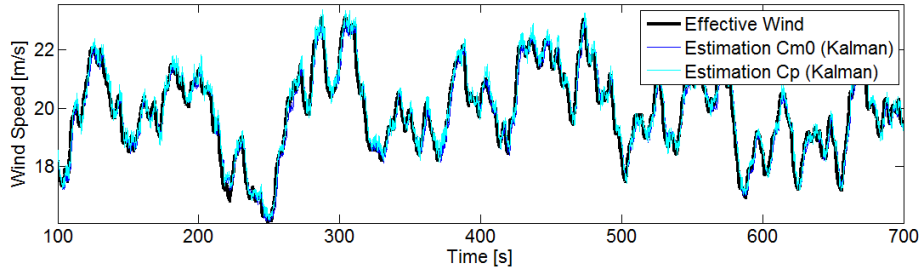


Figure 2. Effective wind speed time history and its estimates, obtained by the cone estimator using the C_{m0} coefficient and by the classical formulation based on the power coefficient C_p [12].

Next, the method is specialized to the estimation of wind speed on sectors of the rotor disk. To this end, considering the i th blade, the previous moment equation is modified as

$$m_i(t) = \frac{1}{2B} \rho A R V_{LE}^2(t, \psi) C_{m0}(\lambda_{LE}(t, \psi), \beta_i(t), V_{LE}(t)), \quad (5)$$

where β_i is the i th blade pitch angle, whereas the blade local-effective wind speed is defined as

$$V_{LE}(\psi) = \frac{1}{A_B} \int_{A_B} V dA_B(\psi), \quad (6)$$

A_B being the planform area of the rotor blade. From the blade local-effective wind speed, a sector-effective wind speed is obtained by averaging over an azimuthal interval of interest. The concept is

illustrated in Fig. 3, which shows how the passage of a blade over a disk sector can be used for estimating a sector-effective wind speed:

$$V_{SE}(\bar{t}) = \frac{1}{A_S} \int_{A_S} V_{LE}(t, \psi) dA_S = \frac{1}{\psi_2 - \psi_1} \int_{\psi_1}^{\psi_2} V_{LE}(t, \psi) d\psi. \quad (7)$$

Finally, from the knowledge of the wind speed, the sector turbulence intensity can be readily computed.

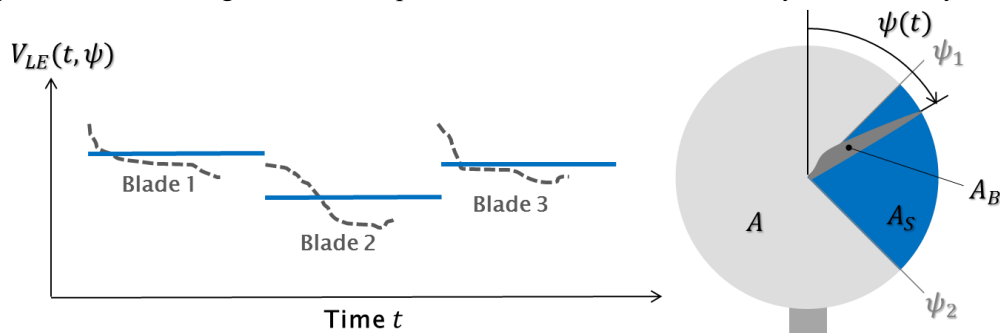


Figure 3. Estimation of local-effective and sector-effective wind speed and turbulence intensity, from the loads of a blade passing through a rotor disk sector.

3. Results

Both the wind speed estimator and the wake detector based on it were validated using field test data, aeroservoelastic simulations and wind tunnel testing.

3.1. Validation with field test data

At first, the new method was tested using field data of the NREL CART 3 wind turbine [14]. As this machine does not experience significant waked conditions, due to the location of its neighboring wind turbines, the proposed method was used to estimate the different velocities in the top and bottom quadrants of the rotor, providing this way an estimate of the vertical wind shear.

A nearby met-mast, shown in Fig. 4, provides reference anemometric measurements. In order to compare the estimates provided by the proposed method with the two measurements available at the met-mast at different heights, it is useful to derive a point measurement from the sector-effective wind speed obtained from blade loads. As shown in Ref. [6], the estimator can be interpreted as sampling the wind field at about 66% of the blade span. Consequently, the anemometer measurements were interpolated at hub height $\pm 2/3 R$ and used as reference measurements in the following plot to judge the quality of the load-based estimates.

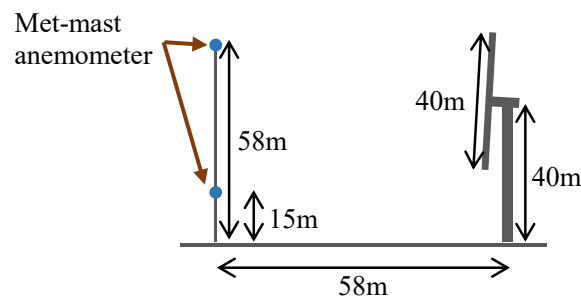


Figure 4. Sketch of met-mast anemometer position wrt the NREL CART 3 wind turbine.

Figure 5 shows a good agreement between the estimated sector-effective wind speeds with the interpolated point-wise anemometric measurements. The trends are reasonably well followed and a higher wind speed is typically detected in the top than in the bottom quadrant.

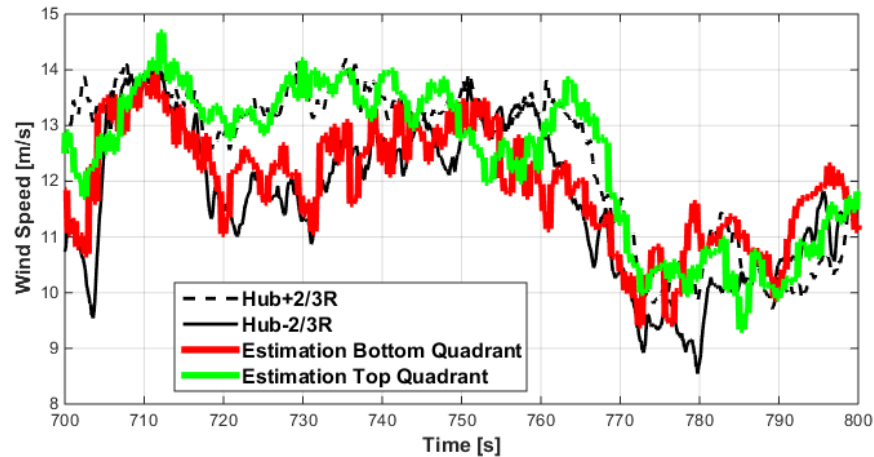


Figure 5. Estimation of top and bottom quadrant effective wind speeds, and comparison with interpolated met-mast data for the NREL CART 3 wind turbine.

3.2. Validation using aeroservoelastic simulations

Next, the new method was used for estimating the local wind speed separately on the left and right parts of the rotor, thereby detecting the possible presence of an area of reduced speed and increased turbulence intensity, which may indicate the presence of a wake. As no experimental data was available for this case, a simulation study was conducted, by using a high-fidelity aeroservoelastic model [15] of a multi-MW wind turbine operating in different partial and full wake conditions. The turbulent wind field was obtained by the superposition of Mann's turbulence with Larsen wake model.

The results of the estimation are summarized by Figs. 6 and 7, which show the actual and estimated local wind speeds and turbulence intensities in two lateral quadrants of the rotor. Each subplot refers to a different overlap indicated by the lateral distance between rotor and wake center.

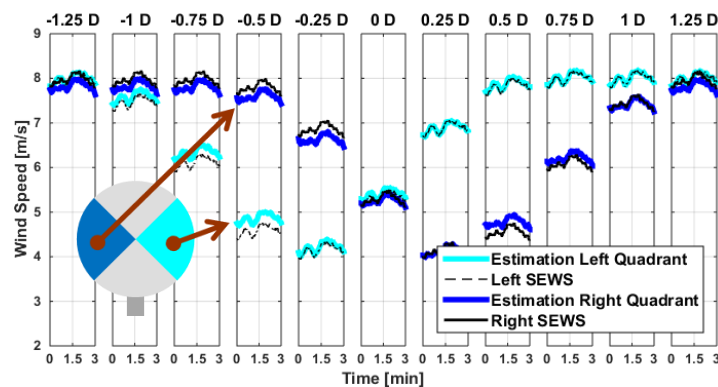


Figure 6. Estimation of local wind speed on two lateral rotor quadrants.

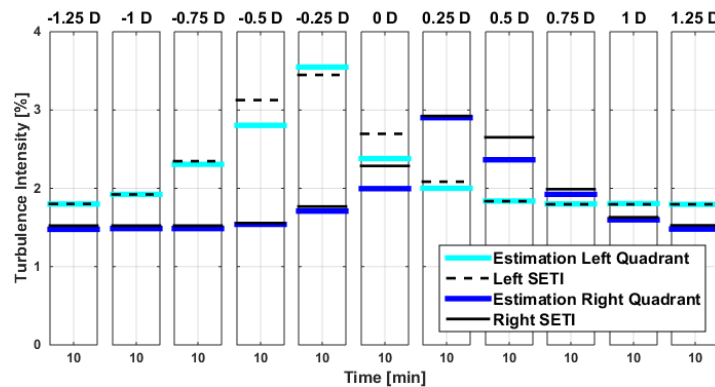


Figure 7. Estimation of local wind turbulence intensity on two lateral rotor quadrants.

To simulate the effects of a meandering wake, the wake position was laterally displaced between far out-of-wake and full-waked conditions as a function of time according to $y = -1D + 1D \sin(2\pi ft)$ (cf. Fig. 8), where the frequency f was set to 0.05 Hz. As shown in the picture, the method reliably detects the waked conditions, with a small delay of about 2 sec, which correspond to about one third of a revolution.

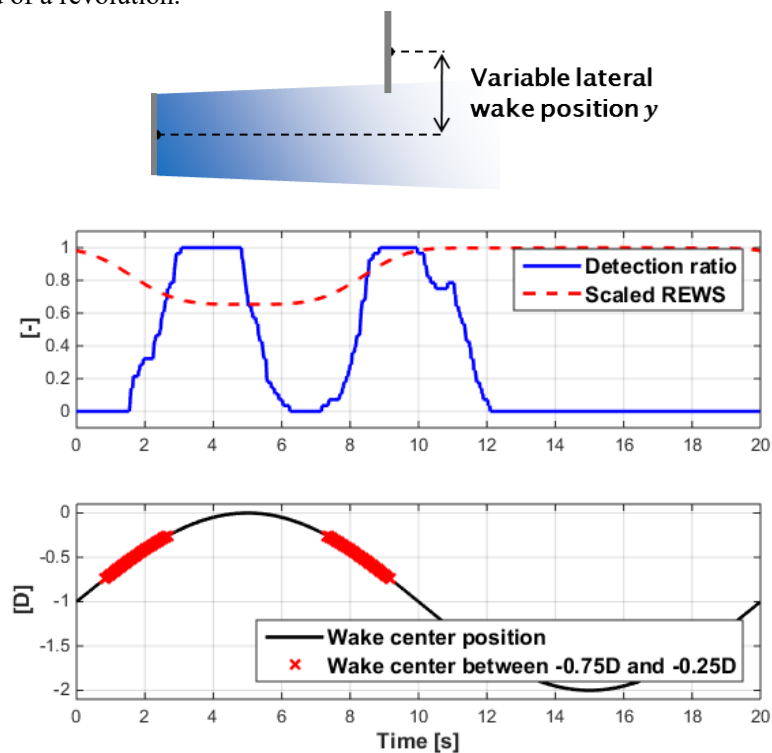


Figure 8. Detection of a meandering wake.

3.3. Validation using scaled models in a boundary layer wind tunnel

Finally, the method was validated using experimental data obtained using scaled models (Fig. 9) tested in the large boundary wind tunnel of the Politecnico di Milano [16].

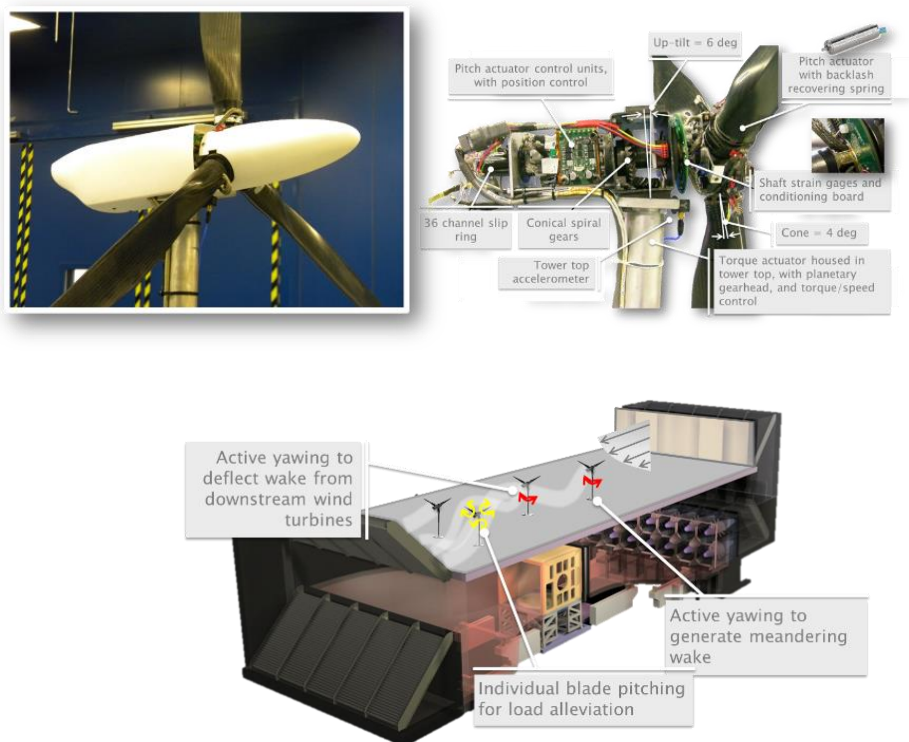


Figure 9. Scaled wind turbine models, and experimental setup in the wind tunnel for the testing of wind farm control strategies.

One wind turbine model was operated in the wake of an upstream machine, at a distance of four diameters, representative of a closely spaced wind power plant layout. The machine, equipped with load sensors on the blades, was controlled in closed loop both by a standard collective pitch and torque controller, as well as by an individual blade pitch controller used for load alleviation in partial wake conditions. Loads measured on the machine in various different interference conditions were used for estimating wake impingement, as previously explained. During all tests the ambient turbulence intensity was about 7%, with a wind shear layer characterized by a power law exponent equal to $\kappa = 0.26$.

Figure 10 shows the estimation of the local wind speed on two lateral rotor quadrants for the standard collective pitch controller. Similarly, Fig. 11 shows the estimations during tests with the individual pitch controller. Not all lateral displacements could be tested for the latter controller, but a comparison between the available results indicates that the local wind speed can be estimated independently of the controller choice.

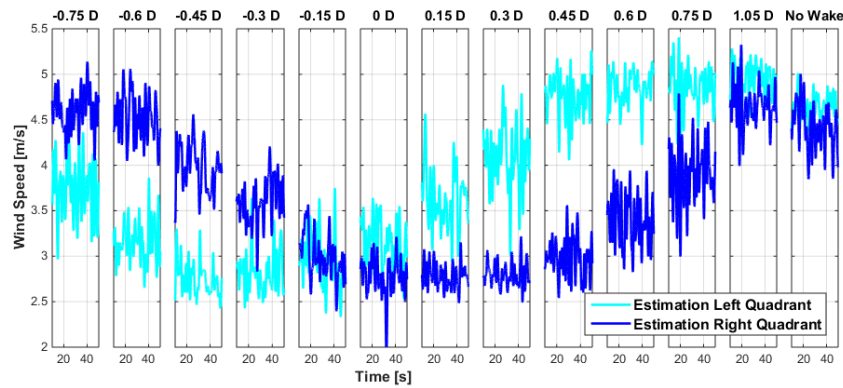


Figure 10. Estimation of local wind speed, collective pitch control case.

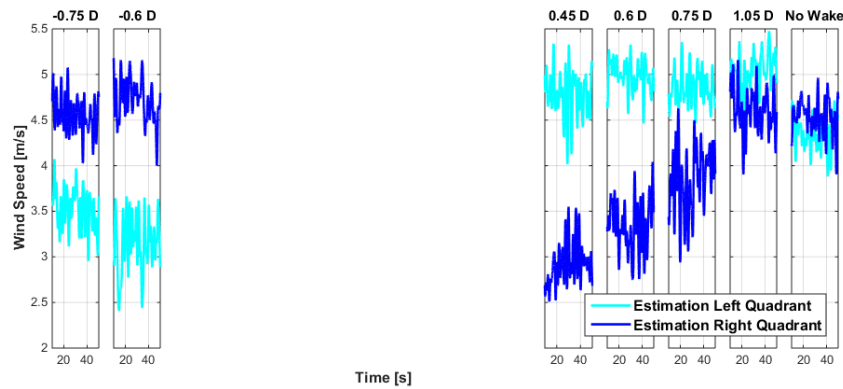


Figure 11. Estimation of local wind speed, individual pitch control case.

By comparing the estimations in the horizontal quadrants, scaled by the estimated rotor effective wind speed, the wake can be detected with good accuracy on either side of the rotor. Figure 12 shows the detection ratio for the collective pitch control case. The small asymmetry between the left and right wake impingement cases can be explained by a slight overestimation of the wind speed in the left quadrant due to turbine up-tilt. This problem is currently being corrected in a new release of the observer.

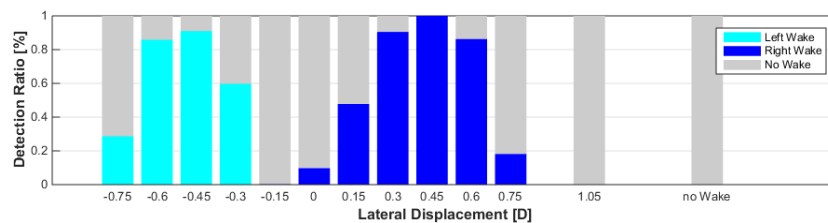


Figure 12. Wake impingement detection ratio for different lateral displacements.

The robustness of the wake impingement detector is evaluated for another set of measurements where no upwind turbine is present. As clearly shown in Fig. 13, for all wind speeds between 2.9 and 6.5 m/s, representing several operating points in control regions II and III, there are no false detection events.

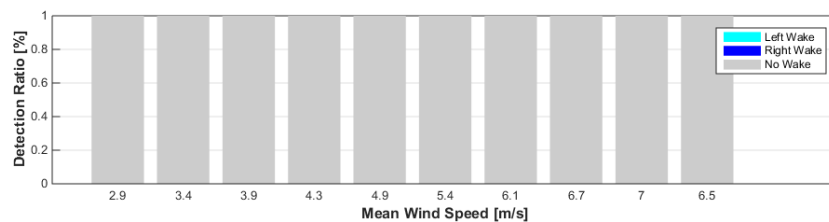


Figure 13. Detection ratio at different wind speeds without wake impingement.

4. Conclusions and outlook

A method was described that can be used for detecting wake impingement on a wind turbine within a wind power plant. The proposed method is capable of estimating with good accuracy the local wind speed and turbulence intensity, and in particular it is able to detect variations of these quantities on the two sides of the rotor that may be indicative of a wake interference condition. Similar results can be derived for various wind conditions, demonstrating the robustness of the local wind speed estimator. The verification and validation of the observer is obtained by using field test data, aeroservoelastic simulations, as well as scaled experiments performed in a boundary layer wind tunnel with sophisticated wind turbine models.

The new wake detector is currently being used for driving wake deflection strategies by active wind turbine yaw. Such form of wind power plant control will also be tested in forthcoming wind tunnel entries using the scaled wind farm facility developed by our group.

References

- [1] Lund B F, Oma P N and Jakobsen T 2014 Wind farm production maximization through joint optimization of turbine efficiency and yaw. Simulated case studies. *Poster EWEA* (Barcelona, Spain)
- [2] Park J, Kwon S and Law K H 2013 Wind farm power maximization based on a cooperative static game approach *Proceedings of the SPIE Active and Passive Smart Structures and Integrated Systems Conference* (San Diego, USA)
- [3] Fleming P, Gebraad P, Lee S, van Wingerden J, Johnson K, Churchfield M, Michalakes J, Spalart P, Moriarty P 2013 High-fidelity simulation comparison of wake mitigation control strategies for a two-turbine case *Proceedings of ICOWES Conference* (Lyngby, Denmark)
- [4] Bingöl F, Mann J, Larsen G. 2010 Light detection and ranging measurements of wake dynamics. Part I: one-dimensional scanning. *Wind Energy* **13** 51–61
- [5] Bottasso C L, Croce A and Riboldi C E D 2010 Spatial estimation of wind states from the aeroelastic response of a wind turbine *Proc. TORQUE* (Heraklion, Greece)
- [6] Bottasso C L, Cacciola S and Schreiber J 2015 A wake detector for wind farm control *J. Phys.: Conf. Ser.* **625** 012007
- [7] Bottasso C L and Riboldi C E D 2015 Validation of a wind misalignment observer using field test data *Renewable Energy* **74** 298–306
- [8] Bottasso C L and Riboldi C E D 2014 Estimation of wind misalignment and vertical shear from blade loads *Renewable Energy* **62** 293–302
- [9] Simley E and Pao L Y 2014 Evaluation of a wind speed estimator for effective hub-height and shear components. *Wind Energy* DOI: 10.1002/we.1817 Available online
- [10] Bottasso C L, Campagnolo F and Petrović V 2014 Wind tunnel testing of scaled wind turbine models: beyond aerodynamics *J Wind Eng Ind Aerod* **127** 11–28
- [11] Bottasso C L, Croce A, Riboldi C E D and Bir G 2009 Real-time estimation of structural and wind states for wind turbine advanced control *Proc. EWEC* (Marseille, France)
- [12] Soltani M and Wisniewsky R 2013 Estimation of rotor effective wind speed: a comparison *IEEE Trans. Contr. Syst. Technol.* **21**(4) 1155–1167

- [13] Østergaard K Z, Brath P, Stoustrup J 2007 Estimation of effective wind speed *Journal of Physics: Conference Series* 75, EWEA
- [14] Fleming P A, Wright A D, Fingersh L J and van Wingerden J W 2011 Resonant vibrations resulting from the re-engineering of a constant-speed 2-bladed turbine to a variable-speed 3-bladed turbine *Proc. 49th AIAA Aerospace Sciences Meeting* (Orlando, Florida)
- [15] Bottasso C L and Croce A 2006–2015 *Cp-Lambda – User’s Manual* Politecnico di Milano (Milano, Italy)
- [16] Bottasso C L, Campagnolo F Petrović 2014 Wind Tunnel Testing of Scaled Wind Turbine Models: beyond Aerodynamics *Journal of Wind Engineering & Industrial Aerodynamics* **127** 11-28

Paper 4: Field testing of a local wind inflow estimator and wake detector

6.1 Summary

Within this paper, a field test of the wind observer described in **Paper 1** is conducted. The validation study employs two full-scale 3.5 MW wind turbines and a nearby met-mast. For one of the turbines, two blades are equipped with blade root bending sensors allowing the application of the wind sensing method.

Results show that the load-based vertical inflow shear estimation correlates very well with met-mast reference values. As the met-mast is only reaching turbine hub height, load-based shear estimates using only the lower part of the rotor disc are compared and consequently correlate better with the met-mast reference than full rotor estimates. The load-based estimation of the horizontal shear could not be quantitatively compared to any reference value, however the shed wake of the second turbine could be used for qualitative assessment: depending on the wind direction, the wake impinges on different parts of the sensing turbine thus leading to a distinct fingerprint in the horizontal shear and the corresponding sector-effective wind speeds. Thereby, a left, right or full wake overlap could be clearly identified. As the method relies on the accuracy and calibration of sensors, procedures are also presented and demonstrated which correct for possible sensor miscalibration.

6.2 Contribution

The author of this dissertation has conducted the main research work and prepared a first draft of the manuscript. Carlo L. Bottasso developed the core idea of load-based wind sensing, supervised the research and contributed to the writing of the paper. Marta Bertelè assisted in the measurement post-processing and analysis. All authors provided important input to this research work through discussions, feedback and by improving the manuscript.

6.3 Reference

J. Schreiber, C. L. Bottasso, and M. Bertelè, “Field testing of a local wind inflow estimator and wake detector,” *Wind Energy Science*, vol. 5, no. 3, pp. 867–884, 2020. doi: 10.5194/wes-5-867-2020

Wind Energ. Sci., 5, 867–884, 2020
<https://doi.org/10.5194/wes-5-867-2020>
 © Author(s) 2020. This work is distributed under
 the Creative Commons Attribution 4.0 License.



Field testing of a local wind inflow estimator and wake detector

Johannes Schreiber, Carlo L. Bottasso, and Marta Bertelè

Wind Energy Institute, Technische Universität München, 85748 Garching bei München, Germany

Correspondence: Carlo L. Bottasso (carlo.bottasso@tum.de)

Received: 4 February 2020 – Discussion started: 11 March 2020

Revised: 20 May 2020 – Accepted: 3 June 2020 – Published: 7 July 2020

Abstract. This paper presents the field validation of a method to estimate the local wind speed on different sectors of a turbine rotor disk. Each rotating blade is used as a scanning sensor that, traveling across the rotor disk, samples the inflow. From the local speed estimates, the method can reconstruct the vertical wind shear and detect the presence and location on an impinging wake shed by an upstream wind turbine. Shear and wake awareness have multiple uses, from turbine and farm control to monitoring and forecasting.

This validation study is conducted with an experimental data set obtained with two multi-megawatt wind turbines and a hub-tall met mast. Practical and simple procedures are presented and demonstrated to correct for the possible miscalibration of sensors.

Results indicate a very good correlation between the estimated vertical shear and the one measured by the met mast. Additionally, the proposed method exhibits a remarkable ability to locate and track the motion of an impinging wake on an affected rotor.

1 Introduction

Knowledge of the wind turbine inflow can enable several applications. For example, a turbine controller can be improved when scheduled as a function of wind speed (Østergaard et al., 2007). Similarly, a farm controller benefits from knowledge of the atmospheric stability, because of its strong effect on wake recovery, and from an improved understanding of wake position (Vollmer et al., 2017), because of its crucial implications on power output and loading. Apart from control applications, other usage scenarios include lifetime assessment and fatigue consumption estimation, which are clearly dictated by the inflow conditions experienced by each turbine (Ziegler and Muskulus, 2016). Moreover, wind farm power and wind forecasting, post-construction site assessment, sector management triggered by wake detection for closely spaced turbines, and estimation of available wind farm power are all additional applications that can profit from knowledge of the inflow affecting each single turbine. Unfortunately, this information is not available on today's wind turbines that, as a consequence, operate “in the dark” based

only on a limited awareness of the environment in which they are immersed.

Indeed, turbines are equipped with wind sensors, typically located on the nacelle or the spinner, which are used for aligning the rotor axis into the wind and for identifying whether the cut-in or cut-out wind speeds have been reached. Even though these measurements might be accurate enough for these simple tasks, the actual complexity of the turbine inflow remains completely beyond the reach of such sensors. In addition, wind vanes and anemometers provide pointwise information, while wind conditions exhibit significant spatial variability not only at the large scale of the farm, as in offshore plants (Peña et al., 2018) and at complex terrain sites (Lange et al., 2017; Schreiber et al., 2020), but also at the smaller scale of the individual turbine rotor disk (Murphy et al., 2019). More sophisticated measurements can be provided by lidars (Held and Mann, 2019) and other remote sensing technologies, which are however still costly and – being mostly used for assessment, validation, and research – are not yet commonly used for production installation.

The concept of using the wind turbine rotor as a wind sensor has been proposed to improve wind condition awareness (Bottasso et al., 2010; Simley and Pao, 2016; Bertelè et al., 2017). In a nutshell, wind sensing uses the response of the rotor – in the form of loads, accelerations, and other operational data – to infer the characteristics of the wind blowing on the turbine. Therefore, wind sensing is a sort of model inversion, where the response of the system is used to estimate the disturbance (in this case, the wind). The simplest and probably most widely used wind sensing technique is torque-balance estimation (Ma et al., 1995; Soltani et al., 2013). Thereby, turbine power or torque is used to estimate the rotor-effective wind speed by the power curve or power coefficient. The concept has been more recently extended to estimate other characteristics of the inflow, notably the wind directions and shears, as reviewed in Bertelè et al. (2017).

This paper considers the approach first formulated by Bottasso et al. (2018). Through an aerodynamic “cone” coefficient, this method uses the blade out-of-plane bending moment to estimate the local wind speed at the position occupied by a blade. The method is very similar to the torque-balance estimation of the wind speed, with the important difference that it produces a localized speed estimate instead of a rotor-effective one. The rotating blades therefore operate as scanning sensors that, traveling across the rotor disk, sample the local variability of the inflow. In turn, the local wind speed estimates are used for obtaining two key pieces of information on the inflow: the vertical shear, which is an important load driver and an indicator of atmospheric stability, and the horizontal shear, which can be used to detect the presence and location of an impinging wake. Today, only a scanning lidar would be able to provide similar information on the inflow, albeit not exactly at the rotor disk – as done here, as the rotor itself is the sensor in this case – and with a very different level of complexity and cost.

The present method has some very interesting features. First, it is model-based, and therefore it does not necessitate extensive data sets for its training. Second, it is based on an extremely simple model of the rotor (expressed through the cone coefficient), which can be readily computed from a standard aeroelastic model of a wind turbine. Third, the resulting estimator is in the form of a simple lookup table that is computed offline, resulting in an online onboard implementation of negligible computational cost. Fourth, when load sensors are already installed on the turbine for load-alleviating control or monitoring, this wind sensing technique requires no additional hardware, and therefore its implementation simply amounts to a software upgrade. The wind sensing method considered here has already been tested with blade element momentum (BEM) aeroelastic simulations (Bottasso et al., 2018), large-eddy simulations (Schreiber and Wang, 2018), and scaled wind tunnel tests (Campagnolo et al., 2017). Applications related to wake position tracking within a wind farm have been presented in Schreiber et al. (2016) and Bottasso and Schreiber (2018).

The goal of the present paper is to validate the wind sensing approach of Bottasso et al. (2018) in the field. To this end, the method is exercised on a data set obtained with two 3.5 MW turbines, one of which has two blades equipped with load sensors, and a meteorological mast (met mast). Since a perfect calibration of the sensors cannot always be guaranteed, another goal of the paper is to present and demonstrate simple and effective methods to correct the measurements and improve accuracy.

The paper is organized as follows. First, the formulation of the wind sensing method is reviewed, including the estimation of rotor-effective and sector-effective wind speeds, as well as of horizontal and vertical shears. Next, the experimental setup is described, including the site layout and the available measurements. The result section represents the core of the paper and illustrates in detail the performance of the wind sensing technique. A first part of the analysis is concerned with the validation of the vertical shear estimates. Then, the attention is turned to the detection of wake impingement, which is studied by exploiting the waking induced at the site for some wind directions by a neighboring turbine. Finally, the effects of cross-flow are considered, demonstrating that the typical inevitable misalignments between turbine and wind vector do not pollute the estimates. Conclusions and an outlook on future work are given in the last section.

2 Methods

2.1 Rotor and blade-effective wind speed estimation

Considering a steady and uniform wind speed V , the power coefficient C_p and cone coefficient C_m (as introduced in Bottasso et al., 2018) are defined as

$$C_p(\beta, \lambda, q) = \frac{T_{\text{aero}}\Omega}{0.5\rho AV^3}, \quad (1a)$$

$$C_m(\beta, \lambda, q, \psi_i) = \frac{m_i}{0.5\rho ARV^2}, \quad (1b)$$

where β is the blade pitch angle, $\lambda = \Omega R/V$ the tip speed ratio, Ω the rotor speed, R the rotor radius and $A = \pi R^2$ the swept disk area, ρ the air density, and $q = 1/2\rho V^2$ the dynamic pressure, while T_{aero} is the aerodynamic torque. The azimuthal position of the i th blade is given by ψ_i , while m_i is its out-of-plane root bending moment. Coefficients C_p and C_m are readily computed using an aeroelastic model of the turbine, today customarily based on a BEM method that, in the present work, is the one implemented in the FAST code (Jonkman and Jonkman, 2018).

Different approaches to estimate wind speed from the power coefficient are reviewed in detail by Soltani et al. (2013). However, following Bottasso et al. (2018), here we use both the power and the cone coefficients: while the former yields a rotor-effective wind speed (i.e., an average quantity over the entire rotor disk), the latter is used to sample

the *local* wind speed at the azimuthal position occupied by a blade. A local radial sampling would require a more sophisticated approach and additional sensors along the blade span, with increased complexity and cost. Given coefficients C_p and C_m computed for a reference air density ρ_{ref} , lookup tables (LUTs) are generated that return wind speeds given measured loads T_{aero} and m_i , blade pitch β , rotor speed Ω , and air density ρ . Noting the rotor-effective wind speed estimated from the torque balance equilibrium as V_{TB} and the one from blade loads as V_i , the inversion of Eqs. (1) yields

$$V_{\text{TB}} = \text{LUT}_{C_p} \left(\beta, \Omega, T_{\text{aero}}, \frac{\rho}{\rho_{\text{ref}}} \right), \quad (2a)$$

$$V_i = \text{LUT}_{C_m} \left(\beta, \Omega, \psi, m_i, \frac{\rho}{\rho_{\text{ref}}} \right). \quad (2b)$$

Instead of the simple nonlinear model inversion adopted here for simplicity, more sophisticated methods can be used, for example based on Kalman filters or input observers (Soltani et al., 2013), which may slightly improve the results at the cost of an increased complexity. A rotor-effective wind speed can also be obtained from the blade-effective ones by simple averaging over all (three) blades:

$$V_B = 1/3 \sum_{i=1}^3 V_i. \quad (3)$$

Although in a nonuniform inflow the two rotor-effective speeds V_{TB} and V_B are not necessarily identical, they are in practice very similar, as shown later on in the results section. The redundancy offered by V_{TB} and V_B offers opportunities for sensor calibration, as also described later on.

In Eq. (2a), T_{aero} is computed from the dynamic torque balance equilibrium $J\dot{\Omega} = T_{\text{aero}} - T_{\text{meas}} - T_{\text{loss}}$, where J is the total rotor, drivetrain, and generator rotational inertia, while $\dot{\Omega}$ is the rotor acceleration and T_{meas} is the measured torque at the generator. Mechanical losses in the drivetrain are taken into account by the term T_{loss} (Soltani et al., 2013). Here, for the accuracy of the wind speed estimate, a dynamic model is used to compute the aerodynamic torque. In fact, the energy converted into rotor acceleration or deceleration is typically large, given the large rotational inertia of the system.

A simpler approach is used for Eq. (2b), where the blade dynamic equilibrium is neglected. This way, the out-of-plane bending moment is directly set to the corresponding measured load, i.e., $m_i = m_{i,\text{meas}}$, where $m_{i,\text{meas}}$ is provided by blade-mounted strain gages, optical sensors, or similar devices. The introduction of a flapwise dynamic equilibrium equation, although certainly possible, would not be straightforward because of the coupling with the tower fore-aft motion and the need to estimate additional relevant modeling parameters. Therefore, in the interest of simplicity and practical applicability, the phase delay caused by the dynamic response of the blade was taken into account by estimating an azimuth bias in the response, as described in Sect. 3.7. Due

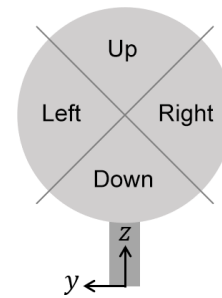


Figure 1. Wind turbine rotor disk with sectors and inflow coordinate system. This naming convention is in the downstream viewing direction.

to the high damping of the flap degree of freedom, even the present simplified method seems able to provide accurate results, as also shown in previous simulation studies (Bottasso et al., 2018).

The power and cone coefficients of Eqs. (1) are computed when the rotor axis is aligned with the ambient wind direction. Hence, strictly speaking, Eqs. (2) can be used to estimate wind speeds only in the same aligned conditions. However, this is typically not the case in practice, as turbines are often misaligned with respect to the wind by several degrees. It will be shown later on that moderate misalignments do not significantly affect the estimation of wind speeds and that the effects of larger misalignments can be corrected for.

2.2 Sector-effective wind speed estimation

An average wind speed over a rotor sector can be readily computed by averaging the blade-effective estimate V_i between two azimuthal angles ψ_a and ψ_b :

$$V_S = \int_{A_S} V_i(\psi) dA_S, \quad (4)$$

where $A_S = (\psi_b - \psi_a)R^2/2$ is the area of the sector. A new sector-effective speed estimate is generated as soon as a blade leaves the sector.

The sector width can be arbitrarily defined. Figure 1 shows the case of the four equally sized 90° wide sectors used in this work, yielding the four sector-effective wind speed estimates $V_{S,\text{left}}$, $V_{S,\text{right}}$, $V_{S,\text{up}}$, and $V_{S,\text{down}}$. Clearly, a finer sampling of the inflow over the rotor disk can be achieved by using smaller sectors. With three blades, each of the sectors is updated three times per rotor revolution. With one single instrumented blade, the update frequency reduces to once per revolution. The effects of sampling frequency on the local wind speed estimates are analyzed in Sect. 3.3.

It was shown in Bottasso et al. (2018) that, for a linear inflow shear and a 90° wide sector, the sector-effective wind speed corresponds to the inflow speed at a distance of approximately $2/3R$ from the hub center.

2.3 Shear estimation

The vertical wind shear is modeled as a power-law profile with exponent α , while the horizontal shear is assumed to be linear with coefficient κ . The inflow wind speed V can therefore be written as

$$V(z, y) = V_H \left(\left(\frac{z}{z_H} \right)^\alpha + \kappa \frac{y}{R} \right), \quad (5)$$

where z and y are the vertical and lateral coordinates, respectively, with origin at the turbine foundation, as shown in Fig. 1. Furthermore, V_H is the speed at the hub center, which is located at $z = z_H$ and $y = 0$.

Assuming that the sector-effective speed samples the inflow profile at $\pm 2/3R$ along the z and y axes, according to Bottasso et al. (2018), the shear coefficients can be estimated from the sector-effective wind speeds by using Eq. (5), which yields

$$\alpha_B = \ln \left(\frac{V_{S,\text{up}}}{V_{S,\text{down}}} \right) \left(\ln \left(\frac{z_H + 2/3R}{z_H - 2/3R} \right) \right)^{-1}, \quad (6a)$$

$$\kappa_B = \frac{3}{2} \frac{V_{S,\text{left}} - V_{S,\text{right}}}{V_{S,\text{left}} + V_{S,\text{right}}}. \quad (6b)$$

This way, the vertical shear is estimated by using the top and bottom sectors, while the horizontal shear is estimated by using the two lateral sectors. One could also use all four sectors together, and solve Eq. (5) simultaneously in a least-squares sense for both α_B and κ_B . However, this does not lead to appreciable differences in the results of this paper.

The vertical shear estimate is validated in this work by comparison with an IEC-compliant met mast, reaching up to hub height. However, shears computed over the whole rotor or over only its lower half can be significantly different; therefore, one should not compare the full-rotor shear obtained by Eq. (6a) with a lower-half-rotor shear provided by a hub-tall met mast. To address this issue, a *lower-half-rotor shear estimate* is defined here. This quantity is computed by first averaging the two lateral (left and right) sectors to provide a hub-height speed that, together with the lower sector, is then used to estimate the shear on the sole lower portion of the rotor disk. Using Eq. (5), the lower-half-rotor shear estimate is obtained as

$$\alpha_{\text{lower},B} = \ln \left(\frac{V_{S,\text{left}} + V_{S,\text{right}}}{2V_{S,\text{down}}} \right) \left(\ln \left(\frac{z_H}{z_H - 2/3R} \right) \right)^{-1}. \quad (7)$$

3 Results

3.1 Experimental setup

This validation study is conducted using an eno114 wind turbine manufactured by Eno Energy Systems GmbH. This turbine, in the following named WT1, has a rated power of 3.5 MW, a rotor diameter $D = 114.9$ m, and a hub height

$z_H = 92$ m. Two of the blades are equipped with blade load sensors, mounted in close proximity to the root and capable of measuring the two flapwise and edgewise components.

The site is located approximately 10 km south of the western Baltic Sea in a slightly hilly terrain without abrupt changes in elevation, approximately 1 km east of the village of Brusow (Germany), as described by Bromm et al. (2018). During the time of the year of the test campaign, the site is characterized by prevailing westerly wind directions, mostly neutral atmospheric stratification, and wind veers between 0 and 10° (Bromm et al., 2018).

At the site, a second turbine of the same type, named WT2, and a meteorological mast are also installed. Figure 2 shows a satellite image of the site, including the waking directions and distances among the three installations. WT1 is downstream of the met mast for a wind direction $\Gamma_{\text{MM} \rightarrow \text{WT1}} = 192.5^\circ$, while WT1 is waked by WT2 for $\Gamma_{\text{WT2} \rightarrow \text{WT1}} = 145^\circ$. The met mast is equipped with a wind vane (manufactured by Thies GmbH, catalogue number 4.3150.00.212) installed at 89.4 m and three cup anemometers (also manufactured by Thies GmbH, catalogue number 4.3351.00.000) at different heights, the topmost reaching 91.5 m, which is just half a meter shy of the turbine hub height. The relevant heights of the turbine and met-mast anemometers are shown in Fig. 3.

3.2 Measurements

Synchronized measurements of WT1 and the met mast were made available by the turbine manufacturer and operator for 41 d from 19 October to 29 November 2017. The measurements include main shaft torsion T_{meas} , blade root out-of-plane bending moments for two blades $m_{1,2}$, rotor speed Ω , blade pitch β , and rotor azimuth position ψ . The air density ρ was computed by the ideal gas law using measured air pressure and temperature. Met-mast measurements include wind speed $V_{\text{MM},1-3}$ at the three heights $z_{\text{MM},1-3}$ and wind direction Γ_{MM} at 89.4 m.

All measurements were sampled at 10 Hz. To eliminate higher-frequency turbine dynamics and measurement noise, the rotor speed and torque signals were low-pass filtered using a fifth-order Butterworth filter with a -3 dB cutoff frequency of 6 rpm.

The long-term average readings of the two blade load sensors are expected to be equal. However, when comparing the mean sensor values for any of the available days, the relative difference between the two blades was found to be between 4.8 and 5.8 %, whereas the absolute differences varied between -100 and -300 kN m. This mismatch between the two blades suggests a consistent measurement error of one or both sensors. The cause for this error could not be ascertained but might be due to miscalibration, sensor drift, or pitch misalignment. As an exact determination of the root reason of such inconsistencies is often difficult in a field environment (Bromm et al., 2018), a cause-independent correc-

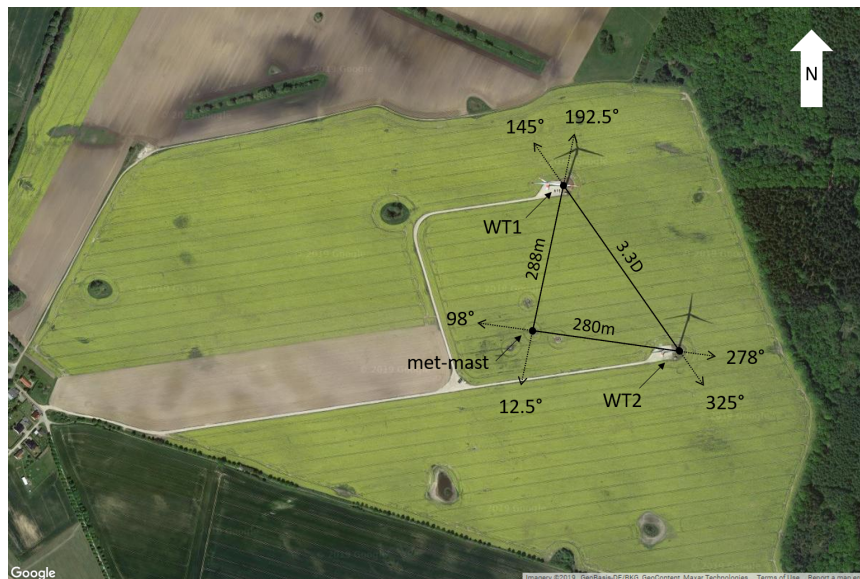


Figure 2. Satellite image with WT1, WT2, and met mast, including waking directions and distances (© Google Maps).

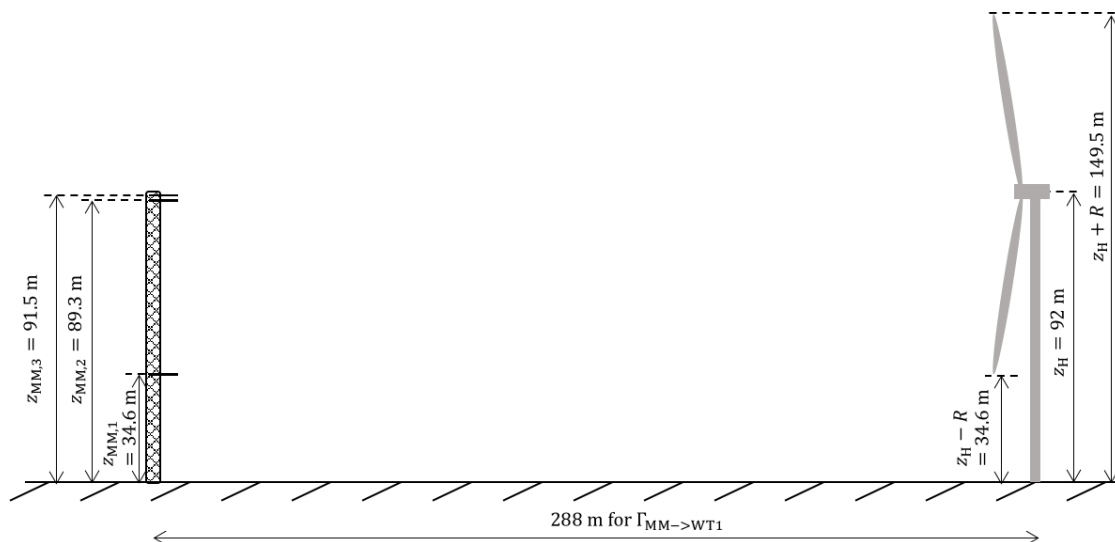


Figure 3. Sketch (to scale) of met mast and WT1 with relevant dimensions.

tion method was used here. The first 24 h of data were used to identify a scaling factor $s = 0.0274$ such that $\bar{m}_1(1 + s) = \bar{m}_2(1 - s)$, where $(\bar{\cdot})$ indicates a mean value. This scaling factor was then used to correct the sensor readings for the whole data set. For a long-term implementation, a similar correction could be applied periodically to compensate for time drifts. Notice that this scaling simply ensures consistent measurements between the two sensors, but not their absolute accuracy, which is corrected later in Sect. 3.6 by comparison between the rotor-effective wind speeds V_{TB} and V_B . In fact, as these two quantities are based on independent measure-

ments (torque and blade loads), they provide an opportunity to calibrate one or the other sensor.

The data set was filtered, retaining only measurements corresponding to normal turbine operation with pitch and rotor speed within the LUT limits (see Sect. 3.5). Measurements taken during yawing maneuvers were also discarded. In fact, yaw generates additional loads on the blades that would be erroneously interpreted by the observer, resulting in a pollution of the wind estimates. For an observer to accurately estimate wind even during yaw maneuvers, yaw-induced loads could be pre-computed and stored in a lookup

table; during operation, one could interpolate within the table in terms of the current yawing rate and possibly wind speed (in case yaw-induced aerodynamic loads, in addition to the inertial ones, also need to be taken into account) and remove the resulting loads from the measured ones. This procedure was however not tested in this work, and therefore yaw maneuvers were eliminated from the data set. After each discarded measurement, an interval of 1 min for the estimator re-initialization was accounted for.

The statistical analysis reported below is conducted with 10 min averages, which are standard in several wind energy applications. However, higher-frequency estimates are indeed possible, as shown in Sect. 3.7. Of the initial data set, a total of 4279 consecutive 10 min quantities were obtained, representing approximately 30 d of operation.

3.3 Estimator update frequency

The sampling rate of the sector-effective wind estimator varies depending on rotor speed and the number of instrumented blades. For the present case, where only two blades are equipped with load sensors and the rotor speed varies between 5 and 12 rpm, the wind speed estimate update frequency varies approximately between 0.17 and 0.4 Hz. Notice that, since only two out of three blades are instrumented, the update frequency is not constant – even at constant rotor speed.

To quantify the effects of a limited update frequency, Fig. 4 shows the met-mast-measured shear coefficient. The solid black line represents the shear computed based on the signals provided by the cup anemometers at a 10 Hz sampling frequency. The red dashed line reports that same signal down-sampled at 0.17 Hz, which is the estimator update frequency for low rotational speeds. A comparison between the two curves shows that even this slowest update frequency is high enough to capture the most energetic fluctuations of the inflow.

3.4 Reference inflow

The ambient inflow measured by the met mast is assumed to obey the vertical power law given by Eq. (5). Consequently, the met-mast-measured hub-height reference speed V_{ref} and power exponent α_{MM} were computed as best fits of the mast measurements at the three different available heights, i.e.,

$$(V_{\text{ref}}, \alpha) = \arg \min_{V_{\text{ref}}, \alpha} \sum_{i=1}^3 (V_{\text{PL}}(z_{\text{MM},i}, V_{\text{ref}}, \alpha) - V_{\text{MM},i})^2. \quad (8)$$

Only two measurements at two different heights are strictly necessary in order to compute the two parameters of the power-law V_{ref} and α . In the present case three measurements are available, although the highest two anemometers, being only about 2 m apart, essentially provide the same information.

Depending on wind direction, the met mast is located up to 288 m upstream of WT1, as shown in Fig. 2 for $\Gamma_{\text{MM} \rightarrow \text{WT1}}$. To synchronize met-mast and turbine measurements, assuming Taylor's frozen turbulence hypothesis, each 10 min met-mast measurement was time-shifted by $\Delta t = s_{\text{MM} \rightarrow \text{WT1}} / V_{\text{ref}}$, where $s_{\text{MM} \rightarrow \text{WT1}}$ is the downstream distance from met mast to WT1.

3.5 Lookup-table implementation

An aeroelastic model of the turbine was provided by the turbine manufacturer, implemented in the software FAST (Jonkman and Jonkman, 2018). To compute the power and cone coefficients of Eq. (1), a total of 10 626 dynamic simulations were performed in steady and uniform wind conditions for all combinations of $\beta \in [0 : 1 : 20]^\circ$, $\Omega \in [3 : 0.5 : 14]$ rpm, and $V \in [1 : 1 : 22]$ m s⁻¹, which took just a few hours on a standard desktop PC. Eliminating the tower and drivetrain dynamics, a converged periodic response was achieved in three rotor revolutions.

Considering the last revolution, the power coefficient was computed from the mean torque, while the cone coefficient was obtained from the blade root out-of-plane bending moment of one of the blades as a function of ψ . The lookup tables were compiled, for each β , Ω , and – if applicable – ψ , by computing speed as a function of load. If the blade is stalled or partially stalled, the speed–load relationship is non-monotonic. When this happens, the rotor-effective wind speed V_{TB} of Eq. (2a) can be used to resolve the indeterminacy and identify the correct speed corresponding to the measured load.

3.6 Validation of rotor-effective wind speed estimation

First, the rotor-effective speed estimates V_{TB} (computed through the torque balance equilibrium by Eq. 2a) and V_{B} (computed using blade bending moments by Eq. 3) are compared to each other and to the reference met-mast speed given by Eq. (8). A direct comparison between V_{TB} and V_{B} revealed that the latter provides systematically slightly higher wind speeds than the former. This discrepancy may be caused by sensor drift, miscalibration, pitch misalignment, and/or deficiencies of the simulation model used to compute the aerodynamic coefficients. Unfortunately, the root causes of the discrepancy could not be determined within the scope of the present work, nor could the simulation model be systematically validated; this is also probably the norm rather than the exception in many practical cases when working in the field. To pragmatically correct these sources of estimation bias, all speed estimates (V_{B} , $V_{\text{S,left}}$, $V_{\text{S,right}}$, $V_{\text{S,up}}$, and $V_{\text{S,down}}$) in the remainder of the paper were scaled by a factor $c = 0.928$. This scaling ensures the best correlation between V_{B} and V_{TB} and was identified based on the first 7 d of measured data. Note that a direct scaling of the load measurements is also possible and potentially even more accurate.

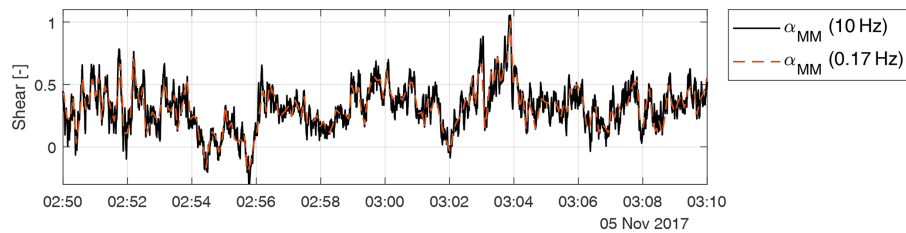


Figure 4. Time series of the met-mast-measured shear coefficient, at the original acquisition frequency of the cup anemometers (10 Hz) and downsampled at 0.17 Hz, which is the sector-effective wind estimation frequency for low rotor speeds.

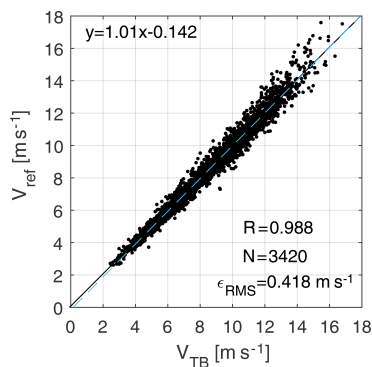


Figure 5. Torque-balance-based rotor-effective wind speed V_{TB} (Eq. 2a) vs. met-mast reference wind speed V_{ref} (Eq. 8).

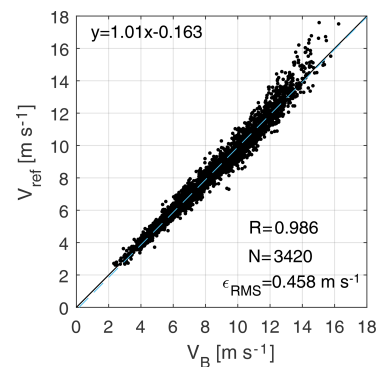


Figure 6. Corrected bending-load-based rotor-effective wind speed V_B (Eq. 3) vs. met-mast reference wind speed V_{ref} (Eq. 8).

It is worth pointing out that the redundancy of the two estimates V_B and V_{TB} offers the opportunity to ensure the consistency between different sets of sensors (the ones measuring blade loads and the ones providing rotor torque). For example, here the torque sensors were properly calibrated, as indicated by the independent measurements of the met mast, while the blade load sensors were not. Therefore, the redundancy was used to calibrate the load sensors against the torque ones. Similar recalibration procedures might also be used in situations where a met mast is not available, if one can ensure that at least one set of sensors is properly calibrated.

After correction, a comparison between met-mast reference speed V_{ref} and torque balance estimates V_{TB} and V_B is shown in Figs. 5 and 6, respectively. These results include only 3420 data points where the met-mast wind direction lies between 180 and 337.5° , to avoid conditions where the turbine or the met mast operate in the wake of either WT1 or WT2 (assuming a $\pm 35^\circ$ margin). The Pearson correlation coefficient R is approximately equal to 0.99, while the root-mean-squared error is $\epsilon_{RMS} \approx 0.44 \text{ m s}^{-1}$ and the linear best fit ($y = ax + b$) has a slope $a = 1.01$ and an offset $b \approx -0.15 \text{ m s}^{-1}$. These results indicate that, after calibration, the two methods correlate well with the (approximate) ground truth provided by the met mast and that both yield very similar estimates.

3.7 Validation of vertical shear estimation

After discarding waked conditions from turbine WT2 (with a $\pm 35^\circ$ margin), an analysis of the long-term mean horizontal shear revealed it to be nonzero. This finding is in contrast to expectations. In fact, while for a narrow wind direction sector some horizontal shear due to local orography or vegetation can be expected, such effects should disappear considering the complete wind rose.

This behavior can be explained by a possible bias in the measurement of the azimuthal position of the rotor, which has the consequence of generating a nonzero horizontal shear and reducing the vertical one. In addition, another effect should be considered: as no blade dynamics were included in the model (see Sect. 2.1), the response of the blade is assumed to instantaneously follow a wind speed change. This is in reality not true, and the actual response will have a phase delay, which appears as yet another source of azimuthal bias.

The expected behavior of the horizontal shear can be used for eliminating these effects. In fact, enforcing a null long-term average horizontal shear corrects both for azimuth sensor bias and for having neglected blade dynamics. To this end, the vertical and horizontal shears were rotated by ψ_{bias} , until a null mean horizontal shear was obtained. Accordingly, the mean vertical shear also reached its maximum. Using again the first 7 d of measurements, the azimuth bias was identified as $\psi_{bias} = 14.8^\circ$. In the remainder of this work, the

sector-effective wind speeds and the two shears are computed using the corrected azimuth signal $\psi_{\text{corr}} = \psi + \psi_{\text{bias}}$.

The effects of blade dynamics would be more precisely rendered by a rotor-speed-dependent azimuth bias. In fact, by repeating the shear-rotation for binned values of the rotor speed, a clear bias-rotor speed correlation was observed, with bias values in the range between about 12 and 19°. In addition, other effects could cause the azimuth bias to drift over time; indeed, a bias of 16.3° was found by using the last 7 d of data, a slightly different value than the one obtained using the first 7 d. However, these slight variations in the bias and its variability with rotor speed have only a very limited effect on the quality of the results. Therefore, for simplicity, it was decided to use the constant average value of 14.8°.

As previously discussed, the reference inflow profile measured by the met mast with Eq. (8) only includes measurements up to hub height. Accordingly, the load-based lower-half-rotor vertical shear $\alpha_{\text{lower,B}}$ (computed by Eq. 7 in terms of the two horizontal and the bottom sectors) is the only shear that can be validated with respect to met-mast measurements.

A 12 h excerpt from the complete set of results is shown in Fig. 7, where 10 min means of measurements and estimates are provided as functions of time. Notice that the data points are not equally spaced because of the elimination of yawing maneuvers and other conditions not accounted for in the LUTs.

Panel (a) shows the wind direction Γ_{MM} measured at the met mast and the turbine yaw orientation γ_{WT1} ; the direction for which the met mast is directly upstream of the sensing turbine is $\Gamma_{\text{MM} \rightarrow \text{WT1}} = 192.5^\circ$, and it is shown by a horizontal solid line.

Panel (b) shows the reference wind speed V_{ref} measured at the met mast, together with the torque-balance V_{TB} and blade-load-based V_{B} rotor-effective speeds. As already noticed, both methods provide very similar results; in addition, especially for wind directions where mast and turbine are nearly aligned, both follow the reference very closely.

Panel (c) shows again the met-mast reference wind speed at hub height (solid line) and the one at $z_{\text{H}} - 2/3R$ (dashed line). The respective load-based estimates are indicated with a blue solid line and • symbols for the hub-height speed and with a red solid line and × symbols for the lower-height speed. Both estimates correlate well with their respective references, especially when mast and turbine are aligned. The small rotor icon shows, using the color code of the panel, the two horizontal sectors (used to estimate the hub-height wind speed $1/2(V_{\text{S,left}} + V_{\text{S,right}})$) and the lower sector.

Panel (d) finally shows the mast vertical shear α_{MM} and the load-based estimate $\alpha_{\text{lower,B}}$, computed based on the data shown in panel (c) using Eq. (7). Except for some small underestimation and noise, the load-based shear follows the reference quite accurately. The load-based horizontal shear κ_{B} is also reported in the same figure. Although no met-mast reference is available in this case, as expected the horizontal shear is always essentially null.

Figure 8 shows the correlation between the lower-half-rotor shears $\alpha_{\text{lower,B}}$ and α_{MM} . Only wind directions from 190 up to 200° are included in the figure, resulting in $N = 155$ 10 min data points. These conditions contain the direction where the met mast is directly upstream of WT1. The Pearson correlation coefficient is $R = 0.92$. The shear is underestimated with respect to the met-mast reference by a factor $1/a = 0.88$, obtained by the linear best fit ($y = ax + b$) shown in the figure with a blue dashed line. By looking at Fig. 7c, a comparison of the wind speed at hub height and at $z_{\text{H}} - 2/3R$ with their respective met-mast references indicates that the former is quite accurate, while the latter has a small positive bias. This difference could possibly be caused by a nonideal power-law inflow profile (Møller et al., 2020), leading to a biased met-mast reference shear, although a definitive explanation of this mismatch could not be reached with the present data set. Figure 9 shows the correlation between the full-rotor shear $\alpha_{\text{lower,B}}$ and the lower-half-rotor shear α_{MM} . As the two shears are computed over two different vertical distances, their correlation is lower than in the case of Fig. 8, as expected.

A more complete overview of the results, including a broader range of wind directions, is shown in Fig. 10. The x axis reports wind directions from 180 to 340°, in 10° wide bins. All results of Fig. 8 fall in the second bin from the left. The number of available measurements N within each bin is shown in Fig. 10a. Panel (b) shows the Pearson correlation coefficient R , between the met-mast reference α_{MM} and the load-based shear estimate $\alpha_{\text{lower,B}}$. Here and in the other plots, a blue solid line indicates results for the lower-half-rotor shear, while a red dashed line is used for the full-rotor shear. The best correlation is achieved for the wind direction where the met mast is directly upstream of the turbine ($\Gamma_{\text{MM} \rightarrow \text{WT1}} = 192.5^\circ$). For the same wind direction bin, the minimum root-mean-squared error is also achieved, as shown in panel (c). Considering that all wind directions are for un-waked met mast and turbine, these results suggest the presence of a spatial shear variation, probably caused by the local vegetation and/or the village in the west that is partially visible in Fig. 2. This interpretation is also confirmed by panels (d) and (e), which show the linear best-fit coefficients a and b . For wind directions up to 235°, the slope coefficient a achieves values between 1.02 and 1.18, increasing up to 1.67 in the remaining wind directions. The constant b is nearly zero for all wind direction values.

Looking at the plots, it appears that the full-rotor shear differs from the lower-half-rotor shear, as already reported by Murphy et al. (2019) and as also observed earlier here in Fig. 8. The validation of the full-rotor shear estimated by the proposed method would necessitate a met mast reaching the rotor top height or a velocity-azimuth display (VAD) lidar, which however were not available for the present research. Nonetheless, the results obtained for the lower-half-rotor shear appear to be very encouraging, and there is no

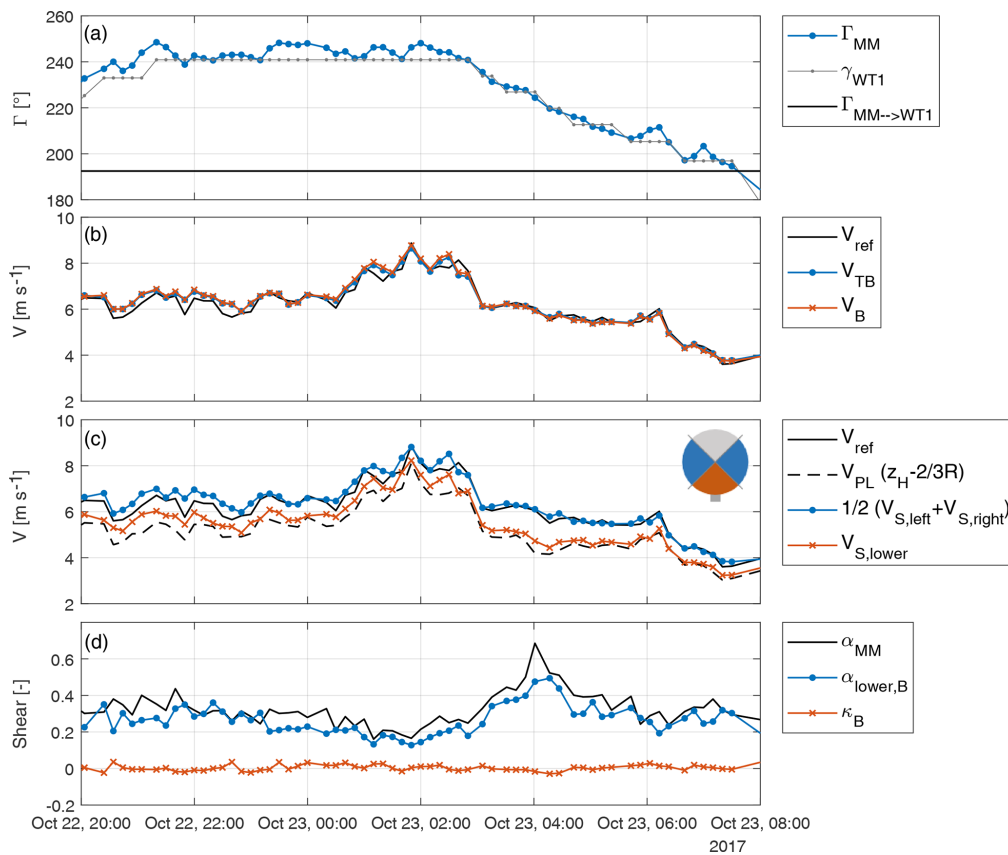


Figure 7. Time series reporting met-mast wind direction and turbine yaw orientation (a), met-mast and estimated rotor-effective wind speeds (b), speeds at different heights (c), and met-mast and estimated vertical and horizontal shears (d).

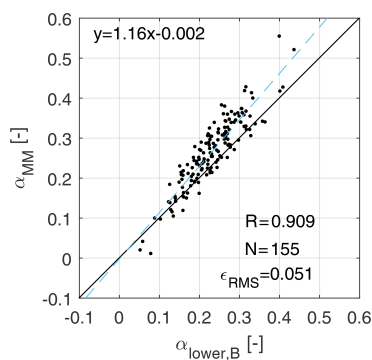


Figure 8. Correlation between the lower-half-rotor vertical shear $\alpha_{lower,B}$ and the met-mast shear (up to hub height) α_{MM} , for wind directions from 190 to 200°.

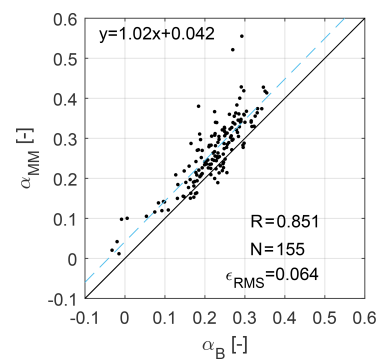


Figure 9. Correlation between the rotor-equivalent (full rotor) vertical shear α_B and the met-mast shear (up to hub height) α_{MM} , for wind directions from 190 to 200°.

technical reason why similar results should not be achievable for shear estimates over the entire rotor disk.

Finally, the effects of a higher temporal resolution are considered. Figure 11 compares the 10 Hz lower-half-rotor vertical shear to the met-mast reference; this figure is there-

fore similar to Fig. 7d, which was however obtained with 10 min averages. Within the 20 min considered in the figure, the wind direction was approximately constant and equal to 190°, resulting in the met mast being 2D directly upstream of the turbine, while the wind speed was approximately equal to

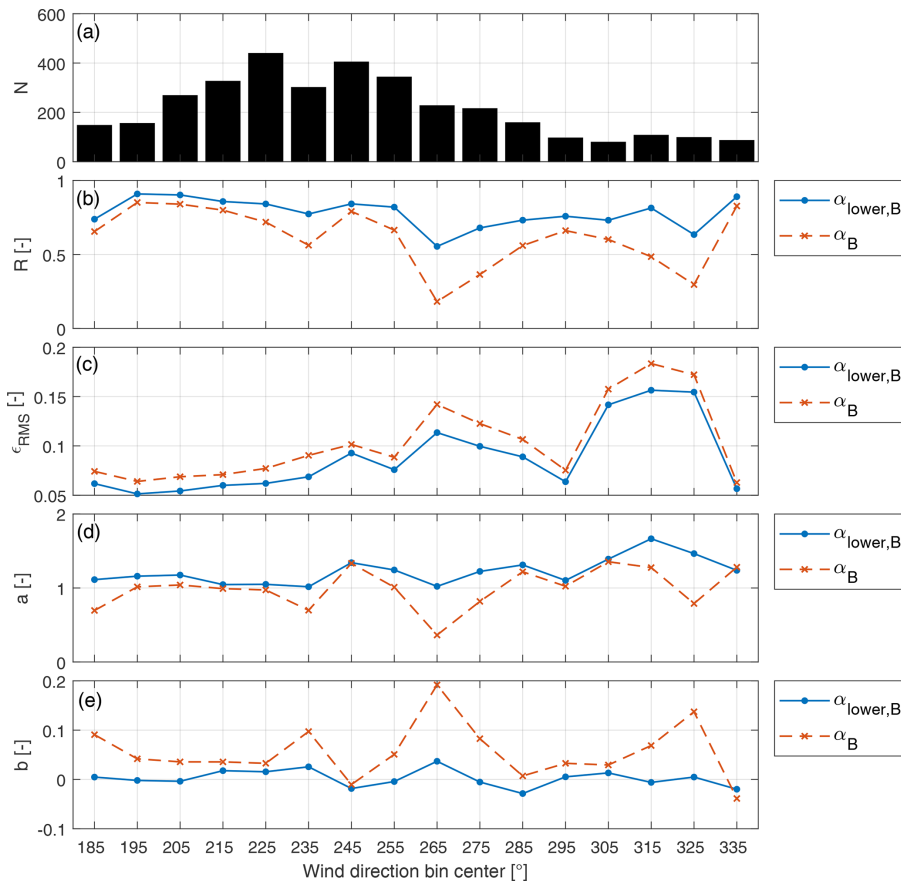


Figure 10. Statistics of the shear estimates as functions of wind direction. Blue solid line: lower-half-rotor shear; red dashed line: full-rotor shear. (a) Number of 10 min data points; (b) Pearson correlation coefficient; (c) root-mean-squared errors; (d, e) linear best-fit coefficients ($y = ax + b$).

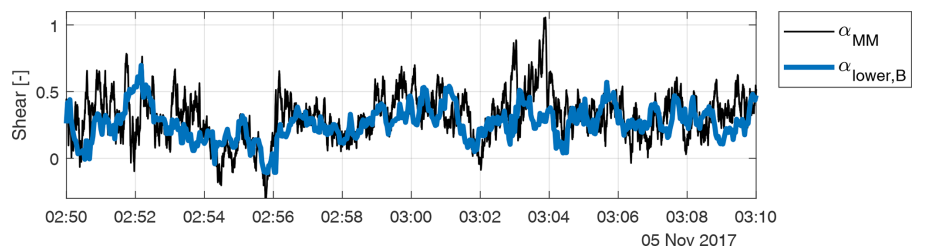


Figure 11. Comparison of 10 Hz met-mast vertical shear α_{MM} with lower-half-rotor shear $\alpha_{lower,B}$ during a period of 20 min.

7 m s^{-1} . Based on the wind speed, the met-mast signal was time-shifted assuming Taylor's frozen turbulence hypothesis. The plot shows that the load-based estimate $\alpha_{lower,B}$ follows the main trends of the met-mast reference α_{MM} . There are however discrepancies at the higher frequencies. It is not possible to conclusively determine the causes of these differences based exclusively on the available data. However, the non-collocation of the measurements might clearly be among the reasons. For example, the spike of the met-mast shear at

03:04 is not visible in the load signals, which might indicate a local turbulent fluctuation at one of the met-mast anemometers not rigidly convecting downstream to the turbine rotor.

3.8 Validation of wake detection

As no measured reference for the horizontal shear was available for this study, the wake of the second turbine was used for a qualitative validation. This wake interference study

nicely illustrates the very interesting wake detection capabilities of the proposed method.

Figure 12 reports a time series corresponding to 12 h of operation, which experienced wind direction changes from approximately 100 to 180° . This data subset includes a significant duration where WT1 is waked by WT2. Panel (a) shows the met-mast wind direction Γ_{MM} and turbine yaw orientation γ_{WT1} , where the waking direction $\Gamma_{WT2 \rightarrow WT1}$ is reported as an horizontal solid line (see also Fig. 2). Panel (b) shows the reference met-mast wind speed V_{ref} , as well as the load-based rotor-equivalent estimates V_{TB} and V_B . The reference 10 min turbulence intensity TI_{ref} computed from V_{ref} is shown on the right y axis. Panel (c) shows the sector-effective wind speeds $V_{S,right}/V_{ref}$ and $V_{S,left}/V_{ref}$ for the two horizontal sectors, nondimensionalized by the met-mast reference wind speed. The small rotor icon shows, using the color code of the panel, the left (red) and right (blue) sectors. Panel (d) reports the horizontal shear estimate κ_B computed according to Eq. (6b).

Vertical dashed lines are used to highlight four time instants, labeled with the letters from A to D. For each of these time instants, the position of the wakes of the two turbines is visualized in Fig. 12e using the FLORIS wake model (Doekemeijer and Storm, 2019). The yellow color indicates the ambient wind speed, while the blue color is used for the lower speed in the wakes. The rotor disk of WT2 is shown with a solid black line, while a red line is used for the left sector of WT1 and a blue line for the right one. Finally, the small cross symbol indicates the met-mast (MM) position.

At instant A (time equal to 02:05), Fig. 12 shows that the wind direction reaches 130° and the left sector of WT1 gets waked by WT2, as clearly illustrated by a reduced speed in the left sector and a negative horizontal shear. At time instant B (02:35), the wind direction has turned back to 122° : as the turbine is not waked anymore, the estimated shear is null and an equal wind speed is estimated on both the left and right sectors. The rotor-effective wind speed is slightly smaller than the met-mast reference value; however, for this wind direction, the met mast is not aligned with the turbine, which might explain this small discrepancy. At time instant C (03:45), the wind direction has increased and WT1 is waked again ($\Gamma_{WT2 \rightarrow WT1} = 145^\circ$): after an initial reduction in the left sector speed, the right sector is also affected (dropping below 0.7), indicating a full waked condition. This is further confirmed by the reduction in the rotor-effective wind speeds with respect to the one measured by the met mast. Later, a wake impingement on the right sector is observed at time D (05:00), followed by a second full waking at time 05:30. At 06:00, the wind direction has increased to 156° and both sectors operate again in nearly free stream. Accordingly, the rotor-effective wind speeds increase to reach the met-mast reference. Later again, the wind direction varies slightly, leading to partial wake impingements on the right side until, finally (at ≈ 12.00), the wind direction increases further and the horizontal shear becomes almost zero.

Note that the horizontal shear deviates slightly from 0 between 06:00 and 10:30 even though the wind direction is approximately constant around 155° . An explanation can be potentially found in the increased turbulence (after sunrise, at around 07:58), which might enhance wake meandering and increase the expansion of the wake. The high turbulence before 02:00 can be attributed to the met mast being affected by WT2.

This time series very nicely illustrates how the horizontal sector-effective wind speeds and the horizontal shear can be used to understand the instantaneous position of a wake with respect to an affected turbine rotor disk.

Figure 13 reports extended results, showing all available 10 min values as functions of met-mast wind direction within the range from $\Gamma_{WT2 \rightarrow WT1} - 45^\circ = 100^\circ$ to $\Gamma_{WT2 \rightarrow WT1} + 45^\circ = 190^\circ$. The waking wind direction from WT2 onto WT1 ($\Gamma_{WT2 \rightarrow WT1}$) is indicated by a vertical dashed line.

Panel (a) shows the rotor-effective wind speed V_B/V_{ref} , nondimensionalized by the reference speed of the met mast. Values larger than 1 can be observed for wind directions close to 100° , as the wake of WT2 is affecting the met mast (see Fig. 2). For wind directions close to 145° , lower speeds are observed, caused by the wake of WT2 impinging on WT1. For other wind directions, the speed stays close to 1, even though some scatter can be observed.

Panel (b) shows the nondimensional sector-effective wind speeds $V_{S,right}/V_{ref}$ and $V_{S,left}/V_{ref}$. The small rotor icon shows, using the color code of the panel, the left (red) and right (blue) sectors. For wind directions between $\approx 125^\circ$ and 140° , the local wind speed is smaller in the left sector, indicating that the wake of WT2 mainly affects that portion of the rotor disk. Similarly, for wind directions between 145° and about 160° , the right sector is affected by the presence of the wake.

Panel (c) shows the horizontal shear estimate. This quantity is close to zero for all wind conditions, except around the waking direction. Negative values indicate a left-sided wake impingement, while positive values indicate a right-sided one. Note that the scatter observed in panels (a) and (b), e.g., for wind directions between 160 and 170° , seems not to be caused by wake interaction but rather by variations in the reference wind speed, as the horizontal shear is not affected.

For wind directions close to 140° , only very few measurement points are available. This suggests that the lower-than-ambient wind speed within the wake of WT2 triggers frequent shutdowns of WT1. The load-based estimator does not operate during turbine shutdowns. Figure 14 shows in 2° wide bins the probability of the WT1 status indicating “no operation”. Wind directions were obtained from the met mast, using all available days without discarding any data point. Indeed, mean direction bins close to $\Gamma_{WT2 \rightarrow WT1} = 145^\circ$ support the hypothesis of frequent wake-induced turbine shutdowns. Additionally, Fig. 14 reports a maximum for the bin centered at 141° . This, together with the shear

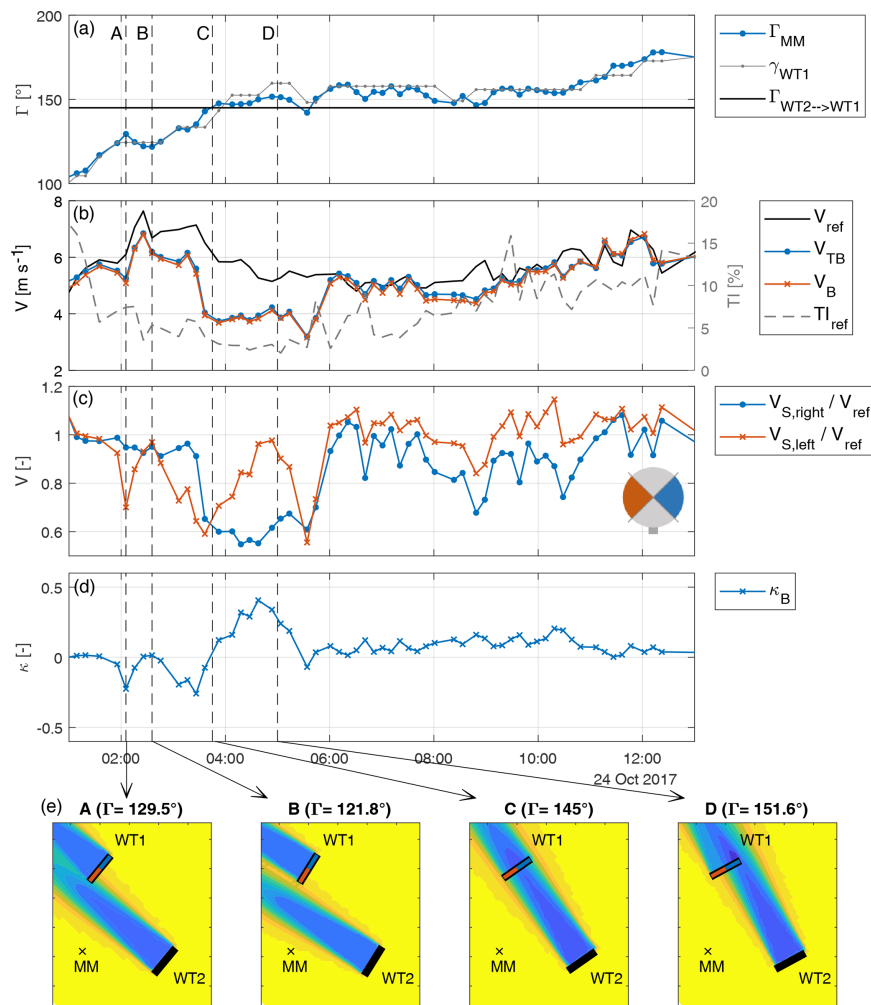


Figure 12. Time series characterized by varying wake interference conditions, with met-mast wind direction and turbine yaw orientation (a), reference met-mast wind speed, rotor-effective wind speed estimates and reference turbulence intensity (b), left and right sector-effective speed estimates (c), and horizontal shear estimate (d). (e) Wake visualizations based on the FLORIS model for different wind directions at time instants A through D.

shown in Fig. 13, suggests a small bias in the met-mast wind direction measurement and/or that the wake is not developing exactly along the downstream direction. Indeed, the latter is a phenomenon observed in stable atmospheric conditions when the flow presents a significant vertical shear (Vollmer et al., 2016; Bromm et al., 2018).

These results demonstrate a remarkable ability of the proposed local speed and shear estimates to identify whether and to which extent a downstream turbine operates in the wake of an upstream machine. Note also that the met-mast reference wind direction is just a point measurement at one single height above the ground. In addition, other unknown inflow parameters, such as for example veer, may affect wake development. Therefore, the scatter of some of the data points in Fig. 13 is not necessarily due to inaccuracies of the wind

estimator, but might be rather due to the indirect, incomplete, and pointwise measurement of the reference wake position.

3.9 Effect of turbine misalignment on estimates

As previously mentioned in Sect. 2.1, in theory the present method is formulated for turbines aligned with the ambient wind direction. However, in practice this happens only quite rarely, as every turbine in general operates with some degree of misalignment with respect to the incoming wind vector. This is mainly due to two reasons. First, the onboard wind vane(s) may not always provide an exact measurement of the local wind direction. Second, yaw control strategies generally avoid an excessively aggressive tracking of wind direction changes. In fact, a turbine will typically yaw only

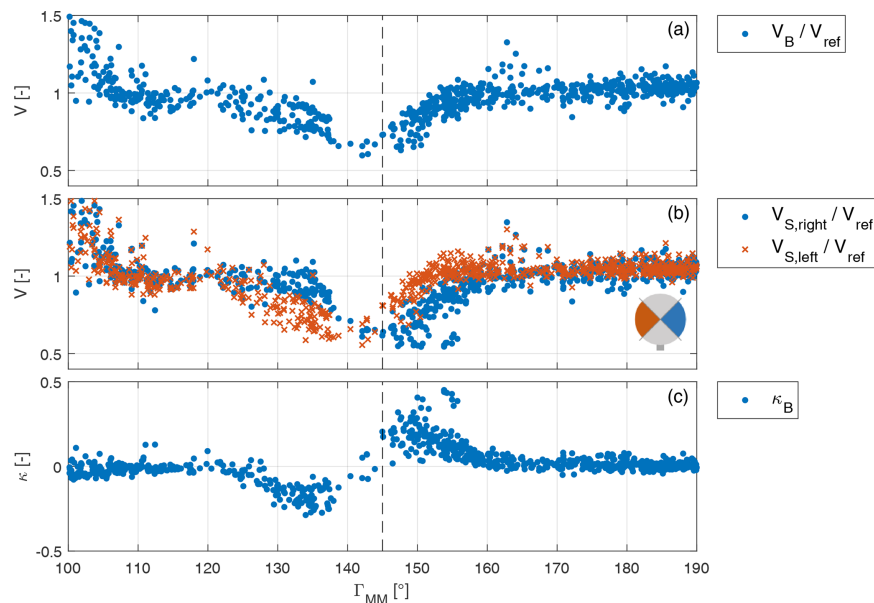


Figure 13. Wind speeds and shear at the WT1 rotor disk as functions of wind direction. (a) Nondimensional load-based rotor-effective wind speed. (b) Left and right sector-effective wind speeds. (c) Horizontal shear.

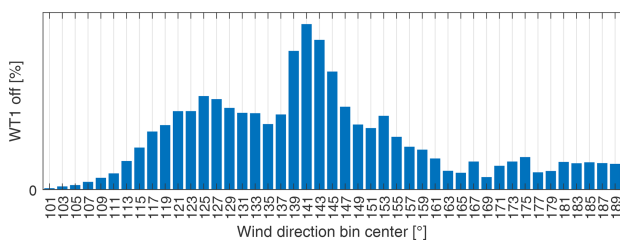


Figure 14. Probability of WT2 being in “no operation” state as a function of met-mast wind direction (using 10 Hz measurements of all available days).

when its misalignment with the wind has been above a certain threshold for a long-enough duration of time. This is done to limit duty cycle and yaw expenditure, given the very considerable mass of the rotor–nacelle system and the rather modest power capture loss caused by a misalignment of a few degrees.

Since the hypothesis on which the theory is based differs from the situation encountered in practice, it is necessary to show that the typical misalignments of normal turbine operation do not pollute the speed and shear estimates provided by the proposed method. This is achieved here by showing that shears and misalignment are indeed uncorrelated.

To this end, Fig. 15 shows the rotor-effective wind speed as well as the horizontal and vertical shear estimates as functions of the turbine–wind misalignment angle $\Gamma_{\text{rel,WT1}}$. The misalignment is measured using the onboard wind vane. As this instrument may not always be very precise on some tur-

bines, the misalignment angle was also computed by using the met-mast wind direction together with the turbine absolute orientation; however, in the present case no significant difference was observed between these two methods of computing the misalignment angle. The results of the figure only include data points for wind directions between 180 and 337.5°, to avoid waked conditions.

Panel (a) reports the nondimensional rotor-effective wind speed V_B . This quantity decreases for increasing misalignment angle, as shown by the second-order polynomial fit reported with a dashed line. Such behavior is completely expected and can be corrected for, if the misalignment is known, by using the cosine law (Gebraad et al., 2015; Fleming et al., 2017; Schreiber et al., 2017).

As shown, the rotor-equivalent wind speed is clearly correlated with misalignment, because the effective speed orthogonal to the rotor plane varies as a function of this angle. However, there is no reason why the vertical and horizontal shears – which are physical characteristics of the inflow – should also exhibit a similar dependency. To verify this fact, panel (b) shows the horizontal shear estimate κ_B , which is almost constant with respect to misalignment angle (and also very close to zero). Finally, panel (c) shows the vertical shear α_B . It appears that both shears have only a very marginal dependency on wind misalignment, as shown by the parabolic best fits reported with dashed lines in the plots. The larger fluctuations of the vertical shear compared to the horizontal one are probably caused by time-varying ambient inflow conditions, as also visible in Fig. 9.

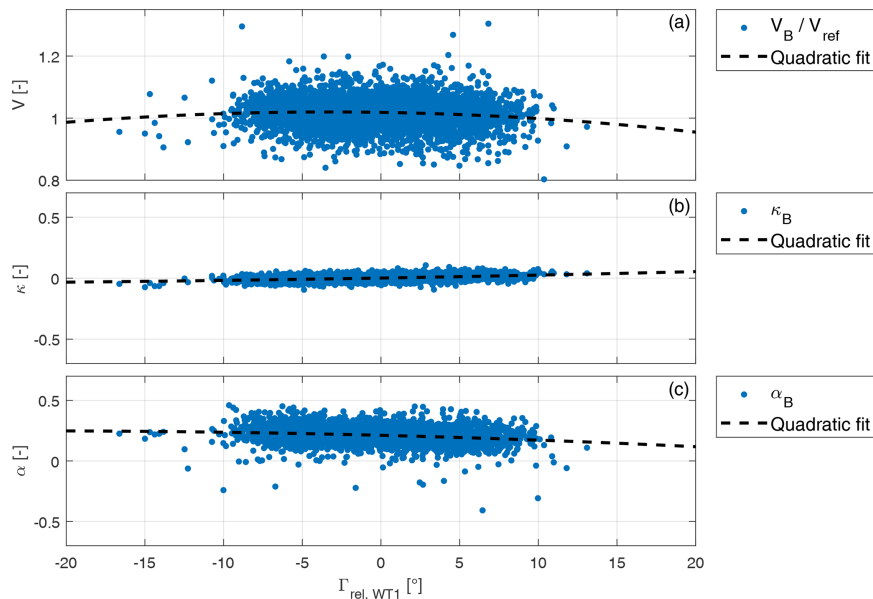


Figure 15. From top to bottom: rotor-effective wind speed V_B , horizontal shear κ_B , and vertical shear α_B , all plotted as functions of wind turbine misalignment angle $\Gamma_{\text{rel,WT1}}$.

The data show that the shears are essentially uncorrelated with misalignment. These results demonstrate that the proposed method works without significant errors for turbine-wind misalignment angles up to $\approx \pm 10^\circ$.

Larger turbine misalignment angles would be necessary for wake steering control (Fleming et al., 2017), where the rotor is intentionally pointed away from the wind to deflect the wake laterally. The performance of the proposed method could not be tested in such conditions within the present research, as no large misalignment angles were present in the available data set. However, even in that case, the procedure illustrated here could be used for pragmatically correcting possible errors caused by misalignment. In fact, by plotting shears as functions of misalignment angle, a best-fit correction function could be readily derived and used for adjusting the estimates, if necessary.

4 Conclusions

A method to estimate the local wind speeds over sectors of the rotor disk has been tested on a 3.5 MW wind turbine. Results have been compared to reference values obtained with a nearby met mast. For some wind directions, the sensing turbine is waked by a second machine. This feature of the test site has been exploited to test the ability of the proposed local wind sensing technique to detect wake impingement.

The wind sensing method has been previously studied and evaluated in simulations and scaled experiments. The present work has presented the first full-scale demonstration. Based

on the field test results shown herein, the following conclusions can be drawn.

- A rotor-effective wind speed can be estimated from blade out-of-plane bending moments, with a quality that is nearly indistinguishable from the well-known torque-balance method.
- The vertical wind shear estimated from out-of-plane bending moments correlates very well with the met-mast reference. The best results were obtained when the mast is directly upstream of the turbine. This suggests that some of the scatter in the results might be due to a lack of knowledge of the exact ground truth, rather than to a lack of accuracy of the proposed method.
- The vertical shear measured by the met mast up to hub height differs from the shear measured over the whole rotor disk. This is likely a feature of the flow, and not of the method tested here.
- The local wind speeds estimated on two lateral sectors of the rotor disk show the clear fingerprint of an impinging wake shed by a neighboring turbine. By looking at the two sectors, one can distinguish left, right, or full wake overlaps.
- Simple and very practical techniques can be used to correct for various sources of error, including not perfectly calibrated load or azimuth sensors, as well as model approximations.

J. Schreiber et al.: Field testing of a wind estimator and wake detector

881

The present load-based wind estimation method provides for a remarkably simple and effective opportunity to estimate atmospheric inflow conditions on operating turbines. The method is based on readily available quantities that can be easily computed from a standard model of a wind turbine and does not need to be trained from extensive data sets. The onboard implementation uses pre-computed lookup tables and hence has a negligible computational cost. When load sensors are already installed on a turbine, for example for load-reducing control, this novel wind sensing capability is simply obtained as a software upgrade. Wind sensing opens up a number of opportunities that can profit from a better knowledge of the inflow, including turbine and wind farm control, lifetime consumption estimation, predictive maintenance, and forecasting, among others.

Appendix A: Nomenclature

BEM	Blade element momentum	α	Vertical shear exponent
LUT	Lookup table	α_B	Load-based estimated vertical shear exponent
MM	Met mast or meteorological mast	$\alpha_{\text{lower,B}}$	Load-based estimated vertical shear exponent on lower half of rotor disk
WT1	Wind turbine 1 (sensing turbine)	α_{MM}	Met-mast-measured vertical shear exponent
WT2	Wind turbine 2	β	Blade pitch angle
a	Linear best-fit constant ($y = ax + b$)	γ	Turbine yaw orientation (clockwise from due north)
A	Rotor disk area	Γ	Wind direction (clockwise from due north)
A_S	Sector area	$\Gamma_{A \rightarrow B}$	Direction of wind blowing from point A to point B (clockwise from due north)
b	Linear best-fit constant ($y = ax + b$)	Γ_{MM}	Wind direction at met mast
C_m	Cone coefficient	$\Gamma_{\text{rel,WT1}}$	Relative wind direction at nacelle of WT1
C_p	Power coefficient	Δt	Time delay between measurement at met mast and turbine
c	Speed estimate scaling factor	ϵ_{RMS}	Root-mean-squared error
D	Rotor diameter	κ	Horizontal shear coefficient
J	Total rotational inertia	κ_B	Load-based estimated horizontal shear coefficient
m_i	Blade root out-of-plane bending moment of blade i	λ	Tip speed ratio
$m_{i,\text{meas}}$	Measured blade root out-of-plane bending moment of blade i	ρ	Air density
N	Number of measurements	ρ_{ref}	Reference air density
q	Dynamic pressure	ψ	Blade azimuth position
R	Rotor radius or Pearson correlation coefficient	ψ_a	Blade azimuth position, beginning of sector
s	Load scaling factor	ψ_b	Blade azimuth position, end of sector
$s_{\text{MM} \rightarrow \text{WT1}}$	Downstream distance between met mast and wind turbine WT1	ψ_{bias}	Blade azimuth measurement offset
T_{aero}	Aerodynamic torque	ψ_{corr}	Corrected azimuth measurement
T_{meas}	Measured torque	Ω	Rotor speed
TI_{ref}	Met-mast-measured reference turbulence intensity	$\dot{\Omega}$	Rotor acceleration
V	Wind speed		
V_B	Blade-load estimated rotor-effective wind speed		
V_H	Wind speed at hub height		
V_i	Blade-effective wind speed estimate of blade i		
$V_{\text{MM},i}$	Met-mast-measured wind speed at height i		
V_{PL}	Power-law inflow profile		
V_{ref}	Met-mast-measured reference wind speed of inflow profile		
V_S	Sector-effective wind speed		
$V_{S,\text{left/right/up/down}}$	Load-based estimation of left/right/up/down sector		
V_{TB}	Torque-balance estimated rotor-effective wind speed		
y	Lateral position		
z	Height above ground		
z_H	Hub height		
$z_{\text{MM},i}$	Installation height of sensor i on met mast		

Code and data availability. The operational data and turbine model used in this research are the property of Eno Energy Systems GmbH. An implementation of the estimator can be obtained by contacting the authors.

Author contributions. JS conducted the main research work and prepared a first draft of the manuscript. CLB developed the core idea of load-based wind sensing, supervised the research, and contributed to the writing of the paper. MB assisted in the measurement post-processing and analysis. All authors provided important input to this research work through discussions and feedback and by improving the manuscript.

Competing interests. The authors declare that they have no conflict of interest.

Acknowledgements. The authors express their gratitude to Stefan Bockholt and Alexander Gerds of Eno Energy Systems GmbH, who granted access to the measurement data and turbine model, and to Marijn van Dooren, Anantha Sekar, and Martin Kühn of ForWind Oldenburg, who shared insight into the data.

Financial support. This research has been supported by the German Federal Ministry for Economic Affairs and Energy (FKZ: grant no. 0325492G, CompactWind II project).

This work was supported by the German Research Foundation (DFG) and the Technical University of Munich (TUM) in the framework of the Open Access Publishing Program.

Review statement. This paper was edited by Christian Masson and reviewed by three anonymous referees.

References

- Bertelè, M., Bottasso, C. L., Cacciola, S., Daher Adegas, F., and Delpont, S.: Wind inflow observation from load harmonics, *Wind Energ. Sci.*, 2, 615–640, <https://doi.org/10.5194/wes-2-615-2017>, 2017.
- Bottasso, C. L. and Schreiber, J.: Online model updating by a wake detector for wind farm control, in: 2018 Annual American Control Conference (ACC), Hilton Milwaukee City Center Hotel, Milwaukee, WI, USA, 27–29 June 2018, IEEE, 676–681, <https://doi.org/10.23919/ACC.2018.8431626>, 2018.
- Bottasso, C. L., Croce, A., and Riboldi, C.: Spatial estimation of wind states from the aeroelastic response of a wind turbine, in: TORQUE 2010, The Science of Making Torque from Wind, Forth, Heraklion, Crete, Greece, 28–30 June 2010.
- Bottasso, C. L., Cacciola, S., and Schreiber, J.: Local wind speed estimation, with application to wake impingement detection, *Renew. Energ.*, 116, 155–168, <https://doi.org/10.1016/j.renene.2017.09.044>, 2018.
- Bromm, M., Rott, A., Beck, H., Vollmer, L., Steinfeld, G., and Kühn, M.: Field investigation on the influence of yaw misalignment on the propagation of wind turbine wakes, *Wind Energy*, 21, 1011–1028, <https://doi.org/10.1002/we.2210>, 2018.
- Campagnolo, F., Schreiber, J., Garcia, A. M., and Bottasso, C. L.: Wind tunnel validation of a wind observer for wind farm control, Proceedings of the International Offshore and Polar Engineering Conference, 25–30 June 2017, San Francisco, CA, USA, available at: <https://www.onepetro.org/conference-paper/ISOPE-I-17-410> (last access: 26 June 2020), 2017.
- Doekemeijer, B. M. and Storm, R.: FLORISSE M, https://github.com/TUdelft-DataDrivenControl/FLORISSE_M/tree/ed2885107ca2600d0616f86cab3b3d59c5f0cb38, last access: 30 July 2019.
- Fleming, P., Annoni, J., Shah, J. J., Wang, L., Ananthan, S., Zhang, Z., Hutchings, K., Wang, P., Chen, W., and Chen, L.: Field test of wake steering at an offshore wind farm, *Wind Energ. Sci.*, 2, 229–239, <https://doi.org/10.5194/wes-2-229-2017>, 2017.
- Gebraad, P., Fleming, P. A., and Van Wingerden, J. W.: Comparison of actuation methods for wake control in wind plants, in: American Control Conference (ACC), 2015, 1–3 July 2015, Chicago, IL, USA, IEEE, 1695–1701, <https://doi.org/10.1109/ACC.2015.7170977>, 2015.
- Held, D. P. and Mann, J.: Detection of wakes in the inflow of turbines using nacelle lidars, *Wind Energ. Sci.*, 4, 407–420, <https://doi.org/10.5194/wes-4-407-2019>, 2019.
- Jonkman, J. and Jonkman, B.: FAST v7, available at: <https://web.archive.org/web/20170107091945/https://nwtc.nrel.gov/system/files/FAST.pdf> (last access: 26 June 2020), 2018.
- Lange, J., Mann, J., Berg, J., Parvu, D., Kilpatrick, R., Costache, A., Chowdhury, J., Siddiqui, K., and Hangan, H.: For wind turbines in complex terrain, the devil is in the detail, *Environ. Res. Lett.*, 12, 094020, <https://doi.org/10.1088/1748-9326/aa81db>, 2017.
- Ma, X., Poulsen, N., and Bindner, H.: Estimation of Wind Speed in Connection to a Wind Turbine, Informatics and Mathematical Modelling, Technical University of Denmark, Lyngby, Denmark, 1995.
- Møller, M., Domagalski, P., and Sætran, L. R.: Comparing abnormalities in onshore and offshore vertical wind profiles, *Wind Energ. Sci.*, 5, 391–411, <https://doi.org/10.5194/wes-5-391-2020>, 2020.
- Murphy, P., Lundquist, J. K., and Fleming, P.: How wind speed shear and directional veer affect the power production of a megawatt-scale operational wind turbine, *Wind Energ. Sci. Discuss.*, <https://doi.org/10.5194/wes-2019-86>, in review, 2019.
- Østergaard, K. Z., Brath, P., and Stoustrup, J.: Estimation of effective wind speed, *J. Phys. Conf. Ser.*, 75, 012082, <https://doi.org/10.1088/1742-6596/75/1/012082>, 2007.
- Peña, A., Schaldemose Hansen, K., Ott, S., and van der Laan, M. P.: On wake modeling, wind-farm gradients, and AEP predictions at the Anholt wind farm, *Wind Energ. Sci.*, 3, 191–202, <https://doi.org/10.5194/wes-3-191-2018>, 2018.
- Schreiber, J. and Wang, C.: Load-based Wind Speed Estimation and Wake Detection (CL-Windcon Deliverable Report D3.3, Demonstration of wind turbine controllers and supporting technologies by simulations), available at: <http://www.clwindcon.eu/wp-content/uploads/2017/03/>

884

J. Schreiber et al.: Field testing of a wind estimator and wake detector

- CL-Windcon-D3.3-Demonstration-WT-controllers.pdf (last access: 26 June 2020), 2018.
- Schreiber, J., Cacciola, S., Campagnolo, F., Petrović, V., Mourembles, D., and Bottasso, C. L.: Wind shear estimation and wake detection by rotor loads – First wind tunnel verification, *J. Phys. Conf. Ser.*, 753, 032027, <https://doi.org/10.1088/1742-6596/753/3/032027>, 2016.
- Schreiber, J., Nanos, E. M., Campagnolo, F., and Bottasso, C. L.: Verification and Calibration of a Reduced Order Wind Farm Model by Wind Tunnel Experiments, *J. Phys. Conf. Ser.*, 854, 012041, <https://doi.org/10.1088/1742-6596/854/1/012041>, 2017.
- Schreiber, J., Bottasso, C. L., Salbert, B., and Campagnolo, F.: Improving wind farm flow models by learning from operational data, *Wind Energ. Sci.*, 5, 647–673, <https://doi.org/10.5194/wes-5-647-2020>, 2020.
- Simley, E. and Pao, L. Y.: Evaluation of a wind speed estimator for effective hub-height and shear components, *Wind Energy*, 19, 167–184, <https://doi.org/10.1002/we.1817>, 2016.
- Soltani, M. N., Knudsen, T., Svenstrup, M., Wisniewski, R., Brath, P., Ortega, R., and Johnson, K.: Estimation of rotor effective wind speed: A comparison, *IEEE T. Contr. Syst. T.*, 21, 1155–1167, <https://doi.org/10.1109/TCST.2013.2260751>, 2013.
- Vollmer, L., Steinfeld, G., Heinemann, D., and Kühn, M.: Estimating the wake deflection downstream of a wind turbine in different atmospheric stabilities: an LES study, *Wind Energ. Sci.*, 1, 129–141, <https://doi.org/10.5194/wes-1-129-2016>, 2016.
- Vollmer, L., Lee, J. C.-Y., Steinfeld, G., and Lundquist, J. K.: A wind turbine wake in changing atmospheric conditions: LES and lidar measurements, *J. Phys. Conf. Ser.*, 854, 012050, <https://doi.org/10.1088/1742-6596/854/1/012050>, 2017.
- Ziegler, L. and Muskulus, M.: Fatigue reassessment for lifetime extension of offshore wind monopile substructures, *J. Phys. Conf. Ser.*, 753, 092010, <https://doi.org/10.1088/1742-6596/753/9/092010>, 2016.

Paper 5: Brief communication: A double Gaussian wake model

7.1 Summary

This work presents an analytical turbine wake model, based on a double Gaussian velocity distribution function, correcting and improving a previous publication. The wake model, which has also been employed in **Paper 11**, is derived applying the principle of momentum conservation, and the stream tube theory was used to estimate the conditions at the stream tube outlet.

The model is exemplary tuned and validated using high-fidelity large eddy simulations (LES) of a scaled turbine, replicating wind tunnel experiments. It is shown that especially for the near wake, where a double Gaussian wake profile is clearly visible, the presented model is superior to a widely used single Gaussian reference wake profile.

7.2 Contribution

Within this peer-reviewed publication, the author of this dissertation has conducted the main research work. Amr Balbaa identified the mistakes of the previous paper and implemented the correct model. Carlo L. Bottasso supervised the research. All authors provided important input to this research work through discussions, feedback and by writing the paper.

7.3 Reference

J. Schreiber, A. Balbaa, and C. L. Bottasso, “Brief communication: A double-gaussian wake model,” *Wind Energy Science*, vol. 5, no. 1, pp. 237–244, 2020. doi: 10.5194/wes-5-237-2020

Wind Energ. Sci., 5, 237–244, 2020
<https://doi.org/10.5194/wes-5-237-2020>
© Author(s) 2020. This work is distributed under
the Creative Commons Attribution 4.0 License.



Brief communication: A double-Gaussian wake model

Johannes Schreiber, Amr Balbaa, and Carlo L. Bottasso

Wind Energy Institute, Technische Universität München, 85748 Garching bei München, Germany

Correspondence: Carlo L. Bottasso (carlo.bottasso@tum.de)

Received: 9 August 2019 – Discussion started: 23 August 2019

Revised: 3 December 2019 – Accepted: 8 January 2020 – Published: 14 February 2020

Abstract. In this paper, an analytical wake model with a double-Gaussian velocity distribution is presented, improving on a similar formulation by Keane et al. (2016). The choice of a double-Gaussian shape function is motivated by the behavior of the near-wake region that is observed in numerical simulations and experimental measurements. The method is based on the conservation of momentum principle, while stream-tube theory is used to determine the wake expansion at the tube outlet. The model is calibrated and validated using large eddy simulations replicating scaled wind turbine experiments. Results show that the tuned double-Gaussian model is superior to a single-Gaussian formulation in the near-wake region.

1 Introduction

Analytical engineering wind farm models are low-fidelity approximations used to simulate the performance of wind power systems. A wind farm model includes both a model of the wind turbines and a model of the modifications to the ambient flow induced by their wakes, together with their mutual interactions. Analytical wake models, as opposed to high-fidelity computational fluid dynamics (CFD) models, are simple, easy to implement, and computationally inexpensive. In fact, they only simulate macroscopic average effects of wakes and not their small scales or turbulent fluctuations. Engineering wake models find applicability in all those cases that do not need to resolve small spatial and fast temporal scales, such as the calculation of the power production of a wind plant over a sufficiently long time horizon. Such models are also extremely useful in optimization problems, where a large number of simulations might be required before a solution is reached or where calculations need to be performed on the fly in real time. Analytical wake models are thus often utilized in wind farm layout planning and in the emerging field of wind farm and wake control (Scholbrock, 2011; Churchfield, 2013; Boersma et al., 2017).

Because of their indisputable usefulness, engineering wake models have been extensively studied in the literature. The Jensen (PARK) formulation is one of the most widely used wake models, to the extent that it is sometimes consid-

ered the industry standard (Keane et al., 2016). The model was first introduced by Jensen (1983) and later further developed by Katić et al. (1986). Other widely used and cited wake models include the Frandsen model (Frandsen et al., 2006), the FLORIS model (Gebraad et al., 2014), and the EPFL Gaussian models (Bastankhah and Porté-Agel, 2014, 2016).

All such models have been designed to faithfully represent the average flow properties of the far-wake region. However, in the near wake (which is usually defined as the region up to about 4 diameters (4D) downstream of the rotor disk), the models seem to lack accuracy. Nowadays, onshore wind farms tend to be closely packed, and turbine spacing often reaches values close to or even below 3D (Schreiber et al., 2018; energiespektrum.de, 2015). This raises the necessity of developing models that accurately represent the wake not only far away from the rotor disk but also in the near and mid-wake regions.

Keane et al. (2016) developed a wake model featuring a double-Gaussian velocity deficit distribution in an attempt to formulate a model that closely resembles observed speed distributions in both the near- and far-wake regions. In fact, while a single-Gaussian function is considered to be a good approximation of the wake velocity distribution in the far wake (Bastankhah and Porté-Agel, 2014, 2016), the near wake is better approximated using a double-Gaussian distribution. This is due to the presence of two minima in the

speed profiles close to the rotor disk, as also observed in experimental measurements and high-fidelity CFD simulations (Wang et al., 2017). The double-Gaussian model by Keane et al. (2016), which is referred to as the Keane model in this paper, was developed in a similar fashion to the EPFL Gaussian model (Bastankhah and Porté-Agel, 2014), and it was intended to respect the principles of mass and momentum conservation.

In this short note, a double-Gaussian wake model, based on Keane's model and with emphasis on near-wake flow behavior, is derived, calibrated, and validated. The present formulation addresses and resolves some issues found in the original implementation of Keane et al. (2016), primarily concerning momentum conservation. In addition, the wake expansion function is defined such that mass flow deficit conservation is achieved at the stream-tube outlet.

This paper is organized as follows. The derivation of the double-Gaussian wake model is detailed in Sect. 2, along with the formulation of the wake expansion function. In Sect. 3, the model is tuned and validated, using both experimental measurements obtained with scaled models in a boundary layer wind tunnel and by numerical results of high-fidelity large eddy simulations (LESs). Additionally, the performance of the double-Gaussian model is compared to a standard single-Gaussian formulation. Concluding remarks and future work recommendations are given in Sect. 4. Finally, Appendix A derives some integrals appearing in the formulation.

2 Wake model description

2.1 Double-Gaussian velocity deficit

The double-Gaussian wake model is derived in a similar way to the Frandsen (Frandsen et al., 2006) and EPFL single-Gaussian models (Bastankhah and Porté-Agel, 2014). Following their approach, the conservation of momentum principle is applied on an ansatz velocity deficit distribution, which includes an amplitude function. Thereby, an expression for the amplitude is obtained that assures conservation of momentum.

At the downstream distance x from the wind turbine rotor and at the radial distance r from the wake centerline, the wake velocity deficit $U_\infty - U(x, r)$ is modeled as the product of the normalized double-Gaussian function $g(r, \sigma(x))$, which dictates the spatial shape of the deficit, with the amplitude function $C(\sigma(x))$. This yields

$$\frac{U_\infty - U(x, r)}{U_\infty} = C(\sigma(x))g(r, \sigma(x)), \quad (1)$$

where U_∞ represents the ambient wind speed and $U(x, r)$ the local flow velocity in the wake. The double-Gaussian wake shape function, which is symmetric with respect to the wake

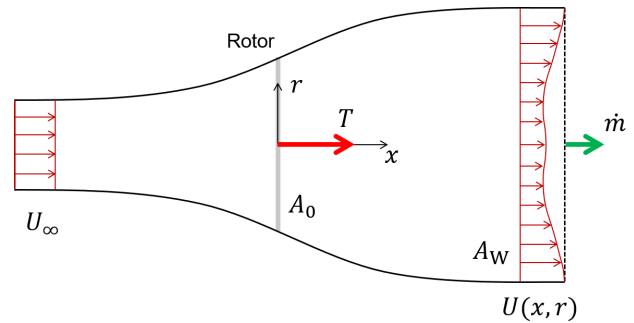


Figure 1. Stream tube with nomenclature: U_∞ is the ambient wind speed; $U(x, r)$ is the local flow velocity in the wake at the downstream position x and radial distance r from the wake centerline; \dot{m} is the mass flow rate through the stream tube; A_W is a planar cross-sectional area large enough to contain the wake deficit; A_0 is the rotor disk area; and T is the thrust force (by the principle of action and reaction, an equal and opposite force is applied by the rotor onto the flow).

center, is defined as

$$g(r, \sigma(x)) = \frac{1}{2} \left(e^{D^+} + e^{D^-} \right), \quad D_\pm = \frac{-(r \pm r_0)^2}{2\sigma^2(x)}, \quad (2)$$

where r_0 is the radial position of the Gaussian extrema. The standard deviation of the Gaussian function, noted $\sigma(x)$, represents the width (cross section) of each of the two single-Gaussian profiles. The wake expands with downstream distance x , causing the transformation of the initial double-Gaussian profile in the near wake, through a flat-peak transition region, into a nearly single-Gaussian profile in the far wake. The wake expansion function is discussed in further detail in Sect. 2.2. A possible improvement to the present model might include an azimuth-dependent double-Gaussian function. This would allow one to model a non-axisymmetric double-peaked wake profile, caused by a sheared inflow and/or by the misalignment of the rotor axis with respect to the wind, at the cost of extra tuning parameters.

The conservation of momentum principle is now applied on the ansatz velocity deficit distribution, using the amplitude function $C(\sigma(x))$ as a degree of freedom. Accordingly, the axial thrust force T is related to the rate of change of momentum p of the flow throughout the stream tube (see Fig. 1), i.e.,

$$T = \frac{dp}{dt} = \dot{m} \Delta \tilde{U} = \rho \int_{A_W} U(x, r) (U_\infty - U(x, r)) dA_W, \quad (3)$$

where \dot{m} is the mass flow rate through the stream tube, $\Delta \tilde{U}$ an effective wake velocity deficit, ρ the air density, and A_W a planar cross section at least large enough to contain the wake deficit. Equation (3) is only valid if there is an equal pressure and negligible flow acceleration at the inlet and outlet sections of the stream tube and, additionally, if shear forces

on the control volume can be neglected. The thrust force T is customarily expressed through the nondimensional thrust coefficient C_T as

$$T = \frac{1}{2} \rho A_0 U_\infty^2 C_T, \quad (4)$$

where A_0 is the rotor swept area.

If the wake velocity, defined in Eqs. (1) and (2), is substituted into the Eq. (3), one obtains

$$T = \rho \pi U_\infty^2 C(\sigma) \int_0^\infty \left(e^{D_+} + e^{D_-} - \frac{C(\sigma)}{2} \left(e^{2D_+} + e^{2D_-} + 2e^{D_+ + D_-} \right) \right) r dr. \quad (5)$$

Note that as the double-Gaussian wake expands all the way to infinity, the integral boundary is set accordingly. The integration of Eq. (5), whose details are provided in Appendix A, yields

$$T = \rho \pi U_\infty^2 C(\sigma) (M - C(\sigma)N), \quad (6)$$

where

$$M = 2\sigma^2 e^{-\frac{r_0^2}{2\sigma^2}} + \sqrt{2\pi} r_0 \sigma \operatorname{erf} \left(\frac{r_0}{\sqrt{2}\sigma} \right), \quad (7a)$$

$$N = \sigma^2 e^{-\frac{r_0^2}{\sigma^2}} + \frac{\sqrt{\pi}}{2} r_0 \sigma \operatorname{erf} \left(\frac{r_0}{\sigma} \right). \quad (7b)$$

By substituting the thrust given by Eq. (4) into Eq. (6), and solving the resulting quadratic equation for the amplitude function $C(\sigma)$, one obtains

$$C_{\pm}(\sigma(x)) = \frac{M \pm \sqrt{M^2 - \frac{1}{2} N C_T d_0^2}}{2N}, \quad (8)$$

where $d_0 = \sqrt{4A_0/\pi}$ is the rotor diameter. Both solutions of the amplitude function $C(\sigma)$ would theoretically lead to the conservation of momentum at all downstream distances. However, the velocity profiles obtained by using $C_+(\sigma)$ are characterized by a negative speed (i.e., in the direction opposite to the ambient flow), and thus $C_+(\sigma)$ is deemed to be a nonphysical solution. Therefore, the true solution for the amplitude function is $C_-(\sigma)$. In addition, a momentum-conserving solution exists only if $M^2 - 1/2 N C_T d_0^2 \geq 0$, which might not always be the case for large values of C_T .

The derived expressions for M and N presented in this paper differ from the results reported in the original publication by Keane et al. (2016), even though all assumptions are identical. The expressions reported in the original paper were also evaluated numerically, yielding nonphysical results that violate the conservation of mass and momentum underlying the formulation.

2.2 Wake expansion function

In the previous section, following the conservation of momentum, the shape of the double-Gaussian wake deficit has been defined as a function of the Gaussian parameter σ . In this section, a wake expansion function $\sigma(x)$ is introduced, which is linear with respect to the downstream distance x . By mass conservation, the wake expansion at the position of the stream tube outlet is therefore identified.

In previous work by Frandsen et al. (2006) and Bastankhah and Porté-Agel (2014), stream tube theory was employed to derive an equation for the initial wake width at the turbine rotor. Thereby, the number of tunable parameters of the wake expansion function is reduced, facilitating model calibration. However, this approach includes the assumption that the stream tube outlet is located exactly at the turbine rotor itself, which is hardly true. Results indicate that the derived initial wake width is too large to fit experimental measurements, which in turn requires a model retuning (Bastankhah and Porté-Agel, 2014).

In the present work, the stream tube outlet is not assumed to be located at the turbine rotor ($x = 0$) but at the unknown downstream position x_0 . Therefore, the expansion function is defined as

$$\sigma(x) = k^*(x - x_0) + \epsilon, \quad (9)$$

where parameter k^* controls the rate of expansion, while ϵ represents the wake expansion at x_0 . The wake expansion function is assumed to be linear as in Bastankhah and Porté-Agel (2014).

To derive ϵ , mass conservation between the Betz stream tube and the wake model is enforced. Starting from Eq. (3), Frandsen et al. (2006) and Bastankhah and Porté-Agel (2014) show that the mass flow deficit rate at the outlet of a Betz stream tube (noted ST) can be written as

$$\begin{aligned} \dot{m}_{ST} &= \rho \int_{A_{ST}} \frac{U_\infty - U_{ST}}{U_\infty} dA_{ST} \\ &= \rho \frac{\pi}{8} d_0^2 \beta \left(1 - \sqrt{1 - \frac{2}{\beta} C_T} \right), \end{aligned} \quad (10)$$

where U_{ST} is the uniform cross-sectional wake velocity. In this expression, β is the ratio between the stream tube outlet area A_{ST} and the rotor disk area A_0 , which can be expressed as a function of the thrust coefficient C_T as

$$\beta = \frac{A_{ST}}{A_0} = \frac{1}{2} \frac{1 + \sqrt{1 - C_T}}{\sqrt{1 - C_T}}. \quad (11)$$

At the Betz stream tube outlet ($x = x_0$), the mass flow deficit rate of the double-Gaussian (noted DG) wake model

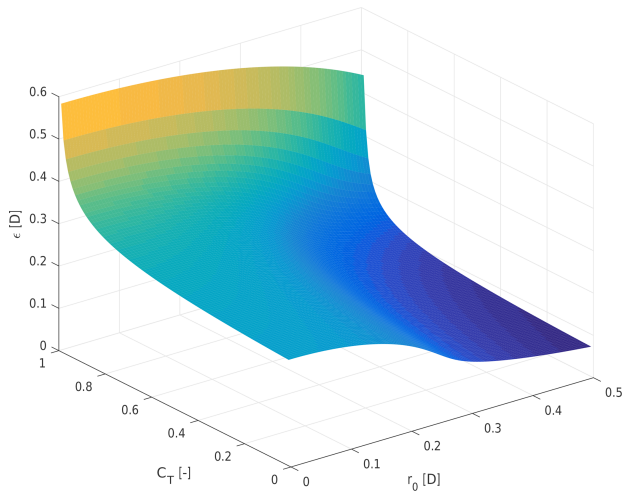


Figure 2. Visualization of the width of the double-Gaussian function ϵ at the stream tube outlet, as a function of the thrust coefficient C_T and the position of the Gaussian extrema r_0 .

writes as

$$\begin{aligned} \dot{m}_{DG} &= \rho \int_{A_w} \frac{U_\infty - U(x_0, r)}{U_\infty} dA_w \\ &= \rho \pi M(\epsilon) \frac{M(\epsilon) - \sqrt{M(\epsilon)^2 - \frac{1}{2} N(\epsilon) C_T d_0^2}}{2N(\epsilon)}. \end{aligned} \quad (12)$$

By equating both mass flow deficits (i.e., $\dot{m}_{DG} = \dot{m}_{ST}$), the initial wake expansion ϵ can be derived. The solution was computed numerically as a function of the thrust coefficient C_T and the spanwise location of the Gaussian extrema r_0 . The resulting surface is presented in Fig. 2. Note that the solution to stream tube theory is defined only in the range $0 \leq C_T < 1$, and ϵ tends to infinity as the thrust coefficient approaches the value of 1, due to mass conservation.

The remaining parameters, x_0 and k^* , in the linear wake expansion function expressed by Eq. (9) are not explicitly modeled, and they should be tuned based on experimental measurements or high-fidelity simulations, as shown in the next section. Note that the underlying momentum conservation statement expressed by Eq. (3) has only been defined for ambient pressure. Therefore, the formulation is, strictly speaking, only valid for $x \geq x_0$. However, as pressure recovers rapidly immediately downstream of the rotor, reasonable approximations can also be expected for $x < x_0$. Finally, k^* is expected to depend on atmospheric conditions (Peña et al., 2016) and turbine thrust (Campagnolo et al., 2019).

3 Model calibration and validation

3.1 Experimental and simulation setup

To calibrate and validate the double-Gaussian wake model, time-averaged flow measurements from an LES numerical solution have been used. The CFD simulation replicates an experiment conducted with the scaled G1 wind turbine (Campagnolo et al., 2017, 2019), which has a 1.1 m rotor diameter and a 0.8 m hub height. Its design operating tip speed ratio is 8 and its rated rotor speed is 850 rpm. The G1 model is designed such that the characteristics of its wake are realistic in terms of shape, velocity deficit, and recovery. In addition, the model features closed-loop pitch, torque and yaw control, and load sensors located at the shaft and tower base (Campagnolo et al., 2017). The experiment was conducted with a single G1 wind turbine model in the $36 \text{ m} \times 16.7 \text{ m} \times 3.84 \text{ m}$ boundary layer wind tunnel at Politecnico di Milano. The wake profile was measured using hot-wire probes at the downstream distances $x/D = \{1.4, 1.7, 2, 3, 4, 6, 9\}$ from the turbine. At each downstream location, the velocity was measured at hub height at different lateral positions y and then time averaged to obtain a steady-state value. The ambient wind velocity within the wind tunnel was measured using a pitot tube placed upwind of the G1 model. The wind tunnel experiment was conducted with a 5 m s^{-1} hub height wind speed, a power law exponent of 0.144, and a turbulence intensity of approximately 5%, with the wind turbine operating at $C_T \approx 0.75$.

A complete digital copy of the experiment was developed with the LES simulation framework developed by Wang et al. (2017), which includes the passive generation of a sheared and turbulent flow, an actuator line model of the wind turbine implemented with the FAST aeroservoelastic simulator (Jonkman and Buhl Jr., 2005) and the tunnel walls. The simulation model includes also a slight lateral nonuniformity of the inflow, in the form of a 2.7% horizontal shear, caused by the wind tunnel internal layout upstream of the test chamber and by the tunnel fans. The proposed double-Gaussian wake model was calibrated and validated using time-averaged CFD simulation results at the same downstream distances as the experiments, numerical and experimental measurements being in excellent agreement with each other.

3.2 Parameter identification and results

The double-Gaussian model proposed in this work has three tunable parameters: k^* , x_0 , and k_r . Parameters k^* and x_0 are used to describe the wake expansion downstream of the turbine rotor, as expressed by Eq. (9). The third parameter, k_r , is defined as $r_0 = k_r/2$, and it describes the position of the Gaussian extrema. When $k_r = 1$ the curve extrema are located at the tip of the rotor blades, while for $k_r = 0$ the two

Table 1. Identified model parameters.

Operating conditions		Parameters		
U_∞ (m s ⁻¹)	C_T (-)	k^* (-)	x_0 (D)	k_r (-)
5.00	0.75	0.011	4.55	0.535

Gaussian functions coincide at the wake center, leading to a single-Gaussian wake profile.

In the original formulation by Keane, k_r was fixed at 75 % blade span, as it was argued that most lift is extracted from the flow at this location. In the present work the parameter is tuned based on measurements, as the assumed 75 % blade-span position did not lead to satisfactory results.

The goal of model calibration is to ensure that the wind velocity profiles match the reference data set as closely as possible. To this end, the squared error between the wake model and CFD-computed wake profiles is minimized with respect to the free parameters. This estimation problem was solved using the Nelder–Mead simplex algorithm implemented in the MATLAB function `fminsearch` (Lagarias et al., 1998). To ensure the generality of the results, only a subset of the reference data was used for parameter estimation (namely the downstream distances 1.7, 3, and 6 D), while the others were used for verification purposes.

The identified parameters are presented in Table 1. The Gaussian extrema were found to be at approximately 53.5 % of blade span ($k_r = 0.535$), while the wake width at x_0 is $\epsilon = 0.23$ D. Model calibration also resulted in the positioning of the stream tube outlet at $x_0 = 4.55$ D, which appears to be a realistic value for the investigated turbine.

Figure 3 shows the experimental wake measurements using black circles, for all available downstream distances. The CFD results, shown using red \times symbols, are almost identical to the experimental measurements, highlighting the quality of the LES simulations. The predictions of the double-Gaussian model are shown in solid blue lines.

The model exhibits good generality, as demonstrated by the good matching of the profiles at distances that were not used for model estimation. Especially in the near-wake region up to about 3 D, the placement of the Gaussian extrema appears to be in good agreement with the measured one.

The performance of the model clearly depends on the data used for its calibration. Using reference data close to the turbine rotor is important for accurately gauging the positions of the velocity profile extrema, while a wider range of distances leads to an improved expansion behavior. In the present case, more data from the near-wake region (1.7 and 3 D) were considered in the tuning process than in the far wake (6 D). This leads to a slight overestimation of the velocity deficit at 9 D, which could be attributed to an underestimation of the expansion slope k^* . However, tuning the model using the entire set of reference data points leads to only small differences in

the identified parameters, which in turn produce wake profiles that are fairly similar to the ones presented here. On the other hand, identifying the model using only data points from the far wake resulted in better fitting results at 9 D but with either very small values of r_0 – which led to nearly single-Gaussian profiles – or with high values of the k^* expansion slope – which led to nonphysical solutions of Eq. (8) for the amplitude function in the near-wake region, due to excessively small Gaussian widths.

Figure 4 depicts with a solid blue line and * symbols the root mean square error (RMSE) between the DG wake model (based on the parameters reported above, obtained from measurements at 1.7, 3, and 6 D) and the reference CFD data as a function of downstream distance. To identify a lower error bound, the DG wake model parameters were also tuned separately at each downstream distance, obtaining seven different local parameterizations. The corresponding RMSE with respect to the CFD solution is reported in the same figure using a dashed blue line. The small difference between the two curves shows that the single (global) parameterization computed using only three distances is only marginally suboptimal, in the sense that it is very close to the best possible fitting that a double-Gaussian shape function can achieve. The plot shows also a slight increase in the difference between the two curves in the far-wake region, which can again be attributed to the fact that only one large-distance (6 D) measurement was used in the global tuning.

As a comparison, Fig. 4 also shows the results obtained with the EPFL single-Gaussian (SG) model (Bastankhah and Porté-Agel, 2014). The SG model was identified with the same procedure and measurements used for the DG model, obtaining $\epsilon_{SG} = 0.3177$ and $k_{SG}^* = 0.0082$; the corresponding RMSE with respect to the CFD results is reported in the figure using a solid red line with circles. The lower error bound for the SG model, here again obtained by tuning the parameters independently at each one of the seven available downstream distances, is shown using a dashed red line. As expected, the SG wake model shows a significantly larger RMSE in the near-wake region than in the DG case. In fact, here the wake profile is indeed characterized by two peaks, so that the double-Gaussian shape function allows for a more precise representation of the actual flow characteristics. Here again it should be noted that the difference between the global and local parameterizations is quite small, which strengthens the conclusion that improved results are due to the ansatz velocity deficit distribution and not to the specific parameterizations. Comparing the SG with the DG model, Fig. 4 shows that both reach very similar RMSEs for 9 D. The similarity between the two models continues for larger downstream distances.

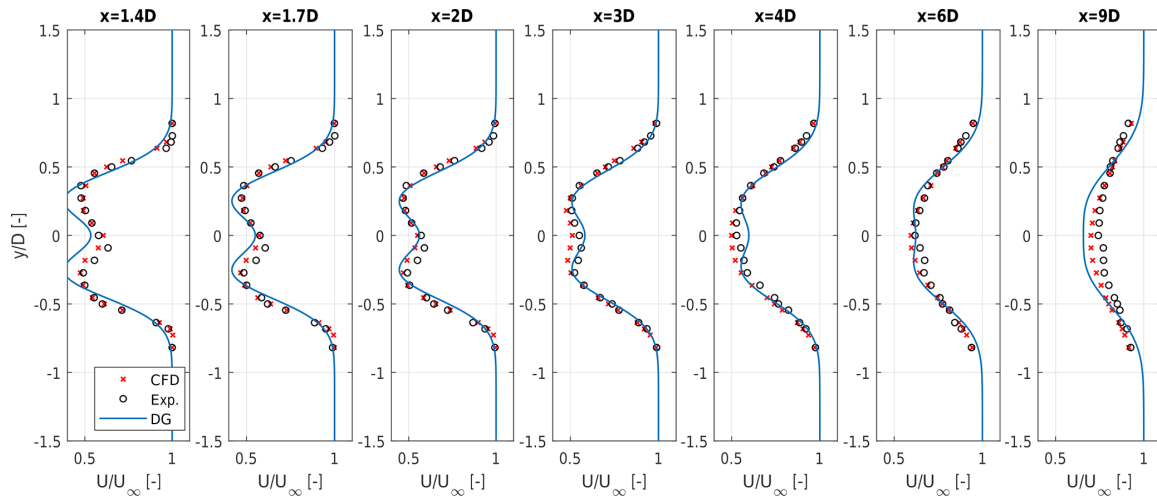


Figure 3. Normalized wind velocity profiles of the double-Gaussian model (solid blue line) compared to experimental measurements (black circles) and CFD simulations (red \times symbols). The distances 1.7, 3, and 6 D were used for model calibration.

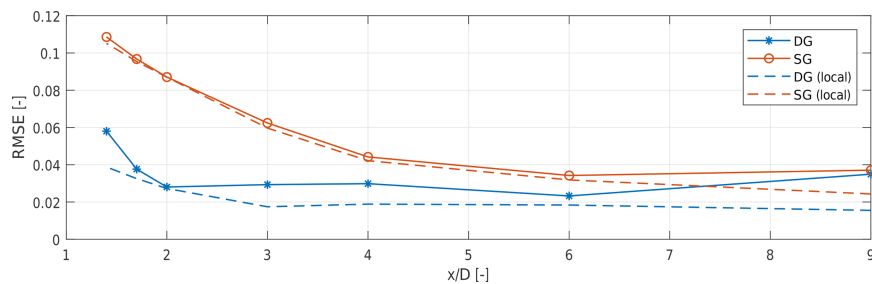


Figure 4. Root mean square error between the reference CFD velocity deficit data and the engineering wake models. Double-Gaussian (DG) wake model identified using measurements at 1.7, 3, and 6 D: solid blue line with * symbols. DG wake model parameterized locally at each downstream distance: dashed blue line. Single-Gaussian (SG) EPFL wake model identified using measurements at 1.7, 3, and 6 D: solid red line with circles. SG EPFL wake model parameterized locally at each downstream distance: dashed red line.

4 Conclusions

This short paper presented an analytical double-Gaussian wake model. The proposed formulation corrects and improves a previously published model proposed by Keane et al. (2016). The shape of the velocity deficit distribution in the wake is described by two Gaussian functions, which are symmetric with respect to the wake center, while the amplitude of the velocity deficit is derived using the principle of momentum conservation. A linear expansion of the width of the Gaussian profiles was assumed, and stream tube theory was used to estimate the conditions at the stream tube outlet.

The model was calibrated and validated using a set of time-averaged CFD simulation results, which replicate wind tunnel experiments performed with a scaled wind turbine in a boundary layer wind tunnel. Results show that the model fits the reference data with good accuracy, especially in the near-wake region where a single-Gaussian wake is unable to describe the typically observed bimodal velocity profiles. In

the far wake, a slight overestimation of the wake deficit could be observed. It is speculated that this might be due to the wake expansion gradient being slightly different in the near- and far-wake regions. This claim, however, would need additional work to be substantiated. The different shape of the wake in the near- and far-wake regions also suggests stitching the two models together, the double Gaussian being used in the near-wake region and the single Gaussian further downstream. This would avoid the need for a single tuning that has to cover such a long distance and different behaviors. Additional future work could extend the wake model to include wake deflection, which could be done in a rather straightforward manner by following Bastankhah and Porté-Agel (2016). In this case, a nonsymmetric double-Gaussian shape function could be used to model the kidney shape of a deflected wake (Bartl et al., 2018). More in general, an azimuth-dependent double Gaussian might be used to account for the effects of both misalignment and a sheared inflow.

Appendix A: Integration of the momentum flux conservation formula

Equation (5) can be written as

$$T = \rho\pi U_\infty^2 C(\sigma)(M - C(\sigma)N), \quad (\text{A1})$$

where

$$M = \int_0^\infty (e^{D_+} + e^{D_-}) r dr, \quad (\text{A2a})$$

$$N = \int_0^\infty \left(\frac{1}{2} (e^{2D_+} + e^{2D_-} + 2e^{D_+ + D_-}) \right) r dr. \quad (\text{A2b})$$

In the following, integrals M and N are solved to obtain Eq. (7a) and (7b).

A1 Derivation of M

M can be split into two terms:

$$M = I_1 + I_2. \quad (\text{A3})$$

Term I_1 is defined as

$$I_1 = \int_0^\infty e^{D_+} r dr = \lim_{R \rightarrow \infty} \int_0^R r e^{-\frac{(r+r_0)^2}{2\sigma^2}} dr. \quad (\text{A4})$$

Noting that $D_\pm = -\frac{(r \pm r_0)^2}{2\sigma^2(x)}$, one gets

$$I_1 = \lim_{R \rightarrow \infty} \left[-\sigma^2 e^{-\frac{(r+r_0)^2}{2\sigma^2}} - \frac{\sqrt{\pi} r_0 \sigma \operatorname{erf}\left(\frac{r+r_0}{\sqrt{2}\sigma}\right)}{\sqrt{2}} \right]_0^R, \quad (\text{A5a})$$

$$= \sigma^2 e^{-\frac{r_0^2}{2\sigma^2}} - \frac{\sqrt{2\pi} r_0 \sigma}{2} \operatorname{erfc}\left(\frac{r_0}{\sqrt{2}\sigma}\right), \quad (\text{A5b})$$

where erf is the Gauss error function,

$$\operatorname{erf}(x) = \frac{1}{\sqrt{\pi}} \int_{-x}^x e^{-t^2} dt, \quad (\text{A6})$$

and $\operatorname{erfc}(x) = 1 - \operatorname{erf}(x)$ its complementary function. Similarly, I_2 writes as

$$I_2 = \int_0^\infty e^{D_-} r dr = \lim_{R \rightarrow \infty} \int_0^R r e^{-\frac{(r-r_0)^2}{2\sigma^2}} dr, \quad (\text{A7})$$

and its integral is computed as

$$I_2 = \lim_{R \rightarrow \infty} \left[-\sigma^2 e^{-\frac{(r-r_0)^2}{2\sigma^2}} + \frac{\sqrt{\pi} r_0 \sigma \operatorname{erf}\left(\frac{r-r_0}{\sqrt{2}\sigma}\right)}{\sqrt{2}} \right]_0^R, \quad (\text{A8a})$$

$$= \sigma^2 e^{-\frac{r_0^2}{2\sigma^2}} + \frac{\sqrt{2\pi} r_0 \sigma}{2} \operatorname{erfc}\left(\frac{r_0}{\sqrt{2}\sigma}\right). \quad (\text{A8b})$$

Combining the previous results, one gets Eq. (7a), i.e.,

$$M = I_1 + I_2 = 2\sigma^2 e^{-\frac{r_0^2}{2\sigma^2}} + \sqrt{2\pi} r_0 \sigma \operatorname{erf}\left(\frac{r_0}{\sqrt{2}\sigma}\right). \quad (\text{A9})$$

A2 Derivation of N

Term N can be split into three terms

$$N = \frac{1}{2} (I_3 + I_4 + 2I_5). \quad (\text{A10})$$

Terms I_3 and I_4 are collectively defined as

$$I_3 + I_4 = \int_0^\infty (e^{2D_+} + e^{2D_-}) r dr$$

$$= \lim_{R \rightarrow \infty} \int_0^R r e^{-\frac{(r+r_0)^2}{\sigma^2}} + r e^{-\frac{(r-r_0)^2}{\sigma^2}} dr. \quad (\text{A11})$$

Solving the integral yields

$$I_3 + I_4 = \lim_{R \rightarrow \infty} \left[\frac{-\sigma^2}{2} \left(e^{-\frac{(r+r_0)^2}{\sigma^2}} + e^{-\frac{(r-r_0)^2}{\sigma^2}} \right) - \frac{\sqrt{\pi}}{2} r_0 \sigma \left(\operatorname{erf}\left(\frac{r+r_0}{\sigma}\right) - \operatorname{erf}\left(\frac{r-r_0}{\sigma}\right) \right) \right]_0^R, \quad (\text{A12a})$$

$$= \sigma^2 e^{-\frac{r_0^2}{\sigma^2}} + \sqrt{\pi} r_0 \sigma \operatorname{erf}\left(\frac{r_0}{\sigma}\right). \quad (\text{A12b})$$

Finally, I_5 is defined as

$$I_5 = \int_0^\infty e^{D_+ + D_-} r dr = \lim_{R \rightarrow \infty} \int_0^R r e^{-\frac{(r+r_0)^2}{2\sigma^2} - \frac{(r-r_0)^2}{2\sigma^2}} dr, \quad (\text{A13})$$

which, once integrated, gives

$$I_5 = \lim_{R \rightarrow \infty} \left[\frac{-\sigma^2}{2} e^{-\frac{(r^2+r_0^2)}{\sigma^2}} \right]_0^R, \quad (\text{A14a})$$

$$= \frac{\sigma^2}{2} e^{-\frac{r_0^2}{\sigma^2}}. \quad (\text{A14b})$$

Therefore, one gets

$$N = \frac{1}{2} (I_3 + I_4 + 2I_5) = \sigma^2 e^{-\frac{r_0^2}{\sigma^2}} + \frac{\sqrt{\pi}}{2} r_0 \sigma \operatorname{erf}\left(\frac{r_0}{\sigma}\right), \quad (\text{A15})$$

which corresponds to Eq. (7b).

Code and data availability. A MATLAB implementation of the wake model and the data contained in this article can be obtained by contacting the authors.

Author contributions. JS conducted the main research work, AB implemented the correct model and CLB closely supervised the whole research. All three authors provided important input to this research work through discussions, feedback and by writing the paper.

Competing interests. The authors declare that they have no conflict of interest.

Acknowledgements. The authors express their gratitude to Jesse Wang and Filippo Campagnolo of the Technical University of Munich, who respectively provided the numerical and experimental wake measurements.

Financial support. This research has been partially supported by the European Commission, H2020 Research Infrastructures (CL-Windcon (grant no. 727477)).

This work was supported by the German Research Foundation (DFG) and the Technical University of Munich (TUM) in the framework of the Open Access Publishing Program.

Review statement. This paper was edited by Gerard J. W. van Bussel and reviewed by Matthew J. Churchfield and one anonymous referee.

References

- Bartl, J., Mühle, F., Schottler, J., Sætran, L., Peinke, J., Adaramola, M., and Hölling, M.: Wind tunnel experiments on wind turbine wakes in yaw: effects of inflow turbulence and shear, *Wind Energy Sci.*, 3, 329–343, <https://doi.org/10.5194/wes-3-329-2018>, 2018.
- Bastankhah, M. and Porté-Agel, F.: A new analytical model for wind-turbine wakes, *Renew. Energ.*, 70, 116–123, 2014.
- Bastankhah, M. and Porté-Agel, F.: Experimental and theoretical study of wind turbine wakes in yawed conditions, *J. Fluid Mech.*, 806, 506–541, 2016.
- Boersma, S., Doekemeijer, B., Gebraad, P., Fleming, P., Annoni, J., Scholbrock, A., Frederik, J., and van Wingerden, J.: A tutorial on control-oriented modeling and control of wind farms, in: 2017 American Control Conference (ACC), Seattle, WA, USA, 24–26 May 2017, IEEE, 1–18, 2017.
- Campagnolo, F., Schreiber, J., Garcia, A. M., and Bottasso, C. L.: Wind Tunnel Validation of a Wind Observer for Wind Farm Control, *International Society of Offshore and Polar Engineers*, San Francisco, California, USA, ISOPE-I-17-410, 2017.
- Campagnolo, F., Petrović, V., Bottasso, C. L., and Croce, A.: Wind tunnel testing of wake control strategies, *American Control Conference (ACC)*, Boston, MA, USA, 6–8 July 2016, IEEE, 513–518, <https://doi.org/10.1109/ACC.2016.7524965>, 2016.
- Churchfield, M. J.: A Review of Wind Turbine Wake Models and Future Directions, in: 2013 North American Wind Energy Academy (NAWEA) Symposium, Boulder, Colorado, 6 August 2013.
- energiespektrum.de: Produzieren auf engem Raum, available at: <https://www.energiespektrum.de/produzieren-auf-engem-raum-8918> (last access: 11 December 2019), 2015.
- Frandsen, S., Barthelmie, R., Pryor, S., Rathmann, O., Larsen, S., Højstrup, J., and Thøgersen, M.: Analytical modelling of wind speed deficit in large offshore wind farms, *Wind Energy*, 9, 39–53, 2006.
- Gebraad, P. M. O., Teeuwisse, F. W., van Wingerden, J. W., Fleming, P. A., Ruben, S. D., Marden, J. R., and Pao, L. Y.: A data-driven model for wind plant power optimization by yaw control, in: 2014 American Control Conference (ACC), Portland, OR, USA, 4–6 June 2014, IEEE, 3128–3134, 2014.
- Jensen, N. O.: A note on wind generator interaction, *Risø National Laboratory*, Roskilde, M-2411, 1983.
- Jonkman, J. M. and Buhl Jr., M. L.: “FAST user’s guide”, NREL/EL-500-29798, National Renewable Energy Laboratory, Golden, Colorado, available at: <https://nwtc.nrel.gov/FAST7> (last access: 29 January 2020), 2005.
- Katić, I., Højstrup, J., and Jensen, N. O.: A simple model for cluster efficiency, in: *European Wind Energy Association Conference and Exhibition*, Rome, Italy, 7–9 October 1986, 407–410, 1986.
- Keane, A., Aguirre, P. E. O., Ferchland, H., Clive, P., and Gallacher, D.: An analytical model for a full wind turbine wake, *J. Phys. Conf. Ser.*, 753, 032039, <https://doi.org/10.1088/1742-6596/753/3/032039>, 2016.
- Lagarias, J. C., Reeds, J. A., Wright, M. H., and Wright, P. E.: Convergence Properties of the Nelder–Mead Simplex Method in Low Dimensions, *SIAM J. Optimiz.*, 9, 112–147, <https://doi.org/10.1137/S1052623496303470>, 1998.
- Peña, A., Réthoré, P.-E., and van der Laan, M. P.: On the application of the Jensen wake model using a turbulence-dependent wake decay coefficient: The Sexbierum case, *Wind Energy*, 19, 763–776, <https://doi.org/10.1002/we.1863>, 2016.
- Scholbrock, A. K.: Optimizing Wind Farm Control Strategies to Minimize Wake Loss Effects, Master’s thesis, University of Colorado, Boulder, USA, 2011.
- Schreiber, J., Salbert, B., and Bottasso, C. L.: Study of wind farm control potential based on SCADA data, *J. Phys. Conf. Ser.*, 1037, 032012, <https://doi.org/10.1088/1742-6596/1037/3/032012>, 2018.
- Wang, J., Foley, S., Nanos, E., Yu, T., Campagnolo, F., Bottasso, C., Zanotti, A., and Croce, A.: Numerical and Experimental Study of Wake Redirection Techniques in a Boundary Layer Wind Tunnel, *J. Phys. Conf. Ser.*, 854, 012048, <https://doi.org/10.1088/1742-6596/854/1/012048>, 2017.

Paper 6: Verification and Calibration of a Reduced Order Wind Farm Model by Wind Tunnel Experiments

8.1 Summary

In this work a wind farm flow and power model (FLORIS) is calibrated and tested on a scaled wind farm consisting of three G1 turbines. Thereto, the wind farm model and wake parameters are identified based on wake velocity measurements at hub height of an isolated turbine using a least squares approach. Different operating conditions and yaw misalignments with respect to the incoming flow are taken into account to also capture wake steering.

In three different wind farm layouts, each evaluated including various combinations of turbine misalignments, the model predicted power production of each turbine is compared to experimental measurements. Results show a good correlation of the overall trends. Notably the model predicted optimal yaw misalignments for maximum wind farm power are close to the experimentally identified values. The absolute power measurements are not always well predicted and various possible causes for the mismatch are discussed and taken into account in subsequent **Paper 9**.

8.2 Contribution

Within this peer-reviewed publication, the author of this dissertation has conducted the main research work. Emmanouil Nanos implemented a first version of the wind farm model. Filippo Campagnolo conducted the wind tunnel experiments and Carlo L. Bottasso supervised the whole research. All authors provided important input to this research work through discussions, feedback and by writing the paper.

8.3 Reference

J. Schreiber, E. M. Nanos, F. Campagnolo, and C. L. Bottasso, "Verification and calibration of a reduced order wind farm model by wind tunnel experiments," *Journal of Physics: Conference Series*, vol. 854, p. 012041, 2017. doi: 10.1088/1742-6596/854/1/012041

Verification and Calibration of a Reduced Order Wind Farm Model by Wind Tunnel Experiments

J Schreiber¹, E M Nanos¹, F Campagnolo¹, C L Bottasso^{1,2}

¹ Wind Energy Institute, Technische Universität München, Boltzmannstraße 15, D-85748 Garching bei München, Germany

² Dipartimento di Scienze e Tecnologie Aerospaziali, Politecnico di Milano, Via La Masa 34, I-20156 Milano, Italy

E-mail: {johannes.schreiber, em.nanos, filippo.campagnolo, carlo.bottasso}@tum.de

Abstract. In this paper an adaptation of the FLORIS approach is considered that models the wind flow and power production within a wind farm. In preparation to the use of this model for wind farm control, this paper considers the problem of its calibration and validation with the use of experimental observations. The model parameters are first identified based on measurements performed on an isolated scaled wind turbine operated in a boundary layer wind tunnel in various wind-misalignment conditions. Next, the wind farm model is verified with results of experimental tests conducted on three interacting scaled wind turbines. Although some differences in the estimated absolute power are observed, the model appears to be capable of identifying with good accuracy the wind turbine misalignment angles that, by deflecting the wake, lead to maximum power for the investigated layouts.

1. Introduction

In a wind farm environment wind turbine wakes, which are characterized by a lower wind speed and higher turbulence intensity than the free stream, can adversely affect other turbines. This in turn may lead to higher fatigue loads and a significantly reduced power output on affected turbines.

To increase total wind farm power and/or reduce fatigue loads, several techniques have been proposed [1, 2]. At present, one of the most promising approaches seems to be a technique where the wake is deflected by operating the wind turbine in yaw-misalignment condition with respect to the incoming wind [3]. In fact, as the wind turbine is yawed out of the wind, its wake is laterally deflected, which may reduce its interaction with downstream machines. Wind farm control strategies based on wake deflection have been proposed to increase the total energy capture and/or decrease fatigue loading [3, 4]. In this context, reduced order wind farm models as the FLORIS (FLOW Redirection and Induction in Steady-state) approach [4] may be used to enable model-based wind farm control.

This paper describes first a FLORIS-like wind farm model. Next, its parameters are calibrated based on wake measurements of a scaled wind turbine in a wind tunnel environment. Finally, the tuned model is used to estimate the wind farm power output for several different wind farm layouts comprising three scaled interacting wind turbines. For each layout, a variety of different yaw-misalignment combinations are tested and the turbine power is compared to the model-predicted one. Results and the causes for the observed mismatches are discussed.



2. Wind farm model

In this section a reduced order wind farm model is presented, following the work of Gebraad et al. [4]. In the present study, the model has been re-implemented with some modifications. First, the model describing expansion, reduction and deflection of a single wind turbine wake is presented. Next, the models that describe wind turbine power extraction and multiple wake interactions are presented. Finally, the process of calculating wind farm flow and power is summarized.

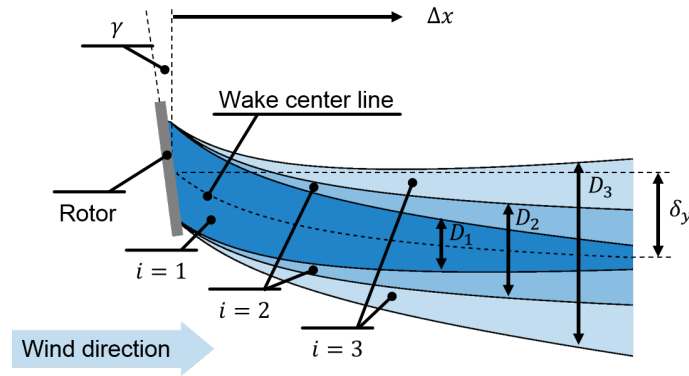


Figure 1. Wake model with three zones.

It is assumed that every wind turbine wake consists of three wake zones, as depicted in figure 1. In the generic wake zone i , the Jensen model [5] is used to describe wake expansion in terms of coefficient $k_{e,i}$. Experimental results suggest that the wake diameter of a turbine operated in a misaligned condition with respect to the wind direction is reduced (see the results section later on in this work). Taking this effect into account, the wake zone outer diameter is defined as

$$D_i(\Delta x, \gamma) = \max\left(0, (D + 2\Delta x k_{e,i}) \cos(\gamma)^{k_{e,\gamma}}\right), \quad (1)$$

where Δx is the distance downstream of the wind turbine, D the rotor diameter, γ the wind turbine yaw-misalignment angle and $k_{e,\gamma}$ a parameter that describes the reduced wake expansion due to wind turbine yaw-misalignment. As the wake zones can have a negative expansion coefficient, the wake diameter has to be limited to positive values.

The wake velocity in each wake zone is described by the Jensen wake model as

$$U_i(\Delta x) = U_\infty \left(1 - r_i(\Delta x)\right), \quad (2)$$

where U_∞ is the ambient free stream velocity and r_i the reduction factor defined as

$$r_i(\Delta x) = 2a \left(\frac{D}{D + 2\Delta x k_{r,i}}\right)^2, \quad (3)$$

where a is the wind turbine induction and $k_{r,i}$ the wake reduction parameter of wake zone i .

The wake center line deflection due to yaw-misalignment is taken into account as described in [4], leading to

$$\delta_y(\Delta x, \gamma) = \frac{C_T(\gamma) \left(15(2k_d \frac{\Delta x}{D} + 1)^4 + C_T(\gamma)^2\right)}{30 \frac{k_d}{D} (2k_d \frac{\Delta x}{D} + 1)^5} - \frac{C_T(\gamma) D \left(15 + C_T(\gamma)^2\right)}{30k_d}, \quad (4)$$

where k_d is the single parameter describing the recovery of the wake flow direction and C_T the turbine thrust coefficient, which in turn is defined as a function of the rotor induction a and the yaw-misalignment as

$$C_T(\gamma) = \frac{1}{2} \cos(\gamma)^2 \sin(\gamma) (4a(1-a)). \quad (5)$$

For calculating the power extracted by a wind turbine, its rotor disk is split into m discrete elements e . The turbine power is obtained by summing up the power extracted in each element

$$P = \sum_{e=1}^m \frac{1}{2} \rho A_e C_P(\gamma) V_e^3, \quad (6)$$

where ρ is the air density, A_e the element area, V_e the wind velocity at the discrete element and $C_P(\gamma)$ the power coefficient expressed as a function of yaw-misalignment as

$$C_P(\gamma) = C_{P,\gamma=0} \cos(\gamma)^{k_p}. \quad (7)$$

Furthermore, $C_{P,\gamma=0}$ is the power coefficient of the turbine operating aligned with the wind, while k_p is the parameter taking into account power reduction due to yaw-misalignment. Speed V_e is calculated based on the wake deficits of all upstream turbines

$$V_e = U_\infty \left(1 - \left(\sum_{w=1}^n r_w^2 \right)^{\frac{1}{2}} \right), \quad (8)$$

where n is the number of wake zones overlapping with the turbine rotor, while r_w the reduction factor of a wake zone impinging the element. In case $n = 0$, no wake is impinging on the element and therefore $V_e = U_\infty$.

The implemented algorithm is organized as follows. First, the power and wake characteristics of the first upwind turbine is calculated. In a second step, the next wind turbine is considered and the wake position, reduction, and expansion of all upwind turbines are interpolated at the given downwind position. Based on this, the turbine power can readily be computed by equation (6) and (8). Finally, the turbine wake is also computed, using equations (1,2) and (4), and the second step is repeated until the last turbine is reached.

3. Results

3.1. Experimental setup

The experiments described in this section were conducted with a scaled wind farm (see figure 2) composed of three identical scaled wind turbine models, longitudinally spaced 4 diameters (D) apart, whose rotor diameter is equal to 1.1 m (in the following named G1s for Generic 1 m diameter rotor), which were already used in other research projects [3, 6, 7]. The models were operated in the boundary-layer test section of the wind tunnel of the Politecnico di Milano, which has a cross-sectional area of 13.84 m by 3.84 m and a length of 36 m. Atmospheric boundary-layer conditions were simulated by the use of spires placed at the chamber inlet. The vertical profile of the longitudinal wind speed was measured prior to testing, resulting in the following best-fitted exponential law

$$U(z) = U_H \left(\frac{z}{z_H} \right)^{0.088}, \quad (9)$$

where $U_H \approx 5.7$ m/s and $z_H = 0.825$ m are the free-stream wind speed at hub height and the elevation of the rotor axis from the ground, respectively. The turbulence intensity (TI) at hub

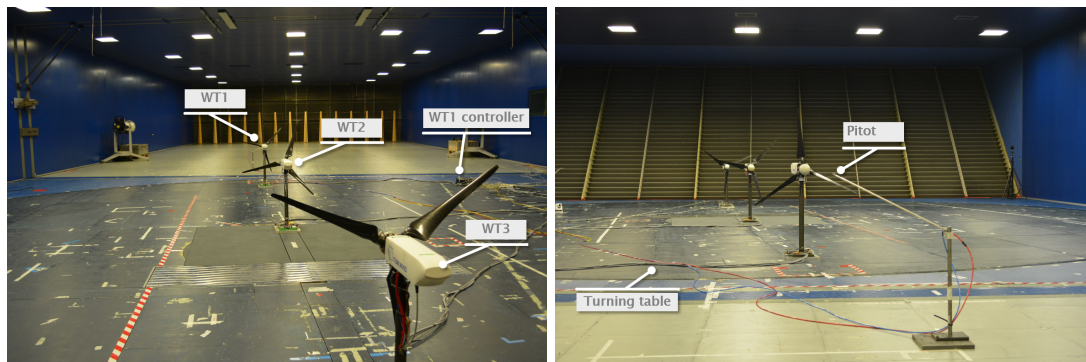


Figure 2. Wind farm layout in the wind tunnel.

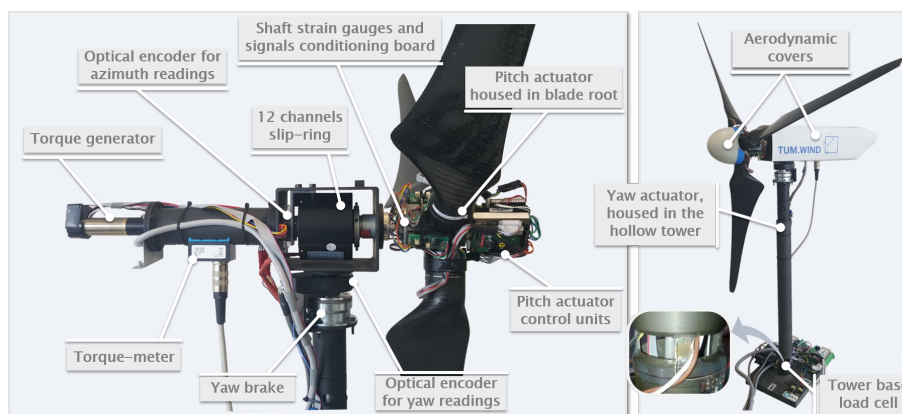


Figure 3. G1 rotor-nacelle assembly (left) and overall model layout (right).

height was circa 5%. The undisturbed wind speed was measured by means of a pitot tube, also shown in figure 2, placed at hub height and 3D in front of the upstream model.

The dimensions of the model (see figure 3) are a compromise among the need for miniaturization, wind tunnel blockage, Reynolds effects and the need to realize multiple wind turbine interference conditions typical of wind farm operations. The scaled wind turbine is characterized by realistic aerodynamic performance, both at the airfoil and rotor levels, and generates a wake with shape, deficit and recovery that match closely the ones of a full scale machine. Moreover, the model features active individual pitch, torque and yaw control that, together with a comprehensive onboard sensorization of the machine (including measures of shaft and tower loads), enables the testing of modern control strategies.

Each model is controlled by a M1 Bachmann module that hard-real-time executes, similarly to what is done on real wind turbines, control laws similar to the ones described in [8] and references therein. In the present study, only operation below rated wind speed was considered. Therefore, the turbines were torque controlled according to a precomputed quadratic relation between rotor speed and torque.

3.2. Model parameter identification

For the identification of the model parameters, the wake velocity of an isolated G1 wind turbine was measured with hot wire probes and compared to model-predicted velocities. In the wind

conditions described above (TI of circa 5%), wake measurements were available at hub height at several downwind distances (3D, 4D, 6D, 9D). In this first set of experiments, no wake measurements in yawed condition had been conducted ($\gamma = 0$). Therefore, a second set of experiments had to be used for identifying the parameters that influence the wake in case of yaw-misalignment ($k_{e,\gamma}$ and k_d). In this second set of experiments, TI was much lower (TI of circa 1%), but the wind turbine was operated with yaw-misalignments between $-20^\circ < \gamma < +20^\circ$. The wake velocity was measured at a distance of 4D downwind of the wind turbine, again at hub height.

For the parameter identification, the hot wire velocity measurements V_{HW} were utilized to solve the minimization problem

$$\min_p \int (V_{HW}(x) - V_M(x,p))^2 dx, \quad (10)$$

where x is the lateral position of the measurement, V_M the model-predicted wake velocity for a set of model parameters p . The problem is solved by the Nelder-Mead simplex direct search algorithm implemented in the MATLAB function `fminsearch`. The wind turbine induction was obtained from a G1 blade element momentum simulation and set to $a = 0.35$ for operation below rated wind speed.

For the first set of experiments, the model parameters to be identified are defined as

$$p_1 = \{k_{e,1}, k_{e,2}, k_{e,3}, k_{r,1}, k_{r,2}, k_{r,3}\}. \quad (11)$$

Figure 4 shows the hot wire measurements $V_{HW}(x)$ (red dashed line) and the model-predicted wake velocity $V_M(x,p)$ (blue solid line) for the identified set of parameters. Only measurements at 4D were utilized for the identification (red solid line). The good quality matching of the profiles at 3D, 6D and 9D, since they were not used for calibrating the model, demonstrate its good generality.

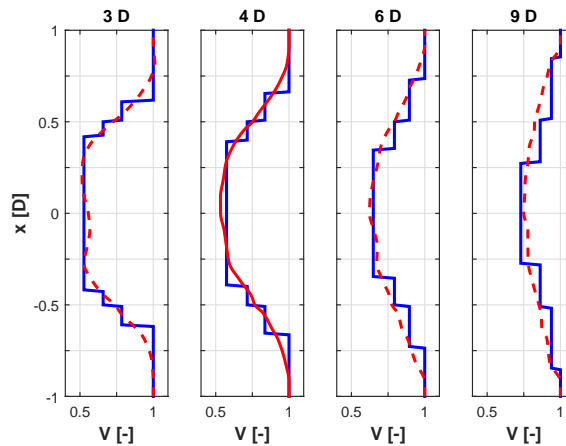


Figure 4. First measurement set (TI circa 5%), modeled (blue solid line) and measured (red solid and dashed lines) wake deficit for different distances behind the wind turbine.

To identify the wake parameters that play a role in turbine yaw-misalignment, the second set of experiments was used and the parameters to be identified by equation (10) were set to be

$$p_2 = \{k_{e,\gamma}, k_d\}. \quad (12)$$

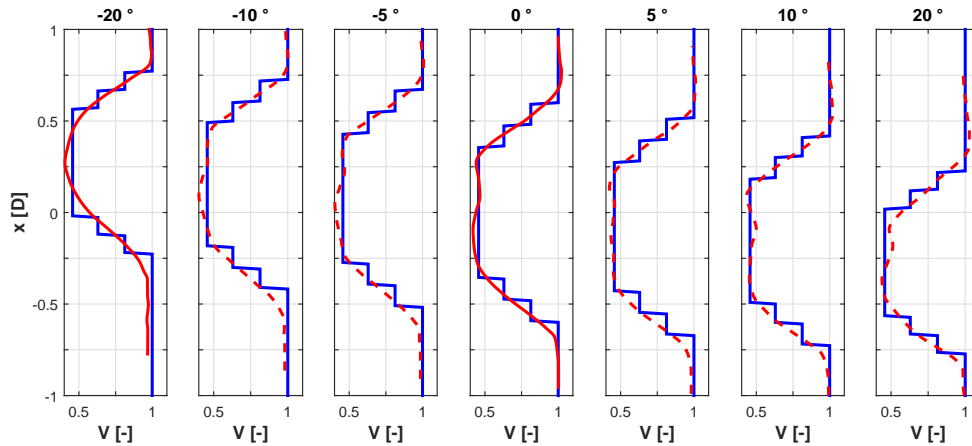


Figure 5. Second measurement set (TI circa 1%), modeled (blue solid line) and measured (red solid and dashed lines) wake deficit for different yaw-misalignments.

The parameters p_1 were re-identified for the low TI case to take the slower wake recovery of this different flow condition into account. Figure 5 shows the hot wire measurements $V_{HW}(x)$ and the model-predicted wake velocity $V_M(x, p)$ for the identified set of parameters. Again, the generality of the wake model is demonstrated by only taking the measurements of $\gamma = -20^\circ$ and $\gamma = 0^\circ$ into account during the identification. Note the wake diameter reduction in the cases characterized by larger yaw-misalignment. The modeled maximum wake diameter for $\gamma = 0^\circ$ is 1.2D, whereas for $\gamma = \pm 20^\circ$ the wake diameter is only 1D, giving a good fit with the wake measurements.

It is assumed that the parameters $k_{e,\gamma}$ and k_d are independent of TI. Therefore, they can be used to describe the wake also for the higher TI cases used in the wind farm experiments.

Parameter k_p was identified based on a subset of the wind farm experiments in which the first turbine yaw-misalignment was $-36^\circ < \gamma < 0^\circ$. In this subset, the first wind turbine experimental power coefficient $C_{P,Exp}(\gamma)$ was calculated based on turbine power measurements and pitot tube measurements 3D in front of the hub, as shown in figure 6 (red circles). The squared error between the measured and modeled power coefficients, given by equation (7), was minimized with respect to the free parameters k_p and $C_{P,\gamma=0}$, yielding the modeled power coefficient shown in figure 6 (blue solid line). Coefficient $C_{P,\gamma=0}$ was included in the free parameters to account for a low precision in the pitot tube measurements.

The full set of identified model parameters is reported in Table 1. For the sake of completeness, Table 1 also reports the identified parameters for low TI, which correspond to Figure 5.

Table 1. Identified model parameters.

	$k_{e,1}$	$k_{e,2}$	$k_{e,3}$	$k_{r,1}$	$k_{r,2}$	$k_{r,3}$	$k_{e,\gamma}$	k_d	k_p
high TI	-0.0251	0.0011	0.0386	0.0320	0.0669	0.2130	2.8808	0.1219	1.7870
low TI	-0.0363	-0.0062	0.0236	0.0140	0.0433	0.1864	2.8808	0.1219	1.7870

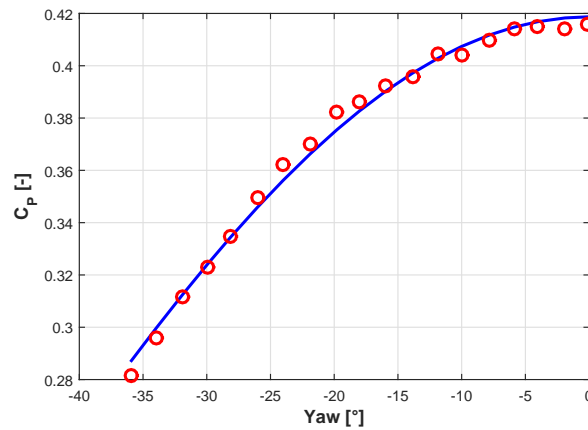


Figure 6. Measured (red circles) and modeled (blue solid line) power coefficients plotted as functions of wind turbine yaw-misalignment.

3.3. Wind farm experiments

In the wind farm experiments, three G1s were operated in the wind tunnel in three different layouts (noted A, B and C) as shown in figure 7. In each layout, the most upwind wind turbine is labeled WT1, the middle turbine is noted WT2, while the most downwind wind turbine is termed WT3. The turbines were torque controlled below rated wind speed, and the reduced order model assumed a constant operation of all turbines with $C_{P,\gamma=0} = 0.419$ and $a = 0.35$.

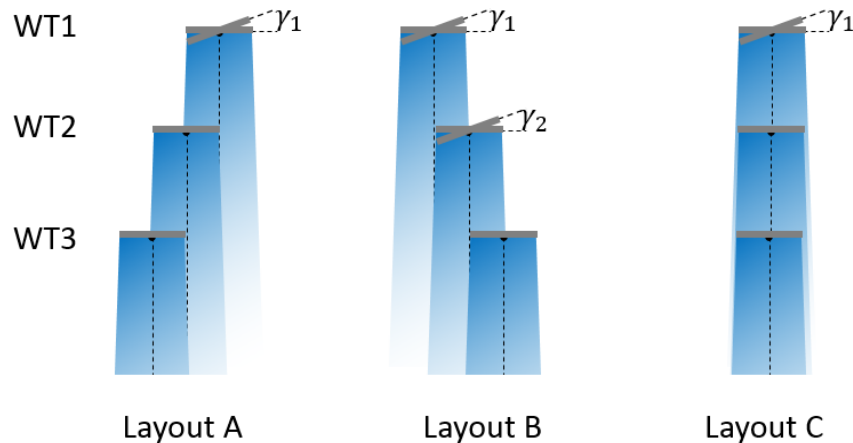


Figure 7. Wind farm layouts A, B, C with lateral displacements of $\pm 0.5D$ and $0D$. The longitudinal displacement is approximately $4D$. Note that the sketch is not to scale.

First, for every layout several experiments were conducted with different yaw-misalignments of WT1 (γ_1), in order to deflect the wake away from the downstream turbines. For these experiments, figure 8 shows the power coefficient of all three wind turbines and the total wind farm in layouts A, B and C, as indicated by the column title. The red circles indicate the measured and the blue solid line the modeled power coefficient, respectively.

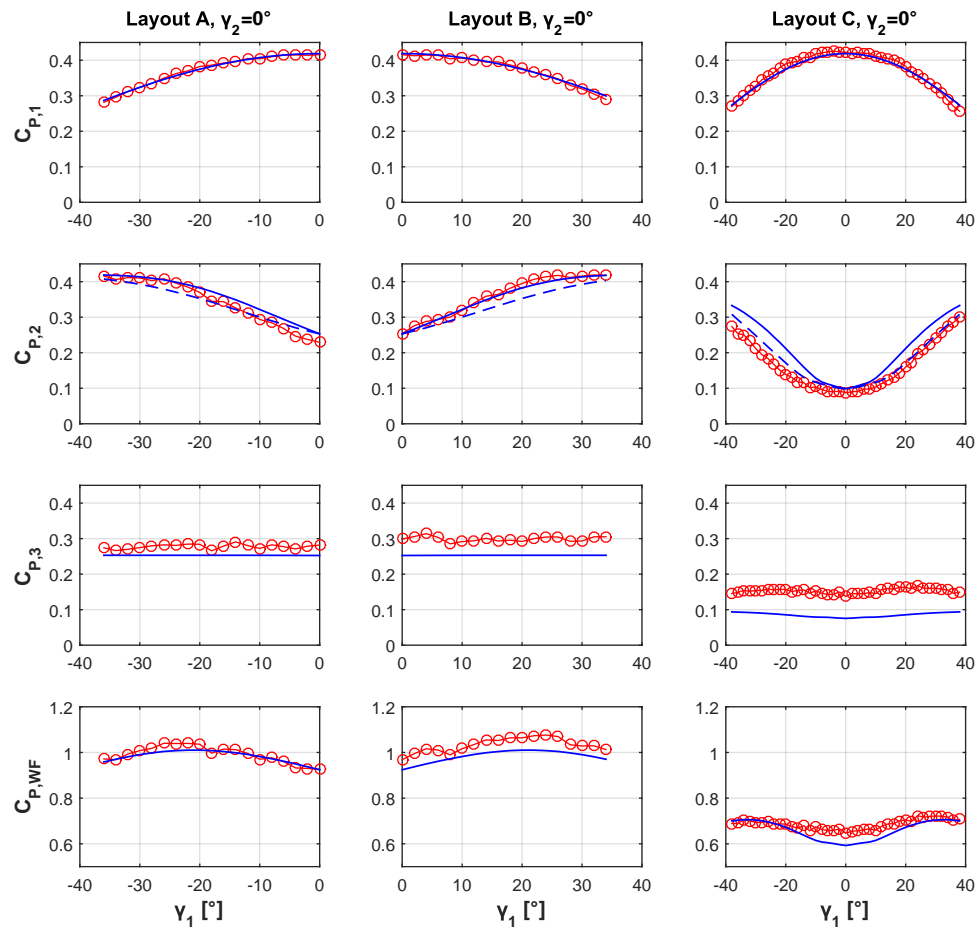


Figure 8. Measured (red circles) and modeled (blue solid line) power coefficient for WT1, WT2, WT3 and the total wind farm, for layouts A, B and C.

The first row of subplots shows the power coefficient of WT1 ($C_{P,1}$) in each layout. As expected from the identification of parameter k_p , the model-predicted and measured results correlate very well.

The second row of subplots shows the power coefficient of WT2 ($C_{P,2}$). For $\gamma_1 = 0^\circ$, the model predicts well the downwind turbine power for all layouts. However, a small asymmetric behavior in the measurements can be observed between the symmetric layouts A and B — perhaps due to asymmetric wake behavior or due to a small horizontal variation in the wind tunnel inflow speed. In the experiments of layout B, maximum power is reached already at $\gamma_1 \approx 25^\circ$ and further upwind turbine yawing does not influence the second wind turbine power anymore. In the full wake case of layout C, the model significantly over-predicts power for $|\gamma_1| > 10^\circ$. A first hypothesis that could explain this behavior is that the model predicts a slightly inaccurate wake location in the yawed cases (which is possible, given that the corresponding parameter was identified at a much lower TI). Indeed, simulations with a larger wake deflection parameter ($k_d = 0.28$, see blue dashed line) show improved results for layout C, but the new parameter

affects also the results in layouts A and B, where now the modeled power coefficient exhibits an increased error. Results in layout C might improve by adjusting the model in such a way that in yaw-misalignment conditions the wake speed decreases or the wake diameter reduces further than currently predicted, but this would worsen the results in layouts A and B. The previously mentioned slight lateral variation in the inflow speed, which cannot be captured by the use of a single pitot tube, could also be a partial cause of the mismatch seen here. It is also possible that the wake deflection position is affected by the downwind turbine position. Understanding the reasons causing these discrepancies will be part of further studies, involving additional wind farm flow measurements.

The third row of subplots shows the power coefficient of WT3 ($C_{P,3}$). In layout A and B, no significant γ_1 -dependency can be observed in the experiments as well as in the model. Nevertheless, the power is constantly under-predicted. The cause might be a faster wake recovery of the wake of WT2 that, operating within the wake of WT1, experiences a higher turbulence intensity, leading to a faster wake mixing. Conversely, a strongly deflected wake (i.e. $|\gamma_1| > 25^\circ$) should in that case also lead to lower power at WT3 — an effect that however is not observed in the experiments. Again, further studies and measurements are necessary to better explain this contradiction. For layout C, the power of WT3 is clearly affected by γ_1 . The model correctly predicts an increase of power for increased γ_1 . However, above $|\gamma_1| > 20^\circ$ the experimental results show a decrease of power, which might be caused by a slower wake recovery of the WT2 wake compared to the full wake case ($\gamma_1 = 0$).

The total power coefficient of all three wind turbines ($C_{P,WF} = C_{P,1} + C_{P,2} + C_{P,3}$) is shown in the last row of figure 8. Taking into account the discrepancies noted above, the overall correlation is rather good. In layouts A and B the predicted power achieves a maximum for $|\gamma_1| = 20^\circ$, which correlates well with the experimental data. In the full wake case, the predicted power is maximum at $|\gamma_1| = 34^\circ$, which again correlates well with the experimental data.

For layout B, experiments were also conducted in which WT2 is operating in yaw-misalignment (γ_2). Figure 9 shows experiments in which WT2 is yawed by $\gamma_2 = 8^\circ$ (first column), $\gamma_2 = 18^\circ$ (second column) and $\gamma_2 = 28^\circ$ (third column). The power of WT1 is again well predicted. For WT2 the modeled and measured power decreases for increased γ_2 , even though the model under-predicts this effect slightly at higher γ_2 . The power of WT3 increases as expected with increased γ_2 . Surprisingly, for $\gamma_2 = 28^\circ$ the WT3 power exceeds the maximum power coefficient in four experiments — possibly due to a flow acceleration just outside of the wakes of WT1 and WT2. The total power of all three turbines follows the trend of the experiments, but the previously observed power over-prediction becomes smaller for increased γ_2 , mainly due to the under estimation at WT2 and the smaller error at WT3.

The full set of experiments, not shown here for brevity, includes all combinations of γ_1 and γ_2 in steps of 2° around the point of maximum power. By using this data, the experimental optimum yaw configuration could be readily identified and was found to be at $\gamma_1 = 20^\circ$ and $\gamma_2 = 16^\circ$. The model-predicted point of maximum wind farm power was on the other hand found to be located at $\gamma_1 = 20^\circ$ and $\gamma_2 = 22^\circ$.

4. Conclusions and outlook

In this paper, the parameters of a reduced order wind farm model were identified with the help of wake measurements along a hub-height horizontal line for an isolated wind turbine. The modeled wakes are in good agreement with the measurements, even though only a small subset of the measurements were taken into account for the model identification procedure.

For three different wind farm layouts, including a variety of yaw angles of the two upstream wind turbines, the model-predicted wind turbine power coefficient was compared with experimental measurements. The comparison shows a good correlation in the overall trends, but the absolute values are not always well predicted especially for the last downstream wind turbine.

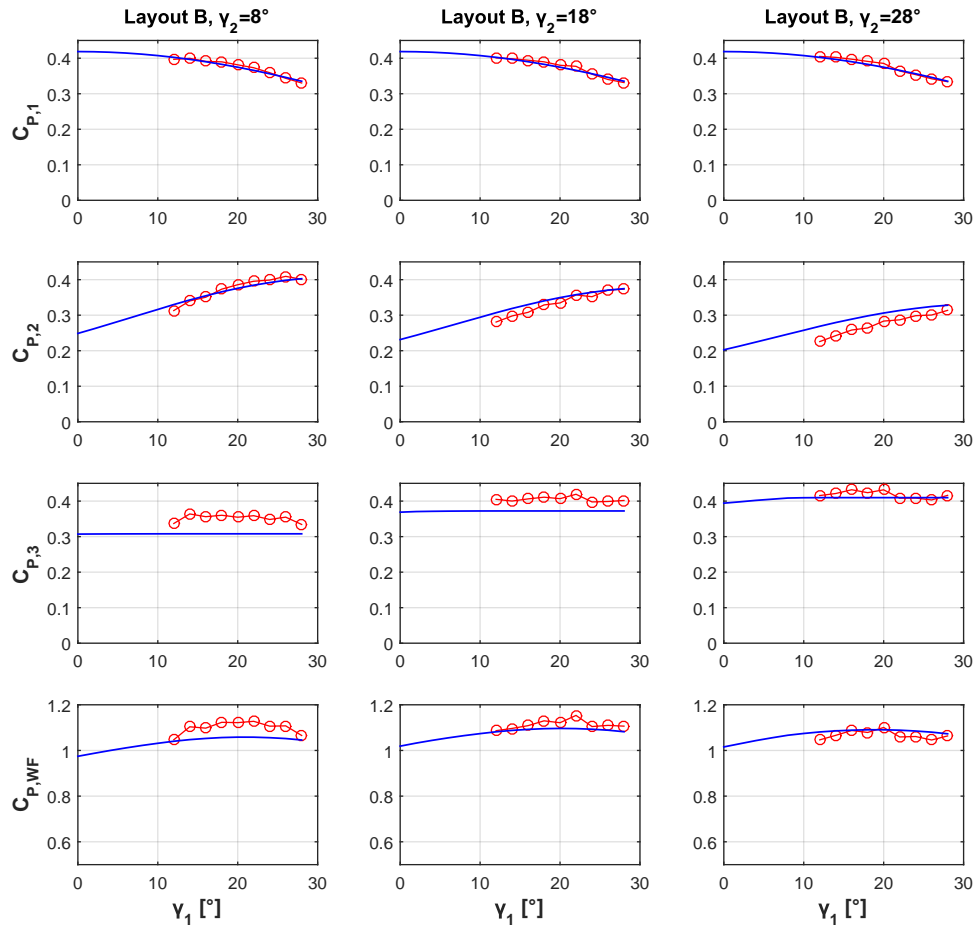


Figure 9. Measured (red circles) and modeled (blue solid line) power coefficient for WT1, WT2, WT3 and the total wind farm, for layout B for different γ_2 values.

The causes are believed to be a combination of various effects, including a faster recovery of wakes shed by waked turbines, flow acceleration outside the wakes, lateral flow speed variations in the wind tunnel, Reynolds number effects in the experiments, the assumption of a uniform power coefficient on each rotor, the assumption of axisymmetric wakes and certainly additional not modeled and fully understood effects like the influence of the downwind turbines on the upstream wake development.

Regardless of these open questions, it is important to note that the employed rather simplistic wind farm model, after a tuning by wake measurements, predicts well the operating point of maximum wind farm power. This is a promising result in view of the use of the model for wind farm control. It is also worth noting that the power gradient is very small around the optimum yaw angles for all studied layouts, implying that for wind farm control purposes a rough estimation of the optimum yaw configuration should be enough to harvest most of its potential.

Future work will try to clarify the open points and improve the model, taking into account

the various deficiencies stated above. In addition, rotor load-based wind estimation and wake detection techniques [9] will be coupled with the model for the development of robust model-based closed-loop wind farm control.

Acknowledgments

The authors wish to thank Dr. Vlaho Petrović for his help in the preparation and realization of the experiments, and Mr. Amr Balbaa for the assistance with the parameter identification.

This research was partially supported by the European Union Horizon 2020 research and innovation program under the Marie Skłodowska-Curie grant agreement No. 642108, and it was also partially supported by the German Federal Ministry for Economic Affairs and Energy (BMWi) within the CompactWind project (FKZ: 0325492D).

References

- [1] Wang J, Bottasso C L and Campagnolo F 2016 Wake redirection: comparison of analytical, numerical and experimental models *Journal of Physics: Conference Series* **753** 32064
- [2] Fleming P A, Gebraad P M O, Lee S, van Wingerden J-W, Johnson K, Churchfield M, Michalakes J, Spalart P and Moriarty P 2014 Evaluating techniques for redirecting turbine wakes using SOWFA *Renewable Energy* **70** 211-8
- [3] Campagnolo F, Petrović V, Schreiber J, Nanos E M, Croce A and Bottasso C L 2016 Wind tunnel testing of a closed-loop wake deflection controller for wind farm power maximization *Journal of Physics: Conference Series* **753** 32006
- [4] Gebraad P M, Teeuwisse F W, Van Wingerden J W, Fleming P A, Ruben S D, Marden J R and Pao L Y 2016 *Wind Energy* **19** 95–114 ISSN 10954244
- [5] Jensen N O 1983 A note on wind generator interaction (Roskilde, Denmark: Risø National Laboratory)
- [6] Campagnolo F, Petrović V, Bottasso, C L and Croce A 2016 Wind tunnel testing of wake control strategies *Proceedings of the American Control Conference* 513–518
- [7] Campagnolo F, Petrović V, Nanos E M, Tan C W, Bottasso C L, Paek I, Kim H and Kim K 2016 Wind tunnel testing of power maximization control strategies applied to a multi-turbine floating wind power platform *Proceedings of the International Offshore and Polar Engineering Conference* 309–316
- [8] Bossanyi, E 2000 The design of closed loop controllers for wind turbines *Wind Energy*, **3** 149–163.
- [9] Schreiber J, Cacciola S, Campagnolo F, Petrović V, Mourembles D and Bottasso C L 2016 Wind shear estimation and wake detection by rotor loads - First wind tunnel verification *Journal of Physics: Conference Series* **753** 32027

Paper 7: Comparison of Analytical Wake Models with Wind Tunnel Data

9.1 Summary

In this work several different analytical wake models are tuned and a comparison of wake velocity, wake deflection and turbulence intensity predictions against wind tunnel measurements is conducted.

For model tuning, hub height wake measurements at different downstream distances of a single scaled G1 wind turbine are employed and a Maximum Likelihood Estimation is used for parameter estimation. Compared to the work presented in **Paper 6**, a more complete data set has been available.

The wake model comparisons base on the same tuning data set and quantify the respective mismatches using a root mean squared relative error. Results show that the Porté-Agel wake model, with only four parameters, is superior to all other investigated wake models.

9.2 Contribution

Within this peer-reviewed publication, the author of this dissertation has supervised and assisted in the technical implementation of the model tuning and comparison. Filippo Campagnolo led the whole research work, conducted the experiments and analysis. Anil Molder conducted the coding and data analysis. Carlo L. Bottasso supervised the whole research. All authors provided important input to this research work through discussions, feedback and by writing the paper.

9.3 Reference

F. Campagnolo, A. Molder, J. Schreiber, and C. L. Bottasso, “Comparison of analytical wake models with wind tunnel data,” *Journal of Physics: Conference Series*, vol. 1256, p. 012006, 2019. doi: 10.1088/1742-6596/1256/1/012006

Comparison of Analytical Wake Models with Wind Tunnel Data

F Campagnolo¹, A Molder¹, J Schreiber¹, C L Bottasso¹

¹ Wind Energy Institute, Technische Universität München, Boltzmannstraße 15, D-85748 Garching bei München, Germany

E-mail: {filippo.campagnolo, anil.molder, johannes.schreiber, carlo.bottasso}@tum.de

Abstract. In this paper a comparison between the wake velocity, wake deflection and turbulence intensity predictions of several wake models was carried out against wind tunnel data obtained with a state-of-the-art scaled wind turbine model. In order to achieve a fair comparison, the models' parameters were all tuned with respect to the same experimental dataset using the Maximum Likelihood Estimation (MLE) method. A quantitative assessment of all models' predictions highlighted that the Porté-Agel model seems to provide, for a wide range of inflow and wind turbine operating conditions, the most accurate estimation of the wake flow field. Further improvements to the model are also suggested in the conclusions.

1. Introduction

In recent years, many research activities have focused on formulating cooperative control strategies for wind turbines that aim at maximizing the power produced by a wind farm. Among the developed strategies, the ones that showed so far the greatest potential are based on de-rating or misaligning, with respect to the wind, the upstream wind turbines [1]. In this regard, many research institutes have developed analytical models to predict the effects that these strategies have on the wake shed by a wind turbine. Many of these models require the calibration of tuning parameters, an activity that implies the availability of experimental data, often obtained through wind tunnel tests, or data obtained by means of CFD simulations. However, the data set used for the calibration of the various models is often heterogeneous: experimental/numerical data, different inflow conditions, different characteristics and operating conditions of the used wind turbine models. All this hampers an objective and quantitative comparison of the accuracy of these models, whose calibration parameters are often optimized for a specific inflow or wind turbine operating condition. This article therefore aims at comparing the prediction of different analytical wake models with data obtained by testing a state-of-the-art wind turbine scaled model in a boundary layer wind tunnel. To this end, and in order to ensure a fair comparison, the models' parameters are all re-tuned using the data itself. This paper is therefore organized as following: at first an overview of the investigated analytical wake models, including the related equations and tunable parameters, is provided in §2. Next, the experimental setup is presented in §3, followed by the description of the approach adopted for the tuning of the parameters, given in §4. Successively, the comparison between the models' predictions and the experimental data is discussed in §5, while the conclusions are drawn in §6.



2. Overview of analytical wake models

2.1. Jensen wake model

The Jensen one-dimensional wake model proposed in [2] is a pioneering work in the field. It assumes a top hat shape of the velocity $U(x)$ within the wake by means of Eq. 1, where the tunable parameter α governs the wake recovery, U_0 is the inflow speed, D_0 is the rotor diameter, x is the downstream distance to the rotor disk and a the rotor axial induction.

$$U(x) = U_0 \left\{ 1 - 2a \left(\frac{D_0}{D_0 + 2\alpha x} \right)^2 \right\}. \quad (1)$$

2.2. Frandsen wake model

The Frandsen [3] wake model also estimates the flow velocity in the wake assuming a top hat shape distribution. Differently than the Jensen model, the wake diameter $D(x)$ and wake expansion coefficient $\alpha(x)$ are calculated as

$$\frac{U(x)}{U_0} = \frac{1}{2} + \frac{1}{2} \sqrt{1 - 2 \frac{D_0^2}{D(x)^2} C_T}, \quad \text{with } \frac{D(x)}{D_0} = (\beta^{k/2} + \alpha s)^{1/k}, \quad (2a)$$

$$\alpha(x) = \beta^{k/2} [(1 + 2\alpha_{(noj)} s)^k - 1] s^{-1}, \quad \text{with } \beta = \frac{1}{2} \frac{1 + \sqrt{1 - C_T}}{\sqrt{1 - C_T}}, \quad (2b)$$

with $s = x/D_0$ and C_T the rotor thrust coefficient, while $\alpha_{(noj)}$ and k are the tunable parameters that govern the wake recovery.

2.3. FLORIS wake model

The FLOW Redirection and Induction in Steady-state (FLORIS) wake model [4] considers the flow within the wake as the superimposition of three wake zones, each characterized by an expansion and decay rates governed by different coefficients, denoted with subscript q in Eqs. 3, in turn function of tunable parameters $m_{e,q}$, $M_{U,q}$, a_U and b_U . The model is also capable of predicting the wake lateral displacement $y_{w,yaw}(x)$ associated to a rotor that operates misaligned, of an angle γ , with respect to the wind direction, as shown in Eqs. 3c-3d, where k_d is a tunable parameter. The overall wake lateral displacement from the rotor centerline $y_w(x)$ also accounts for the combined effect of rotor rotation and wind shear, as shown in Eq. 3e, with a_d and b_d being tunable parameters.

$$D_q(x) = \max(D_0 + 2k_e m_{e,q} x, 0), \quad (3a)$$

$$U(x, r) = U_0 [1 - 2ac(x, r)], \quad \text{with } c(x, r) \text{ function of } c_q(x) = \left[\frac{D_0}{D_0 + 2k_e m_{U,q}(\gamma) x} \right]^2, \quad (3b)$$

$$m_{U,q}(\gamma) = \frac{M_{U,q}}{\cos(a_U + b_U \gamma)}, \quad (3c)$$

$$y_{w,yaw}(x) \approx \frac{\tilde{C}_T(a, \gamma) \left[15 \left[\frac{2xk_d}{D_0} + 1 \right]^4 + \tilde{C}_T(a, \gamma)^2 \right]}{\frac{30k_d}{D_0} \left[\frac{2xk_d}{D_0} + 1 \right]^5}, \quad (3d)$$

$$y_w(x) = y_{w,rot}(x) + y_{w,yaw}(x), \quad \text{with } y_{w,rot}(x) = a_d + b_d x. \quad (3e)$$

2.4. Porté-Agel wake model

The Porté-Agel wake model was firstly proposed in [9], further improved in [10] and presented in its final form in [11]. The model is capable of computing the relative wake deficit $\Delta U/U_0$ in a 3-D domain using Eqs. 4a-4c, where the wake decay rate depends, through the tunable parameters k_a and k_b , to the inflow turbulence intensity. The wake deflection δ associated to misaligned condition is computed with Eq. 4e, which accounts for the the deflection in the near and far wake. The first one is governed by the wake skew angle at the rotor disk θ_{C_0} and by the length of the wake potential core x_0 , which is a function of two tunable parameters α^* and β^* . The wake turbulence intensity is calculated with the model proposed in [12] (Eq. 4g), where $TI_{a,b,c,d}$ are tunable parameters.

$$\frac{\Delta U(x, y, x)}{U_0} = \left(1 - \sqrt{1 - \frac{C_T \cos \gamma}{8(\sigma_y \sigma_z / D_0^2)}}\right) \exp\left(-0.5 \left(\frac{y - \delta}{\sigma_y}\right)^2\right) \exp\left(-0.5 \left(\frac{z - z_h}{\sigma_z}\right)^2\right), \quad (4a)$$

$$\frac{\sigma_y(x, \gamma)}{D_0} = k_y \frac{(x - x_0)}{D_0} + \frac{\cos \gamma}{\sqrt{8}} \quad \text{and} \quad \frac{\sigma_z(x)}{D_0} = k_z \frac{(x - x_0)}{D_0} + \frac{1}{\sqrt{8}}, \quad (4b)$$

$$k_y = k_z = \mathbf{k}_a I_0 + \mathbf{k}_b, \quad (4c)$$

$$\frac{x_0(I_0, \gamma)}{D_0} = \frac{\cos \gamma (1 + \sqrt{1 - C_T})}{\sqrt{2}(\alpha^* I_0 + \beta^* (1 - \sqrt{1 - C_T}))}, \quad (4d)$$

$$\frac{\delta}{D_0} = \theta_{C_0} \frac{x_0}{D_0} + \frac{\theta_{C_0}}{14.7} \sqrt{\frac{\cos \gamma}{k_y k_z C_T}} (2.9 + 1.3\sqrt{1 - C_T} - C_T) \ln \left[\frac{(1.6 + \sqrt{C_T}) \left(1.6 \sqrt{\frac{8\sigma_y \sigma_z}{D_0^2 \cos \gamma}} - \sqrt{C_T}\right)}{(1.6 - \sqrt{C_T}) \left(1.6 \sqrt{\frac{8\sigma_y \sigma_z}{D_0^2 \cos \gamma}} + \sqrt{C_T}\right)} \right], \quad (4e)$$

$$\theta_{C_0}(\gamma) = \frac{0.3\gamma}{\cos \gamma} (1 - \sqrt{1 - C_T \cos \gamma}), \quad (4f)$$

$$I_{wake}^2 = \sqrt{I_0^2 + I_+^2}, \quad \text{with } I_+(I_0, x) = \mathbf{TI}_a a^{\mathbf{TI}_b} I_0^{\mathbf{TI}_c} (x/D_0)^{\mathbf{TI}_d}. \quad (4g)$$

2.5. 2D_k Jensen wake model

The 2D_k Jensen wake model, proposed in [5] and improved in [6], provides equations for modeling the flow velocity and turbulence intensity within the wake. At first the one-dimensional flow velocity is computed using a wake decay coefficient that is proportional, through the tunable parameter k_0 , to both the inflow (I_0) and wake turbulence intensity. The turbulence within the wake is then predicted with the Larsen model [7] (Eq. 5b), where $TI_{a,b}$ are tunable parameters. The 2-D velocity deficit is then approximated by a cosine function (Eq. 5c).

$$u^*(x) = U_0 \left[1 - \frac{1 - \sqrt{1 - C_T}}{\left(1 + \frac{kx}{D_0/2}\right)^2} \right], \quad \text{with } k = \mathbf{k}_0 \frac{I_{wake}}{I_0}, \quad (5a)$$

$$I_{wake} = \sqrt{I_0^2 + I_{add}^2}, \quad \text{with } I_{add}(x) = \mathbf{TI}_a (x/D_0)^{\mathbf{TI}_b} \sqrt{1 - \sqrt{1 - C_T}}, \quad (5b)$$

$$U(x, r) = (U_0 - u^*(x)) \cos\left(\frac{\pi}{r_x} r + \pi\right) + u^*(x), \quad \text{with } r_x = kx + \frac{D_0}{2}. \quad (5c)$$

2.6. Jensen-Gaussian wake model

The Jensen-Gaussian wake model [8] is similar to the previous 2D_k Jensen. The one-dimensional flow velocity is calculated first through the tunable parameters k_0 and K_n , with K_n also affecting the turbulence intensity in the wake, while the velocity distribution, assumed Gaussian, is calculated according to Eq. 6b:

$$u^*(x) = u_0 \left[1 - \frac{2a}{\left(1 + \frac{kx}{r_1}\right)^2} \right], \quad \text{with } k = k_0 \frac{I_{wake}}{I_0}, \quad I_{wake}(x) = \left(K_n \frac{C_T}{(x/D)^{0.5}} + I_0^{0.5} \right), \quad (6a)$$

$$U(x, r) = U_0 - (u_0 - u^*) \frac{5.16}{\sqrt{2\pi}} e^{\frac{-r^2}{2(r_x/2.58)^2}}, \quad \text{with } r_x = kx + r_1 \quad \text{and } r_1 = \frac{D_0}{2} \sqrt{\frac{(1-a)}{(1-2a)}}. \quad (6b)$$

3. Experimental setup

The experimental data were obtained by means of wind tunnel testing. In detail, experiments were conducted in the boundary-layer test section of the Politecnico di Milano wind tunnel using a scaled G1 wind turbine [13]. Two different inflows were simulated: one characterized by a moderate turbulence intensity (mod-TI) equal to 6.1%, and one characterized by high turbulence intensity (high-TI), equal to 11%. The mean undisturbed wind speed, measured at hub height with a pitot tube placed 5D upstream of the G1, was 5.60 and 5.46 m/s, respectively for mod-TI and high-TI inflow.

For both inflows, 11 experimental observations were conducted, each one characterized by a different wind turbine operating condition. Nine observations were performed with the rotor disk misaligned of $\gamma = -40^\circ : 10^\circ : +40^\circ$ with respect to the wind tunnel axis (positive misalignment corresponds to a counter-clockwise rotation from the wind to the rotor axis looking down onto the terrain), while two observations were conducted with the the aligned G1 operated under power de-rating conditions. During each test, a closed-loop wind turbine controller [13] was used to find the optimal rotational speed Ω and collective blade pitch β . Their average values are reported in Table 1 together with the rotor thrust coefficient C_T . These were computed by means of a Blade Element Momentum (BEM) model that makes use of tuned airfoil polars [14], and were extremely close to the thrust coefficients computed using the fore-aft load sensor placed at tower base.

The speed in the wake was measured, at 5D, 7.5D and 10D downwind of the G1, using a hot-wire traversing system [15] and along horizontal lines at hub height, thus generating a total of 66 data sets.

4. Formulation of the tuning method

From the the experimental data-set, average normalized flow velocities and turbulence intensities were derived at specific locations expressed in Cartesian coordinates (x, y, z) . To account for the inhomogeneity of the flow within the wind tunnel [16], the normalized flow velocities were obtained by dividing the average speed in the wake by the corresponding velocity previously measured at the same coordinate (y, z) , but three diameters upstream of the model. In this work, the model outputs $\hat{\mathbf{y}}^i$, associated to the i^{th} experimental observation $\tilde{\mathbf{y}}^i$, are therefore defined as

$$\hat{\mathbf{y}}^i = \left[\dots, \left(\hat{\mathbf{v}}^{i,d} \right)^T, \left(\hat{\mathbf{t}}^{i,d} \right)^T, \dots \right]^T, \quad d = 5D, 7.5D, 10D \quad (7)$$

Table 1. Wind turbine operating conditions for all performed tests with mod-TI and high-TI inflow conditions.

mod-TI, $U_0 = 5.60$ m/s					high-TI, $U_0 = 5.46$ m/s				
Ω [rpm]	β [°]	γ [°]	C_T [-]	ID	Ω [rpm]	β [°]	γ [°]	C_T [-]	ID
806.3	1.42	0	0.79	1	770.6	1.45	0	0.79	12
806.0	1.99	0	0.73	2	773.3	2.05	0	0.73	13
796.1	2.50	0	0.68	3	770.0	2.44	0	0.69	14
656.4	1.42	-40	0.51	4	631.2	1.42	-40	0.51	15
729.4	1.42	-30	0.63	5	693.2	1.42	-30	0.62	16
773.2	1.42	-20	0.72	6	734.8	1.42	-20	0.72	17
798.4	1.42	-10	0.77	7	758.5	1.43	-10	0.77	18
797.6	1.42	10	0.77	8	760.9	1.43	10	0.77	19
774.9	1.42	20	0.71	9	737.8	1.42	20	0.72	20
731.9	1.42	30	0.62	10	696.2	1.42	30	0.62	21
659.4	1.42	40	0.51	11	629.6	1.42	40	0.51	22

where $\hat{\mathbf{v}}^{i,d}$ and $\hat{\mathbf{t}}^{i,d}$ are respectively the normalized velocities and turbulence intensities predicted by a model at a downwind distance d and at the same points where the flow was measured during the experimental campaign.

The tuning process was then carried out in two steps, both requiring the minimization of a cost function, which was performed using MATLAB's `fminsearch`. At first, the adopted cost function (SRE) was defined as

$$SRE = \sum_{i=1}^M \sum_d \left[w_v \sum_{j=1}^{N^{i,d}} \left(\frac{\hat{v}_j^{i,d} - \tilde{v}_j^{i,d}}{\tilde{v}_j^{i,d}} \right)^2 + w_t \sum_{j=1}^{N^{i,d}} \left(\frac{\hat{t}_j^{i,d} - \tilde{t}_j^{i,d}}{\tilde{t}_j^{i,d}} \right)^2 \right], \quad (8)$$

where M is the number of used observations, $N^{i,d}$ is the number of data points measured, for the i^{th} observation, at the downwind distance d , while w_v and w_t are weighting factors. The output of the minimization problem was then used as initial guess for a successive minimization that seeks for a maximum likelihood estimate (MLE) of the models' tunable parameters, an approach that can account for the inevitable presence of various sources of errors and noise in the measurements. To this aim, the adopted cost function was defined, as in [17], equal to

$$J = \frac{Mn}{2} \ln(2\pi) + \frac{M}{2} \ln \det(\mathbf{R}) + \frac{1}{2} \sum_{i=1}^M \mathbf{r}_i^T \mathbf{R}^{-1} \mathbf{r}_i, \quad (9)$$

where \mathbf{R} , the error covariance matrix of the residuals computed as

$$\mathbf{R} = \frac{1}{M} \sum_{i=1}^M \mathbf{r}_i \mathbf{r}_i^T, \quad (10)$$

is nonsingular if M , the dimension of the residual vector \mathbf{r} , is smaller than the number of used observations M . In this regard, the residual \mathbf{r}_i associated to the i^{th} observation was defined as

$$\mathbf{r}_i = \left[\dots, w_v \left\| \left(\frac{\hat{\mathbf{v}}^{i,d} - \tilde{\mathbf{v}}^{i,d}}{\tilde{\mathbf{v}}^{i,d}} \right) \right\| + \sqrt{w_t} f^{i,d} \left(\hat{\mathbf{t}}^{i,d}, \tilde{\mathbf{t}}^{i,d} \right), \dots \right]^T \quad d = 5D, 7.5D, 10D, \quad (11)$$

where the function $f^{i,d}$ was defined as $f^{i,d} = \frac{\overline{\hat{\mathbf{t}}^{i,d}} - \overline{\tilde{\mathbf{t}}^{i,d}}}{\overline{\tilde{\mathbf{t}}^{i,d}}}$ when tuning the Porté-Agel model's parameters, while it was defined as $f^{i,d} = \left\| \left(\frac{\hat{\mathbf{t}}^{i,d} - \tilde{\mathbf{t}}^{i,d}}{\tilde{\mathbf{t}}^{i,d}} \right) \right\|$ when tuning the 2D.k Jensen and Jensen-Gaussian models, with $\overline{\hat{\mathbf{t}}^{i,d}}$ and $\overline{\tilde{\mathbf{t}}^{i,d}}$ respectively the predicted and measured average turbulence within the wake at a distance d .

5. Results

In order to account for the different capabilities of the the various investigated models, different set of observations were used for their parameters' tuning. Moreover, since it is well-known that the inflow turbulence strongly affect the wake decay rate [18], two distinguished set of parameters were tuned using, separately, observations performed with mod-TI and high-TI inflows. However, only a single set of the Porté-Agel model's parameters was tuned, using observations pertaining to both inflows. This model, indeed, already accounts, through Eq. 4c, for the relationship between the inflow turbulence and the wake recovery. Despite the 2D.k Jensen and Jensen-Gaussian models also account for this relationship (Eqs. 5a and 6a), preliminary verifications showed that a single set of tunable parameters would have provided poor predictions of the speed in the wake.

Table 2. Models' tuned parameters.

	mod-TI			high-TI		
Jensen	$\alpha = 0.033$			$\alpha = 0.047$		
Frandsen	$\alpha_{(noj)} = 0.008$	$k = 3.023$		$\alpha_{(noj)} = 0.020$	$k = 1.740$	
FLORIS	$M_{U,1} = 0.227$ $m_{e,1} = -0.694$ $k_d = 0.105$ $a_U = 13.551$	$M_{U,2} = 0.719$ $m_{e,2} = 0.369$ $a_d = -0.071$ $b_U = -0.112$	$M_{U,3} = 2.341$ $m_{e,3} = 0.876$ $b_d = 0.014$	$M_{U,1} = 0.388$ $m_{e,1} = -0.646$ $k_d = 0.168$ $a_U = 7.666$	$M_{U,2} = 0.692$ $m_{e,2} = 0.250$ $a_d = -0.077$ $b_U = 0.040$	$M_{U,3} = 1.809$ $m_{e,3} = 1.097$ $b_d = 0.011$
2D.k Jensen	$k_0 = 0.0343$	$TI_a = 0.1252$	$TI_b = -0.0287$	$k_0 = 0.0524$	$TI_a = 0.3624$	$TI_b = -0.5998$
Jensen-Gaus.	$k_0 = 0.0307$	$Kn = 0.2628$		$k_0 = 0.0879$	$Kn = 0.141$	
Porté-Agel	$k_a = 0.089, k_b = 0.027, \alpha = 0.952, \beta = 0.262, TI_a = 0.082, TI_b = 0.608, TI_c = -0.551, TI_d = -0.277$					

The parameters of the Jensen, Frandsen, 2D.k Jensen and Jensen-Gaussian models were calibrated using observations obtained with the aligned wind turbine rotor (ID 1-3 for mod-TI, ID 12-14 for high-TI, see Table 1). Concerning the FLORIS model, the parameters that govern the wake deficit were tuned first using the non-yawed cases, while the parameters that govern the wake deflection were tuned after, using the observations gathered with a misaligned wind turbine (ID 1/4-11 for mod-TI, ID 12/15-22 for high-TI). Concerning the weighting factors w_v and w_t of Eqs. 8 and 11, they were set respectively equal to 1 and 0 when tuning the parameters of those models that do not provide sub-models for the turbulence intensity prediction, while they were set respectively equal to 1 and 0.1 when tuning the parameters of the 2D.k Jensen and Jensen-Gaussian models. These two models, indeed, make use of prediction of the turbulence intensity within the wake to estimate its deficit; an higher value of w_v was then used to guide the optimizer toward the research of a set of parameters that provide a better estimation of the wake velocity deficit, rather than a proper estimation of its turbulence intensity. Concerning the tuning of the parameters of the Porté-Agel model, those that govern the wake deficit/deflection were tuned first, setting $w_v = 1$ and $w_t = 0$, and using all observations except the ones with $\gamma = \pm 40^\circ$. Successively, the parameters of the turbulence sub-models were tuned, setting $w_v = 0$ and $w_t = 1$, and using observations obtained with the aligned wind turbine rotor. The resulting tuned parameters are reported in Table 2.

5.1. Comparison between experiments and models' predictions

Figures 1 and 2 depict the models' predicted normalized flow velocity and the corresponding measurement data for the non-yawed cases, and for moderate and high turbulence intensity inflow conditions, respectively.

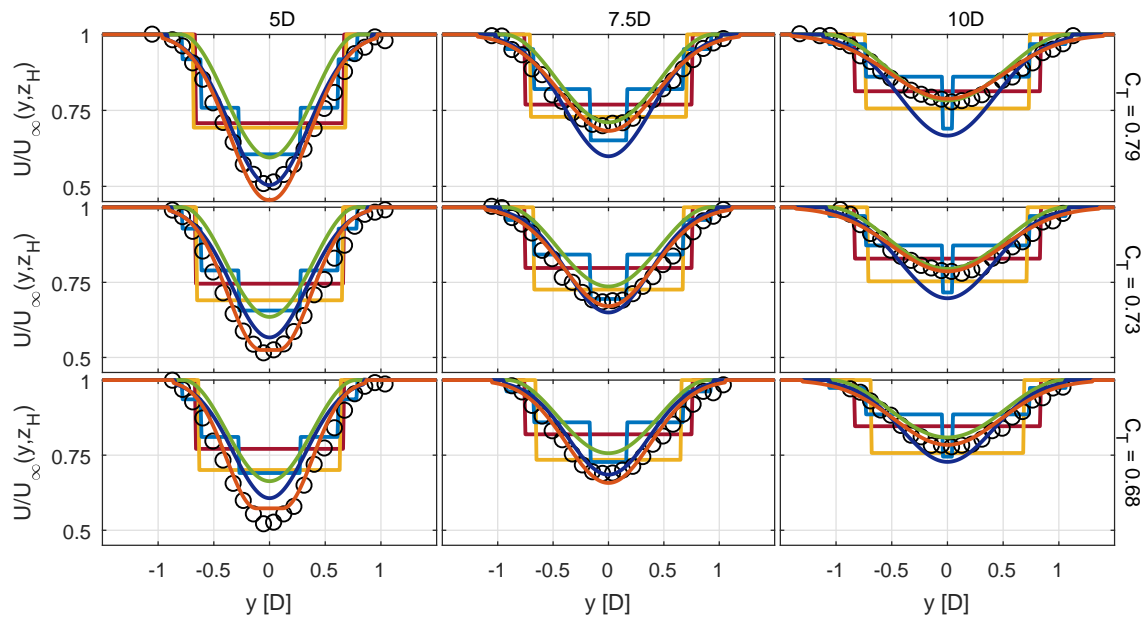


Figure 1. Flow velocity estimations for the Jensen (—), Frandsen (—), FLORIS (—), 2D.k Jensen (—), Jensen-Gaussian (—) and Porté-Agel (—) models compared to wind tunnel measurements (o) performed at hub height, with mod-TI inflow, null yaw misalignment and three C_T settings (ID 1-3).

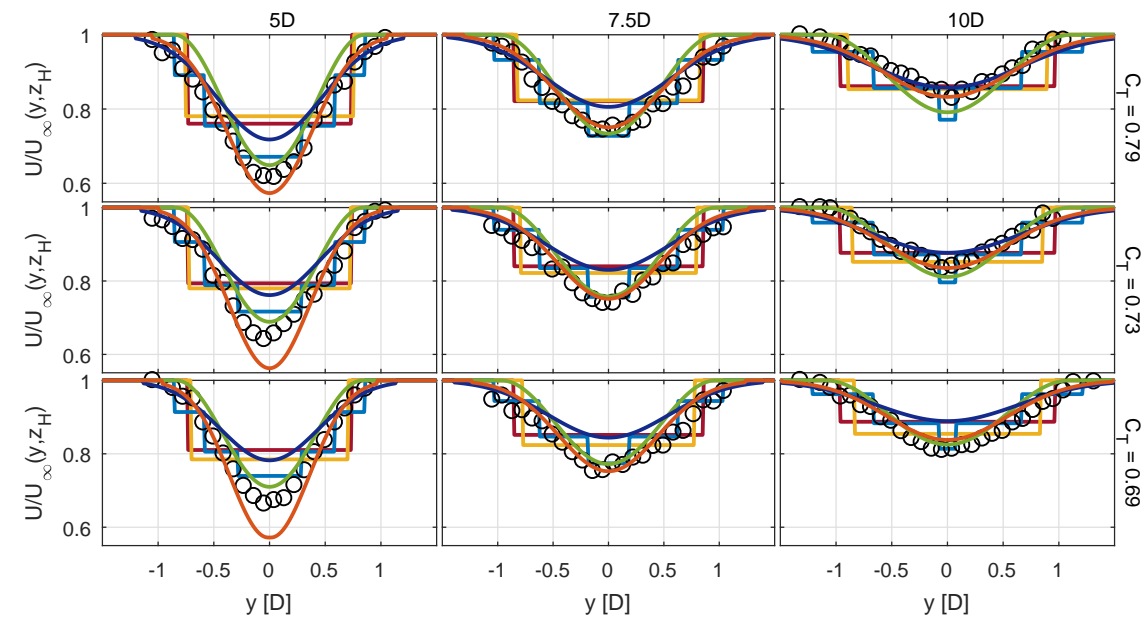


Figure 2. Flow velocity estimations for the Jensen (—), Frandsen (—), FLORIS (—), 2D.k Jensen (—), Jensen-Gaussian (—) and Porté-Agel (—) models compared to wind tunnel measurements (o) performed at hub height, with high-TI inflow, null yaw misalignment and three C_T settings (ID 12-14).

The plots highlight that the Jensen and Frandsen models' predictions are quite inaccurate, especially for mod-TI inflow, while the predictions of the other models are quite satisfactory, particularly for high-TI inflow. Quite outstanding are the wind speed estimations of the Porté-Agel model, especially for mod-TI inflow conditions, while it seems that the same model is overestimating the wake deficit at 5D for high-TI inflow and with the wind turbine operating under de-rated power conditions.

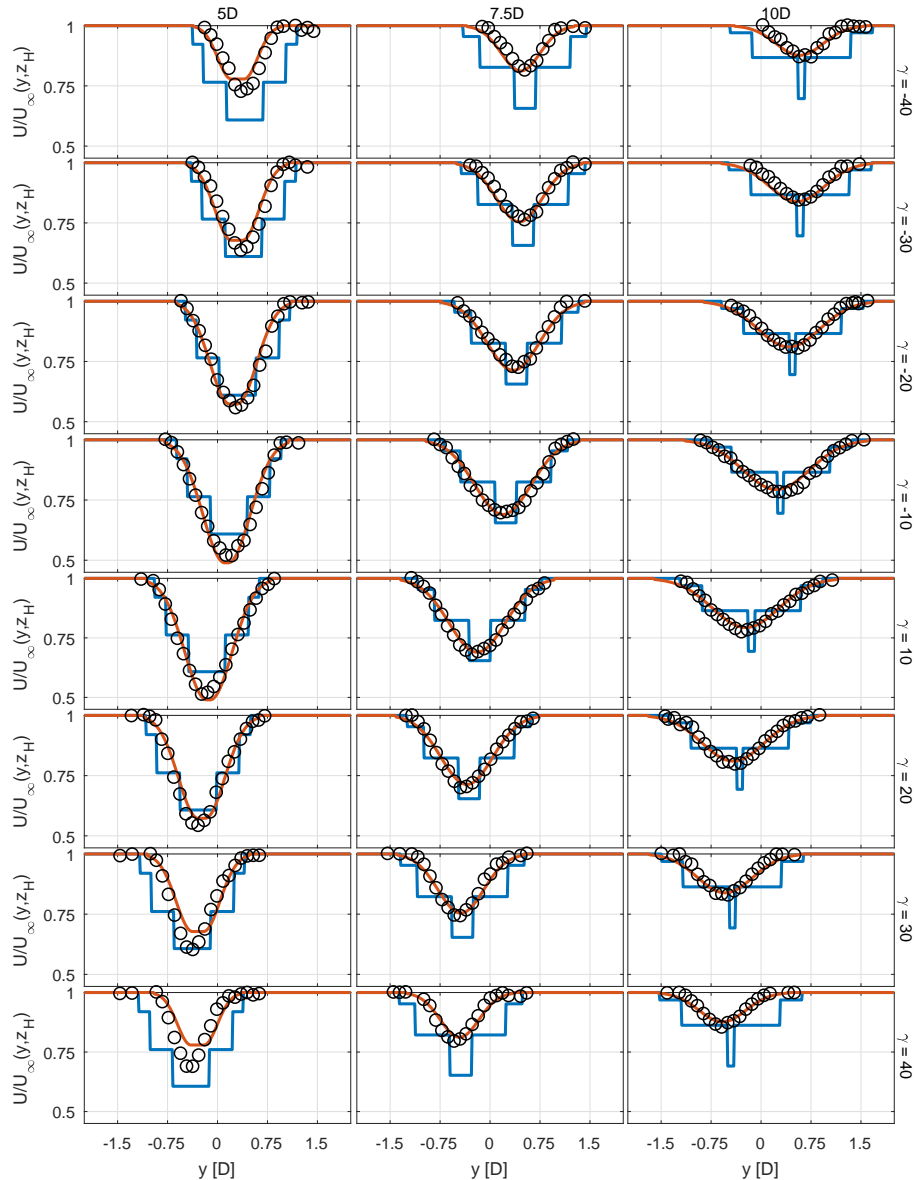


Figure 3. Flow velocity estimations for the FLORIS (—) and Porté-Agel (—) models compared to wind tunnel measurements (o) performed at hub height, mod-TI inflow, $\gamma = -40:10:10$ & $10:10:40$ (ID 4-11).

Since only the FLORIS and Porté-Agel models are capable of predicting the wake deflection

due to yaw-misaligned conditions, Figs. 3 and 4 report, respectively for mod-TI and high-TI inflow conditions, the comparison between the experimental data and the normalized wake speed estimated by these two models when the G1 was yawed of $\gamma = \pm 40, \pm 30, \pm 20, \pm 10$.

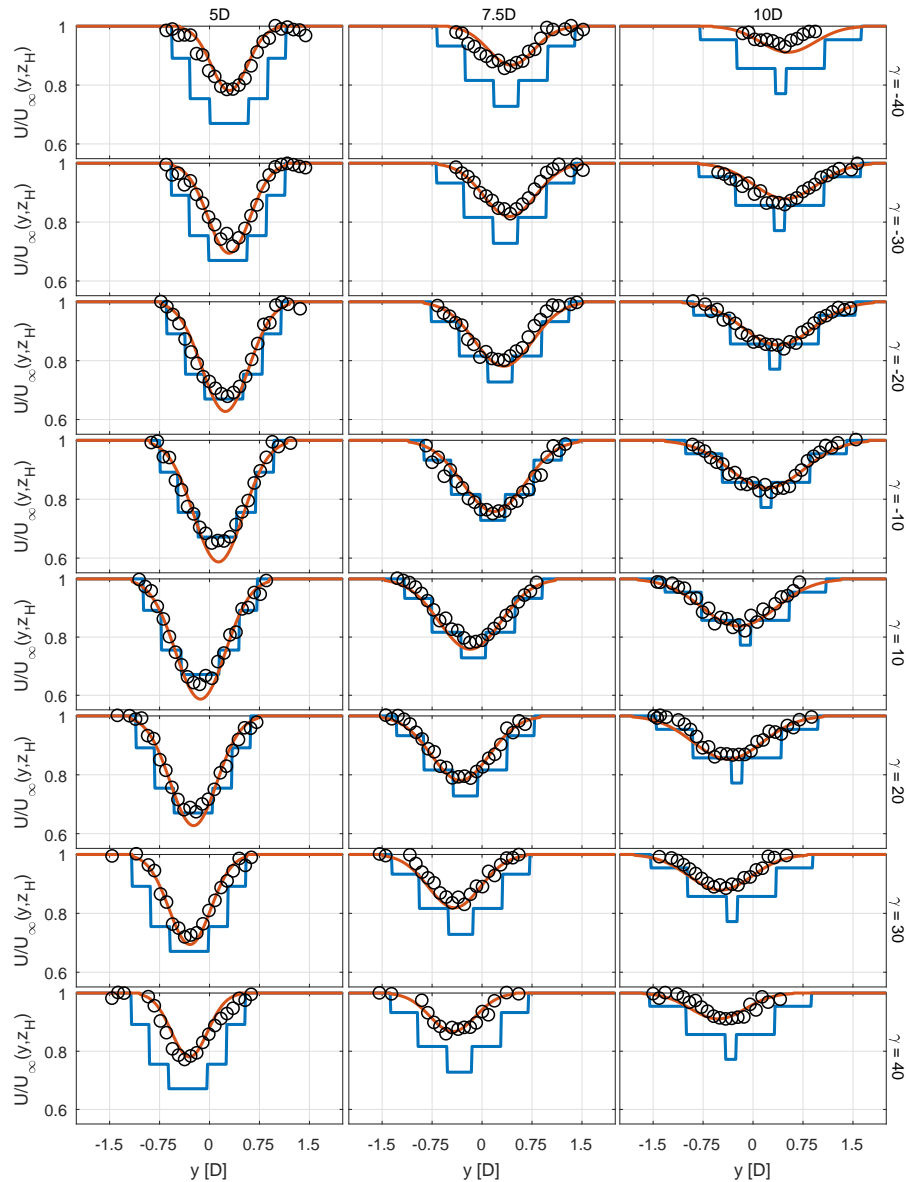


Figure 4. Flow velocity estimations for the FLORIS (—) and Porté-Agel (—) models compared to wind tunnel measurements (o) performed at hub height, high-TI inflow, $\gamma = -40:10:-10$ & $10:10:40$ (ID 15-22).

The plots within the figures allow to appreciate the impact of yaw misaligned operations on the wake shed by the scaled wind turbine model: as expected, as higher the misalignment is, as lower is the wake velocity deficit and higher is the wake deflection. Concerning the models' predictions, both the FLORIS and Porté-Agel are quite accurate, specially for γ between the

range of $\pm 20^\circ$. The FLORIS model seems however less accurate for $\gamma = \pm 30^\circ$, and quite inaccurate for those conditions characterized by very high yaw misalignment, i.e with $\gamma = \pm 40^\circ$. The Porté-Agel's prediction are overall outstanding, despite a moderate mismatch with the experimental observations can be observed for $\gamma = \pm 40^\circ$ and mod-TI inflow conditions.

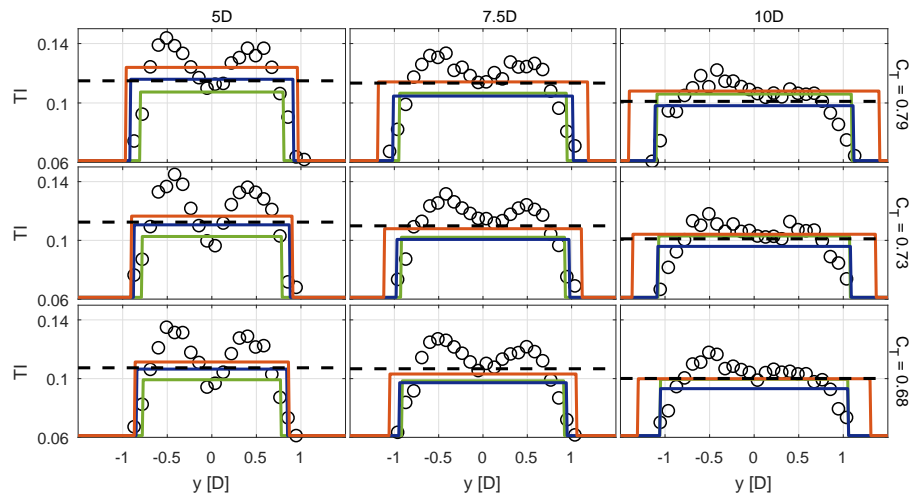


Figure 5. Turbulence intensity estimations for the 2D_k Jensen (—), Jensen-Gaussian (—) and Porté-Agel (—) models compared to wind tunnel measurements (o) performed at hub height, with mod-TI inflow, null yaw misalignment and three C_T settings (ID 1-3). The experimental average turbulence intensity within the wake is reported with a black dashed line.

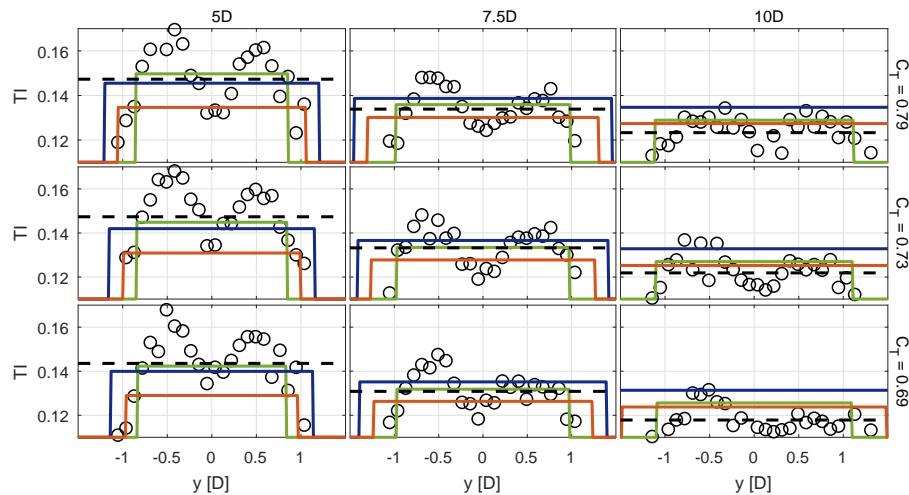


Figure 6. Turbulence intensity estimations for the 2D_k Jensen (—), Jensen-Gaussian (—) and Porté-Agel (—) models compared to wind tunnel measurements (o) performed at hub height, with high-TI inflow, null yaw misalignment and three C_T settings (ID 12-14). The experimental average turbulence intensity within the wake is reported with a black dashed line.

Three of the investigated models (2D_k Jensen, Jensen-Gaussian and Porté-Agel) are also

capable of estimating the turbulence intensity within the wake. These are compared to the experimental observations in Figs. 5 and 6. Since all models assume a spatially constant turbulence, they are not capable of correctly reproducing the distribution of the turbulence along the horizontal line. In any case, it is possible to evaluate the accuracy of the three models in predicting the average value of the wake turbulence, whose experimental data is also reported in the subplots. In this sense, all three models produce satisfactory estimates for low-TI inflow, with the Porté-Agel model that seems to perform slightly better than the others. However, the data related to the high-TI inflow show that the 2D_k Jensen model is more effective than the other two in predicting the wake turbulence at 5D, while predictions for greater distances tend to get closer. It seems, in fact, that the Jensen-Gaussian and Porté-Agel models are not able to properly estimate the rate of decrease of the turbulence in the wake associated with its speed recovery.

5.2. Overall assessment of the models' accuracy

In order to quantitatively assess the average accuracy of the investigated models, in terms of prediction of the wake speed, deflection and turbulence intensity for all tested conditions, three average Root Mean Squared Relative Error (RMSRE) were calculated as

$$\text{RMSRE}_v = \frac{1}{M} \sum_{i=1}^M \sqrt{\frac{1}{3} \sum_d \frac{1}{N^{i,d}} \sum_{j=1}^{N^{i,d}} \left(\frac{\hat{v}_j^{i,d} - \tilde{v}_j^{i,d}}{\tilde{v}_j^{i,d}} \right)^2}, \quad (12a)$$

$$\text{RMSRE}_t = \frac{1}{M} \sum_{i=1}^M \sqrt{\frac{1}{3} \sum_d \left(\frac{\hat{\bar{t}}^{i,d} - \tilde{\bar{t}}^{i,d}}{\tilde{\bar{t}}^{i,d}} \right)^2}. \quad (12b)$$

In particular, six RMSRE_v were computed, for all models, using prediction and observations related to all the non-yawed cases. Similarly, two RMSRE_v were computed, for the FLORIS and Porté-Agel models, using prediction and observations related to all the yawed cases. Finally, three RMSRE_t were computed using data related to all the non-yawed cases.

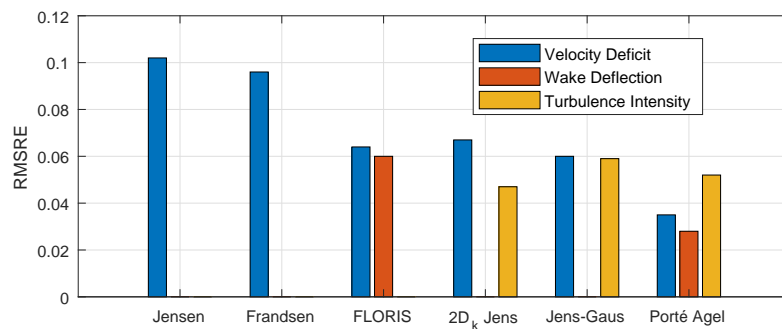


Figure 7. Average RMSRE of model estimations for velocity deficit, wake deflection and turbulence intensity.

The obtained RMSRE, reported in Fig. 7, confirm the observations discussed in the previous section. The Porté-Agel model, indeed, provide the best predictions of the velocity deficit and wake deflection. However, different conclusions can be given by looking at the accuracy of the turbulence intensity predictions: in this case, indeed, the 2D_k Jensen model exhibits the best performance.

6. Conclusions and outlook

The comparison between the experimental data and the numerical predictions, as well as the overall evaluation of the accuracy of the various models, allows to conclude that the Porté-Agel model seems to be the most accurate in terms of prediction of the wake speed and deflection related to a wide range of inflow and wind turbine operating conditions (thrust coefficient and yaw misalignment). Moreover, the model tuning requires the identification of solely four parameters, i.e. less than all the other models except the Jensen-Gaussian, which, however, do not provide estimation of the wake deflection.

However, further improvements could still be added to the model. One of this could be accounting, as suggested by [19], for the dependency of the wake decay rate to the operating thrust coefficient by modifying Eq. 4c into

$$k_y = k_z = \mathbf{k}_a I_0 + \mathbf{k}_b + \mathbf{k}_c C_T. \quad (13)$$

By utilizing this approach, a new set of parameters ($k_a=0.054$, $k_b=0.025$, $k_c=0.003$, $\alpha=1.642$, $\beta=0.155$) can be found, leading to a reduction, from 0.0350 to 0.0281, of the RMSRE_v related to all the non-yawed cases. Finally, another minor improvement to the Porté-Agel would be the implementation of a difference turbulence intensity sub-model, like the one of 2D.k Jensen model. A better prediction of the turbulence in the wake would lead, in fact, to a better prediction of the recovery associated to a wake shed by a downstream turbine.

Acknowledgments

This work has been supported by the CL-WINDCON project, which receives funding from the European Union Horizon 2020 research and innovation program under grant agreement No. 727477.

References

- [1] Knudsen T, Bak T and Svenstrup M 2015 *Wind Energy* **18** 1333-1351
- [2] Jensen, N O 1983 A note on wind generator interaction
- [3] Frandsen, S, Barthelmie, R, Pryor, S, Rathmann, O, Larsen, S, Højstrup, J, and Thgersen, M (2006). *Wind Energy: An International Journal for Progress and Applications in Wind Power Conversion Technology* **9(12)** 39-53
- [4] Gebraad, P M, Teeuwisse, F W, Van Wingerden, J W, Fleming, P A, Ruben, S D, Marden, J R, and Pao, L Y 2014 *In American Control Conference (ACC)* 3128-3134
- [5] Tian, L, Zhu, W, Shen, W, Zhao, N, and Shen, Z 2015 *Journal of Wind Engineering and Industrial Aerodynamics*, **137** 90-99
- [6] Tian, L, Zhu, W, Shen, W, Song, Y, and Zhao, N 2017 *Renewable Energy* **102** 457-46
- [7] Larsen, G C, Højstrup, J, and Madsen, H A 1996 *EWEC 1996 Proceedings*
- [8] Gao, X, Yang, H, and Lu, L 2016 *Applied Energy* **174** 192-200
- [9] Bastankhah, M, and Porté-Agel, F 2014 *Renewable Energy* **70** 116-123
- [10] Niayifar, A, and Porté-Agel, F 2015 *J. Phys. Conf. Ser.* **625** 012039
- [11] Bastankhah, M, and Porté-Agel, F 2016 *Journal of Fluid Mechanics* **806** 506-541
- [12] Crespo, A, and Herna, J 1996 *Journal of wind engineering and industrial aerodynamics* **61(1)** 71-85
- [13] Campagnolo F, Petrović, V, Schreiber, J, Nanos, E M and Bottasso, C L 2016 *J. Phys. Conf. Ser.* **753(3)** 032006
- [14] Bottasso, C L, Cacciola, S, and Iriarte, X 2014 *Journal of wind engineering and industrial aerodynamics* **124** 2945.
- [15] Bottasso, C L, Campagnolo, F and Petrović, V 2014 *Journal of wind engineering and industrial aerodynamics* **127** 1128.
- [16] Wang, J, Foley, S, Nanos, E, Yu, T, Campagnolo, F, Bottasso, C, Zanotti, A, and Croce, A 2017 *J. Phys. Conf. Ser.* **854** 012048
- [17] Jategaonkar, R V 2015 *American Institute of Aeronautics and Astronautics, Inc.*
- [18] Göçmen, T, Van der Laan, P, Réthoré, P-E, Diaz, A P, Larsen, G C, and Ott, S 2016 *Renewable and Sustainable Energy Reviews* **60** 752769
- [19] Campagnolo, F, Petrović, V, Bottasso, C L and Croce, A 2016 *In American Control Conference (ACC)* 513-518

Paper 8: Wind shear estimation and wake detection by rotor loads – First wind tunnel verification

10.1 Summary

This work builds upon **Papers 1, 2 and 3**, and extends the load-based wake detection to also estimate the exact position of an impinging wake. In details, the new method uses two different load-based turbine inflow estimates: a rotor-effective horizontal inflow shear estimate, which is computed from the sector-effective wind speed estimates, and a rotor-effective wind speed estimate. A wake model, in this work for simplicity solely based on experimental single turbine wake measurements, is used to generate corresponding reference values as function of lateral wake position. An optimization problem is formulated as minimization of the difference between load-based inflow estimates and wake model references as function of wake position. Its solution is the wake position estimate.

The method is tested within the paper on a scaled wind turbine of type G2 that is installed within a boundary layer wind tunnel 4 diameters behind an upstream turbine. The sensing turbine is operated in 12 different lateral displacements, to simulate a variety of different wake positions. Results, also taking into account the effect of possible load-based inflow estimation errors, show a robust wake position estimation.

10.2 Contribution

Within this peer-reviewed publication, the author of this dissertation has developed the methodology and conducted the main analysis. The experiments have been conducted by Filippo Campagnolo and Vlaho Petrović. Stefano Cacciola and Delphine Mourembles supported the analysis. Carlo Bottasso supervised the whole research. The discussion of results and the writing of the publication was shared in equal parts among all authors.

10.3 Reference

J. Schreiber, S. Cacciola, F. Campagnolo, V. Petrović, D. Mourembles, and C. L. Bottasso, “Wind shear estimation and wake detection by rotor loads — first wind tunnel verification,” *Journal of Physics: Conference Series*, vol. 753, p. 032027, 2016. doi: 10.1088/1742-6596/753/3/032027

Wind shear estimation and wake detection by rotor loads — First wind tunnel verification

J Schreiber¹, S Cacciola¹, F Campagnolo¹, V Petrović¹,
D Mourembles¹, C L Bottasso^{1,2}

¹ Wind Energy Institute, Technische Universität München, Boltzmannstraße 15, D-85748 Garching bei München, Germany

² Dipartimento di Scienze e Tecnologie Aerospaziali, Politecnico di Milano, Via La Masa 34, I-20156 Milano, Italy

E-mail: {johannes.schreiber, stefano.cacciola, filippo.campagnolo, vlaho.petrovic, carlo.bottasso}@tum.de

Abstract. The paper describes a simple method for detecting presence and location of a wake affecting a downstream wind turbine operating in a wind power plant. First, the local wind speed and shear experienced by the wind turbine are estimated by the use of rotor loads and other standard wind turbine response data. Then, a simple wake deficit model is used to determine the lateral position of the wake with respect to the affected rotor. The method is verified in a boundary layer wind tunnel using two instrumented scaled wind turbine models, demonstrating its effectiveness.

1. Introduction

The wake shed by a wind turbine is mainly characterized by a lower wind speed and higher turbulence intensity than the free stream. In a wind farm environment, a wake can adversely affect other downwind turbines, leading to reduced power output and increased fatigue loads. It has been suggested that there is a large potential in wind farm control (WFC) by means of active wake deflection or wake management [1]. For example, using a WFC algorithm for wake deflection by yawing, a CFD simulation study showed a possible increase of power production for a specific favourable configuration of more than 10% [2]. Wind tunnel experiments confirm that a power increase of the same magnitude can indeed be achieved [3]. If brought to maturity and eventually deployed in the field, such technology has the potential of leading to significant increases in energy capture and reduced loading, and might also impact the way wind power plants are designed.

Knowing the wind conditions within a wind farm is of major importance for any WFC algorithm. In fact, wake management may lead to a positive outcome if one knows the correct location of the affecting wake. On the contrary, an erroneous knowledge of the conditions may lead to a detrimental effect on power, loads, or both.

The wake position in a wind farm depends on the ambient wind direction, the conditions of the atmosphere and the neighboring orography of the terrain, and the possible misalignment of the turbine with the wind. There are several methods to measure wind characteristics. However, nacelle sensors or met-masts provide only point-wise measurements, which might not be sufficient for enabling sophisticated wind farm control. Scanning LiDAR systems on the other hand might



very effectively map the flow field, but they are not available in most wind farms yet. Another approach uses the rotor response to estimate wind properties. Based on the turbine power or torque, the rotor effective wind speed can be estimated, which gives an indication of the mean wind speed at each turbine [4]. In addition, it was shown that shear can be also detected by a linearized wind turbine model [5] or by a data driven approach based on blade load harmonics, a method that can also estimate wind direction [6, 7].

In this paper a method is proposed for estimating the position of a wake relative to an affected wind turbine rotor. The method first estimates the local wind speed and horizontal shear using measured blade root bending moments, as more fully described in Ref. [8]. Then, by using a model of the wake deficit, the wake position is determined. The paper first formulates the proposed approach and then experimentally demonstrates it by using scaled wind turbines operated in a large boundary layer wind tunnel. Experiments included several different operating conditions, characterized by different degrees of wake interference between an upstream and a downstream wind turbine. Results give evidence of the fact that the horizontal shear and relative wake position experienced by a waked turbine can be estimated in operation.

2. Formulation

The method relies on measurements of the blade root bending moments, which are typically available on modern MW-turbines. By the definition of a cone coefficient, these loads are correlated with the local effective (LE) wind speed at the rotor blade. This is a similar approach to the well-known method based on the power coefficient, where torque is correlated with the rotor effective wind speed.

The cone coefficient is defined as

$$C_{m_0}(\lambda_{LE}, \beta, q) = \frac{m(\psi)}{\frac{1}{2}\rho ARV_{LE}^2}, \quad (1)$$

where λ_{LE} is the local effective tip speed ratio, β the pitch angle, q the dynamic pressure, m the out-of-plane root bending moment of the blade occupying the azimuthal position ψ , V_{LE} the local effective wind speed, ρ the density of air, A the rotor disc area and R the rotor radius. Based on the knowledge of the measured loads and other operational parameters, Eq. (1) can be solved at every time instant for the V_{LE} wind speed.

Next, the LE wind speed of each blade can be used to calculate average velocities in predefined non-rotating sectors on the rotor disc. By choosing four equally sized quadrants, four sector effective (SE) wind speed estimates on the rotor disc (left, right, top and bottom quadrant) can be inferred.

The observed SE wind speed can be further processed to estimate a horizontal shear coefficient κ_{lin} , defined by

$$V(y) = V_h \left(1 + \kappa_{lin} \frac{y}{R}\right), \quad (2)$$

where $V(y)$ is the longitudinal wind speed at the lateral position y , and V_h the wind speed at the hub. For linear shear profiles, it was shown that the SE speed represents the wind speed sampled at about $2/3R$ [8]. Assuming that the hub wind speed is known through a rotor effective (RE) wind speed estimate ($V_h \approx V_{RE}$), one can then infer the linear horizontal shear coefficient $\kappa_{lin,obs}$ as

$$\kappa_{lin,obs}(t) = \frac{V_{SE,left}(t) - V_{SE,right}(t)}{4/3V_{RE}(t)}. \quad (3)$$

Based on the knowledge of wind conditions as the ambient turbulence intensity (TI) and wind speed, engineering wake models [9] can be used to estimate the wake shape and its speed deficit. In turn, one can calculate the expected shear $\kappa_{lin,exp}(d)$ and expected rotor effective wind speed

$V_{\text{RE,exp}}(d)$ that a turbine operating within the wake at a given lateral distance d to the wake center should be exposed to. The idea is then to match expected and observed shear and rotor effective wind speed, in order to estimate the lateral distance d of the wake. This is obtained by solving the following optimization problem

$$\min_d \left(\begin{bmatrix} V_{\text{RE,obs}} - V_{\text{RE,exp}}(d) \\ \kappa_{\text{lin,obs}} - \kappa_{\text{lin,exp}}(d) \end{bmatrix}^T \begin{bmatrix} \frac{c}{V_\infty^2} & 0 \\ 0 & \frac{1-c}{\kappa_{\text{ref}}^2} \end{bmatrix} \begin{bmatrix} V_{\text{RE,obs}} - V_{\text{RE,exp}}(d) \\ \kappa_{\text{lin,obs}} - \kappa_{\text{lin,exp}}(d) \end{bmatrix} \right), \quad (4)$$

where scaling is performed by weights based on the mean ambient wind speed V_∞ and a reference shear κ_{ref} , while $c \in [0, 1]$ allows one to give more emphasis to one term or the other. For example, the actual value of V_∞ can be set to the low pass filtered RE wind speed estimation of the first row of wind turbines, while κ_{ref} can be set to the maximum expected shear.

3. Results

The present method was verified with two scaled wind turbines (termed G2s, for Generic wind turbine, 2 m diameter) operated in one-to-one interference conditions within in the boundary layer wind tunnel of the Politecnico di Milano [10].

Each G2 is managed by a torque-pitch controller and a supervisory system, similarly to a full scale machine. The G2 wind turbine has a hub height of 1.7 m, and a rated rotor speed of 380 rpm (clockwise rotation). The machine is equipped with three blades each housing, in the hollow root, its own pitch actuator commanded by an electronic control board mounted on the shaft. The shaft rotates on two bearings, held by a rectangular carrying box and it is instrumented with strain gages to measure torsional and bending loads. Similarly, each blade root is equipped with strain gages that measure bending moments. The transmission of all electrical signals from the rotating system to the fixed one and vice versa is provided by a slip ring. At the tower base a balance provides measurements of the three force and three moment components. The general arrangement of a one-to-one interference condition realized with two G2s is shown in Fig. 1.

The rotor blades were designed using special low-Reynolds airfoils. The aerodynamic performance of the rotors was measured, for different values of the airfoil Reynolds numbers, by operating the models at several combinations of tip speed ratio (TSR) λ and collective pitch settings β . Measurements were then corrected for wall blockage [10]. Non-negligible differences were observed between the experimentally measured and theoretical Blade Element Momentum (BEM)-based rotor aerodynamic performance computed using nominal polars. To correct for this problem, an identification procedure [11] was used to calibrate the nominal airfoil polars obtained by other authors from wind tunnel measurements or numerical simulations. Based on this calibrated polars, the cone coefficient of the turbines was computed with an aeroelastic turbine model implemented in the simulation environment Cp-Lambda [12].

The ambient wind tunnel mean wind speed was measured with a pitot tube and set to $\bar{V} = 4.8$ m/s, which represents an operating condition below rated wind speed. By placing spires at the wind tunnel inlet, a turbulent flow characterized by a TI of 8% and a vertical shear with power law exponent $\kappa = 0.26$ could be modeled. The second turbine was placed four diameters (4D) downwind of the first turbine at different lateral displacements.

To establish the reference against which to compare observations, this study directly utilizes wake measurements instead of an engineering wake model. In order to define the expected shear $\kappa_{\text{lin,exp}}(d)$ and wind speed $V_{\text{RE,exp}}(d)$, the mean wake wind speed was measured 4D downstream of an isolated turbine along a horizontal line at hub height, by using triple hot wire probes. Figure 2a shows the nondimensional longitudinal wind speed measurements, together with a symmetric Gaussian fit. Therein, each measurement point represents a 60-second recording at a sampling frequency of 100 Hz. The wake center is located at a small lateral distance

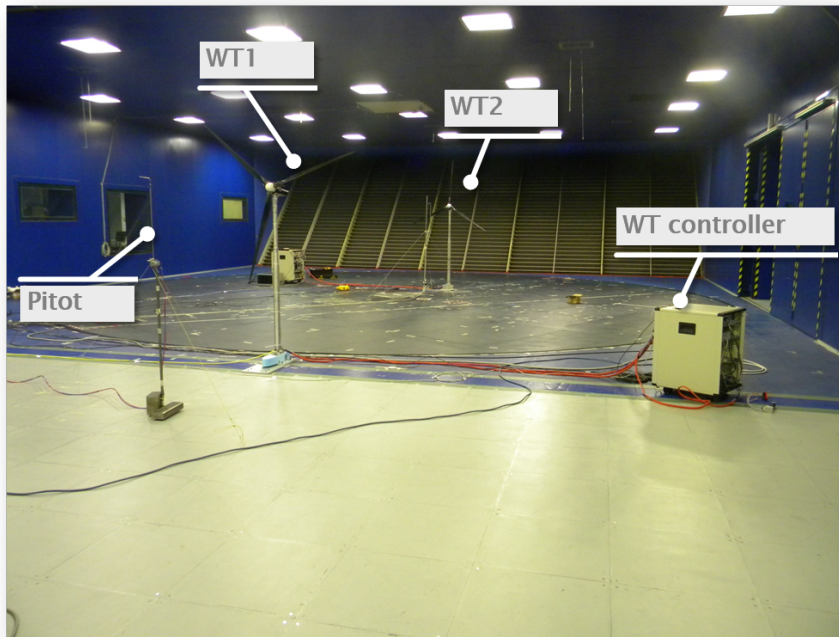


Figure 1: G2 models for one-to-one interference conditions.

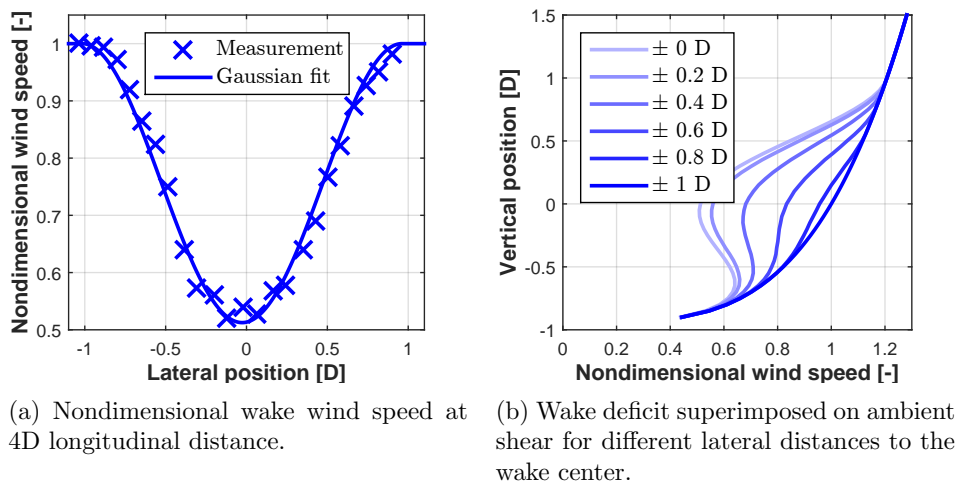


Figure 2: Wake measurements and symmetric wake modeling.

$d_0 = -0.03 D$ with respect to the upwind turbine. This translation is believed to be caused by several effects, including the complex aerodynamic interaction between wake rotation and vertical shear as well as the up-tilt of the turbine. Assuming a rotationally symmetric wake, the Gaussian fit is superimposed to the ambient shear as shown in Fig. 2b. Based on this wake shape, a least squares algorithm is used to calculate the expected shear $\kappa_{\text{lin,exp}}(d)$ and wind speed $V_{\text{RE,exp}}(d)$ that should be experienced by a turbine operating in that wake at a given

lateral displacement to the wake center d .

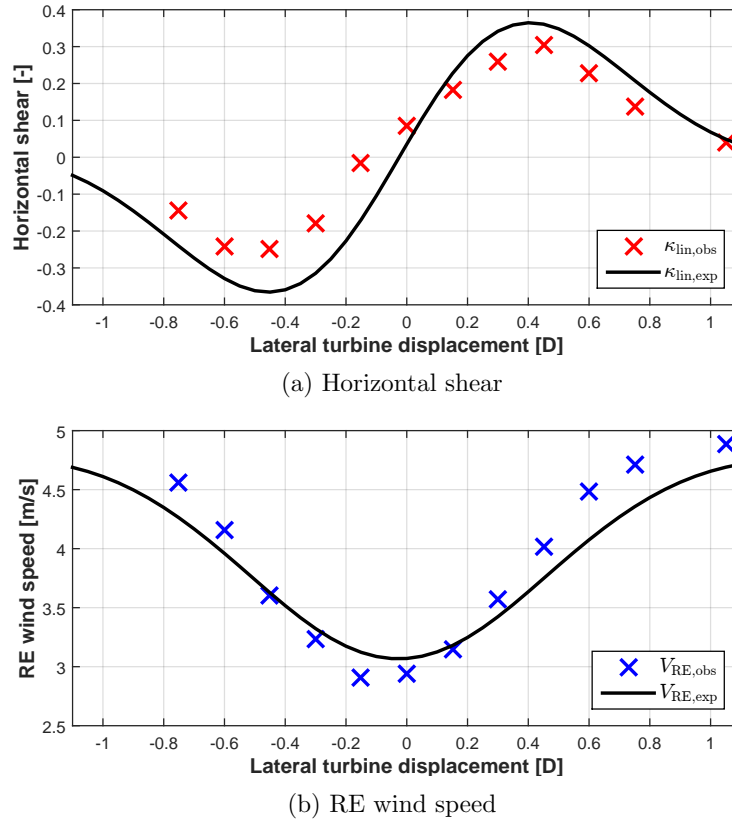
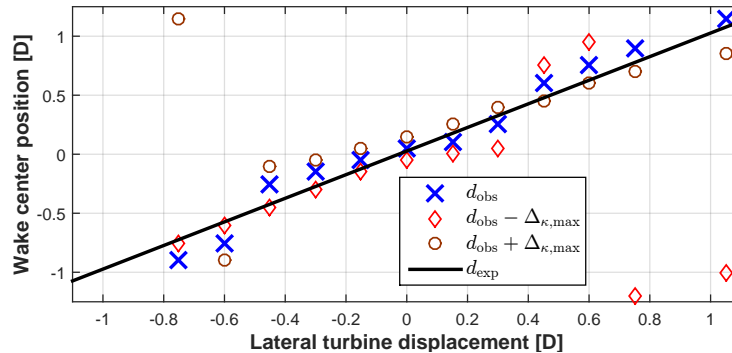


Figure 3: Estimated and expected wind properties for a turbine operating in the wake of an upstream turbine at different lateral turbine displacements.

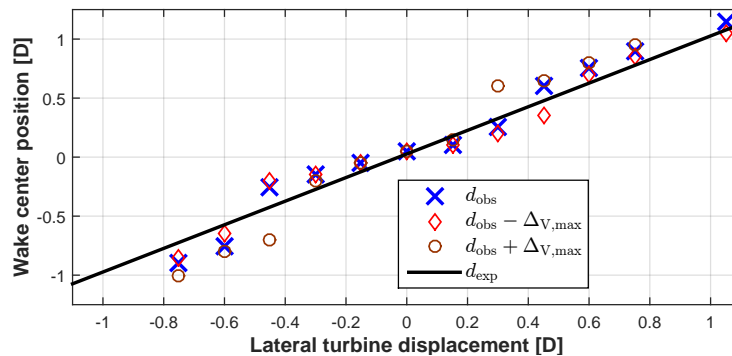
Figure 3a shows the expected shear $\kappa_{lin,exp}$ as a function of the lateral turbine displacement. For a turbine displacement of 0D the expected shear is slightly positive due to the small lateral displacement of the wake center described above. For 12 different lateral downwind turbine displacements, the average observed horizontal shear $\kappa_{lin,obs}$ (see Eq. (3)) is also displayed. The expected and observed shear correlate well, even though the observed absolute values tend to be smaller than the expected ones (maximum absolute error $\Delta_{\kappa,max} = 0.15$). This might be caused by estimation errors as well as by the simple approach used here for modeling the wake. Most importantly, the downwind turbine itself certainly affects the wake development, so that the expected wind properties used by the algorithm might differ from the real ones.

Figure 3b shows the expected and observed RE wind speed using the torque balance estimation. Both show a good correlation, but small errors are present also in this case ($\Delta_{V,max} = 0.40$ m/s), due to the same reasons noted above.

By solving Eq. (4) (with $V_{\infty} = 4.8$ m/s, $\kappa_{ref} = 0.3$ and $c = 0.5$) the wake center position d_{obs} can be estimated. Results are reported in Fig. 4a using blue cross symbols. In addition, the same plot reports results obtained by polluting the shear estimates with errors of $\pm\Delta_{\kappa,max}$. As a reference, the figure plots also the expected wake center position d_{exp} , which is the sum of the lateral turbine displacement and d_0 . As expected, a significant error in shear estimation can lead to a wake center position estimate on the wrong side of the wind turbine, especially for a



(a) Wake center position with pollution in observed shear.



(b) Wake center position with pollution in observed RE wind speed.

Figure 4: Estimated and expected wake center position at different lateral turbine displacements.

large lateral turbine displacement. Nevertheless, in most instances the observed and expected wake positions correlate well.

Figure 4b shows the observed RE wind speed, including the effects of errors of $\pm\Delta_{V, max}$. Here again, the observed and expected wake positions correlate well.

4. Conclusions and outlook

The paper has presented a simple algorithm to determine the lateral position of a wake impinging on a wind turbine. Experimental results obtained in a large boundary layer wind tunnel show that the estimated wake center position correlates well with the expected one even in the face of uncertainties, showing the robustness of the presented method.

Estimation errors are likely to be caused by the reference wake characteristics used for detecting the position of the wake. In fact these quantities were here based on the symmetric wake model of an isolated wind turbine, while it is clear that the real wake is not exactly symmetric and it is in general distorted by the interaction with the downstream machine. The hypothesis that reference quantities are the main culprit of estimation errors is supported by a recent simulation study [13] which, not being affected by such effects, was in fact able to achieve very accurate wake position estimates. To overcome these uncertainties, results from wind tunnel experiments with a scanning LiDAR will be used in a continuation of this work, together with an ongoing CFD simulation study.

Acknowledgments

This research was supported by the German Federal Ministry for Economic Affairs and Energy (BMWi) within the CompactWind project.

References

- [1] Knudsen T, Bak T and Svenstrup M 2015 *Wind Energy* **18** 1333–1351 ISSN 10954244
- [2] Gebraad P M, Teeuwisse F W, Van Wingerden J W, Fleming P A, Ruben S D, Marden J R and Pao L Y 2016 *Wind Energy* **19** 95–114 ISSN 10954244
- [3] Campagnolo F, Petrović V, Schreiber J and Bottasso C L 2016 Closed loop wind farm control - a wind tunnel experiment (*in preparation*).
- [4] Soltani M N, Knudsen T, Svenstrup M, Wisniewski R, Brath P, Ortega R and Johnson K 2013 *IEEE T. Contr. Syst. Techn.* **21** 1155–1167 ISSN 10636536
- [5] Simley E and Pao L Y 2016 *Wind Energy* **19** 167–184 ISSN 10954244
- [6] Bottasso C L and Riboldi C E 2014 *Renew. Energy* **62** 293–302 ISSN 09601481
- [7] Cacciola S, Bottasso C L and Bertelè M 2016 Simultaneous observation of wind shears and misalignments from rotor loads, TORQUE 2016, *The Science of Making Torque from Wind*, Garching bei München, Germany, Oct. 5–7, 2016.
- [8] Bottasso C L, Cacciola S and Schreiber S 2016 Wind speed sensing and wake detection from rotor loads *Renew. Energy* (*under review*)
- [9] Renkema DJ 2007 Validation of wind turbine wake models. Delft University of Technology. Master thesis.
- [10] Bottasso C L, Campagnolo F and Petrović V 2014 Wind tunnel testing of scaled wind turbine models: Beyond aerodynamics *Journal of Wind Engineering and Industrial Aerodynamics* **127** 11–28 ISSN 01676105
- [11] Bottasso C L, Cacciola S and Iriarte X 2014 Calibration of wind turbine lifting line models from rotor loads *Journal of Wind Engineering and Industrial Aerodynamics* **124** 29–45 ISSN 01676105
- [12] Bottasso C L, Croce A, Cp-Lambda users's manual, Tech. rep., Dipartimento di Scienze e Tecnologie Aerospaziali, Politecnico di Milano (2006-2016).
- [13] Cacciola S, Bertelè M, Schreiber J and Bottasso C L 2016 Wake center position tracking using downstream wind turbine hub loads, TORQUE 2016, *The Science of Making Torque from Wind*, Garching bei München, Germany, Oct. 5–7, 2016.

Paper 9: Improving wind farm flow models by learning from operational data

11.1 Summary

This work is a continuation of **Papers 6** and **7**, which use dedicated flow measurements for model tuning. As such measurements are in real plants typically not available or very costly, this work describes a method to calibrate and correct an analytical wind farm model using operational data. In details, error terms are surgically inserted into the model equations and its parameters are learnt from operational data. Following the method, a baseline model, that often represents reality with already good accuracy, can be improved and even effects that are not present in the baseline model can be accounted for. Examples of those effects include non-uniform wind farm inflow, potentially due to orographic effects, and secondary steering.

Different to **Papers 8** and **11**, which combine wind sensing and wind farm models for wake detection, the presented method is not using the local wind estimation methods, even though an inclusion within the formulation is straight forward and likely to improve performance. The decision is driven by the fact that wind farm operators, that are expected to be the main user of the presented method, usually do not have access to the numerical turbine models that are required for local wind estimation. Indeed, in this work only the turbine power, that is available through standard SCADA systems is used and still a significant improvement of the wind farm model predictions is obtained.

Results are first shown for a scaled wind farm within a wind tunnel that allows detailed and extended measurements to verify that indeed the correct error terms are identified. Note that within the wind farm control experiments in **Paper 12** the here improved model shows better results than the baseline model. Finally, the method is applied to a real wind farm in complex terrain and the improved model prediction is demonstrated.

11.2 Contribution

Within this peer-reviewed publication, the author of this dissertation has conducted the main research work. Carlo L. Bottasso developed the core idea of model augmentation, its formulation and the overall solution methodology, and supervised the whole research. The author of this dissertation and Carlo L. Bottasso wrote the manuscript. Bastian Salbert pre-processed the field measurements. Filippo Campagnolo was responsible for the execution of the wind tunnel tests. All authors provided important input to this research work through discussions, feedback and improving the manuscript.

11.3 Reference

J. Schreiber, C. L. Bottasso, B. Salbert, and F. Campagnolo, "Improving wind farm flow models by learning from operational data," *Wind Energy Science*, vol. 5, no. 2, pp. 647–673, 2020. doi: 10.5194/wes-5-647-2020

Wind Energ. Sci., 5, 647–673, 2020
<https://doi.org/10.5194/wes-5-647-2020>
© Author(s) 2020. This work is distributed under
the Creative Commons Attribution 4.0 License.



Improving wind farm flow models by learning from operational data

Johannes Schreiber, Carlo L. Bottasso, Bastian Salbert, and Filippo Campagnolo

Wind Energy Institute, Technische Universität München, 85748 Garching bei München, Germany

Correspondence: Carlo L. Bottasso (carlo.bottasso@tum.de)

Received: 20 November 2019 – Discussion started: 2 December 2019

Revised: 31 March 2020 – Accepted: 20 April 2020 – Published: 27 May 2020

Abstract. This paper describes a method to improve and correct an engineering wind farm flow model by using operational data. Wind farm models represent an approximation of reality and therefore often lack accuracy and suffer from unmodeled physical effects. It is shown here that, by surgically inserting error terms in the model equations and learning the associated parameters from operational data, the performance of a baseline model can be improved significantly. Compared to a purely data-driven approach, the resulting model encapsulates prior knowledge beyond that contained in the training data set, which has a number of advantages. To assure a wide applicability of the method – also including existing assets – learning here is purely driven by standard operational (SCADA) data. The proposed method is demonstrated first using a cluster of three scaled wind turbines operated in a boundary layer wind tunnel. Given that inflow, wakes, and operational conditions can be precisely measured in the repeatable and controllable environment of the wind tunnel, this first application serves the purpose of showing that the correct error terms can indeed be identified. Next, the method is applied to a real wind farm situated in a complex terrain environment. Here again learning from operational data is shown to improve the prediction capabilities of the baseline model.

1 Introduction

Knowledge of the flow at the rotor disk of each wind turbine in a wind power plant enables several applications, including wind farm control, the provision of grid services, predictive maintenance, the estimation of life consumption, the feed-in to digital twins, and power forecasting, among others.

This paper describes a new method to improve a wind farm flow model directly from standard operational data. The main idea pursued here is to use an existing wind farm flow model to provide a baseline predictive capability; however, as all models contain approximations and may lack the description of some physical phenomena, the baseline model is improved (or “augmented”, which is the term used in this work) by adding parametric correction terms. In turn, these extra elements of the model are learned by using operational data. The correction terms capture effects that are typically not present in standard flow models (such as, for example, secondary steering, Fleming et al., 2018; or wind farm blockage, Blegg et al., 2018) or that are highly dependent on a specific site or

difficult to model upfront (such as, for example, nonuniform inflow caused by local orography and vegetation).

Various wind farm flow models have been developed and are described in the literature. Whereas direct numerical simulation (DNS) is still out of reach for practical applications due to its overwhelming computational cost, large-eddy simulation (LES) methods are now routinely used for the modeling of wind farm flows (Fleming et al., 2014; Breton et al., 2017). Although invaluable for the understanding of the behavior of the atmospheric boundary layer and of wakes, LES is however still very expensive, so that its use outside of some specialized applications is limited. To reduce cost, one can resort to lower-fidelity computational fluid dynamics (CFD) models (Boersma et al., 2019), or to the extraction of reduced-order models (ROMs) from higher-fidelity ones (Bastine et al., 2014). Instead of deriving models from first principles, another widely adopted approach is to use engineering models, which are expressed in the form of parametric analytical formulas with a limited number of degrees of

freedom and hence a much reduced numerical complexity (Frandsen et al., 2006; Gebraad et al., 2014; Bastankhah and Porté-Agel, 2016). The present paper uses this last family of methods, although ideas similar to the ones developed here could also be applicable to higher-fidelity models.

Even though engineering models are constantly improved and refined (Fleming et al., 2018), they will most likely always exhibit only a limited accuracy in many practical applications, for example whenever an important role is played by effects such as orography, (seasonal) vegetation, spatial variability of the wind, sea state roughness, the erection of other neighboring wind turbines, the presence of obstacles, and others. In addition, low-fidelity models often lack some physics, e.g. the flow acceleration caused by wake and rotor blockage, secondary steering, or others. The idea pursued in this paper is then to take a rather pragmatic approach: based on the realization that it will always be difficult – if not altogether impossible – to include all effects and all physics in a model of limited numerical complexity, a given model is corrected by unknown parametric terms, which are then learned by using operational data.

The idea of improving an existing model based on measurements is hardly new, and it is actually an important topic in the areas of controls and system identification. For example, in the field of wind farm flows, a Kalman filtering approach has been proposed by Doekemeijer et al. (2017) to update model predictions based on lidar measurements. Here again the present paper takes a more pragmatic approach, and model updating is based exclusively on data provided by the standard supervisory control and data acquisition (SCADA) systems that are typically available on contemporary wind turbines. On the one hand this has the advantage that the proposed method is applicable to existing assets, as it does not necessitate extra sensors. On the other hand, given that stored SCADA data typically represent 10 min averages, this also implies that the models obtained by this technique are of a steady-state nature. Although unsteady effects in wind farms are clearly important, steady-state models are still very valuable and can support many of the applications listed above. In addition, nothing prevents the generalization of the proposed approach to unsteady flow models, assuming that the relevant higher-frequency data sets are available, which is already the subject of ongoing work from these authors.

The contemporary literature – and not only in the field of wind energy – indicates an increasing interest in data-driven approaches. Just to give one single example related to wake modeling, a purely data-driven approach has been recently described by Göçmen and Giebel (2018). However, the current enthusiasm for data should not make one forget that physics-based and analytical models are also extremely valuable because they often encapsulate significant knowledge on a given problem, often corroborated by long experience. In fact, purely data-driven approaches suffer from a number of limitations that descend directly from a very simple and inevitable fact: a model that is exclusively based on data can

only know what is contained in the data set that was used to build it. Typically, this means that a very significant amount of data is necessary to obtain a model that is sufficiently general and accurate. Furthermore, the data have to cover the entire spectrum of operation of the system. This also means that the model might have very poor knowledge (and hence poor performance) for rare situations or conditions that take place at the boundaries of the operating envelope, where few if any data points might be available.

An alternative to the purely data-driven approach is presented in this work, where a reference baseline model is augmented with parametric error terms, which are then identified using data. The baseline model already includes prior knowledge based on physics, empirical observations, and experience. Therefore, even prior to the use of data, a minimum performance can be guaranteed. The model is augmented with parametric error terms, whose choice is driven by physics and the knowledge of the limitations of the baseline model. Once the errors are identified using operational data, their inspection can clarify the causes of discrepancy between model and measurements. Eventually, this can be used to improve the underlying baseline model. Furthermore, by looking at the magnitude of the identified errors, significant deviations from the baseline model can be flagged to highlight issues with the model itself, the data, or the training process.

Finally, it should be noted that the identification of the error terms can be combined with the tuning of the parameters of the baseline model. This addresses yet another problem: tuning the parameters of a model that lacks some physics may lead to unreasonable values for the parameters, as the model is “stretched” to represent phenomena that it does not contain. By the proposed hybrid approach, the simultaneous identification of the parameters of the baseline model together with the ones of the error terms eases this problem, as unmodeled phenomena can be captured by the model-augmenting terms, thereby reducing the chances of nonphysical tuning of the baseline parameters.

The baseline model parameters and the extra correction terms have a different functional form in the augmented governing equations. Hence, they should be distinguishable from each other, as they imply different effects on the model. However, as for many identification problems, it is in general not possible to guarantee that all unknown parameters are observable and noncollinear given a set of measurements and, hence, given a certain informational content. To address this problem, the method proposed by Bottasso et al. (2014a) is used here, where the original unknown parameters are recast into a new set of statistically uncorrelated variables by using the singular value decomposition (SVD) of the inverse Fisher information matrix. Once the problem has been solved in the space of the orthogonal uncorrelated parameters, the solution is mapped back onto the original physical space. This approach not only avoids the ill-posedness of the original problem, but also allows one to clarify which physical parameters are visible given a certain data set.

The paper is organized as follows. First, the baseline model is introduced in Sect. 2.1, together with a detailed description of the proposed parametric corrections in Sect. 2.2. Next, the SVD-based parameter identification method is presented in Sect. 2.3. The approach is then applied in Sect. 3.1 to a cluster of scaled wind turbines operating in the atmospheric test section of the wind tunnel of the Politecnico di Milano (Bottasso et al., 2014b). The goal of this first application is to show that a correct identification of the error terms can be achieved. This is indeed possible in the controllable and repeatable conditions of a wind tunnel, where inflow and wake characteristics can be precisely measured, something that is hardly possible today in the field. Specifically, it is shown that the method can correctly learn the lack of uniformity of the wind tunnel inflow, which is akin to what happens in a real wind farm because of orographic effects. Similarly, it is shown that secondary steering, which is completely absent from the baseline model used here, can be learned by using turbine power measurements only. A more extended view on the wind tunnel results is reported in Appendix A. After having demonstrated the method in the known and controlled wind tunnel environment, a second application is developed in Sect. 3.2 that targets a real 43-turbine wind farm. Here results indicate that the augmented model has a markedly improved prediction capability when compared to the baseline one, thanks primarily to the identification of orographic effects on the inflow and the tuning of other model parameters. Finally, conclusions are drawn in Sect. 4.

2 Methods

2.1 Baseline wind farm flow model

The proposed method is applied here to the baseline wake model of Bastankhah and Porté-Agel (2016), implemented within the FLORIS framework (Doekemeijer and Storm, 2018). Given ambient wind conditions, steady-state velocities within a wind farm can be computed by this model, together with the corresponding operating states and power outputs of all its turbines. First, ambient conditions are estimated from un-waked machines operating in free stream, which are identified by the turbine yaw orientations and the wake model (Schreiber et al., 2018). Then, power and thrust of the upstream turbines are computed based on the turbine aerodynamic characteristics, regulation strategy, and alignment with the local wind direction. Next, the wakes shed by these turbines are calculated in terms of their trajectory and speed deficit. In turn, this yields the velocity at the rotor disks of the turbines immediately downstream. In the case of multiple wake impingements on a rotor, a combination model is used to superimpose multiple wake deficits. Similarly, an added turbulence model is used to estimate the turbulence intensity at a downstream turbine rotor disk, as this local ambient parameter affects the expansion of the wake. This process

is repeated marching downstream throughout the wind farm until the last downstream turbine is reached.

In this work, the implementation uses the *selfSimilar* FLORIS velocity deficit model, the *rans* deflection model, the *quadraticRotorVelocity* wake combination model, and the *crespoHernandez* added turbulence model. The interested reader is referred to Bastankhah and Porté-Agel (2016), Crespo and Hernández (1996), and Doekemeijer et al. (2019) and references therein for detailed descriptions and derivations of these models.

Engineering wake models depend on a number of parameters, which should be tuned in order to obtain accurate predictions. For the specific model used in this work, these tunable factors are the wake parameters α , β , k_a , k_b , a_d , and b_d and the turbulence model parameters TI_a , TI_b , TI_c , and TI_d (Bastankhah and Porté-Agel, 2016).

In this work, the parameters are first set to an initial value, either taken from the literature or identified with ad hoc measurements; these initial values are held fixed throughout the analysis and not changed further. Corrections to the initial values are then expressed as

$$k = k^* + p_k, \quad (1)$$

where k is a model parameter, k^* its initial value, and p_k the correction. Although this is not strictly necessary, this redundant notation helps highlight the changes to the nominal model parameters obtained by the proposed procedure.

2.2 Model augmentation

The engineering model described earlier is a rather simple approximation of a flow through a wind power plant and it is therefore bound to have only a limited fidelity to reality, with a consequently only limited predictive accuracy. Even for more sophisticated future models, it is difficult to imagine that all relevant physics will ever be precisely accounted for. But even if such a model existed, in practice one might simply not have all necessary detailed information on the relevant boundary and operating conditions that would be required. For example, one might not know with precision the conditions of the vegetation around and within a wind farm, with its effects on roughness and, hence, on the flow characteristics. In other words, it is safe to assume that all models are in error to some extent and probably always will be.

To address this problem, the model can be pragmatically augmented with correction terms. Here one could take two alternative approaches: either a generic all-encompassing error term is added to the model or “surgical” errors are introduced at ad hoc locations in the model to target specific presumed deficiencies. The first approach could be treated with a brute-force parametric modeling approach, for example by using a neural network. Here, the second approach was used, as it allows for more insight into the nature of the identified corrections. The specific parametric corrections used in the present paper are reviewed next. It is clear that these are only

some of the many corrections that could be applied to the present baseline model, so that the following does not pretend to be a comprehensive treatment of the topic. Nonetheless, results indicate that some of these corrections are indeed significant and provide for a marked improvement of the baseline model.

- *Nonuniform inflow.* The inflow to a wind farm can exhibit spatial variability, mostly because of orographic and local effects, especially in complex terrain conditions. For example, commercial wind resource assessment tools include topographic speedup ratios customarily computed by CFD models (Jacobsen, 2019). In contrast to this established practice, no direct or equivalent modeling of orographic effects is at present available in engineering wake models. Another reason for inflow variability may be due to wind farm blockage effects (Bleeg et al., 2018). Indeed, current wake models such as the one used here assume that upstream turbines affect downstream ones through their wakes but do not model the effects of downstream machines on the upstream ones. In a wind farm, depending on the wind direction and cross-wind location considered, the number and operating state of downstream turbines vary, which may induce a cross-wind speed variability in the inflow.

To capture some of these effects, the model ambient flow speed V_∞ is expressed here as a function of height above ground Z , cross-wind lateral position Y , and ambient wind direction Γ as

$$V_\infty(Y, Z, \Gamma) = (1 + f_{\text{augm, speed}}(Y, \Gamma, \mathbf{c}_{\text{speed}}, \mathbf{p}_{\text{speed}})) V_{\infty,0} \left(\frac{Z}{z_h} \right)^{\alpha_{\text{vs}}}, \quad (2)$$

where $V_{\infty,0}$ is the reference (baseline uncorrected) ambient flow speed and z_h the reference height of the vertically sheared flow with exponent α_{vs} . Function $f_{\text{augm, speed}}(Y, \Gamma, \mathbf{c}_{\text{speed}}, \mathbf{p}_{\text{speed}})$ is the speed correction term. This function is defined in the 2D space $Y \in [Y_{\min}, Y_{\max}]$, $\Gamma \in [\Gamma_{\min}, \Gamma_{\max}]$. For each value of the ambient wind direction Γ , Y is a lateral coordinate orthogonal to it that spans the width of the farm; hence, by selecting Γ_{\min} and Γ_{\max} a lateral inflow nonuniformity can be modeled for a given sector or the whole wind rose of directions. The (Y, Γ) space is discretized into rectangular cells with corner nodes $\mathbf{c}_{\text{speed}} = [\dots; (Y_i, \Gamma_i); \dots]$ (for an example, see Fig. 16). The corresponding unknown error nodal values are stored in vector $\mathbf{p}_{\text{speed}}$, and bilinear shape functions interpolate the error in each cell based on the nodal values at its corners. Equation (2) could be extended to also include a longitudinal wind-aligned coordinate, similarly to the localized speedup ratios of Jacobsen (2019), to model wind farm blockage effects.

Local orographic effects and blockage may also induce variability in the wind direction Γ . Similarly, the vertical shear exponent α_{vs} and turbulence intensity I may vary, for example on account of nonuniform roughness induced by vegetation or other obstacles. To include these effects in the farm flow model, the baseline quantities are augmented as

$$\Gamma(Y) = \Gamma_{\text{ref}} + Y f_{\text{augm, dir}}(\Gamma_{\text{ref}}, \mathbf{c}_{\text{dir}}, \mathbf{p}_{\text{dir}}), \quad (3a)$$

$$\alpha_{\text{vs}}(\Gamma) = \alpha_{\text{vs, ref}} + f_{\text{augm, shear}}(\Gamma, \mathbf{c}_{\text{shear}}, \mathbf{p}_{\text{shear}}), \quad (3b)$$

$$I(\Gamma) = I_{\text{ref}} + f_{\text{augm, I}}(\Gamma, \mathbf{c}_I, \mathbf{p}_I). \quad (3c)$$

In all these expressions, $(\cdot)_{\text{ref}}$ indicates a baseline reference quantity, while function $f_{\text{augm, }(\cdot)}$ is a correction term. This function is defined on the 1D space $\Gamma \in [\Gamma_{\min}, \Gamma_{\max}]$, discretized with nodes $\mathbf{c}_{(\cdot)} = [\dots; \Gamma_i; \dots]_{(\cdot)}$, using linear shape functions to interpolate the corresponding nodal values $\mathbf{p}_{(\cdot)}$. Here again, by selecting Γ_{\min} and Γ_{\max} , corrections can be applied to the whole wind rose or just to a sector.

- *Secondary steering.* By misaligning a wind turbine rotor with respect to the incoming flow direction, the rotor thrust force is tilted, thereby generating a cross-flow force that laterally deflects the wake. As shown with the help of numerical simulations by Fleming et al. (2018), this cross-flow force induces two counter-rotating vortices that, combining with the wake swirl induced by the rotor torque, lead to a curled wake shape. As observed experimentally by Wang et al. (2018), the effects of these vortices result in additional lateral flow speed components, which are not limited to the wake itself but also extend outside of it. By this phenomenon, the flow direction within and around a deflected wake is tilted with respect to the upstream undisturbed direction. Therefore, when a turbine is operating within or close to a deflected wake, its own wake undergoes a change of trajectory – termed secondary steering – induced by the locally modified wind direction. Although models of this phenomenon are being developed (Martínez-Tossas et al., 2019), they significantly increase the computational cost and are not yet available in standard implementations of engineering wake models such as the one used here.

The change of wind direction $\Delta\Gamma$ at a downstream turbine induced by secondary steering (indicated by the subscript ss) is modeled here as

$$\Delta\Gamma(y) = f_{\text{augm, ss}}(\tilde{y}, \Gamma_{\text{init}}, \mathbf{p}_{\text{ss}}), \quad (4)$$

where $f_{\text{augm, ss}}$ is the correction term and $\tilde{y} = Y - y_{\text{wc}}$ is the lateral distance to the wake centerline (see Fig. 1), defined in the baseline wind farm model as the locus of the points of minimum flow speed. According to the notation used in Eq. (6.12) of Bastankhah and Porté-Agel (2016), Γ_{init} indicates the initial wake direction of

the closest upstream turbine. The correction term is expressed as the difference of two Gaussian functions and more precisely

$$f_{\text{augm,ss}}(\tilde{y}, \Gamma_{\text{init}}, \mathbf{p}_{\text{ss}}) = \Gamma_{\text{init}} \left(p_{\text{ss},1} \exp \left(-0.5 \left(\frac{\tilde{y} + \text{sgn}(\Gamma_{\text{init}}) p_{\text{ss},3}}{p_{\text{ss},2}} \right)^2 \right) - p_{\text{ss},4} \exp \left(-0.5 \left(\frac{\tilde{y} + \text{sgn}(\Gamma_{\text{init}}) p_{\text{ss},6}}{p_{\text{ss},5}} \right)^2 \right) \right), \quad (5)$$

where $\mathbf{p}_{\text{ss}} = (p_{\text{ss},1}, p_{\text{ss},2}, p_{\text{ss},3}, p_{\text{ss},4}, p_{\text{ss},5}, p_{\text{ss},6})$ is the vector of free parameters, where parameters 1 and 4 are related to the amplitude, 3 and 6 to the standard deviation, and 2 and 5 to the location of the correction functions. Since the Gaussian functions are not centered at the wake centerline and the effect of secondary steering is assumed to be symmetric with respect to the misalignment angle, the correction term also depends on the direction of wake deflection $\text{sgn}(\Gamma_{\text{init}})$.

This particular choice of the shape functions is motivated by the results shown in Fig. 8b of Wang et al. (2018). Indeed, LES simulations and measurements reveal the presence of a stronger lateral velocity component directed towards the wake on the leeward side of the wake itself, and of an opposite and weaker lateral component on the windward side. Such a distribution can be approximated by two Gaussian functions using Eq. (5).

Note that the change in local wind direction also leads to a slight lateral deflection of the nonuniform wind farm inflow introduced previously. More precisely, for a turbine that is located ΔX behind an upstream turbine, the nonuniform inflow expressed by Eq. (2) is evaluated at $Y + \Delta X \sin(\Delta\Gamma)$ instead of Y .

Figure 1a shows the hub height flow speed for two wind turbines modeled in FLORIS, with the turbine rotor disks being indicated with thick black lines. The wake centerlines and the undisturbed free-stream wind direction are indicated by black dotted and dashed lines, respectively. The upstream turbine is misaligned with respect to the incoming flow, and therefore its wake is deflected laterally. Using the baseline wake model, the downstream turbine wake develops along the free-stream wind direction. Panel (b) of the same figure shows the effects of the secondary steering correction term given by Eq. (5). The plot clearly shows that the downstream turbine wake path is affected by the locally changed wind direction.

- *Non-Gaussian wake and flow acceleration.* Engineering wake models are based, among other hypotheses, on assumed shapes of the speed deficit. For example, the present baseline model assumes a Gaussian distribution

of the speed deficit within the wake. Another assumption is that the flow outside the wake is undisturbed and equal to the free stream. However, these assumptions can, at times, not be exactly satisfied, as already observed by Xie and Archer (2017) and Martínez-Tossas et al. (2019), among others. For example, aisle jets are local accelerations of the flow outside of the wake, produced by local blocking in the neighborhood of an operating turbine. It has been reported that aisle jets can induce local flow speedups in excess of 10% of the undisturbed inflow (Dörenkämper et al., 2015).

To account for such effects, the wake velocity V_{wake} of the baseline model is corrected as

$$V_{\text{wake}}(d_{\text{wc}}) = V_{\text{wake,FLORIS}}(d_{\text{wc}}) (1 + f_{\text{augm,acc}}(d_{\text{wc}}, \mathbf{c}_{\text{acc}}, \mathbf{p}_{\text{acc}})), \quad (6)$$

where $V_{\text{wake,FLORIS}}$ is the baseline Gaussian wake speed profile, d_{wc} is the absolute distance to the wake center (which, at hub height, is equivalent to $|\tilde{y}|$), and $f_{\text{augm,acc}}$ represents the correction term, which – similarly to the previous corrections – is modeled with linear shape functions characterized by node locations \mathbf{c}_{acc} (in terms of d_{wc}) and nodal values \mathbf{p}_{acc} .

- *Reduced power extraction due to nonuniform wind turbine inflow.* Numerical simulations conducted in FAST (Jonkman and Jonkman, 2018) using its blade element momentum (BEM) implementation yielded a slight reduction in the rotor power coefficient for horizontally sheared flow, when compared to unsheared conditions with the same hub wind speed. Even though BEM can only give a rough indication for such an effect, a correction of the power coefficient of the baseline model is introduced here in the form

$$C_P = C_{P,\kappa=0} (1 + p_\kappa \kappa^2), \quad (7)$$

where $C_{P,\kappa=0}$ is the nominal power coefficient, κ the equivalent horizontal linear shear coefficient on the rotor disk, and p_κ the free correction parameter. The linear shear κ is either due to a lack of lateral uniformity of the inflow or due to the impingement of a wake, and it is evaluated accordingly within the farm model.

- *Wind-speed-dependent power loss in yaw misalignment.* The baseline formulation models the power extraction of a misaligned wind turbine using the cosine law $C_P(\gamma) = C_P \cos(\gamma)^{pp}$, where C_P is the power coefficient of the wind-aligned turbine, γ the misalignment angle with respect to the local flow direction, and pp the power loss exponent. Different power loss exponents have been reported in the literature, ranging from the value of 1.4 found by Fleming et al. (2017) to 1.8 according to Schreiber et al. (2017), 1.9 for Gebraad et al.

652

J. Schreiber et al.: Wind farm model augmentation

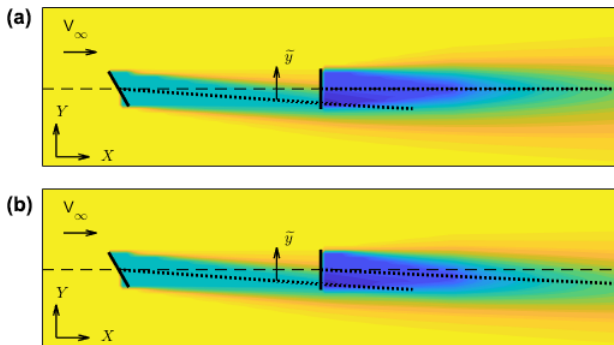


Figure 1. Effect of secondary steering on the trajectory of a downstream turbine. (a) Baseline wake model; (b) baseline model augmented with the empirical correction term of Eq. (5).

(2015), and all the way to the ideal value of 3 that is expected if only the rotor-orthogonal ambient flow component contributes to power extraction (Boersma et al., 2019). In addition, p_P might also depend on the regulation strategy used by the turbine controller. Here, the power coefficient in misaligned operation is augmented as

$$C_P = C_P \cos(\gamma + p_{P0})^{p_P + p_{P,a}(V - V_{\text{rated}}) + p_{P,b}}, \quad (8)$$

where C_P is the power coefficient of the flow-aligned turbine (possibly reduced by shear effects, as argued above), p_{P0} is the misalignment angle at which the turbine produces maximum power, and V and V_{rated} are, respectively, the rotor effective and rated wind speeds. Finally, p_P is the baseline exponent, while $p_{P,a}$ and $p_{P,b}$ are free parameters that model a linear wind speed dependency of the cosine law.

2.3 Parameter identification method

The parameters of the baseline model and of its correction terms are identified with the method developed by Bottasso et al. (2014a). The formulation of the parameter estimation problem is independent of whether the parameters belong to the baseline model or to its correction factors. In this sense, one can use the same method to just tune the baseline parameters without considering the correction terms, just identify the correction terms at the frozen baseline model, or concurrently identify both sets.

The formulation is based on the classical likelihood function, which describes the probability that a given set of noisy observations can be explained by a specific set of model parameters. By numerically maximizing this function, a set of parameters is identified that most probably explains the measurements. Bound constraints are used to guide the process and ensure convergence to meaningful results.

The accuracy with which the parameters can be estimated depends on how flat the likelihood function is with respect to

changes in the parameters. For example, a flat maximum of the function implies that different nearby values of the model parameters are associated with similar values of the likelihood. These characteristics of the solution space are captured by the Fisher information matrix, which can be interpreted as a measure of the curvature of the likelihood function. Furthermore, it can be shown that the variance of the estimates is bound from below (Cramér–Rao bound) by the inverse of the Fisher matrix (Jategaonkar, 2015). Although the analysis of the Fisher information is useful for the understanding of the well-posedness of an estimation problem and of the quality of the identified model, it does not offer a constructive way of reformulating a given ill-posed problem. Indeed, a flat solution space and collinear parameters are to be expected in the present case, given the complex couplings and dependencies that may exist among the various parameters of a wind farm flow model and its correction terms.

To overcome this limitation of the classical maximum likelihood formulation, following Bottasso et al. (2014a), the original physical parameters of the model are transformed into an orthogonal parameter space, by diagonalizing the Fisher matrix using the SVD. This way, as the parameters are now statistically decoupled, one can set a lower observability threshold and in the analysis retain only the ones that are in fact observable given the available set of measurements. Once the problem is solved, the uncorrelated parameters are mapped back onto the original physical space.

As shown later on, this approach achieves multiple goals: it allows one to successfully solve a maximization problem with many free parameters, some of which might be interdependent on one another or not observable in a given data set; it reduces the problem size, retaining only the orthogonal parameters that are indeed observable; it highlights, through the singular vectors, the interdependencies that may exist among some parameters of the model, which provides for a useful interpretation tool that may guide the reformulation of parts of the model and its correction terms.

2.3.1 Maximum likelihood estimation of model parameters

A steady-state wind farm model can be mathematically expressed as

$$\mathbf{y} = \mathbf{f}(\mathbf{p}, \mathbf{u}), \quad (9)$$

where $\mathbf{f}(\cdot, \cdot, \cdot)$ is the nonlinear static function describing the wind farm model, which depends on free parameters $\mathbf{p} \in \mathbb{R}^n$. These parameters can include both wake model parameters and/or model augmentation parameters. The model inputs $\mathbf{u} \in \mathbb{R}^u$ include ambient wind conditions (i.e. ambient wind speed, direction, air density, turbulence intensity) and control inputs (i.e. yaw misalignment, partialization factor, blade pitch, rotor speed of each turbine). The model outputs $\mathbf{y} \in \mathbb{R}^m$ represent quantities of interest for which measurements are available, in the present work these being the

power outputs of each wind turbine in the farm. Experimental observations \mathbf{z} of the simulated outputs \mathbf{y} will in general result in a residual $\mathbf{r} \in \mathbb{R}^m$, caused by measurement and process noise (e.g. plant–model mismatch), so that

$$\mathbf{z} = \mathbf{y} + \mathbf{r}. \quad (10)$$

Given a set $S = \{z_1, z_2, \dots, z_N\}$ of N independent observations, the likelihood function (Jategaonkar, 2015) can be defined as

$$\mathcal{L}(S|\mathbf{p}) = \prod_{i=1}^N p(z_i|\mathbf{p}), \quad (11)$$

where $p(\cdot)$ is the probability of S given \mathbf{p} . Assuming the residuals \mathbf{r} with covariance \mathbf{R} to be statistically independent within the set of measurements (i.e. $E[\mathbf{r}_i \mathbf{r}_j^T] = \mathbf{R} \delta_{i,j}$, where $\delta_{i,j}$ is the Kronecker delta), the likelihood function can be written, following Jategaonkar (2015), as

$$\mathcal{L}(S|\mathbf{p}) = \left((2\pi)^m \det(\mathbf{R}^{-1}) \right)^{-N/2} \exp\left(-\frac{1}{2} \sum_{i=1}^N \mathbf{r}_i^T \mathbf{R} \mathbf{r}_i \right). \quad (12)$$

Maximizing \mathcal{L} (or minimizing its negative logarithm), a maximum likelihood estimate of the parameters can be obtained as

$$\mathbf{p}_{\text{MLE}} = \underset{\mathbf{p}}{\operatorname{argmin}} J(\mathbf{p}), \quad (13)$$

where $J(\mathbf{p}) = -\ln(\mathcal{L}(S|\mathbf{p}))$. The measurement noise covariance matrix \mathbf{R} can be estimated under mild hypotheses as $\mathbf{R} = \sum_{i=1}^N \mathbf{r}_i \mathbf{r}_i^T$, yielding $J(\mathbf{p}) = \det(\mathbf{R})$, leading to an iteration between a solution at given covariance and a covariance update step (Jategaonkar, 2015). However, in this paper the measurement noise covariance matrix is estimated a priori and therefore assumed to be known. The cost function therefore becomes

$$J(\mathbf{p}) = \frac{1}{2} \sum_{i=1}^N \mathbf{r}_i^T \mathbf{R}^{-1} \mathbf{r}_i. \quad (14)$$

To ensure reasonable and physically viable solutions, parameters can be forced to stay within predefined upper (subscript ub) and lower (subscript lb) bounds, by adding the corresponding inequality constraints $\mathbf{p}_{\text{lb}} \leq \mathbf{p} \leq \mathbf{p}_{\text{ub}}$ to problem (13). As the parameter values and constraints can differ in magnitude, it is a good practice to scale all parameters such that a value of 1 corresponds to the upper bound p_{ub} and a value of -1 to the lower one p_{lb} . The optimization problem can finally be solved numerically by a suitable algorithm, such as sequential quadratic programming (SQP) (Nocedal and Wright, 2006).

2.3.2 Identifiability of parameters

The Fisher information matrix $\mathbf{F} \in \mathbb{R}^{n \times n}$ is defined as

$$\mathbf{F} = \sum_{i=1}^N \left[\frac{\partial \mathbf{y}_i}{\partial \mathbf{p}} \right]^T \mathbf{R}^{-1} \left[\frac{\partial \mathbf{y}_i}{\partial \mathbf{p}} \right] \quad (15)$$

and describes the curvature of the likelihood function. It can be shown (Jategaonkar, 2015) that a lower bound (termed Cramér–Rao bound) of the covariance of the estimated parameter is given by

$$\mathbf{F}^{-1} = \mathbf{P} \leq \operatorname{Var}(\mathbf{p}_{\text{MLE}} - \mathbf{p}_{\text{true}}), \quad (16)$$

where \mathbf{p}_{true} represents the true but unknown parameters. The k th diagonal element of \mathbf{P} is a lower bound on the variance of the k th estimated parameter, while the correlation between different parameters is captured by the off-diagonal terms of that same matrix. The correlation coefficient between two parameters i and j is defined as

$$\Psi_{p_i, p_j} = \frac{P_{i,j}}{\sqrt{P_{i,i} P_{j,j}}}, \quad (17)$$

where $P_{i,j}$ denotes the i, j th element (row, column) of \mathbf{P} . By analyzing the estimated parameter variance, as well as the correlation between parameters, valuable insight into the well-posedness of the parameter identification problem can be readily obtained.

2.3.3 Problem transformation and untangling using the SVD

When some parameters are highly correlated or have large variance, the problem is ill-posed: it might exhibit sluggish convergence, or no convergence at all, and small changes in the inputs may lead to large changes in the estimates. Such situations are difficult to solve in physical space, because parameters are typically coupled together to some degree through the model.

To untangle the parameters, one may resort to the SVD (Golub and van Loan, 2013). By this approach (Hansen, 1987; Waiboer, 2007; Bottasso et al., 2014a), the original parameters are mapped into a new set of uncorrelated (orthogonal) parameters. Since the new unknowns are uncorrelated, one can set a threshold to their variance by using the Cramér–Rao bound and only retain those in the optimization that are observable within the given data set.

The Fisher matrix \mathbf{F} is first factorized as $\mathbf{F} = \mathbf{M}^T \mathbf{M}$, where $\mathbf{M} \in \mathbb{R}^{Nm \times n}$ is defined as

$$\mathbf{M} = \begin{bmatrix} \mathbf{R}^{-1/2} \frac{\partial \mathbf{y}_1}{\partial \mathbf{p}} \\ \mathbf{R}^{-1/2} \frac{\partial \mathbf{y}_2}{\partial \mathbf{p}} \\ \dots \\ \mathbf{R}^{-1/2} \frac{\partial \mathbf{y}_N}{\partial \mathbf{p}} \end{bmatrix}. \quad (18)$$

654

J. Schreiber et al.: Wind farm model augmentation

Assuming a larger number of measurements than parameters ($Nm > n$), matrix \mathbf{M} can be decomposed into

$$\mathbf{M} = \mathbf{U}\mathbf{\Sigma}\mathbf{V}^T, \quad (19)$$

where $\mathbf{U} \in \mathbb{R}^{Nm \times Nm}$ and $\mathbf{V} \in \mathbb{R}^{n \times n}$ are the matrices of left and right, respectively, singular vectors, while

$$\mathbf{\Sigma} = \begin{bmatrix} \mathbf{S} \\ \mathbf{0} \end{bmatrix}, \quad (20)$$

where $\mathbf{S} \in \mathbb{R}^{n \times n}$ is a diagonal matrix, whose entries s_i are the singular values sorted in descending order.

By using Eq. (19) and the factorization of \mathbf{F} , the inverse of the Fisher information matrix can be written as

$$\mathbf{P} = \mathbf{V}\mathbf{S}^{-2}\mathbf{V}^T. \quad (21)$$

Note that the columns of the orthogonal matrix \mathbf{V} are also the eigenvectors of \mathbf{P} and s_i^{-2} the corresponding eigenvalues. Furthermore, \mathbf{P} and \mathbf{F} are symmetric and, based on the spectral theorem, diagonalizable.

The physical parameters \mathbf{p} can now be transformed into a new set of orthogonal parameters $\mathbf{\Theta}$ by a rotation performed with the right singular values:

$$\mathbf{\Theta} = \mathbf{V}^T \mathbf{p}. \quad (22)$$

For the transformed set of parameters, the Cramér–Rao bound on the variance of the estimates is the diagonal matrix $\mathbf{S}^{-2} \leq \text{Var}(\mathbf{\Theta}_{\text{MLE}} - \mathbf{\Theta}_{\text{true}})$. Therefore, a small singular value s_i corresponds to a large uncertainty in the corresponding orthogonal parameter estimation.

To remove parameters that cannot be estimated with sufficient accuracy, matrix \mathbf{S} can be partitioned as

$$\mathbf{S} = \begin{bmatrix} \mathbf{S}_{\text{ID}} & \mathbf{0} \\ \mathbf{0} & \mathbf{S}_{\text{NID}} \end{bmatrix}, \quad (23)$$

where \mathbf{S}_{ID} contains the identifiable singular values, i.e. those such that $s_i^{-2} < \sigma_t^2$, σ_t being a threshold on the highest acceptable standard deviation in the estimate. On the other hand, matrix \mathbf{S}_{NID} contains singular values associated with parameters that cannot be identified with sufficient accuracy and are therefore discarded. Accordingly, \mathbf{V} is also partitioned as $\mathbf{V} = [\mathbf{V}_{\text{ID}}, \mathbf{V}_{\text{NID}}]$, while the orthogonal parameters are partitioned as $\mathbf{\Theta} = [\mathbf{\Theta}_{\text{ID}}^T, \mathbf{\Theta}_{\text{NID}}^T]^T$. Finally, the physical parameters are expressed in terms of the sole identifiable orthogonal parameters:

$$\mathbf{p} \approx \mathbf{V}_{\text{ID}} \mathbf{\Theta}_{\text{ID}}. \quad (24)$$

Given that the Fisher matrix depends on the values of the parameters \mathbf{p} , an iterative procedure should be followed, where the diagonalization of the problem is repeated at each update of the parameter vector.

2.3.4 Identification method with variable measurement weights

In some cases, it may be useful to increase the importance of some measurements in the parameter estimation problem. This can be readily obtained by simply treating an observation with weight w as if it appeared w times in the observation data set (Karampatziakis and Langford, 2011). Cost function (14) then becomes

$$J(\mathbf{p}) = \frac{1}{2} \sum_{i=1}^N w_i \mathbf{r}_i^T \mathbf{R}^{-1} \mathbf{r}_i, \quad (25)$$

where w_i is the relative weight of observation i and $\sum_{i=1}^N w_i = N$. Similarly, the Fisher matrix becomes

$$\mathbf{F} = \sum_{i=1}^N w_i \begin{bmatrix} \frac{\partial \mathbf{y}_i}{\partial \mathbf{p}} \end{bmatrix}^T \mathbf{R}^{-1} \begin{bmatrix} \frac{\partial \mathbf{y}_i}{\partial \mathbf{p}} \end{bmatrix}, \quad (26)$$

and its factorization is

$$\mathbf{M} = \begin{bmatrix} \sqrt{w_1} \mathbf{R}^{-1/2} \frac{\partial \mathbf{y}_1}{\partial \mathbf{p}} \\ \sqrt{w_2} \mathbf{R}^{-1/2} \frac{\partial \mathbf{y}_2}{\partial \mathbf{p}} \\ \dots \\ \sqrt{w_N} \mathbf{R}^{-1/2} \frac{\partial \mathbf{y}_N}{\partial \mathbf{p}} \end{bmatrix}. \quad (27)$$

The remainder of the formulation is not affected by the introduction of weights.

3 Results

The proposed method is first applied in Sect. 3.1 to a wind tunnel experiment with a small cluster of three wind turbines and then in Sect. 3.2 to a real wind farm consisting of 43 wind turbines. The former example aims at a verification of the correctness of the identified augmentations, given the known and controllable conditions of the scaled experiments, whereas the latter is meant to offer a first glimpse of the practical applicability of the new method in the field.

3.1 Wind tunnel verification

Whether identified model corrections are indeed physical or only an artifact of the model–measurement mismatch is difficult to prove in general. From this point of view, wind tunnel experiments provide a unique opportunity to verify the concept proposed in this paper. Indeed, the overall flow within a cluster of turbines can be measured with good accuracy, and the experiments can be repeated in multiple desired operating conditions. The aim of this section is then to show that, even in the presence of multiple possibly overlapping model terms, the correct improvements to a baseline model can be learned from operational data only.

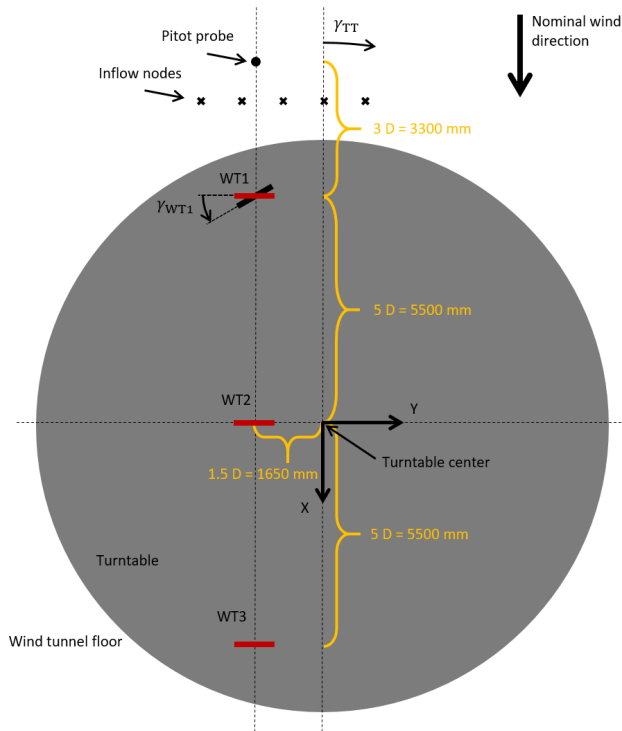


Figure 2. Wind farm layout for a null turntable rotation, looking down onto the wind tunnel floor.

3.1.1 Experimental setup

The experimental setup is composed of a scaled cluster of three G1 wind turbines, each of them equipped with active yaw, pitch, and torque control. The turbines were operated in the boundary layer test section of the wind tunnel of the Politecnico di Milano. Details on the models and the wind tunnel are reported, among other publications, in Campagnolo et al. (2016a, b, c).

The turbines are labeled WT1, WT2, and WT3, starting from the most upstream one and moving downstream. The machines are mounted on a turntable, whose rotation is used to change the wind direction with respect to the wind farm layout. In the nominal configuration, i.e. for a turntable rotation $\gamma_{TT} = 0^\circ$, the three turbines are aligned with the wind tunnel main axis – and hence with the flow velocity vector. The turbines are installed with a longitudinal spacing of 5 diameters (D), as shown in Fig. 2 with a view looking down towards the wind tunnel floor. As indicated in the figure, positive turntable rotations are clockwise. For $\gamma_{TT} \neq 0^\circ$, the longitudinal distance between the turbines decreases slightly. However, considering that in this work the largest investigated turntable angle was $\pm 11.5^\circ$, the longitudinal distance varied only between $4.9D$ and $5D$.

A pitot probe was placed at hub height, $3D$ upstream of the first G1 in the nominal configuration. The probe was there-

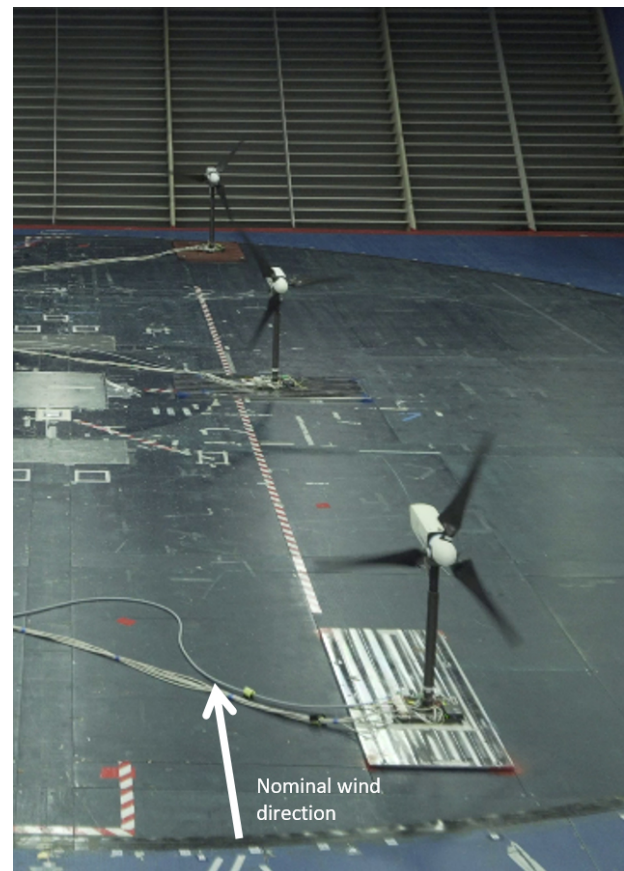


Figure 3. View looking downstream of the cluster of three G1 turbines.

fore not placed on the turntable, and its position remained fixed with respect to the wind tunnel test section. A wind-tunnel-fixed reference frame, used in the following to discuss the results, is also depicted in Fig. 2. Its origin is placed at the turntable center, while the frame x axis is aligned with the wind direction; the y axis points left, looking downstream; and hence Z points vertically up from the floor to complete a right-handed triad.

The yaw angle γ_{WT_i} of the i th wind turbine is positive for a counterclockwise rotation looking down onto the floor, as shown for WT1 in Fig. 2, and null when the rotor disk is orthogonal to X and, therefore, to the nominal wind direction.

Figure 3 shows a photo of the cluster of turbines, looking downstream with WT1 in the foreground. The wind tunnel floor is blue, whereas the turntable is black.

The ambient wind speed $V_{\infty,0}$ measured by the pitot tube was, for all conducted experiments, between 5.20 and 5.75 m s^{-1} , which corresponds to slightly below-rated conditions. The ambient turbulence intensity was equal to 6.12% , while the vertical shear was $\alpha_{vs} = 0.144$.

656

J. Schreiber et al.: Wind farm model augmentation

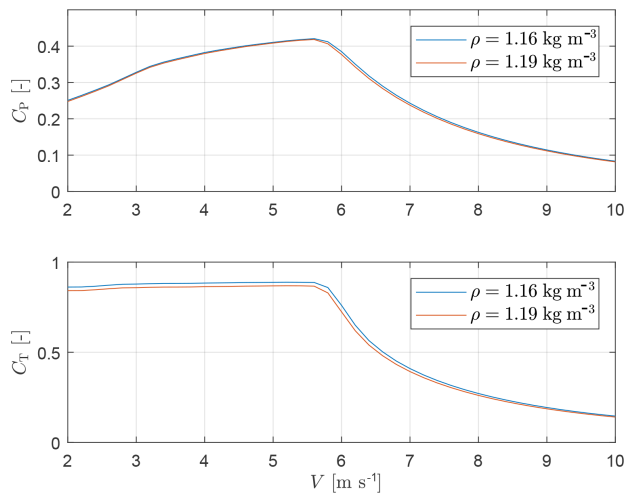


Figure 4. Power and thrust coefficients vs. wind speed for the G1 turbine.

3.1.2 Model setup

The FLORIS model implementation used in this work is the one available online (Doekemeijer and Storm, 2018). All baseline model parameters are reported in Table 1 and taken from Campagnolo et al. (2019), where they were identified based on wake measurements of a single isolated G1 turbine.

Figure 4 shows the G1 power C_P and thrust C_T coefficients as functions of wind speed V . The curves were obtained from dynamic simulations conducted in turbulent inflow, using the same controllers implemented on the scaled models. The C_P and C_T vs. tip speed ratio (TSR) and blade pitch setting curves were obtained with a BEM formulation using experimentally tuned airfoil polars (Bottasso et al., 2014a). As the turbine controller does not consider variations in air density ρ , the coefficients shown in the figure exhibit a slight dependency on this ambient parameter. Within FLORIS, this effect is taken into account by interpolating within the coefficients based on the actual density measured in the wind tunnel during each experiment. For all reported test conditions, air density varied in the range $\rho \in [1.159, 1.185] \text{ kg m}^{-3}$. The power loss exponent in misaligned conditions was evaluated experimentally to be $p_P = 2.1741$, while for thrust the coefficient was found to be $p_T = 1.4248$.

The ambient wind speed was determined from the pitot tube. It was observed that, by using this value, the power of a free-stream turbine predicted by the FLORIS model was slightly underestimated, most probably due to the sheared flow. To correct for this effect, measurements provided by the pitot tube were scaled by the factor 1.0176, which was computed in order to match simulated and measured power. Furthermore, in the original FLORIS implementation the power of a turbine is computed as $P = 1/2 \rho A V_{\text{avg}}^3 C_P$, where V_{avg} is the average wind speed at the rotor disk and A the rotor

disk area. Here, power was computed by integrating over the rotor disk area, i.e. $P = 1/2 \rho \int_A V^3 C_P dA$, which is probably slightly more accurate even though it involves a minor increase in computational effort.

3.1.3 Ranking of correction terms

To initially assess the role of the various parameters, a ranking analysis was conducted. The parameters were clustered in sets, depending on their role in the model. A first identification was performed using all parameter sets, yielding the presumed best value, denoted J_{ref} , of the cost function expressed by Eq. (14). The analysis was then repeated multiple times, each time removing one parameter set from the optimization. By looking at the resulting change in the value of the cost function, one may then rank the various parameter sets in order of importance. The analysis is based on a total of 190 experimental observations, as described in greater detail in the following.

All augmentation terms described in Sect. 2.2 were considered, except for the lateral variation in wind direction and the wind-direction-dependent vertical shear, as they are not applicable to the wind tunnel experiments. The nonuniform flow speed was modeled using five nodes located at $c_{\text{speed}}(Y) = [-3, -2, -1, 0, 1] \text{ m}$ (which correspond to approximately $[-2.7, -1.8, -0.9, 0, 0.9]D$) and also indicated in Fig. 2 using \times symbols. As only the turbine positions with respect to the flow are modified by rotating the turntable, a wind direction dependency was not included in this correction term. Table 2 reports the initial values and lower and upper bounds – chosen based on an educated guess – for the nonuniform inflow and secondary steering correction terms.

Figure 5 shows the relative increase in the cost function when eliminating one parameter set at a time. The figure clearly indicates that the most important parameters are the ones modeling laterally nonuniform speed and secondary steering. Indeed, this particular wind tunnel, due to its internal configuration and large width, does present a significant nonuniform flow speed, as already discussed by Campagnolo et al. (2019). Likewise, the effect of secondary steering is particularly important and should not be neglected for accurate predictions in misaligned conditions, as already reported in various publications. Based on these results, in the following only nonuniform inflow and secondary steering corrections are considered.

3.1.4 Results

A total of 451 observations were available, including 11 different turntable positions and thus wind farm layouts, with turbine yaw misalignments ranging from -40 to $+40^\circ$. A total of 190 observations were used to identify the five parameters associated with nonuniform inflow speed and the six associated with secondary steering, whereas the remaining data points were used for model validation. The various

Table 1. Initial FLORIS parameters for the G1 turbine.

α^*	β^*	k_a^*	k_b^*	a_d^*	b_d^*	TI_a^*	TI_b^*	TI_c^*	TI_d^*
0.9523	0.2617	0.0892	0.027	0	0	0.082	0.608	-0.551	-0.2773

Table 2. Definition of the parameters, together with their initial values, lower and upper bounds, and identified values.

i	p_i	$P_{lb,i}$	$P_{ub,i}$	$P_{init,i}$	$P_{opt,i}$	Implementation
1–5	p_{speed}	$[-0.1, -0.1, \dots, -0.1, -0.1, -0.1]$	$[0.1, 0.1, \dots, 0.1, 0.1, 0.1]$	$[0, 0, 0, 0, 0]$	$[0.079, 0.029, \dots, -0.051, -0.006, 0]$	$f_{augm,speed}(Y, Z, 0, c_{speed}, p_{speed})$ $c_{speed} = [-3, -2, -1, 0, 1] m$
6–11	p_{ss}	$[-3, 0, \dots, -3, -3, \dots, 0, -3]$	$[3, 1.5, \dots, 3, 3, \dots, 1.5, 3]$	$[-0.5, 0.5, \dots, 0.2, -0.25, \dots, 0.5, -0.2]$	$[-0.94, 0.63, \dots, 0.20, -0.48, \dots, 0.73, -0.28]$	$f_{augm,ss}(\tilde{y}, \Gamma_{init}, p_{ss})$

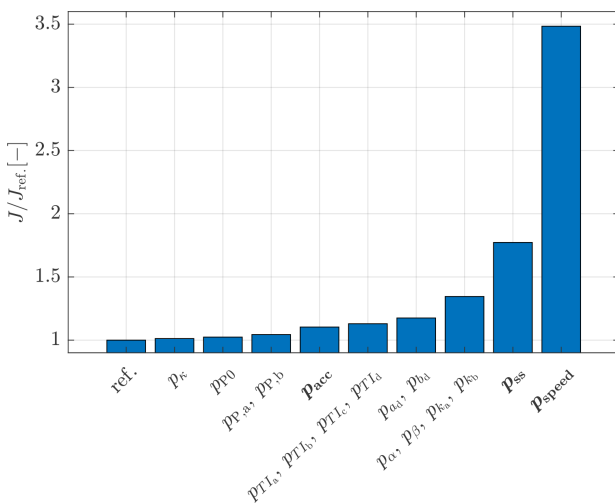


Figure 5. Relative increase in the optimization cost function when eliminating one parameter set at a time.

tested configurations in terms of turbine misalignments and turntable positions are reported in the figures of Appendix A.

Among all the available measurements gathered at each operating condition, only the steady-state power of the wind turbines was utilized, mimicking what could be done at full scale in the field using SCADA data. The model outputs y (see Eq. 9) are defined as

$$y = \frac{1}{P_{ref}} \begin{bmatrix} P_{WT1} \\ P_{WT2} \\ P_{WT3} \end{bmatrix}, \quad (28)$$

where P_{WTi} is the power of the i th wind turbine and $P_{ref} = 37.6W$ is a reference value used as the scaling factor. Based on experience, a diagonal measurement noise covariance matrix \mathbf{R} with all three terms equal to $\sigma^2 = 0.025^2$ was specified.

The threshold of the highest acceptable standard variance σ_r^2 for the orthogonal parameters was set to 0.01. As the parameters are scaled within a range of $[-1, 1]$, the threshold corresponds to a relative variance of 2%. Wind-aligned operating conditions (i.e. $\gamma_{WT1} = \gamma_{WT2} = \gamma_{WT3} = 0^\circ$) were weighted with a factor of 2, to increase their importance in the parameter estimation process.

The constrained optimization problem (13) was solved in MATLAB using the fmincon function with the interior-point algorithm (Mathworks, 2019). As the baseline model with its initial nominal values ($p = p_{init}$) is far away from the optimal solution, a first optimization was performed including only the inflow correction. Afterwards, three iterations were conducted including all 11 parameters. At each iteration, a total of eight orthogonal parameters could be identified within the specified variance threshold. The method converged very quickly, as the identified parameters and the residual did not change significantly after the first iteration. Figure 6a shows the initial variance of all 11 orthogonal parameters, and panel (b) shows the variance computed after the first iteration. The horizontal black line indicates the threshold σ_r^2 .

Interestingly, the 11th orthogonal parameter seems to have a very low observability. Table 3 shows the transformation matrix \mathbf{V}^T that links the physical parameters to the orthogonal ones ($\Theta = \mathbf{V}^T p$; see Eq. 22). The 11th orthogonal parameter is almost entirely associated with $p_{speed,5}$, which corresponds to the inflow speed augmentation node at position $Y = 1 m$. Indeed, the location of this node is such that it has only a very marginal effect on the turbine outputs and, hence, a very low observability, as shown later in Fig. 7. The transformation matrix reported in Table 3 also shows that the other two orthogonal parameters with low observability (9 and 10) represent secondary steering modes, mainly associated with the second Gaussian function of the correction term.

Table 4 presents the correlation matrix Ψ (see Eq. 17) and shows a clear and to be expected dependency among neighboring inflow parameters. Among the secondary steering pa-

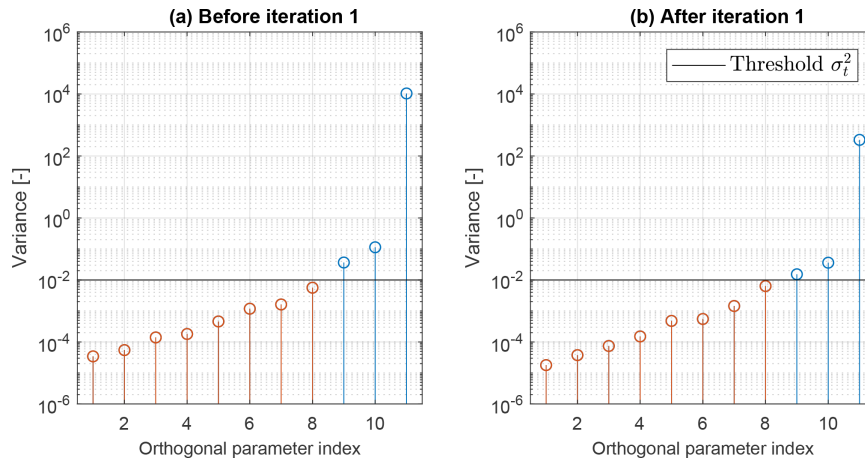


Figure 6. Variance of the orthogonal parameters before (a) and after (b) the first iteration. The identifiable orthogonal parameters are shown in red, whereas all others are shown in blue.

Table 3. Transformation matrix \mathbf{V}^T after the first iteration. Each row corresponds to a different orthogonal parameter.

	$p_{\text{speed},1}$	$p_{\text{speed},2}$	$p_{\text{speed},3}$	$p_{\text{speed},4}$	$p_{\text{speed},5}$	$p_{\text{ss},1}$	$p_{\text{ss},2}$	$p_{\text{ss},3}$	$p_{\text{ss},4}$	$p_{\text{ss},5}$	$p_{\text{ss},6}$
1	-0.0	0.0	0.0	-0.0	-0.0	-0.7	0.2	-0.0	0.7	-0.1	-0.1
2	-0.2	-0.4	-0.3	-0.1	-0.0	0.2	-0.1	-0.7	0.3	0.1	0.3
3	0.0	-0.6	-0.6	-0.1	0.0	-0.1	0.0	0.4	-0.1	-0.0	-0.2
4	-0.4	-0.6	0.6	0.3	0.0	-0.0	0.0	0.1	-0.0	-0.0	-0.0
5	-0.7	0.2	-0.1	-0.2	-0.0	0.2	0.5	0.2	0.1	-0.1	0.1
6	-0.5	0.2	-0.1	-0.1	0.0	-0.4	-0.7	-0.0	-0.2	0.1	-0.2
7	0.1	-0.2	0.3	-0.9	-0.0	-0.0	-0.1	0.1	-0.0	-0.0	0.1
8	0.0	0.0	-0.0	0.1	-0.0	0.3	-0.5	0.5	0.5	0.1	0.4
9	-0.1	0.0	0.0	-0.1	0.0	0.2	0.1	0.0	0.2	0.8	-0.5
10	0.0	-0.0	0.0	-0.0	-0.0	0.4	-0.2	-0.1	0.3	-0.6	-0.6
11	0.0	-0.0	0.0	-0.0	1.0	-0.0	-0.0	0.0	-0.0	-0.0	0.0

rameters, strong but less obvious correlations are present, which suggest that a simplification of the assumed correction term might be possible.

Figure 7 shows the identified inflow augmentation function. In the picture, whiskers indicate the parameter uncertainty σ_i , computed based on the Cramér–Rao lower error bound as $\sigma = \sqrt{\text{diag}(\mathbf{P})}$ (see Eq. 16). The same figure also reports measurements obtained with hot-wire probes in the empty wind tunnel at three different heights above the floor. These measurements, and especially the ones at hub height, are in good agreement with the estimates provided by the proposed method. The figure also reports (with \times symbols) the lateral position of the upstream turbine for the investigated turntable rotations. Noting that all points are shifted to the left helps explain why the parameter associated with

the inflow node at $Y = 1$ m has a very low – but still finite – observability.

The identified secondary steering augmentation term is visualized in Fig. 8. The plot shows the wind direction change $\Delta\Gamma$ as a function of the distance \tilde{y} to the wake centerline for a turbine misalignment of 20° . The gray shaded area shows the uncertainty band $p_{\text{opt},i} \pm \sigma_i$. Consistently with the findings of Wang et al. (2018), the maximum change in wind direction is found at approximately $0.3D$ on the leeward side of a deflected wake. The maximum magnitude of secondary steering in this operating condition is 1.9° , which is again comparable to the results of Wang et al. (2018).

The validity of the augmentation terms, identified as explained, was assessed by comparing the results of the simulation model with experimental wake measurements from a

Table 4. Correlation coefficients Ψ after the first iteration.

	$p_{\text{speed},1}$	$p_{\text{speed},2}$	$p_{\text{speed},3}$	$p_{\text{speed},4}$	$p_{\text{speed},5}$	$p_{\text{ss},1}$	$p_{\text{ss},2}$	$p_{\text{ss},3}$	$p_{\text{ss},4}$	$p_{\text{ss},5}$	$p_{\text{ss},6}$
$p_{\text{speed},1}$	1.0	-0.5	0.2	-0.1	0.2	-0.1	-0.1	-0.0	-0.1	-0.2	0.2
$p_{\text{speed},2}$	-0.5	1.0	-0.7	0.5	-0.2	-0.0	0.0	0.1	0.0	0.2	0.0
$p_{\text{speed},3}$	0.2	-0.7	1.0	-0.7	0.2	0.1	-0.0	-0.1	0.1	-0.1	-0.2
$p_{\text{speed},4}$	-0.1	0.5	-0.7	1.0	-0.4	-0.1	-0.0	0.1	-0.0	0.1	0.2
$p_{\text{speed},5}$	0.2	-0.2	0.2	-0.4	1.0	-0.1	-0.1	0.0	-0.1	-0.3	0.2
$p_{\text{ss},1}$	-0.1	-0.0	0.1	-0.1	-0.1	1.0	-0.6	-0.1	0.9	-0.4	-0.8
$p_{\text{ss},2}$	-0.1	0.0	-0.0	-0.0	-0.1	-0.6	1.0	-0.3	-0.7	0.6	0.3
$p_{\text{ss},3}$	-0.0	0.1	-0.1	0.1	0.0	-0.1	-0.3	1.0	0.2	0.4	0.6
$p_{\text{ss},4}$	-0.1	0.0	0.1	-0.0	-0.1	0.9	-0.7	0.2	1.0	-0.2	-0.6
$p_{\text{ss},5}$	-0.2	0.2	-0.1	0.1	-0.3	-0.4	0.6	0.4	-0.2	1.0	0.3
$p_{\text{ss},6}$	0.2	0.0	-0.2	0.2	0.2	-0.8	0.3	0.6	-0.6	0.3	1.0

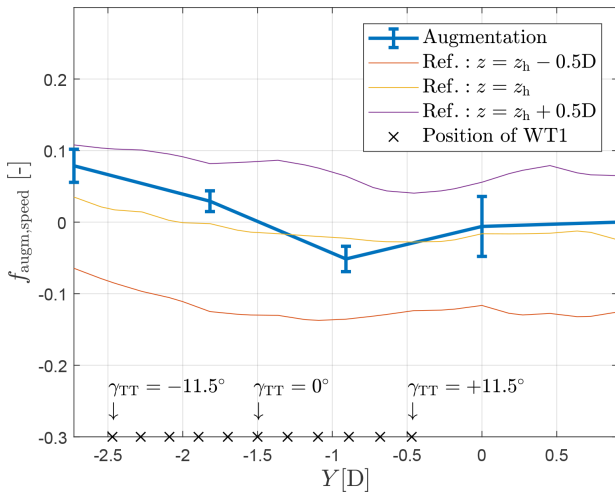


Figure 7. Identified nonuniform inflow speed augmentation term (solid line) and associated standard deviation (whiskers). Hot-wire measurements at different heights above the floor are shown in thin solid lines. The upstream turbine (WT1) y position for all investigated turntable rotations is shown by \times markers placed along the lower edge of the figure.

different test campaign. The setup was identical to the one considered here, except for the fact that only the first two upstream wind turbines were installed in the wind tunnel. At the downstream distance where the third wind turbine should have been installed, flow velocity measurements were obtained at turbine hub height using hot-wire probes. Figure 9 shows wake profiles for the turntable position $\gamma_{TT} = 0^\circ$ for various combinations of turbine yaw misalignments, as indicated by the subplot titles. Each subplot is accompanied by two flow visualizations, one based on the baseline FLORIS model and the other on its augmented version. The figures

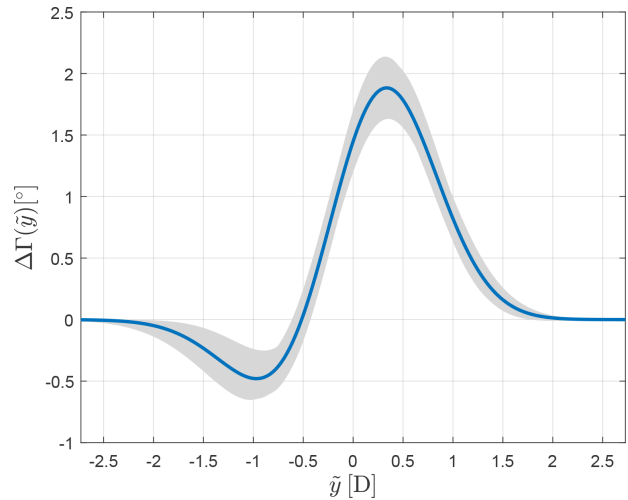


Figure 8. Identified wind direction change $\Delta\Gamma$ due to secondary steering as a function of distance \tilde{y} to the wake centerline for a turbine misalignment of 20° . The gray shaded area shows the uncertainty band.

also include the points at which the flow was measured with the probes.

In the left subplots, the improvements of the augmented model with respect to the baseline FLORIS are exclusively due to the inflow correction, as the upstream turbine is aligned with the flow and therefore there are no secondary steering effects. In the right subplots, the upstream turbine is misaligned ($\gamma_{WT1} = 30^\circ$) and secondary steering effects are present. Taking into account that model augmentation was obtained exclusively by turbine power measurements, the improved matching of the wake profiles is remarkable. Still, even with the extra correction terms some small model

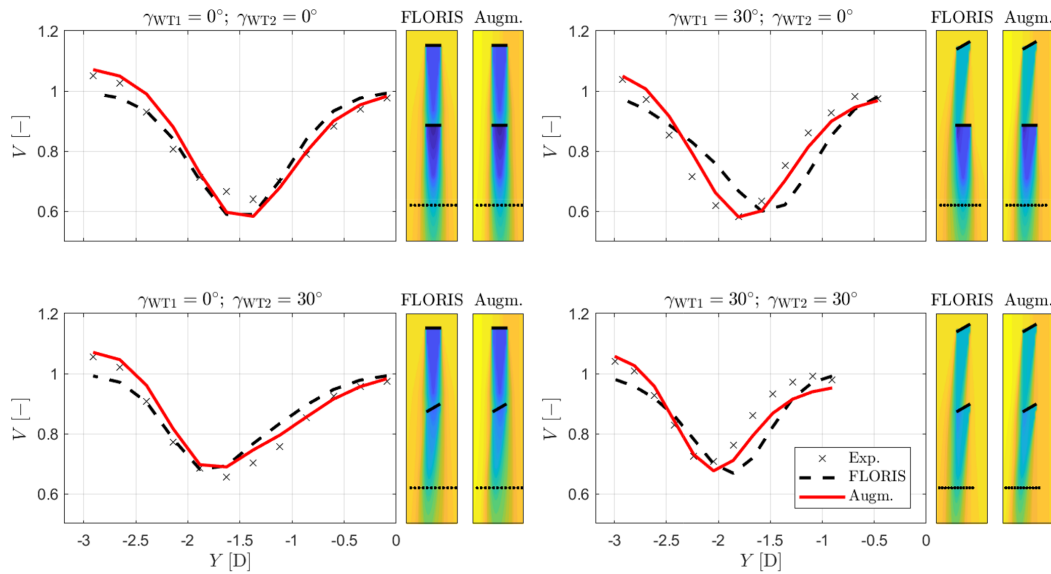


Figure 9. Wake profiles 5D behind WT2 for various combinations of turbine yaw misalignment. Experimental values are indicated by the \times symbols. Each subplot is accompanied by two flow visualizations based on the FLORIS model and its augmented version.

mismatches are present; these might be caused by the wake combination model, which was not augmented in this study.

The turbine power coefficients are computed as

$$C_{P,i} = \frac{P_{WTi}}{0.5\rho AV_\infty(Y_{WTi}, z_h, 0)^3}, \quad (29)$$

where V_∞ is the augmented inflow function given by Eq. (2), evaluated at the respective turbine position Y_{WTi} and hub height z_h . A detailed overview of the results is offered by the figures of Appendix A, which report the power outputs and the model errors for all wind farm configurations. For readability, here a more synthetic overview of the results is presented, by condensing the information contained in Figs. A1, A2, and A3 in the probability density plots of Fig. 10. This figure shows the results for the baseline FLORIS model using a black dashed line, for the 11-parameter augmented model (i.e. including only nonuniform inflow speed and secondary steering corrections) using a red solid line, and for the 27-parameter augmented model (i.e. including all additional augmentation terms presented earlier) using a red dotted line. The root-mean-squared errors ϵ_{RMS} are shown in the respective legends.

Note that the FLORIS error distribution shows two peaks for WT1 and WT3, indicating the presence of two uncorrelated errors. The 11-parameter model removes these peaks, even though a smaller pair of peaks remains for WT2 and WT3, indicating additional errors that only the 27-parameter augmented model is able to capture.

Here again the trend is clear: the addition of nonuniform speed and secondary steering substantially increases the accuracy of the baseline model, with additional small – but

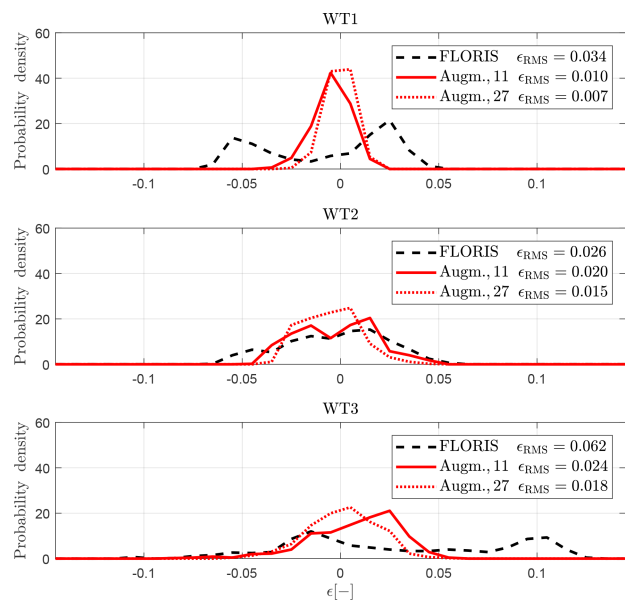


Figure 10. Error distributions for each turbine for all tested configurations, for the baseline FLORIS model (black dashed line), the 11-parameter augmented model (red solid line), and the 27-parameter augmented model (red dotted line).

not insignificant – gains offered by the additional correction terms. Finally, there is still room for improvement, possibly through extra correction terms not yet explored.

Table 5. Turbine specifications.

Type	Rated power (MW)	Cut-in wind speed (m s^{-1})	Rated wind speed (m s^{-1})	Rotor diameter (m)	Hub height (m)	Installed units (-)
GE1.5s	1.5	4	13	70.5	65	36
GE1.5sle	1.5	3.5	12	77	80	7

3.2 Field application

In this section the model augmentation and identification method is applied to a full-scale wind farm, to test its applicability and usability in a realistic scenario. In such conditions, it is often difficult to assess whether the identified model corrections are indeed physical or not, due to a lack of knowledge of the actual ground truth. To deal with this problem, the classical approach of splitting the data set was used here: first, a relatively small subset of measurements is used for model and error identification; then, the rest of the data set is used for a verification of the generality of the identified model and of its improved performance with respect to the baseline one.

3.2.1 Wind farm and data preprocessing

The onshore wind farm is situated close to Sedini, on the Italian island of Sardinia, and it consists of 43 GE1.5s and GE1.5sle wind turbines, as specified in Table 5.

The wind farm is located at a rather complex site, as shown in Fig. 11. Blue turbines are of the type GE1.5sle and black and red turbines are of the type GE1.5s, the latter being used as sensing turbines as explained later. Figure 12 shows a top view of the wind farm, including the turbine identifiers.

Historical 10 min SCADA data were made available for this research for a period of 24 months, throughout the years 2015 and 2016. The recorded turbine yaw orientations exhibit sudden jumps and long-term drifts. An ad hoc algorithm was developed for detecting and correcting these data issues. On average, for each turbine 45 % of the data points were missing, and 23 % were discarded because of low power output ($< 5 \text{ kW}$) or rotor speed ($< 1 \text{ rpm}$). As a result, about 33 700 data points were available for each turbine. Regarding the missing data points, it is unknown whether the turbines were operating or just not reporting. To avoid eliminating a large fraction of the data set, it was assumed that the turbines were indeed operational and thus shedding wakes. This way, even if recordings of one or more turbines were missing at a specific time instance, the data points of the other turbines could still be used.

As no direct measurements of ambient conditions were available, the method described by Schreiber et al. (2018) was used to identify ambient wind speed and direction. The procedure works as follows. First, the ambient wind direction is estimated from turbine yaw orientations. Second, the ambient wind speed is estimated from the rotor effective wind

speed of the free-stream turbines, computed from the turbine power curve below rated wind speed. For this purpose, the three sensing turbines A5-24, A5-25, and A5-26 indicated in red in Fig. 12 were used, checking that they were unwaked by using the flow model; the average of these speeds was attributed to the location of turbine A5-25. This way, 5667 ambient wind conditions could be processed for a range of wind directions $\Gamma \in [184^\circ, 320^\circ]$. Based on the ambient wind conditions, the data of all turbines were aggregated in two-dimensional bins: ambient wind speed (bin width of 2 m s^{-1}) and ambient wind direction (bin width of 5°). Figure 13 shows the scaled number of measurements in each bin between 6 and 12 m s^{-1} .

3.2.2 Model setup

Here again the FLORIS implementation was based on the version available online (Doekemeijer and Storm, 2019). The initial values of both the wake and turbulence model parameters were set according to Bastankhah and Porté-Agel (2016) for (α^*, β^*) , Crespo and Hernández (1996) for $(\text{TI}_a^*, \text{TI}_b^*, \text{TI}_c^*, \text{TI}_d^*)$, Niayifar and Porté-Agel (2015) for (k_a^*, k_b^*) , and Gebraad et al. (2014) for (a_d^*, b_d^*) , as reported in Table 6.

The required turbine power and thrust versus wind speed curves were provided by the turbine manufacturer. The vertical shear exponent of the inflow was set to $\alpha_{\text{vs}} = 0.143$ and the turbulence intensity to 14 %, which represent annual average values measured at 65 m of height by an on-site met mast. Air density was set to the constant value $\rho = 1.177 \text{ kg m}^{-3}$.

The different turbine foundation heights were accounted for by accordingly increasing the tower heights, using the lowest foundation height as reference (turbine A1-02). Indeed, power measurements of the upstream turbines show a correlation with the actual turbine hub height with respect to sea level (SL), as shown in Fig. 14. As indicated by the only approximate correlation shown by the figure, it is clear that such simple correction might not provide satisfactory results for all wind directions and all turbines, because complex orthographic flow effects might also play a role. Nonetheless, this approximate correction seems to be a step in the right direction. In addition, some of these effects may be corrected by the lateral nonuniformity terms added to the augmented model. The reference height of the sheared inflow z_h (see Eq. 2) was set to the hub height of the sensing turbine A5-25.

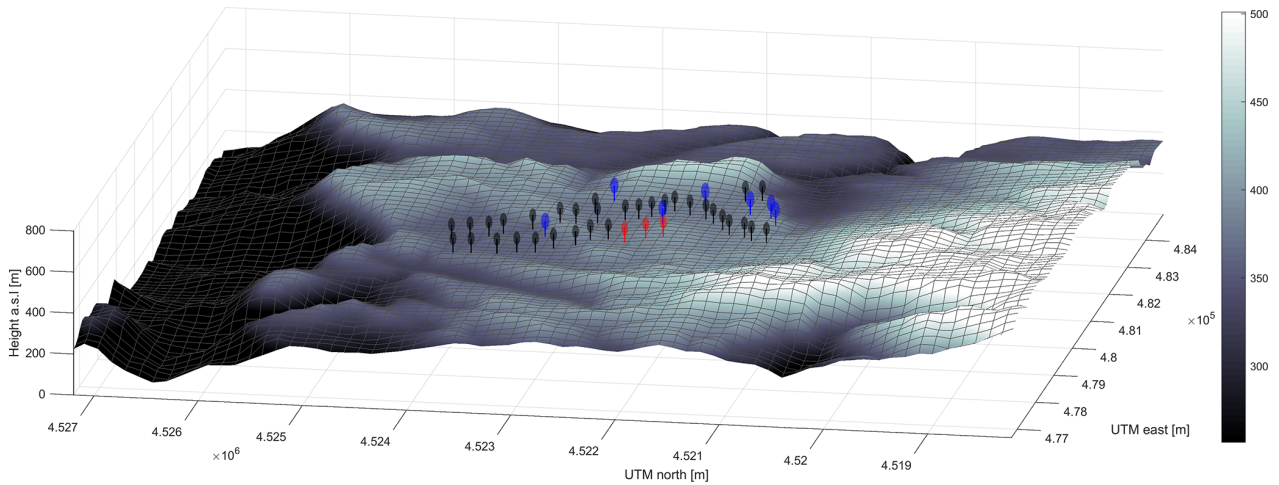


Figure 11. The 3D view of the Sedini wind farm with terrain elevation, as seen from $\Gamma = 260^\circ$.

Table 6. Initial FLORIS parameters for the Sedini wind farm.

α^*	β^*	k_a^*	k_b^*	a_d^*	b_d^*	TI_a^*	TI_b^*	TI_c^*	TI_d^*
2.32	0.154	0.3837	0.0037	-0.0356	-0.01	0.73	0.8325	0.0325	-0.32

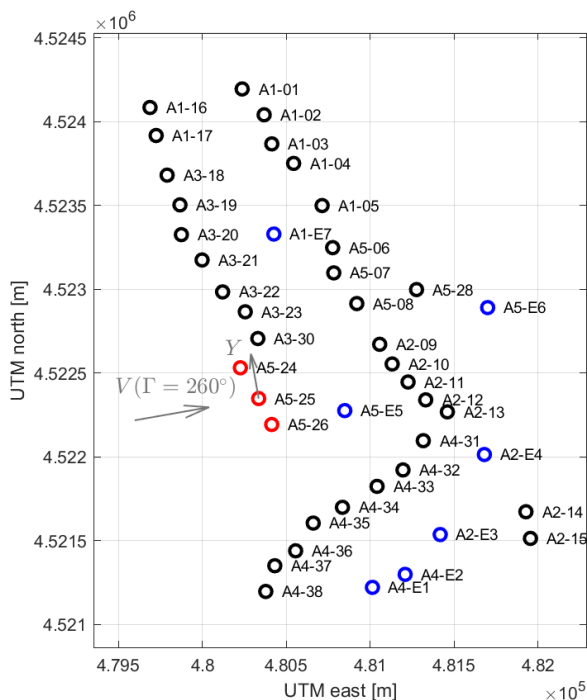


Figure 12. Top view of the Sedini wind farm with turbine identifiers. The gray arrows indicate the x and y axes for an ambient wind direction $\Gamma = 260^\circ$.

3.2.3 Ranking of correction terms

As for the wind tunnel experiments, here again a first analysis was aimed at ranking the various correction terms. However, since the turbines were operated with a conventional wind-aligned strategy, secondary steering corrections were neglected. The ranking is based on data points in the range $V \in [8, 10] \text{ m s}^{-1}$, as described in greater detail in the following.

Figure 15 shows the relative increase in the cost function after optimization eliminating one set of parameters at a time. The results clearly indicate that the nonuniform wind farm inflow speed p_{speed} is the most important correction. In fact, this was to be expected, given that the Sedini wind farm is located at a rather complex site. Results also indicate a non-negligible effect of the wake deflection parameters for non-misaligned operation (a_d, b_d).

On the other hand, the additional model augmentation parameters ($p_{TI}, p_{\text{winddir}}, p_{\text{acc}}, p_{\text{shear}}$) do not seem to contribute to a significant extent. Note also the slight retuning of parameters (α, β, k_a, k_b) and (TI_a, TI_b, TI_c, TI_d), which can be explained with the fact that their initial values were taken from the literature and therefore apply to different turbine types and sites.

Given these results, the rest of the analysis is based only on the subset of parameters $p_{\text{inflow}}, (p_{a_d}, p_{b_d}), (p_\alpha, p_\beta), (p_{k_a}, p_{k_b}),$ and $(p_{TI_a}, p_{TI_b}, p_{TI_c}, p_{TI_d})$. The augmentation term for nonuniform inflow speed is modeled using five nodes along the lateral position Y located at $[-2000; -1000; 0; 1000; 2000] \text{ m}$ (which is approximately

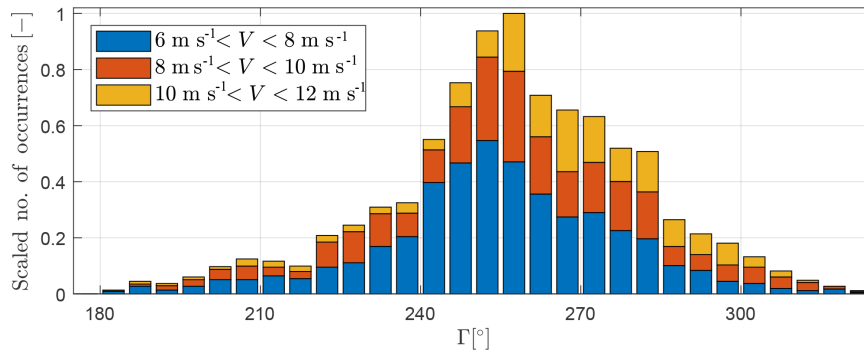


Figure 13. Scaled number of measurement data points (10 min mean) within each speed and direction bin.

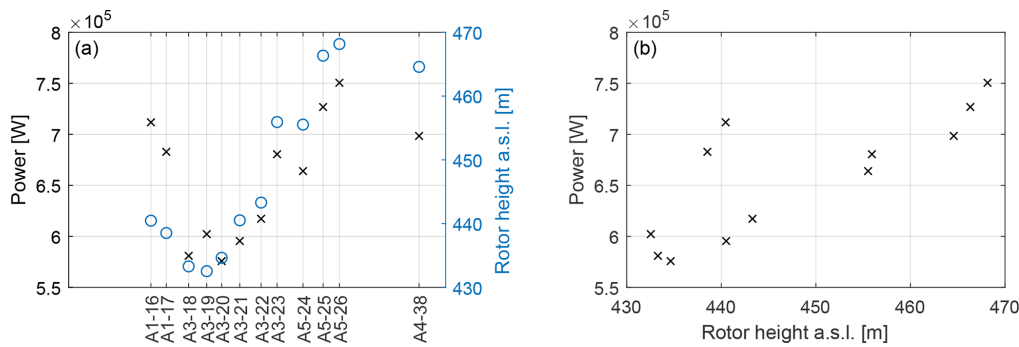


Figure 14. Correlation between power output and hub height with respect to SL. (a) Power (\times symbols and left y axis) and rotor height above SL (\circ symbols and right y axis) vs. lateral turbine position for a wind direction $\Gamma = 240^\circ$. (b) Power vs. rotor height above SL for $\Gamma \in [220^\circ, 275^\circ]$ and $V_\infty \in [8, 10] \text{ m s}^{-1}$. All conditions are free stream and all turbines of type GE1.5s.

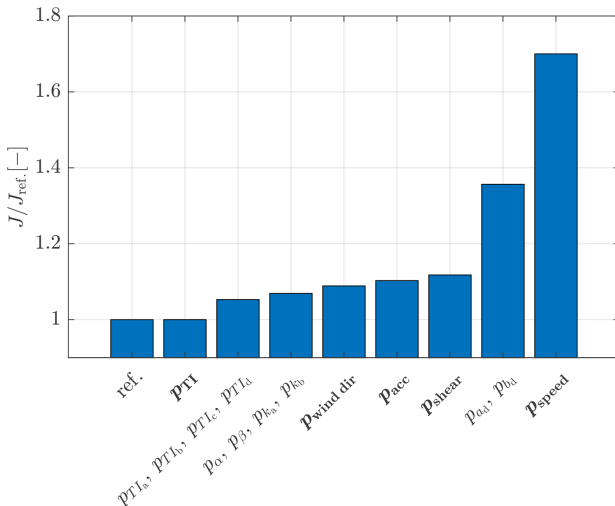


Figure 15. Relative increase in the optimization cost function for the Sedini wind farm when eliminating one parameter set at a time.

$[-28; -14; 0; 14; 28]D_{GE1.5s}$) and six nodes in wind direction Γ at $[180; 210; 140; 270; 300; 330]^\circ$, resulting in 30

nodes. The Y -coordinate axis is orthogonal to the wind direction and its origin $Y = 0 \text{ m}$ is located at the position of wind turbine A5-25, as shown in Fig. 12.

The definitions of the correction parameter, together with their bounds and converged values, are reported in Table 7. Note that all parameters were set to zero at the beginning of the identification process.

3.2.4 Results

To identify the 40 parameters of Table 7, only aggregated mean power measurements for wind speeds $V \in [8, 10] \text{ m s}^{-1}$ were used. In addition, only one-third of all wind direction bins were employed,

The model outputs y (see Eq. 9) were defined as

$$y = \frac{1}{P_{\text{ref}}} \begin{bmatrix} P_{\text{WT1}} \\ \dots \\ P_{\text{WT43}} \end{bmatrix}, \quad (30)$$

where $P_{\text{WT}i}$ is the power of wind turbine i and $P_{\text{ref}} = 1.11 \text{ MW}$ a reference wind turbine value used as a scaling factor. A diagonal measurement noise covariance matrix \mathbf{R} was used, with all diagonal terms equal to $\sigma^2 = 0.01^2$. The threshold of the highest acceptable variance in the orthogonal

Table 7. Definition of the parameters, together with their lower and upper bounds, and initial and identified values. Bold italic numbers indicate vectors containing that number repeated as many times as the vector length.

i	p_i	$p_{lb,i}$	$p_{ub,i}$	$p_{init,i}$	$p_{opt,i}$	Implementation
1–30	p_{inflow}	<i>-0.1</i>	<i>0.1</i>	<i>0</i>	see Fig. 16	$f_{augm, speed}(Y, Z, \Gamma, c_{speed}, p_{speed})$
31	p_α	$-\alpha^*$	4	0	0.7837	$\alpha = \alpha^* + p_\alpha$
32	p_β	$-\beta^*$	2	0	1.063	$\beta = \beta^* + p_\beta$
33	p_{k_a}	$-k_a^*$	1	0	-0.2440	$k_a = k_a^* + p_{k_a}$
34	p_{k_b}	$-k_b^*$	0.1	0	0.01862	$k_b = k_b^* + p_{k_b}$
35	p_{a_d}	-0.5	0.5	0	-0.3169	$a_d = a_d^* + p_{a_d}$
36	p_{b_d}	-0.1	0.1	0	-0.02246	$b_d = b_d^* + p_{b_d}$
37	p_{TI_a}	$-TI_a^*$	1	0	-0.09577	$TI_a = TI_a^* + p_{TI_a}$
38	p_{TI_b}	-1	1	0	0.3403	$TI_b = TI_b^* + p_{TI_b}$
39	p_{TI_c}	-1	1	0	0.4452	$TI_c = TI_c^* + p_{TI_c}$
40	p_{TI_d}	-1	1	0	-0.3337	$TI_d = TI_d^* + p_{TI_d}$

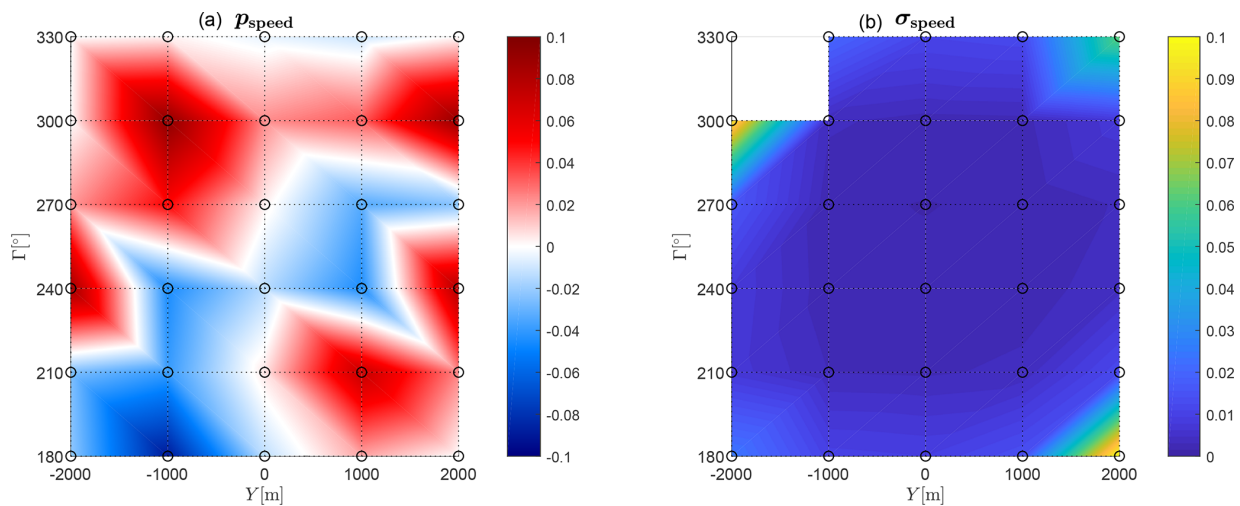


Figure 16. Identified inflow augmentation parameters (a) and their uncertainties (b). Nodal points are indicated by the circle markers.

parameter estimate was set to $\sigma_t^2 = 0.01$, which corresponds to a relative variance of 2%. The relative weight of each observation was set proportional to the number of measurement points within the respective bin. In a first iteration, 29 orthogonal parameters could be identified. In the second and third iterations only 23 and 25 orthogonal parameters fell below the threshold, although results changed only marginally after the first iteration.

The identified optimal parameter values $p_{opt,i}$ are included in Table 7 and, for the inflow augmentation, are also reported in Fig. 16. The plot shows, according to the color map, the inflow augmentation function values $f_{augm, speed}(Y, \Gamma, c_{speed}, p_{speed})$ in panel (a). Each nodal point is indicated by a circle marker. The figure shows that significant variations in the inflow speed have been detected: for example, considering $\Gamma = 270^\circ$, the inflow speed at $Y = +1000$ m (approximately at the location of wind turbines A3-19, A3-20, and A3-21) is 3.5% smaller than the one mea-

sured at the reference turbines A5-24, A5-25, and A5-26. For the same wind direction, the speed at $Y = -1000$ m (approximately located at the wind turbines A4-36, A4-37, and A4-38) is 4.8% larger. These variations are expected to be mainly caused by terrain effects. Panel (b) of Fig. 16 shows the parameter uncertainty (Cramér–Rao bounds). The parameter at the nodal point ($Y = -2000$ m; $\Gamma = 330^\circ$) is completely unobservable, because it lies far outside of the wind farm perimeter (see Fig. 12). Some of the outer nodal points at $Y = \pm 2000$ m do show significantly increased uncertainties. However, the corresponding augmentation parameters (panel a) are approximately zero.

Figure 17 shows the power coefficient of each individual wind turbine, as indicated by the subplot title, as a function of wind direction. The power coefficient is computed as $C_p = P/(0.5\rho AV^3)$, where $\rho = 1.177 \text{ kg m}^{-3}$ is the constant air density, $A = \pi(70.5/2)^2 \text{ m}^2$ a reference rotor area, and V the corresponding estimated ambient wind speed.

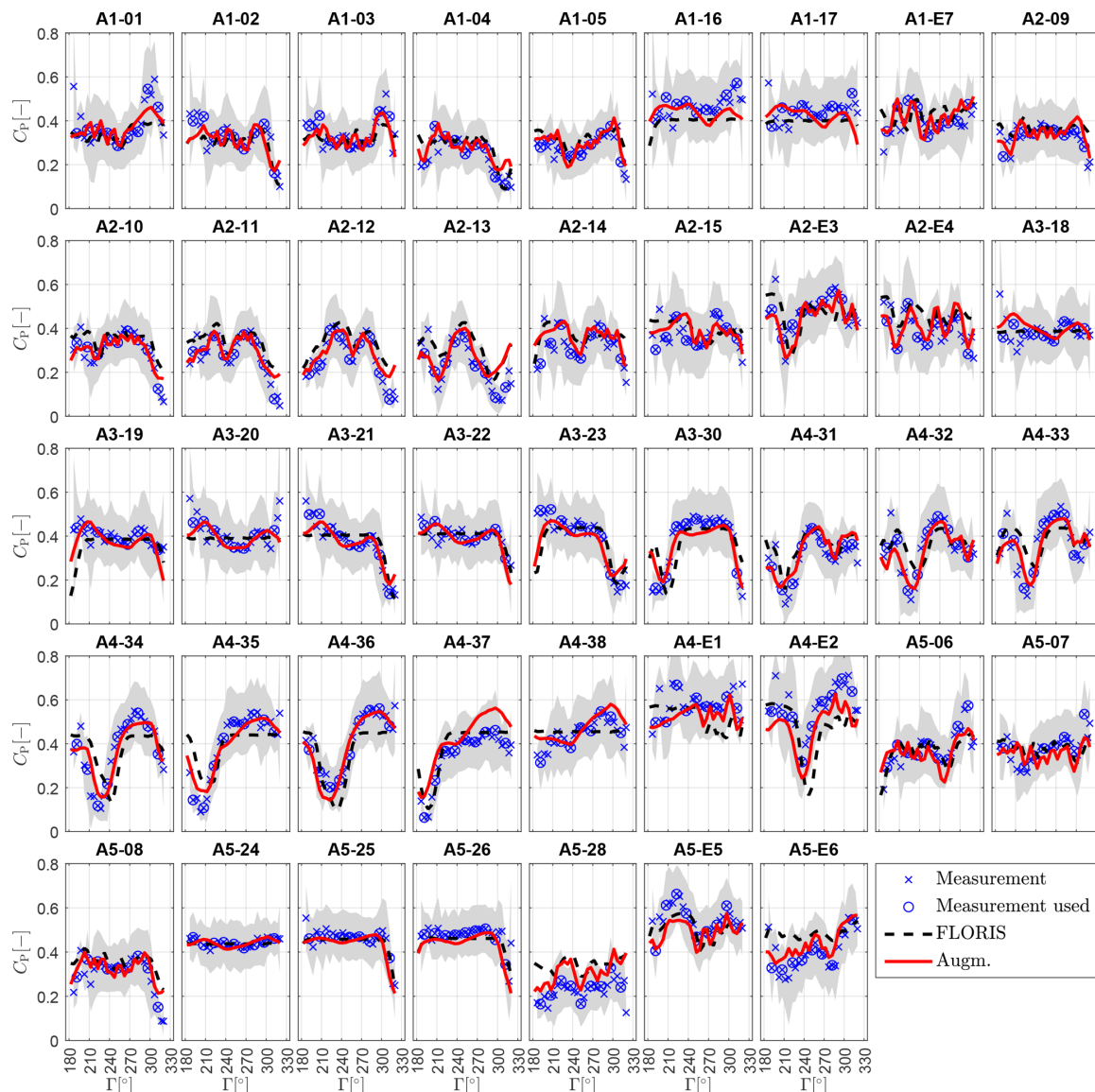


Figure 17. Power coefficient of each individual wind turbine, as indicated by the subplot title, as a function of wind direction Γ for wind speeds $V \in [8, 10] \text{ m s}^{-1}$. The gray shaded area indicates the standard deviation within the binned measurements. The number of measurements within each bin is reported in Fig. 13.

Blue crosses indicate SCADA data points, with the ones used for identification circled. The gray shaded area indicates the standard deviation within the binned measurements. The FLORIS (non-augmented) power estimates are shown by black dashed lines, whereas the augmented model results are shown using red solid lines.

Even though the baseline FLORIS power estimates already exhibit a reasonable correlation with the measurements for many turbines and wind directions, a significant improvement is achieved by the augmented model. Note that for $\Gamma < 210^\circ$ and $\Gamma > 300^\circ$ the number of measurement points

within each bin is reduced (see Fig. 13), limiting the measurement quality and trustworthiness. More specifically, the augmented model shows improvements in the modeling of the free-stream turbine power, due to the effects of the wind farm inflow augmentation terms. Furthermore, the predictions of the wake-induced power deficits are corrected, improving in many cases the deficit depth as well as the deficit location in terms of wind direction.

The same results of Fig. 17 are also presented in a more synthetic form in terms of error probability densities in Fig. 18, where the error is defined as $\epsilon = C_{P, \text{Meas.}} -$

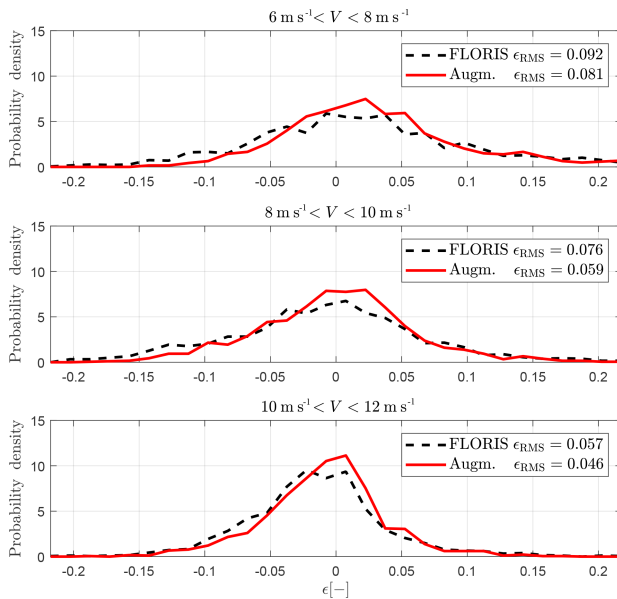


Figure 18. Error probability density functions for different wind speed ranges.

$C_{P,FLORIS/Augm.}$. Each subplot shows the results for a different wind speed range. Note that the modeling error is also reduced for wind speed ranges that have not been used for model identification (i.e. $V \in [6, 8] \text{ m s}^{-1}$ and $V \in [10, 12] \text{ m s}^{-1}$). The overall root-mean-squared error is reported within the legend, showing error reductions of 14 %, 22 %, and 19 %, highlighting the generality of the identified model and augmentation parameters.

4 Conclusions

This paper has presented a new method to calibrate and augment parametric wind farm models. The proposed approach builds on the vast body of knowledge and experience embedded in available reduced wind farm flow models. However, recognizing that any such model will always have only a limited prediction accuracy, the present approach augments a baseline model with extra ad hoc terms designed to correct some of its presumed specific deficiencies. These additional elements of the model are then learned from operational data. Optionally, the baseline model parameters can also be tuned within a single integrated process. By design, the method has been exclusively based here on SCADA power measurements; therefore, it is readily applicable to most operational wind farms, whenever such data are available. However, the concept of model augmentation is very general and could clearly also be used with other measurements.

To limit the number of free parameters and to overcome the fact that the identification problem can be over-parameterized and hence ill-posed, a parameter transforma-

tion into an orthogonal space has been used. Thereby, only parameters that are sufficiently visible within a given data set enter into the identification process.

The method was first applied to a large data set obtained with scaled wind turbines operating in a boundary layer wind tunnel. Thereby, it was shown that a correct learning of the extra modeling terms is achieved. These conclusions are made possible by the fact that, in this case, the flow and wake characteristics are known with good accuracy. Next, the method was tested on a real wind farm, in a realistic and highly complex situation.

Based on the results shown here, the following conclusions can be drawn.

- Within the wind tunnel environment, a correct learning of nonuniform wind farm inflow speed and of secondary steering effects has been achieved. In particular, the latter shows a good match with detailed wake measurements in wind-misaligned conditions. It is remarkable, and very promising, that such detailed features of the solution could be inferred purely from operational power data, even when starting from a baseline model that does not at all consider secondary steering.
- The application to field data has shown that, as expected for the complex-terrain site analyzed here, orographic effects play a driving role. A marked model improvement could be observed, even in conditions where the model was used for extrapolating outside of the training conditions. It is worth noting that, in many practical onshore applications, orographic effects will be present, and the fact that one can learn them from simple and readily available operational data is very encouraging. Again, it should be explicitly pointed out that the baseline model did not include any orographic corrections.
- It has been shown that model tuning and the learning of extra correction terms can be achieved simultaneously. This reduces the risk of adapting the baseline parameters beyond their reasonable limits, driven by unmodeled physics.
- Although the augmented models show a much improved accuracy with respect to the baseline, some model mismatch still remains. Although these remaining errors may often be caused by issues in the data rather than in the model, additional improvements are thought to be possible.

Future work will apply the proposed method to other wind farms, to increase confidence in the obtained results. From longer and richer data sets, possibly in conjunction with meteorological reanalyses, it is presumed that yearly and seasonal variations could be observed. The integration of CFD analyses can be used to support and confirm the identification of orographic effects. Attention should also be paid to

J. Schreiber et al.: Wind farm model augmentation

667

improved and additional forms of model corrections, including wake overlap models. Finally, it is worth pointing out again that an improved knowledge of the flow within a wind farm finds applicability in a potentially large range of digitally driven applications, including wind farm control, lifetime estimation, power forecasting, predictive maintenance, and others. Therefore, it is expected that methods for high-accuracy flow predictions in wind farms will be the subject of significant future research efforts.

Appendix A: Extended wind tunnel results

Figures A1, A2, and A3 report the power outputs of WT1, WT2, and WT3, respectively, for all tested configurations. In each figure, clusters of three subplots represent a unique turntable position, as indicated by the title and the wind farm layout sketch therein. The left part of each subplot shows the turbine power coefficient C_{P,WT_i} as a function of γ_{WT1} (x axis) and γ_{WT2} (y axis). All measured configurations are indicated by a small cross symbol, whereas the measurements used for parameter identification are circled. The central part of each subplot shows the FLORIS model error $\epsilon_{\text{FLORIS}} = C_{P,\text{Meas.}} - C_{P,\text{FLORIS}}$, including an annotation of the root-mean-squared error ϵ_{RMS} . Similarly, the right part of each subplot shows the augmented model error $\epsilon_{\text{Augm.}}$.

For the first upstream wind turbine, WT1, the baseline FLORIS shows significant errors depending on the turntable position. For $\gamma_{\text{TT}} < 0^\circ$ the model underpredicts turbine power because of the lack of uniformity of the flow, as also shown in Fig. 7. The opposite behavior can be seen for $\gamma_{\text{TT}} > 0^\circ$. The augmented model however shows significant improvements, which are due to the inflow correction. Still, some underprediction for $\gamma_{\text{TT}} = -11.5^\circ$ is present, which is probably caused by an excessively small number of parameters in the inflow augmentation function and/or by the third wind turbine power measurements, which are also strongly affected by lateral inflow variations.

The power of WT2, shown in Fig. A2, is only weakly affected or improved by the model corrections. In fact, in all investigated conditions, the second turbine lateral position remains almost constant, such that the inflow correction does not have a significant direct effect. However, secondary steering only slightly changes the inflow direction at WT2; for example, as shown in Fig. 8, a 20° misalignment of WT1 changes the wind direction by about 1.9° . This leads to small misalignments and thus only very small changes in power output considering the cosine law. In addition, secondary steering also leads to a slight lateral deflection of the nonuniform inflow.

The power of WT3, reported in Fig. A3, shows significant improvements when using the augmentation terms. For example, for $\gamma_{\text{TT}} > 0^\circ$ the baseline model underpredicts the real flow velocities – and hence the power output – at WT3, an error that is corrected by the augmented model. In addition, for $|\gamma_{\text{WT1}}| > 0$, secondary steering augmentation affects the deflection of the second turbine wake (as shown in Fig. 8), leading to further improvements.

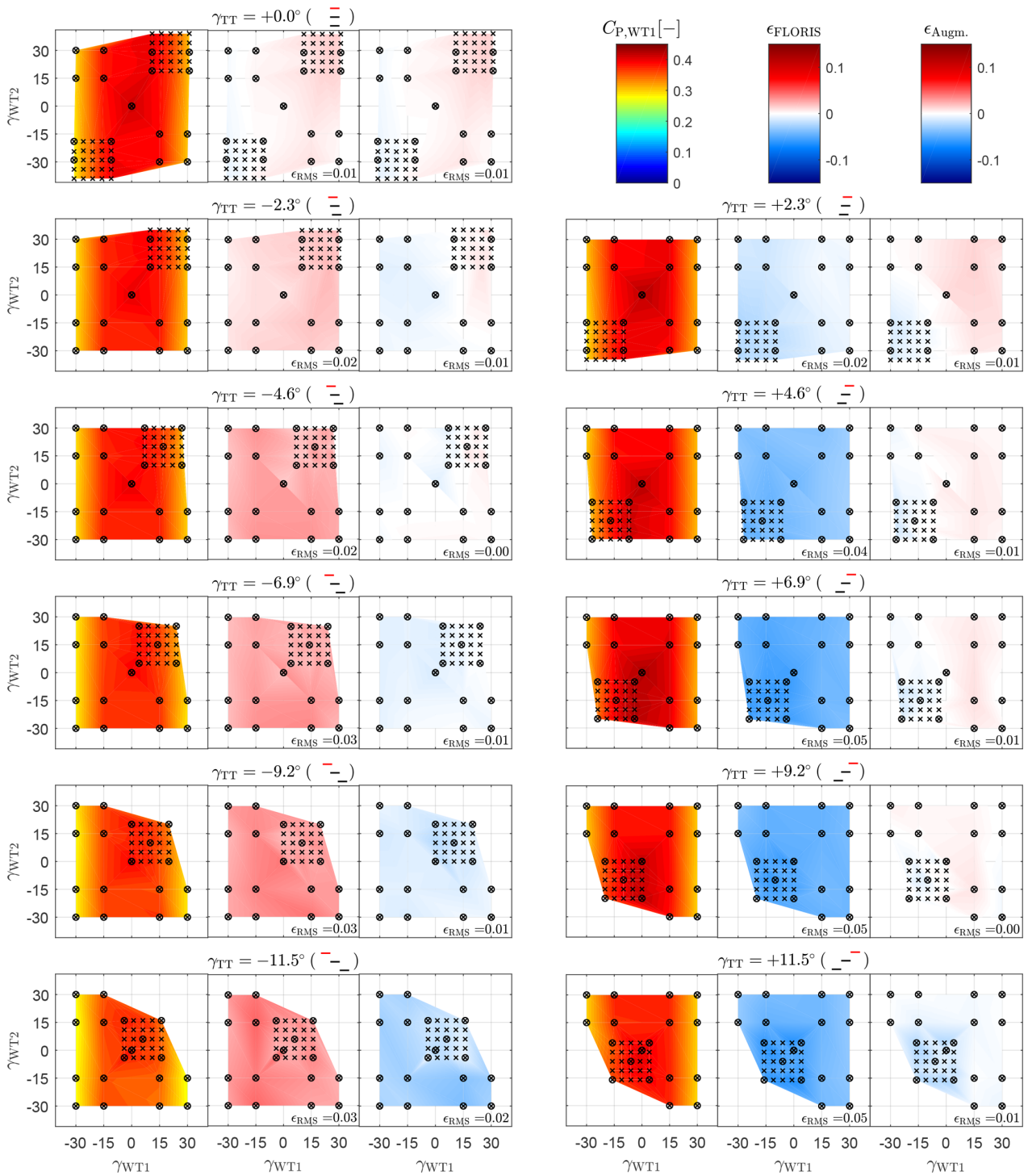


Figure A1. Wind turbine WT1. Each cluster of three subplots represents a unique turntable position, as indicated by the title and the wind farm layout sketch. Left subplot: turbine power coefficient $C_{p,WT1}$ as a function of γ_{WT1} (x axis) and γ_{WT2} (y axis). Middle subplot: FLORIS model error. Right subplot: augmented model error. Cross symbols: all measured configurations. Circles: conditions used for parameter identification.

670

J. Schreiber et al.: Wind farm model augmentation

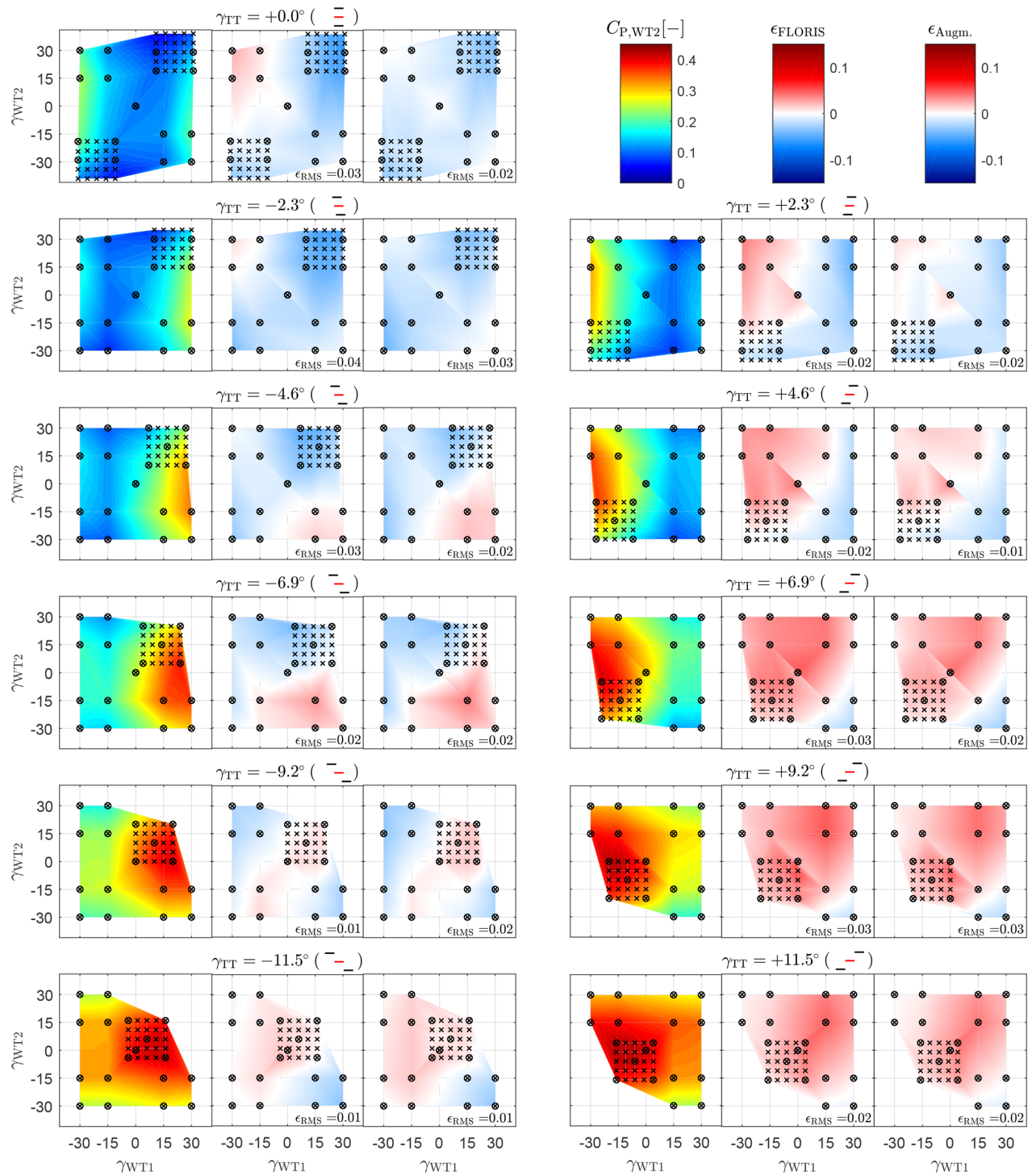


Figure A2. Wind turbine WT2. Each cluster of three subplots represents a unique turntable position, as indicated by the title and the wind farm layout sketch. Left subplot: turbine power coefficient $C_{P,WT2}$ as a function of γ_{WT1} (x axis) and γ_{WT2} (y axis). Middle subplot: FLORIS model error. Right subplot: augmented model error. Cross symbols: all measured configurations. Circles: conditions used for parameter identification.

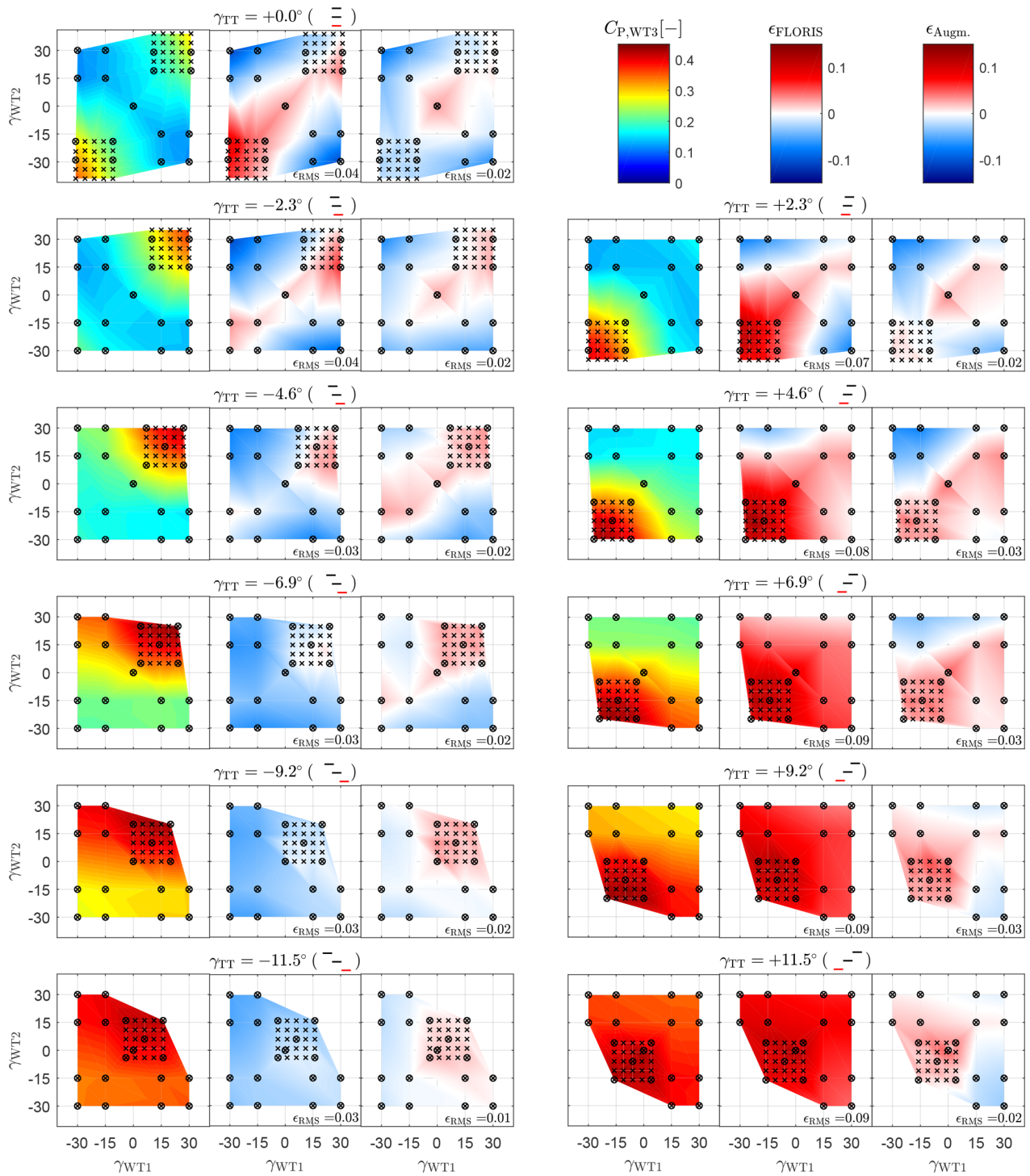


Figure A3. Wind turbine WT3. Each cluster of three subplots represents a unique turntable position, as indicated by the title and the wind farm layout sketch. Left subplot: turbine power coefficient $C_{P,WT3}$ as a function of γ_{WT1} (x axis) and γ_{WT2} (y axis). Middle subplot: FLORIS model error. Right subplot: augmented model error. Cross symbols: all measured configurations. Circles: conditions used for parameter identification.

Code and data availability. A MATLAB implementation of the wind farm model can be obtained by contacting the authors.

Author contributions. JS conducted the main research work. CLB developed the core idea of model augmentation, its formulation and the overall solution methodology and supervised the whole research. JS and CLB wrote the manuscript. BS preprocessed the field measurements. FC was responsible for the execution of the wind tunnel tests and the elaboration of the experimental results. All authors provided important input to this research work through discussions, feedback, and improving the manuscript.

Competing interests. The authors declare that they have no conflict of interest.

Acknowledgements. The authors express their gratitude to Enel Green Power S.p.A., which granted access to the field data, and to Stefan Kern of GE Renewable Energy for helping with the data post-processing. Special thanks go to Robin Weber of Technische Universität München and Stefano Cacciola, Alessandro Croce, Paolo Schito, and Alberto Zasso of Politecnico di Milano for their help in conducting the wind tunnel experiments.

Financial support. This research has been supported by the Horizon 2020 Framework Programme, H2020 Energy (CL-Windcon, grant no. 727477) and the Bundesministerium für Wirtschaft und Energie (CompactWind II, grant no. 0325492G).

Review statement. This paper was edited by Alessandro Croce and reviewed by two anonymous referees.

References

- Bastankhah, M. and Porté-Agel, F.: Experimental and theoretical study of wind turbine wakes in yawed conditions, *J. Fluid Mech.*, 806, 506–541, 2016.
- Bastine, D., Witha, B., Wächter, M., and Peinke, J.: POD Analysis of a Wind Turbine Wake in a Turbulent Atmospheric Boundary Layer, *J. Phys. Conf. Ser.*, 524, 012153, <https://doi.org/10.1088/1742-6596/524/1/012153>, 2014.
- Bleeg, J., Purcell, M., Ruisi, R., and Traiger, E.: Wind Farm Blockage and the Consequences of Neglecting Its Impact on Energy Production, *Energies*, 11, 1609, <https://doi.org/10.3390/en11061609>, 2018.
- Boersma, S., Doekemeijer, B., Vali, M., Meyers, J., and van Wingerden, J.-W.: A control-oriented dynamic wind farm model: WF-Sim, *Wind Energ. Sci.*, 3, 75–95, <https://doi.org/10.5194/wes-3-75-2018>, 2018.
- Bottasso, C. L., Cacciola, S., and Iriarte, X.: Calibration of wind turbine lifting line models from rotor loads, *J. Wind Eng. Ind. Aerod.*, 124, 29–45, <https://doi.org/10.1016/j.jweia.2013.11.003>, 2014a.
- Bottasso, C. L., Campagnolo, F., and Petrović, V.: Wind tunnel testing of scaled wind turbine models: Beyond aerodynamics, *J. Wind Eng. Ind. Aerod.*, 127, 11–28, <https://doi.org/10.1016/j.jweia.2014.01.009>, 2014b.
- Breton, S.-P., Sumner, J., Sørensen, J. N., Hansen, K. S., Sarmast, S., and Ivanell, S.: A survey of modelling methods for high-fidelity wind farm simulations using large eddy simulation, *Philos. T. Roy. Soc. A*, 375, 20160096, <https://doi.org/10.1098/rsta.2016.0097>, 2017.
- Campagnolo, F., Petrović, V., Bottasso, C. L., and Croce, A.: Wind tunnel testing of wake control strategies, *Proceedings of the American Control Conference (ACC)*, 6–8 July 2016, Boston, MA, USA, 513–518, <https://doi.org/10.1109/ACC.2016.7524965>, 2016a.
- Campagnolo, F., Petrović, V., Nanos, E. M., Tan, C. W., Bottasso, C. L., Paek, I., Kim, H., and Kim, K.: Wind tunnel testing of power maximization control strategies applied to a multi-turbine floating wind power platform, in: *Proceedings of the The 26th International Ocean and Polar Engineering Conference*, 26 June–2 July 2016, Rhodes, Greece, 2016b.
- Campagnolo, F., Petrović, V., Schreiber, J., Nanos, E. M., Croce, A., and Bottasso, C. L.: Wind tunnel testing of a closed-loop wake deflection controller for wind farm power maximization, *J. Phys. Conf. Ser.*, 753, 032006, <https://doi.org/10.1088/1742-6596/753/3/032006>, 2016c.
- Campagnolo, F., Molder, A., Schreiber, J., and Bottasso, C. L.: Comparison of Analytical Wake Models with Wind Tunnel Data, *J. Phys. Conf. Ser.*, 1256, 012006, <https://doi.org/10.1088/1742-6596/1256/1/012006>, 2019.
- Crespo, A. and Hernández, J.: Turbulence characteristics in wind-turbine wakes, *J. Wind Eng. Ind. Aerod.*, 61, 71–85, [https://doi.org/10.1016/0167-6105\(95\)00033-X](https://doi.org/10.1016/0167-6105(95)00033-X), 1996.
- Doekemeijer, B. M. and Storm, R.: FLORISSE M, available at: https://github.com/TUDELFT-DataDrivenControl/FLORISSE_M/tree/f0653ef3e8e56e284cdfa0a188aba0a7e42fce5c (last access: 30 July 2019), 2018.
- Doekemeijer, B. M. and Storm, R.: FLORISSE M, available at: https://github.com/TUDELFT-DataDrivenControl/FLORISSE_M/tree/ed2885107ca2600d0616f86cab3b3d59c5f0cb38, last access: 30 July 2019.
- Doekemeijer, B. M., Boersma, S., Pao, L. Y., and Van Wingerden, J. W.: Ensemble Kalman filtering for wind field estimation in wind farms, in: *2017 American Control Conference (ACC)*, 24–26 May 2017, Seattle, USA, IEEE, Piscataway, NJ, USA, 19–24, <https://doi.org/10.23919/ACC.2017.7962924>, 2017.
- Doekemeijer, B. M., Fleming, P. A., and van Wingerden, J.-W.: A tutorial on the synthesis and validation of a closed-loop wind farm controller using a steady-state surrogate model, in: *2019 American Control Conference ACC*, 10–12 July 2019, Philadelphia, PA, USA, 2825–2836, <https://doi.org/10.23919/ACC.2019.8815126>, 2019.
- Dörenkämper, M., Witha, B., Steinfeld, G., Heinemann, D., and Kühn, M.: The impact of stable atmospheric boundary layers on wind-turbine wakes within offshore wind farms, *J. Wind Eng. Ind. Aerod.*, 144, 146–153, <https://doi.org/10.1016/j.jweia.2014.12.011>, 2015.
- Fleming, P. A., Gebraad, P. M., Lee, S., van Wingerden, J.-W., Johnson, K., Churchfield, M., Michalakes, J., Spalart, P., and Moriarty, P.: Evaluating techniques for redirecting

- turbine wakes using SOWFA, *Renew. Energ.*, 70, 211–218, <https://doi.org/10.1016/j.renene.2014.02.015>, 2014.
- Fleming, P., Annoni, J., Shah, J. J., Wang, L., Ananthan, S., Zhang, Z., Hutchings, K., Wang, P., Chen, W., and Chen, L.: Field test of wake steering at an offshore wind farm, *Wind Energ. Sci.*, 2, 229–239, <https://doi.org/10.5194/wes-2-229-2017>, 2017.
- Fleming, P., Annoni, J., Churchfield, M., Martínez-Tossas, L. A., Gruchalla, K., Lawson, M., and Moriarty, P.: A simulation study demonstrating the importance of large-scale trailing vortices in wake steering, *Wind Energ. Sci.*, 3, 243–255, <https://doi.org/10.5194/wes-3-243-2018>, 2018.
- Frandsen, S., Barthelme, R., Pryor, S., Rathmann, O., Larsen, S., Højstrup, J., and Thøgersen, M.: Analytical modelling of wind speed deficit in large offshore wind farms, *Wind Energy*, 9, 39–53, 2006.
- Gebraad, P. M. O., Teeuwisse, F. W., Van Wingerden, J. W., Fleming, P. A., Ruben, S. D., Marden, J. R., and Pao, L. Y.: A data-driven model for wind plant power optimization by yaw control, in: *American Control Conference (ACC)*, 4–6 June 2014, Portland, Oregon, USA, IEEE, Piscataway, NJ, USA, 3128–3134, <https://doi.org/10.1109/ACC.2014.6859118>, 2014.
- Gebraad, P., Fleming, P. A., and Van Wingerden, J. W.: Comparison of actuation methods for wake control in wind plants, in: *American Control Conference (ACC)*, 1–3 July 2015, Chicago, IL, USA, IEEE, Piscataway, NJ, USA, 1695–1701, <https://doi.org/10.1109/ACC.2015.7170977>, 2015.
- Göçmen, T. and Giebel, G.: Data-driven Wake Modelling for Reduced Uncertainties in short-term Possible Power Estimation, *J. Phys. Conf. Ser.*, 1037, 072002, <https://doi.org/10.1088/1742-6596/1037/7/072002>, 2018.
- Golub, G. H. and van Loan, C. F.: *Matrix computations*, Johns Hopkins studies in mathematical sciences, 4th edn., Johns Hopkins Univ. Press, Baltimore, Md., USA, 2013.
- Hansen, P. C.: The truncatedSVD as a method for regularization, *BIT*, 27, 534–553, <https://doi.org/10.1007/BF01937276>, 1987.
- Jacobsen, H. S.: WASP CFD: Wind model for complex terrain, available at: <https://www.wasp.dk/waspcfd#flow-model>, last access: 1 August 2019.
- Jategaonkar, R. V.: *Flight Vehicle System Identification: A Time-Domain Methodology*, 2nd edn., American Institute of Aeronautics and Astronautics, Inc., Reston, VA, USA, ISBN 9781624102783, 2015.
- Jonkman, J. and Jonkman, B.: FAST v8, available at: <https://nwtc.nrel.gov/FAST8> (last access: 13 May 2020), 2018.
- Karampatziakis, N. and Langford, J.: Online Importance Weight Aware Updates, available at: <http://arxiv.org/pdf/1011.1576v4> (last access: 13 May 2020), 2011.
- Martínez-Tossas, L. A., Annoni, J., Fleming, P. A., and Churchfield, M. J.: The aerodynamics of the curled wake: a simplified model in view of flow control, *Wind Energ. Sci.*, 4, 127–138, <https://doi.org/10.5194/wes-4-127-2019>, 2019.
- Mathworks: *Matlab Documentation*, fmincon, available at: <https://www.mathworks.com/help/releases/R2017b/optim/ug/fmincon.html>, last access: 30 July 2019.
- Niayifar, A. and Porté-Agel, F.: A new analytical model for wind farm power prediction, *J. Phys. Conf. Ser.*, 625, 012039, <https://doi.org/10.1088/1742-6596/625/1/012039>, 2015.
- Nocedal, J. and Wright, S. J.: *Sequential Quadratic Programming*, pp. 529–562, Springer New York, New York, USA, https://doi.org/10.1007/978-0-387-40065-5_18, 2006.
- Schreiber, J., Nanos, E. M., Campagnolo, F., and Bottasso, C. L.: Verification and Calibration of a Reduced Order Wind Farm Model by Wind Tunnel Experiments, *J. Phys. Conf. Ser.*, 854, 012041, <https://doi.org/10.1088/1742-6596/854/1/012041>, 2017.
- Schreiber, J., Salbert, B., and Bottasso, C. L.: Study of wind farm control potential based on SCADA data, *J. Phys. Conf. Ser.*, 1037, 032012, <https://doi.org/10.1088/1742-6596/1037/3/032012>, 2018.
- Waiboer, R.: *Dynamic modelling, identification and simulation of industrial robots: for off-line programming of robotised laser welding*, PhD thesis, University of Twente, Veldhoven, the Netherlands, ISBN 978-90-77172-25-4, 2007.
- Wang, C., Wang, J., Campagnolo, F., Carraón, D. B., and Bottasso, C. L.: Validation of large-eddy simulation of scaled waked wind turbines in different yaw misalignment conditions, *J. Phys. Conf. Ser.*, 1037, 062007, <https://doi.org/10.1088/1742-6596/1037/6/062007>, 2018.
- Xie, S. and Archer, C. L.: A Numerical Study of Wind-Turbine Wakes for Three Atmospheric Stability Conditions, *Bound.-Lay. Meteorol.*, 165, 87–112, <https://doi.org/10.1007/s10546-017-0259-9>, 2017.

Paper 10: Wind tunnel testing of a closed-loop wake deflection controller for wind farm power maximization

12.1 Summary

This work presents the application of a closed-loop wind farm controller for power maximization on a scaled wind farm consisting of three G1 turbine models. In details, a model-free gradient based extremum seeking wind farm controller varies the upstream turbine yaw misalignment and thereby the turbine wake is deflected. The resulting gradient of the turbine and neighboring turbine total power is measured and drives the yaw misalignment until a maximum power is reached. This process is overlapped and repeated for all upstream turbines until convergence.

The experimental results show that the optimal yaw misalignment configuration can be reached, leading to a significant—for the investigated wind farm layout and inflow more than 15%—wind farm power increase.

The presented work bases on a model-free approach with the advantage that a properly parameterized wind farm model is not necessary. A drawback is that for reaching the optimal turbine misalignments a significant amount of time is required. The opposed model-based approach, as presented in **Papers 12**, is faster and able to react quickly to changes in inflow conditions.

12.2 Contribution

Within this peer-reviewed publication, the author of this dissertation has conducted parts of the post-processing and analysis. Filippo Campagnolo led the whole research work and conducted the experiments. All authors provided important input to this research work through discussions, feedback and by writing the paper.

12.3 Reference

F. Campagnolo, V. Petrović, J. Schreiber, E. M. Nanos, A. Croce, and C. L. Bottasso, “Wind tunnel testing of a closed-loop wake deflection controller for wind farm power maximization,” *Journal of Physics: Conference Series*, vol. 753, p. 032006, 2016. doi: 10.1088/1742-6596/753/3/032006

Wind tunnel testing of a closed-loop wake deflection controller for wind farm power maximization

Filippo Campagnolo¹, Vlaho Petrović¹, Johannes Schreiber¹,
Emmanouil M. Nanos¹, Alessandro Croce² and Carlo L. Bottasso^{1,2}

¹ Wind Energy Institute, Technische Universität München, Boltzmannstraße 15, D-85748 Garching bei München, Germany

² Dipartimento di Scienze e Tecnologie Aerospaziali, Politecnico di Milano, Via La Masa 34, I-20156 Milano, Italy

E-mail: filippo.campagnolo@tum.de

Abstract. This paper presents results from wind tunnel tests aimed at evaluating a closed-loop wind farm controller for wind farm power maximization by wake deflection. Experiments are conducted in a large boundary layer wind tunnel, using three servo-actuated and sensorized wind turbine scaled models. First, we characterize the impact on steady-state power output of wake deflection, achieved by yawing the upstream wind turbines. Next, we illustrate the capability of the proposed wind farm controller to dynamically driving the upstream wind turbines to the optimal yaw misalignment setting.

1. Introduction

Wind energy production is often organized in wind power plants rather than single isolated wind turbines, because of lower construction, maintenance and commissioning costs. However, the design of a wind farm requires taking into account the complex interactions that take place within the wind power plant itself, since the wakes of upwind wind turbines have a strong impact on the power and loading of downstream machines. In recent years, interest has grown in the area of cooperative control of wind turbines, with the goal of maximizing the total wind farm power output, of achieving a given power setpoint while minimizing fatigue loading, or others that require some form of coordination among the wind turbines.

Among the several approaches investigated so far [7], controlling the direction of the wake by yawing the upwind wind turbines seems to be the most promising one [6]. In fact, by redirecting the wake, one may reduce or eliminate altogether the exposure of downwind wind turbines to the wakes shed upstream. In this paper, we present results obtained by testing a closed-loop wind farm control algorithm in a large boundary layer wind tunnel [3] using servo-actuated and sensorized wind turbine models, described in §2. The model-free controller, which optimizes online the yaw misalignment of the upstream wind turbines to increase the total wind farm power output, is discussed in §3, while results are reported in §4.

2. Experimental setup

Tests were conducted with a scaled wind farm (see Fig. 1) composed of three identical scaled wind turbine models with a rotor diameter of 1.1 m (in the following named G1s). The undisturbed



wind speed was measured by means of a Pitot tube, also shown in the figure, placed at hub height and 3 diameters in front of the upstream model.

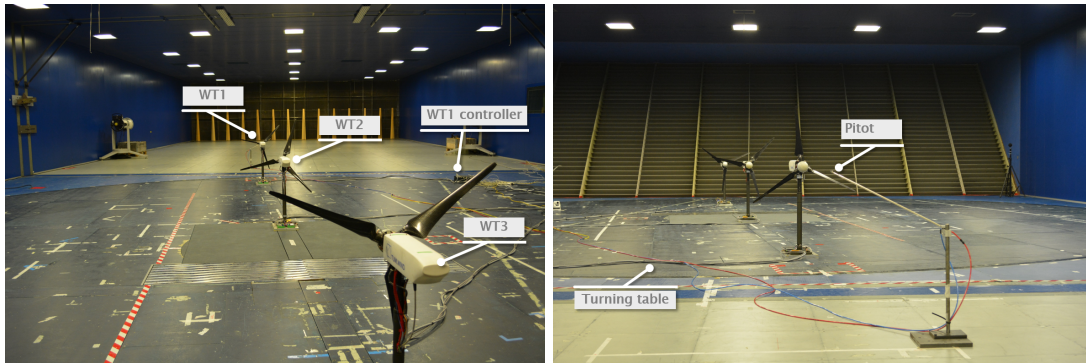


Figure 1: Wind farm layout in the wind tunnel

Each G1 (see Fig. 2), whose rated rotor speed is 850 rpm, is equipped with three blades, which are composed by a layer of unidirectional carbon fiber covering a machined Rohacell core, mounted on the hub with two bearings in order to enable pitch actuation while limiting free-play. The individual pitch angle of each blade can be varied by means of a small brushed motor equipped with a gearhead and built-in relative encoder, used to measure the blade pitch. The three motors are housed within the blades hollow root, and their position is monitored and adjusted by dedicated electronic control boards housed in the hub spinner.

The shaft is held by two bearings, in turn housed in the rectangular carrying box that constitutes the main frame of the nacelle. The shaft also exhibits four small bridges on which strain gages are glued, to provide measurements of the torsional and bending loads. Three miniaturized electronic boards, fixed to the hub, provide for the power supply and conditioning of the shaft strain gages. The transmission of the electrical signals from the rotating system to the fixed one, and vice versa, is guaranteed by a through-bore 12-channels slip ring.

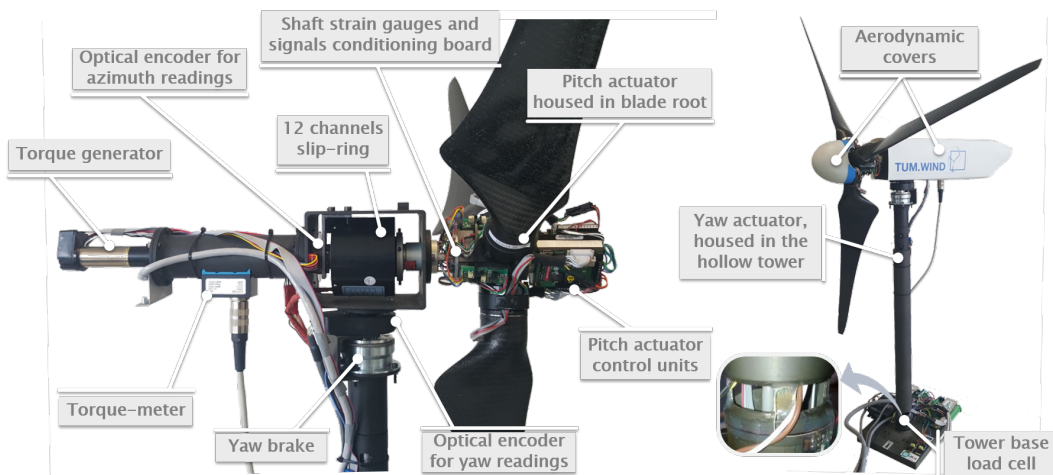


Figure 2: Layout of G1 model

A torque-meter, located after the two shaft bearings, allows for the measurement of the torque provided by a brushless motor equipped with a gearhead and a tachometer. The motor, located

in the rear part of the nacelle, is operated as a generator by using a servocontroller. An optical encoder, located between the slip ring and the rear shaft bearing, allows for the measurement of the rotor azimuth.

The entire nacelle can be yawed by means of a brushed motor, housed within the hollow tower, equipped with a gearhead. This latter element is connected by a multi-beam coupling to a shaft rigidly joined to the rectangular carrying box, and hold in place by two bearings located within the upper portion of the tower. An optical encoder provides feedback to an electronic device that controls both the yaw actuator and a magnetic brake.

The tower, whose stiffness was designed so that the first fore-aft and side-side natural frequencies of the nacelle-tower group are properly placed with respect to the harmonic per-rev excitations, is softened at its base by machining four small bridges, on which strain gages are glued. Bridges were sized so as to have sufficiently large strains to achieve the necessary level of accuracy for the strain gages. Two electronic boards provide for the power supply and adequate conditioning of this custom-made load cell.

Aerodynamic covers of the nacelle and hub ensure a satisfactory quality of the flow in the central rotor area

Due to the small dimensions of the scaled wind turbine, low Reynolds numbers are expected. Therefore, the low-Reynolds airfoil RG14 [8] was chosen for the model wind turbine blades. The aerodynamic performance of the rotor was measured for different values of the airfoil Reynolds by operating the models at several combinations of tip speed ratio (TSR) and collective pitch settings. The measured maximum power coefficients are approximately 0.42 at $\lambda \in [7, 8]$ and $\beta \in [-2^\circ, 0^\circ]$.

3. Control system

The control system of the wind turbine models is organized in three different levels, as shown in Fig. 3. The low level control operates the wind turbine actuators, while the communication with sensors, actuators, and control algorithms are implemented on the industrial real-time controller Bachmann M1 (<http://www.bachmann.info>). Wind farm control algorithms, as well as supervisory control for each model, are implemented on a standard PC, which communicates with each wind turbine controller over an Ethernet network.

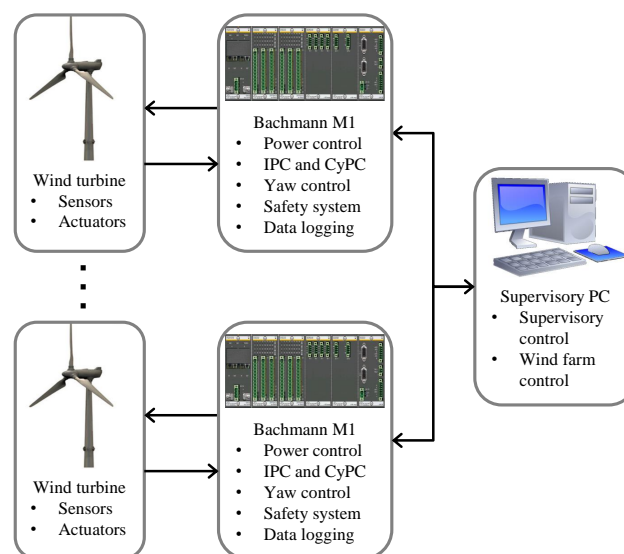


Figure 3: Control structure of the wind turbine models.

3.1. Wind turbine control system

The Bachmann M1 system used for wind turbine control is a modular real-time controller with a CPU module for running control algorithms, a counter module for acquiring rotor speed and azimuth from the digital encoder, a communication module for communication with actuators through a CAN network and two analogue input-output modules for acquiring measurements and sending commands to the torque motor and the yaw break. The Bachmann M1 system is capable of acquiring data with a sample rate of 2.5 kHz, which is used for acquiring aerodynamic torque, shaft bending moments and rotor azimuth position. All other measurements are acquired with a sample rate of 250 Hz.

Each wind turbine model is controlled by a separate Bachmann M1 system with a sampling time of 4 ms. Besides data-logging and safety systems (such as shutdown in case of overspeed), the following control algorithms are implemented on each M1 system:

- **Power control, i.e. torque and collective pitch control (CPC).** A standard power control is implemented based on [1], with two distinct control regions. In the region below rated wind speed, blade pitch angles are kept constant, while the generator torque reference follows a quadratic function of rotor speed in order to maximize energy extraction. Above rated wind speed, the generator torque is kept constant, while a PI controller is used to collectively pitch the rotor blades in order to keep the generated power at the desired level. Additionally, for the purpose of wind farm control, the wind turbine power output can be lowered to an arbitrary percentage of the available power below rated wind speed and of the nominal power above rated wind speed. Since power reduction can be achieved in different ways, it is possible to easily modify the control trajectories while the models are idling.
- **Individual and cyclic pitch control (IPC and CyPC).** Besides collective pitch control, the models are also capable of individually pitching each blade, enabling additional control actions for influencing loading or wakes. To this aim, the reference of each blade follows a harmonic function of the blade azimuth position with adjustable amplitude and phase angle. This leads to continuous blade pitching with frequency 1P, whose maximal amplitude has to be constrained according to the pitch actuator capabilities. This kind of pitch activity has a strong impact on loads, while the generated power remains unaffected above rated wind speed. On the other hand a slight power loss can be observed below rated wind speed, depending on the pitch amplitude [2, 11]. The amplitude and the phase angle of the blade pitch can be determined either in close loop by two decoupled PI controllers trying to reduce 1P oscillations of the shaft bending moments (IPC, for more details see [10]), or in open loop (CyPC).
- **Yaw control.** The misalignment angle of a wind turbine model with respect to the wind can be set by changing the yaw angle. A PI controller is used for controlling the yaw motor, and the yaw reference value is provided from the supervisory controller. An additional control logic is implemented that enables the yaw brake once the nacelle gets in the desired position. Whenever the yaw reference is changed, the brake is released and the PI controller ensures that the nacelle is yawed to the new position. Besides constant yaw references, the yaw controller is also capable of continuous yaw motion, such as a harmonic function with adjustable amplitude and frequency. Such a motion can be useful for wind farm control algorithms or for the generation of wake meandering in the wind tunnel.

3.2. Wind farm control system

High level control is implemented on a standard PC, and communication with the wind turbine Bachmann M1 controllers is established over an Ethernet network. Through a dedicated graphic interface, the supervisory controller allows for the user to monitor the wind turbine conditions, change their operating state, control algorithms and reference values, and to set up and initialize

the data acquisition process. Additionally, a wind farm control algorithm collects measurements from the Bachmann M1 controllers, and can send the following control actions back to them:

- a command to reduce produced power,
- a yaw angle reference,
- CyPC settings.

The wind turbine controller described in §3.1 is in charge of following the references sent by the wind farm controller.

At present, a gradient-based extremum seeking control algorithm is implemented with the goal of increasing energy capture. Gradients are computed by first-order finite differencing the energy capture, properly averaged over a time horizon, at two different wind turbine operating points. The control algorithm is based on [5], where yaw misalignment optimization is performed rather than axial induction. The algorithm uses the simplified assumption that control actions of a wind turbine affect only the closest downstream wind turbine. Therefore, instead of solving a single optimization problem for the entire wind farm, a series of smaller optimization problems (one for each wind turbine) is being solved:

$$\gamma_i^* = \arg \max_{\gamma} P_i + P_{i+1}. \quad (1)$$

The optimal yaw angle γ_i^* is therefore determined based on the power output of the i^{th} wind turbine P_i and its closest downwind neighbor, P_{i+1} . The optimization problems are suitably synchronized by waiting for the propagation of the wakes only to the neighboring wind turbines, thus significantly reducing the convergence time of the algorithm. The time required for the wake to propagate is computed online using Jensen's model to estimate the speed in the wake. The average wind speed measured by the Pitot tube described earlier is used as input to the Jensen's model. The axial induction factor is computed by properly non-dimensionalizing the rotor thrust, in turn derived from the fore-aft bending moment measured at tower base, using the well-known relationship

$$C_T = 4a(1 - a). \quad (2)$$

The wake decay coefficient is obtained by best-fitting experimental data from previous wind tunnel tests [4].

Although such an approach changes the original objective (power maximization in the entire wind farm), and therefore could result in suboptimal performance, it can also lead to significantly faster convergence.

4. Results

Tests were conducted by simulating the atmospheric boundary layer by means of spires placed at the inlet of the wind tunnel, in order to generate a wind speed vertical profile and turbulence intensity typical of offshore applications.

The machines were arranged with a flow-wise longitudinal spacing of 4 diameters and a laterally shift of half a diameter, as depicted in Fig. 1. The average wind speed measured by the Pitot tube described earlier is used to derive the wind turbine and wind farm power coefficients, the latter being defined as the sum of the wind turbine ones.

At first, different combinations of yaw misalignment for the upstream (*WT1*) and second (*WT2*) wind turbine model were tested within the wind tunnel, with the aim of experimentally identifying the operating condition maximizing wind farm power output. Figure 4 shows that, for the tested wind farm layout and wind condition, wind farm power can be substantially increased (up to 15%) by misaligning *WT1* and *WT2* of approximately 20 deg and 16 deg, respectively.

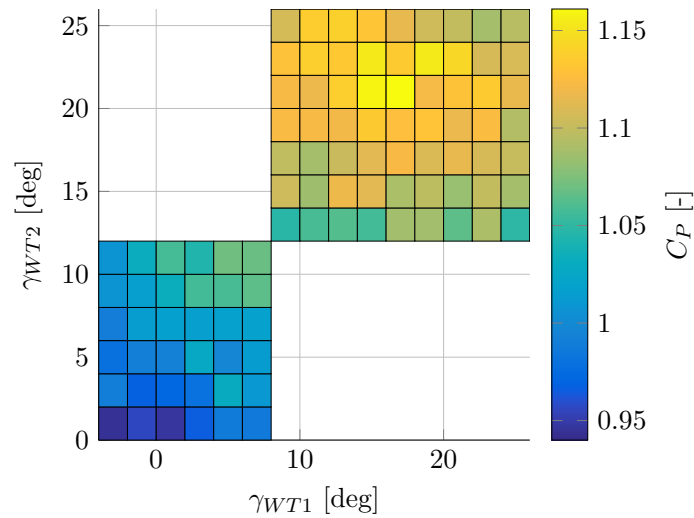


Figure 4: Measured wind farm power coefficient C_P as function of upstream WT yaw misalignment (γ_{WT1}) WT yaw misalignment (γ_{WT2}).

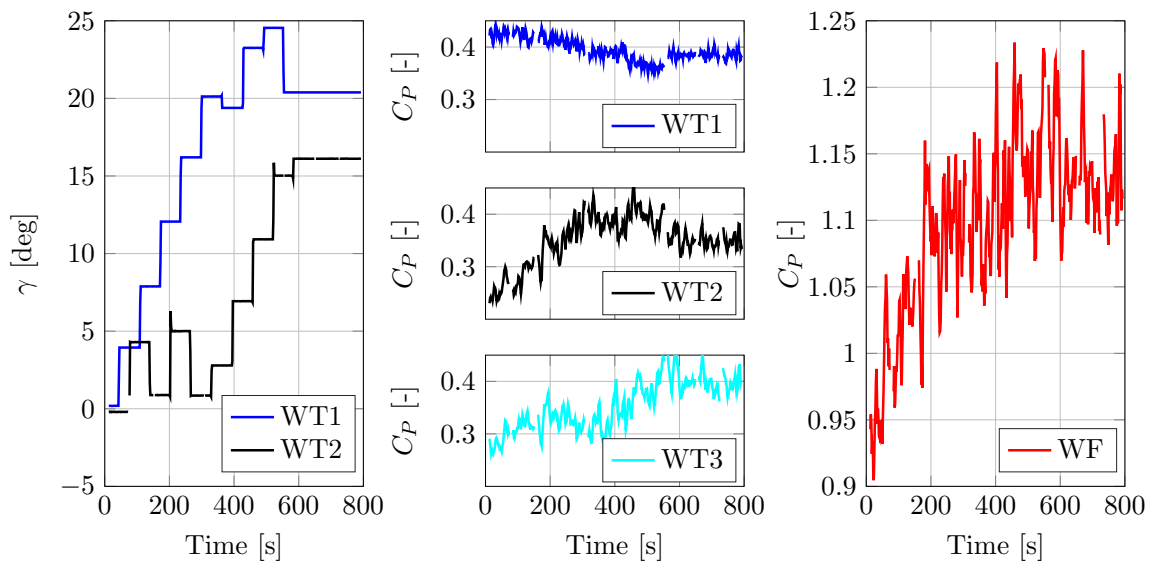


Figure 5: WTs yaw misalignment (on left), WTs power coefficient (center) and wind farm power coefficient as function of time (right)

Figure 5 shows the time evolution of the upstream WT yaw misalignments, as well as the evolution of the power coefficient for the three wind turbines and the whole wind farm, after the activation of the proposed wind farm controller. The data reported in Fig. 5 clearly highlights that the wind farm controller is capable of dynamically driving the wind turbines to yaw misalignment settings that, based on the results shown in Fig. 4, maximize the wind farm power output. This leads to an increase of power in excess of 15%, a result which is in line with what reported by other authors using simulations [6] and wind tunnel testing [9].

5. Conclusions

A closed-loop model-free controller has been developed and tested in a large boundary layer wind tunnel, where one can simulate wind conditions typical of offshore applications. Thanks to the use of sophisticated wind turbine models, extensively instrumented and equipped with individual pitch, torque and yaw control, it has been experimentally demonstrated that wake redirection by means of yaw misalignment can lead to substantial increase in wind farm power output. Moreover, it was shown for the first time that a closed-loop wind farm controller is capable of dynamically driving the upstream wind turbines to the optimal operational conditions.

Acknowledgments

This work was financially supported by the German Federal Ministry for Economic Affairs and Energy (BMWi) within the CompactWind project (FKZ 0325492D).

References

- [1] Bossanyi E 2000 *Wind Energy* **3** 149–163
- [2] Bossanyi E 2005 *Wind Energy* **8** 481–485
- [3] Bottasso C L, Campagnolo, F and Petrović V 2014 *Journal of Wind Engineering and Industrial Aerodynamics* **127** 11–28
- [4] Campagnolo F, Petrović V, Bottasso C L and Croce A 2016 *American Control Conference (ACC)* 513–518
- [5] Gebraad P M Om van Wingerden J W, 2015 *Wind Energy* **18** 429–447
- [6] Gebraad P M O, Teeuwisse FM, van Wingerden JW, Fleming PA, Ruben SD, Marden JR and Pao LY 2014 *Wind Energy* **19** 95–114
- [7] Knudsen T, Bak T and Svenstrup M 2015 *Wind Energy* **18** 1333–1351
- [8] Lyon C A, Broeren A P, Gigure P, Gopalarathnam A, Selig M S 1998 *SoarTech Publications* **3**
- [9] Park J, Law K 2016 *IEEE Transactions on Control Systems Technology* **24** 1655–1668.
- [10] Petrović V and Campagnolo F 2013 *European Control Conference 2013*, Zurich
- [11] Petrović V, Jelavić M and Baotic M 2015 *Renewable Energy* **76** 418–431

Paper 11: Online model updating by a wake detector for wind farm control

13.1 Summary

In this work a method to update an engineering wake model online based on measurements provided by waked downstream turbines is presented. Thereto, the wake model, which has been developed in **Paper 5**, gives an estimate of the wake deficit and position. The wind sensing method, developed in **Paper 1**, provides local velocity estimates on the turbine rotor, which also carry information on the actual location and deficit of the wake. To improve model predictions, the wind sensing estimates are employed to correct the modeled wake deficit and position.

Scaled wind tunnel experimental results show that in case of a slightly erroneous wake model, for example induced by wrong parameterization or inputs, errors in model predictions, relevant in wind farm control applications, can occur. Applying the online model update, the wake position and deficit is corrected and a significant improvement in model prediction has been achieved.

13.2 Contribution

Within this peer-reviewed publication, the author of this dissertation has conducted the main research work. Carlo L. Bottasso supervised the research and both authors provided important input through discussions, feedback and by writing the paper.

13.3 Reference

C. L. Bottasso and J. Schreiber, "Online model updating by a wake detector for wind farm control," in *2018 Annual American Control Conference (ACC)*. IEEE, 2018, pp. 676–681. doi: 10.23919/ACC.2018.8431626

2018 Annual American Control Conference (ACC)
June 27–29, 2018. Wisconsin Center, Milwaukee, USA

Online model updating by a wake detector for wind farm control

C.L. Bottasso, J. Schreiber

Abstract— An engineering wake model is updated online based on measurements provided by shaded turbines. Departing from other approaches, the measurements include information on the impinging wakes, obtained by a wake detector based on measured rotor loads. The updated model exhibits improved prediction capabilities, and it can be used for implementing a model-based wind farm controller.

I. Introduction

Each turbine in a wind farm emits a wake characterized by reduced velocity and increased turbulence, leading to losses in power production and increased loads on downwind turbines. The negative effects of wake interactions may be mitigated by wake management strategies [1]. One possible implementation of such strategies is based on a wind farm flow model: the predictions of the model are used by a controller, whose aim is to energize and/or redirect wakes for improved energy yield and/or reduced loading.

The performance of any such model-based control method is inherently limited by the accuracy of its underlying model. Unfortunately, any model has limitations—at least in some situations—and especially the simple reduced-order or engineering models used for control synthesis. However, the fidelity of a model can be corrected and improved at run-time based on measurements made on the plant. Figure 1 illustrates this concept.

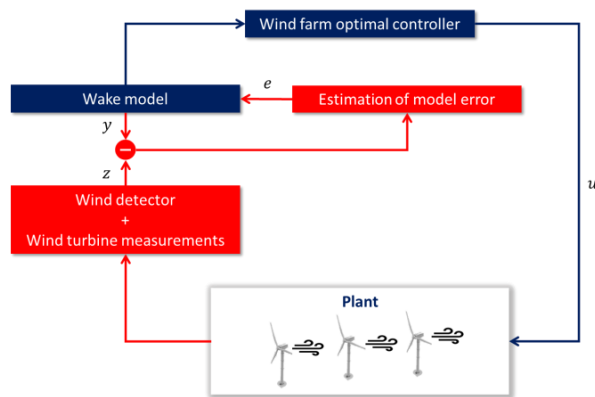


Figure 1. Wind farm control with model updating.

To correct model predictions, one might think of using standard and already available measurements of power and hub-height wind speed, for example using a Kalman filter. Unfortunately, this might not work in general because power and rotor speed might not carry enough informational content to correct for some model errors, as shown later on in this work. In fact, in the case of a wrong power prediction at a

downstream wind turbine, one cannot distinguish whether the error is caused by a wrong wind speed in the wake (for example, due to an inaccurate modeling of wake recovery) or by a wrong location of the wake with respect to the impinged rotor disk.

This impasse is solved by using our newly-developed *wake detector* [2]: by using rotor loads, the detector reveals the presence of a wake by mapping blade loads into local estimates of the wind speed over sectors of the rotor disk. This way, a wake model can be improved online during operation of the wind farm (according to the scheme of Fig. 1), generating high quality predictions of the wake *speed* and *position* within the farm. In turn, this improves the control action computed on the basis of these predictions. This idea is developed in the present work with reference to a static wind farm flow model, although nothing in this approach prevents its extension to the dynamic case. Similar concepts of state estimation have been explored in the context of dynamic wake models in [3, 4]. However, it is unclear whether such formulations are able to cope with simultaneous errors in wake recovery and trajectory, as the method presented herein.

This paper is organized as follows. Section II formulates the model update approach, the wind farm model and the load-based wind detector. Section III describes different possible implementations of the model update method. The various options are then tested with reference to experimental measurements obtained on a scaled wind farm facility operated in a large boundary layer wind tunnel. Finally, Section IV summarizes results and conclusions, and gives an outlook towards future work.

II. Methods

A. State update

The model update method is formulated here based on a generic non-linear static wind farm model. A similar formulation could also be derived for a dynamic model, leading in that case to a standard Kalman filtering problem. The static model is written as

$$x = f(u, m, p), \quad (1)$$

$$y = g(x), \quad (2)$$

where f is a non-linear static function, which depends on the model formulation. The control inputs are noted u , and include the yaw and induction of each wind turbine in the farm. Measurements of ambient conditions are noted m , and include density and free stream wind speed and direction (typically estimated by the upstream wind turbines). Physical tunable coefficients of the model and the wind farm layout are represented by the vector of parameters p . The model states are indicated as x , and in the present study they include the velocity and lateral position of the wake of each turbine.

C. L. Bottasso and J. Schreiber are with the Wind Energy Institute, Technical University of Munich, Boltzmannstraße 15, 85748 Garching bei München, Germany (carlo.bottasso@tum.de, johannes.schreiber@tum.de).

A set of outputs y is defined by function g . As shown later on, the outputs may be represented by the turbine power at the downstream turbines, but they may also include estimated flow velocities at the downstream rotors.

In general, the predictions of the model states will be in error, due to a lack of model fidelity, mistuning of the parameters or inaccuracies in ambient conditions. This can be corrected by introducing a state error e . The corresponding corrected state \hat{x} becomes

$$\hat{x} = x + e. \quad (3)$$

A maximum likelihood estimate of the state error can be readily obtained by solving the following problem

$$\min_e (z - \hat{y})^T R^{-1} (z - \hat{y}), \quad (4)$$

where z are measurements and \hat{y} the corresponding updated model outputs ($\hat{y} = g(\hat{x})$). For a given fixed covariance R , this procedure corresponds to the method of least squares.

Note that, as ambient wind conditions are often uncertain, the presented formulation could be extended by including these same conditions within the list of states. However, it is also clearly necessary to ensure the observability of all chosen states. For example, a wrong wind direction might not be distinguishable from a wrong wake location. The development of a general formulation for the estimation of wind farm flow model states is a problem of great interest [4], which is however outside of the scope of the present paper.

B. Wind farm model

The wind farm model includes two components: a wake model and a power model. The wake model is based on the double Gaussian profile proposed by [5], combined with the yaw-induced wake deflection developed in [6]. The combination of the two models gives the evolution of the flow speed within the wake downstream of each rotor disk, together with its spatial location. The power model yields the turbine power output by computing the mean flow speed at the rotor using a disk-attached grid. The turbine power coefficient $C_{p,\gamma=0}$ is assumed to be constant below rated wind speed. To take into account the power reduction in misaligned conditions, the following relationship is used

$$C_p(\gamma) = C_{p,\gamma=0} \cos(\gamma)^{p_p}, \quad (5)$$

where γ is the turbine misalignment angle and p_p a tunable parameter.

When implementing the state update for wake speed u , Eq. (3) is modified as $\hat{u} = u + r e$, where r is the Keane wake reduction (see Eq. (22) of [5]). Since the Keane wake model uses a Gaussian shape for the speed deficit—and hence does not have a well-defined wake width—, this form of the error avoids changing the ambient wind speed away from the wake.

B. Wind detector

A load-based wind speed detector [2] is used to estimate the flow at the downstream wind turbine. As shown in Fig. 2, the detector works by mapping blade loads into local estimates of the wind speed. These are then averaged over sectors of the rotor disk. The resulting sector-effective (SE)

wind speed measurements on the left and right parts of the rotor (noted $V^{SE, \text{left}}$ and $V^{SE, \text{right}}$, respectively) are then used in the state update formulation described earlier on.

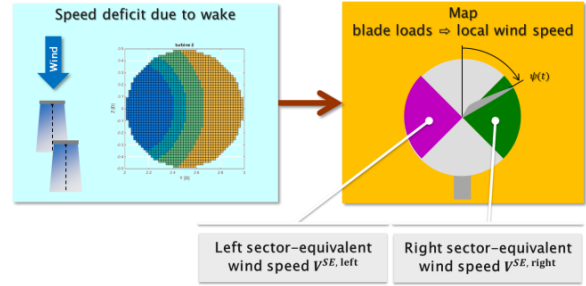


Figure 2. Wind detector estimating the left and right sector-equivalent wind speeds.

III. Implementation & results

A. Implementation

To evaluate the proposed method, three versions of the state update formulation are implemented for a simple farm consisting of two wind turbines. In the notation used below, the upstream wind turbine is indicated as WT1, while the downstream one as WT2.

The *simplistic method* (subscript s) is intended to demonstrate that, by only using power measurements at the downwind turbine ($P_{WT2, \text{exp}}$), it is in general not possible to correct at the same time for errors in lateral wake position (d_{WT1}) and speed (u_{WT1}) of the upstream wind turbine. In contrast to the simplistic method, the *power method* (subscript p) is well-posed, as it only tries to correct the wake speed and not its position based on downstream power measurements. The *wind-sensing method* (subscript ws) includes as measurements also the SE wind speeds $V_{WT2, \text{exp}}^{SE, \text{left/right}}$ obtained by the wind detector on the downwind turbine. This way, the method is able to correct for both speed and position in the wake.

Table 1 gives an overview of the three different approaches. For all cases, the ambient conditions are obtained from the front wind turbine: wind direction is measured by the on-board wind vane, while the ambient wind speed is computed by the rotor effective wind speed corrected for yaw misalignment using Eq. (5).

The diagonal entries of the covariance matrix R are initially set to $1/P_r^2$ for power and to $1/V_r^2$ for the SE wind speed model outputs, where $(\cdot)_r$ indicates a rated quantity. When using maximum likelihood, the covariance is updated after each iteration based on the residuals. Problem (4) is solved using the Nelder-Mead simplex algorithm implemented in the MATLAB function *fminsearch* [7].

TABLE I. STATE UPDATE IMPLEMENTATIONS

Method:	Simplistic (*= s)	Power (*= p)	Wind-sensing (*= ws)
$x_{(*)}$	$\begin{bmatrix} d_{WT1} \\ u_{WT1} \end{bmatrix}$	$[u_{WT1}]$	$\begin{bmatrix} d_{WT1} \\ u_{WT1} \end{bmatrix}$
$\hat{x}_{(*)}$	$\begin{bmatrix} d_{WT1} + e_d \\ u_{WT1} + re_u \end{bmatrix}$	$[u_{WT1} + re_u]$	$\begin{bmatrix} d_{WT1} + e_d \\ u_{WT1} + re_u \end{bmatrix}$
$\hat{y}_{(*)}$	$[P_{WT2}]$	$[P_{WT2}]$	$\begin{bmatrix} P_{WT2} \\ V_{WT2,SE,right} \\ V_{WT2,SE,left} \end{bmatrix}$
$z_{(*)}$	$[P_{WT2,exp}]$	$[P_{WT2,exp}]$	$\begin{bmatrix} P_{WT2,exp} \\ V_{WT2,SE,right,exp} \\ V_{WT2,SE,left,exp} \end{bmatrix}$

B. Experimental setup

Experimental tests with scaled wind turbine models were used to study the performance of the various state update formulations. The scaled turbines, designed for realistic wake behavior, were operated in the boundary layer wind tunnel of the Politecnico di Milano at an ambient hub-height wind speed of 5.8 m/sec and a turbulence intensity of about 5%. A detailed description of the turbines and the wind tunnel can be found in [8, 9]. The wind farm layout is depicted in Fig. 3, where γ_{WT1} is the yaw misalignment of the upstream wind turbine with respect to the wind vector, positive as indicated in the figure. The two turbines are operated at a longitudinal distance of 4 diameters (D) with no lateral displacement.

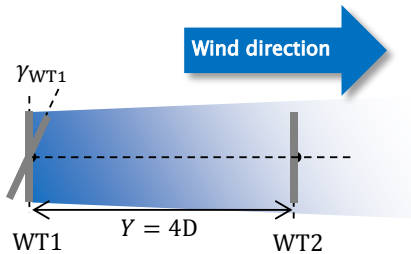


Figure 3. Wind farm layout, top-view.

The wind farm model parameters p include the power loss exponent p_p (see Eq. 5), the coefficients k^* , ϵ , and n that define the wake shape through the expression $\sigma = k^* Y^n + \epsilon$ (where σ is the standard deviation of the double Gaussian wake deficit), and finally the scaling factor c_s [5]. The parameters were first manually tuned with the objective of obtaining a good fit of the model predictions with the experimentally measured wake speed, downstream turbine power and SE speeds at various yaw misalignments of WT1. Figure 4 shows in the upper subplot a comparison between measured (subscript *exp*) and modeled power at both turbines. The lower subplot shows the SE wind speeds for the left and right sectors of WT2. Each experimental data point represents the mean value of a 60 sec time recording. As the scaled turbine models used in these particular experiments are not equipped with blade load sensors, blade loads were reconstructed from shaft loads using the Coleman Transformation as described in [9]. To account for the fact

that the reconstructed experimental blade loads do not contain frequencies above 1P (one per revolution), also the SE wind speed computed from the wind farm model was accordingly filtered. This was obtained by first best-fitting over the turbine rotor disk a linear wind field, and then computing from it the desired quantities $V_{WT2}^{SE,left/right}$.

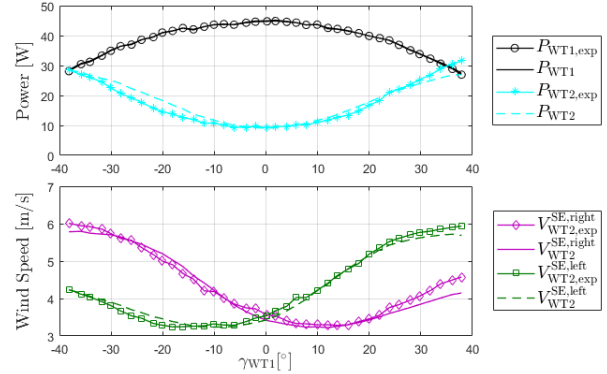


Figure 4. Comparison between experimental and modeled turbine power and SE wind speeds.

C. Results

An experimental time sequence was obtained by stacking one after the other a number of recordings, each one corresponding to a different constant yaw setting of the front machine. Since the flow is turbulent, wake dynamics induced by turbulent fluctuations, including meandering, are included in the recordings. However, the effects of transient changes from one yaw set point to the next are not, including the corresponding travel-time wake delays, which can be estimated to be approximately equal to 1 sec. Since delays are not included in the static model used here, all signals were filtered with a moving average of 4 sec. The filter window size was chosen to reduce effects of short-term fluctuations, which are believed to be of limited interest for plant-level control.

Figure 5 shows the performance of the simplistic state update method. The upper subplot shows the time history of the upwind turbine yaw position γ_{WT1} , which changes in three steps from 0 deg to 30 deg. Previous experiments indicated that the last yaw position in the plot is the approximate point of maximum power production for the present wind farm configuration. The second subplot shows the experimentally measured power produced by the downwind turbine ($P_{WT2,exp}$), together with the state updated model prediction (noted $P_{WT2,s}$, where the second subscript indicates the simplistic formulation). The two lines are essentially identical, indicating an almost perfect prediction of power output by the model. The plot also shows that power increases after each yaw step, which is indeed caused by the wake deflecting laterally and thereby reducing its effects on the downstream rotor.

The third subplot shows the SE wind speeds in the left and right turbine sectors. The experimental measurements from the wind speed detector (solid lines with marker) show the direction of wake deflection: with increasing time and yaw,

the flow velocity in the left sector increases, implying that the wake center is moving to the right. The SE wind speeds of the updated simplistic method are also shown on the same plot. These curves reveal that the model-predicted flow velocities, which were not explicitly taken into account by the method, behave in a radically different way from the measured ones. In fact, the simplistic state update method corrects the wake center position by moving it to the left of the downwind turbine, instead of to the right as it should be. The last subplot of Fig. 5 shows the corresponding state errors. The large error in wake speed significantly alters the wake deficit, while the error in wake position implies that the wake center is located to the left of the rotor.

The simplistic method is clearly ill-posed, as two independent states are corrected using only one measurement. Therefore, multiple combinations of wake speed and displacement can be obtained that, although completely wrong, still apparently lead to a very good power estimate. A controller using the predictions of such a model is invariably bound to fail.

Notice that the ill-posedness of the present formulation is rather obvious, by considering that one single global rotor measurement as power cannot distinguish between changes due to a different wake recovery or position. Indeed, in the context of the present formulation, a well-posedness check can be formulated by considering the linearized version of Eq. (2), i.e. $y = Cx$, where $C = \partial g / \partial x$. The problem can be considered to be well posed if state x can be deduced from measurements z of y , a condition that is satisfied only if $\text{null}(C) = \{0\}$, i.e. if C is of full column rank. This is akin to the observability condition for dynamical systems, specialized to the present static case. For the simplistic approach, C is a 1×2 matrix that cannot satisfy this observability condition.

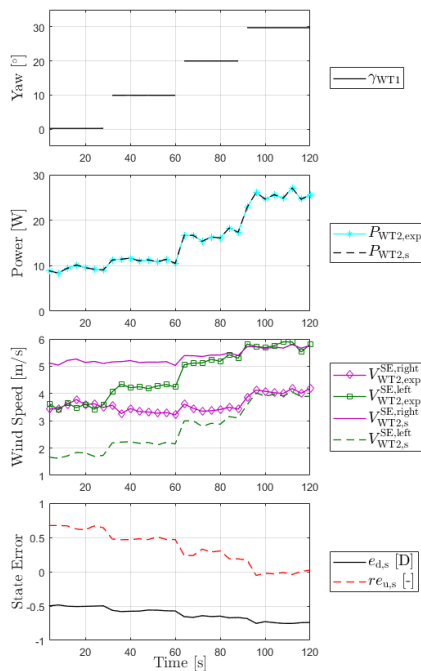


Figure 5. Predictions of the on-line corrected simplistic model (s) compared to experimental measurements (exp).

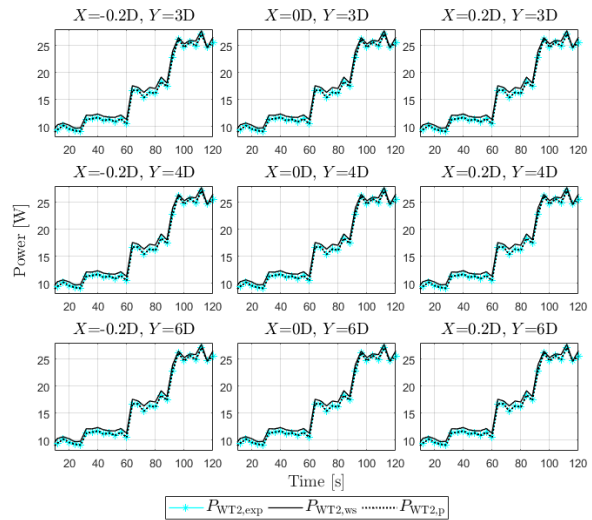


Figure 6. Downwind turbine power predicted by the wind-sensing method ($P_{WT2,ws}$) and the power method ($P_{WT2,p}$), compared with the experimental one ($P_{WT2,exp}$), for various modeling errors.

After having illustrated the ill-posedness of the simplistic method, the power and wind-sensing approaches are compared. In both cases, the problem is now well-posed: for the power method, only wake speed is corrected based on measured power, while for the wind-sensing method the presence of the wake detector allows for the separation of the effects caused by wake speed from those caused by position. To better understand the characteristic of the methods, artificial errors were imposed on the wind farm model. An error in wake recovery and expansion is simulated by changing the modeled longitudinal distance Y between the turbines with respect to the one of the experiments. In addition, to simulate an error in the modeled wake position, the lateral distance X is also varied.

For nine combinations of modeling errors, Fig. 6 reports the model-predicted power together with the experimentally measured one. Independently of the modeling error, it appears that power is always well predicted. The SE wind speeds at the downwind turbine are shown in Fig. 7. Solid lines with markers represent experimental measurements, dash-dotted lines the power method and solid lines without markers the wind-sensing method flow speeds. The wind-sensing method provides predictions that are very close to the experimental measurements, independently of the modeling error. In fact, both wake speed and wake position can be corrected independently by this approach. On the other hand, the power method only corrects wake speed. Therefore, it provides good results only in the case of model errors in the longitudinal displacement (middle column of the subplots). However, as soon as there is also an error in the wake position, flow velocities do not match anymore. These discrepancies may translate into significant deficiencies when it comes to utilizing the wind farm model for control purposes.

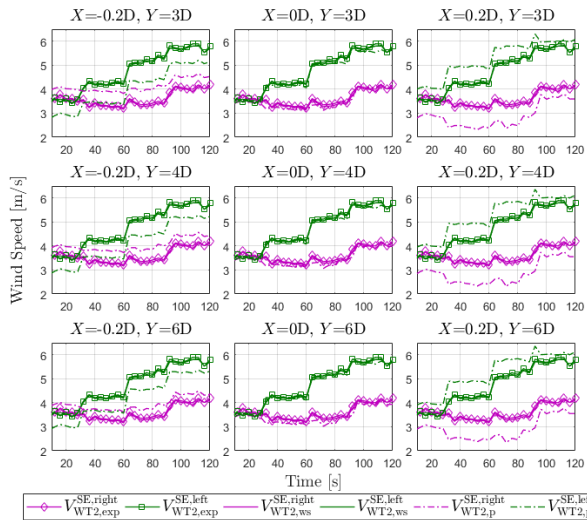


Figure 7. Downwind turbine SE wind speeds predicted by the wind-sensing method ($V_{WT2,ws}^{\text{left/right}}$) and the power method ($V_{WT2,p}^{\text{left/right}}$), compared to the experimental ones ($V_{WT2,exp}^{\text{left/right}}$), for various modeling errors.

To illustrate this point, Fig. 8 shows, for one of the nine cases considered above, the maximum possible wind farm power predicted by the model by yawing the upwind turbine to its optimal position. In the experiment, the optimal position is approximately equal to 30 deg, which are reached after 90 sec. Even though the power method is apparently able to match the downwind turbine power during the experiment, this is in reality based on a wrong prediction of the flow within the farm. Hence, the maximum predicted power is highly overestimated. On the other hand, the wind-sensing method, being capable of a more faithful prediction of the actual flow, provides for a realistic estimate of the maximum achievable power throughout the whole test case. This highlights the importance of correctly modeling the flow within the wind farm for control purposes.

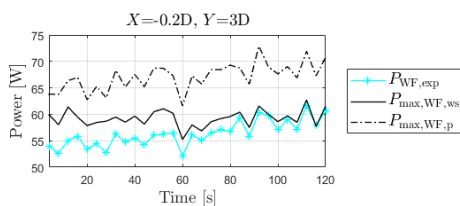


Figure 8. Measured wind farm power ($P_{WF,exp}$) and model-predicted maximum available wind farm power $P_{max,WF}$. For $t > 90$ s, the experiment reaches the optimal solution.

IV. Conclusions

A model-based wind farm control algorithm can only be as good as its underlying model. In a realistic scenario, various sources of uncertainties and model defects limit the predictive capabilities of any wind farm flow model. After having calibrated the model offline, the only remaining way to improve this situation is to correct the predictions of the model online, by using measurements obtained on the plant.

The present paper has considered the problem of model-updating, in the context of a well-known static engineering wake model. The model can predict the flow speed within the wake, as well as its geometry and spatial location depending on environmental and wind turbine operational parameters.

Three possible implementations of the method have been considered. The first, and possibly the most natural, tries to correct model predictions by using power measurements on the downstream turbine. Unfortunately, but quite obviously, the method was shown to fail because of its inability to distinguish between effects caused by wake speed or position.

The second approach uses power to correct only for wake speed. This avoids the problem being ill-posed, but clearly cannot correct the predictions of the model whenever the wake position is in error. It was shown that, even in the very simple two-wind turbine case considered here, this formulation may lead to significant errors in maximum power predictions.

Finally, a novel method based on a wake detector was proposed. The wake detector is capable of estimating the local wind speeds on the left and right sectors of the rotor disk. Clearly, the two velocities carry information on the actual location of the wake with respect to the affected rotor. This allows one to distinguish between wake speed and location, and results in the correct update of both states of the engineering model.

The present work is to be considered only as a preliminary study, and further investigations are planned. These include studies of observability in the case of only partially impinging wakes, as well as the investigation of more complex wake interference scenarios. The model update formulation will also be exploited for designing wind farm control laws using optimal model-based approaches.

ACKNOWLEDGMENT

This work has been supported by the CL-WINDCON project, which receives funding from the European Union Horizon 2020 research and innovation program under grant agreement No. 727477.

REFERENCES

- [1] Fleming, Paul A.; Gebraad, Pieter M. O.; Lee, Sang; van Wingerden, Jan-Willem; Johnson, Kathryn; Churchfield, Matt et al. (2014): Evaluating techniques for redirecting turbine wakes using SOWFA. In: Renewable Energy 70, S. 211-218. DOI: 10.1016/j.renene.2014.02.015.
- [2] Bottasso, C. L.; Cacciola, S.; Schreiber, J. (2018): Local wind speed estimation, with application to wake impingement detection. In: Renewable Energy 116, S. 155-168. DOI: 10.1016/j.renene.2017.09.044.
- [3] Shapiro, Carl R.; Meyers, Johan; Meneveau, Charles; Gayme, Dennice F. (2017): Dynamic wake modeling and state estimation for improved model-based receding horizon control of wind farms. In: 2017 American Control Conference (ACC). 2017 American Control Conference (ACC). Seattle, WA, USA, 24.05.2017 - 26.05.2017: IEEE, S. 709-716.
- [4] Doekemeijer, B. M.; Boersma, S.; Pao, L. Y.; Van Wingerden, J. W. (2017): Ensemble Kalman filtering for wind field estimation in wind farms. In: 2017 American Control Conference (ACC). 24-26 May 2017. Seattle, WA, USA. American Control Conference; American Automatic Control Council; ACC. Piscataway, NJ: IEEE, S. 19-24.

- [5] Keane, Aidan; Aguirre, Pablo E. Olmos; Ferchland, Hannah; Clive, Peter; Gallacher, Daniel (2016): An analytical model for a full wind turbine wake. In: *J. Phys.: Conf. Ser.* 753, S. 32039. DOI: 10.1088/1742-6596/753/3/032039.
- [6] Jiménez, Ángel; Crespo, Antonio; Migoya, Emilio (2010): Application of a LES technique to characterize the wake deflection of a wind turbine in yaw. In: *Wind Energ.* 13 (6), S. 559–572. DOI: 10.1002/we.380.
- [7] Lagarias, Jeffrey C.; Reeds, James A.; Wright, Margaret H.; Wright, Paul E. (1998): Convergence Properties of the Nelder–Mead Simplex Method in Low Dimensions. In: *SIAM J. Optim.* 9 (1), S. 112–147. DOI: 10.1137/S1052623496303470.
- [8] Campagnolo, Filippo; Petrović, Vlaho; Schreiber, Johannes; Nanos, Emmanouil M.; Croce, Alessandro; Bottasso, Carlo L. (2016): Wind tunnel testing of a closed-loop wake deflection controller for wind farm power maximization. In: *Journal of Physics: Conference Series* 753 (3), S. 32006. DOI: 10.1088/1742-6596/753/3/032006.
- [9] Campagnolo, Filippo; Schreiber, Johannes; Garcia, Andrea M.; Bottasso, Carlo L. (2017): Wind Tunnel Validation of a Wind Observer for Wind Farm Control. In: *The proceedings of the Twenty-seventh International Ocean and Polar Engineering Conference, ISOPE.*
- [10] Schreiber, J.; Nanos, E. M.; Campagnolo, F.; Bottasso, C. L. (2017): Verification and Calibration of a Reduced Order Wind Farm Model by Wind Tunnel Experiments. In: *Journal of Physics: Conference Series* 854, S. 12041. DOI: 10.1088/1742-6596/854/1/012041.

Paper 12: Wind tunnel testing of wake steering with dynamic wind direction changes

14.1 Summary

Within this work a model-based wind farm controller is tested in a scaled wind farm environment including dynamic wind direction changes. The open-loop controller bases on look-up-tables which have been pre-computed using different wind farm models with varying accuracy.

Each table contains the turbine yaw misalignments that lead to maximum wind farm power for a variety of given constant wind directions. The wind farm controller is implemented to read the measured ambient direction at each time instant and to set the corresponding optimal yaw misalignments, stored in the look-up-table, on each turbine. As the wind conditions change constantly and a very simple control approach is followed, a measurement uncertainty has been accounted for during the look-up-table computation.

Experimental tests on a wind farm consisting of three scaled wind turbines have been finally conducted based on a measured full-scale wind direction time history. A significant increase in energy production could be measured using each look-up-table. In details, the table computed using the baseline FLORIS wind farm model resulted in gains of approx. 4.5%, the table computed using the improved model of **Paper 9** resulted in approx. 5% and a purely data driven model, obtained using an extensive data set, resulted in approx. 5.5% highlighting the maximum achievable gain following the control approach. The results show that the higher model accuracy obtained through the model improvements developed and shown in **Paper 9** indeed improve power capture.

As the scaled turbine models are equipped with load sensors, the effect of wind farm control on the damage equivalent loads could be also assessed: The wake steering controller reduces loads on the downstream turbines in all cases. Even though, the front turbine experiences an increase of damage loads, they never exceed those of the downstream turbines. Consequently, the load distribution among the turbines becomes more even, resulting in a better balanced lifetime of the turbines.

14.2 Contribution

The author of this dissertation has developed and implemented the wind farm control algorithm and participated in the design and analysis of the experiments. Filippo Campagnolo conducted the experiments and led the whole research work. All authors provided important input to this research work through discussions, feedback and by writing the paper.

14.3 Reference

F. Campagnolo, R. Weber, J. Schreiber, and C. L. Bottasso, “Wind tunnel testing of wake steering with dynamic wind direction changes,” *Wind Energy Science*, vol. 5, no. 4, pp. 1273–1295, 2020. doi: 10.5194/wes-5-1273-2020

Wind Energ. Sci., 5, 1273–1295, 2020
<https://doi.org/10.5194/wes-5-1273-2020>
© Author(s) 2020. This work is distributed under
the Creative Commons Attribution 4.0 License.



Wind tunnel testing of wake steering with dynamic wind direction changes

Filippo Campagnolo, Robin Weber, Johannes Schreiber, and Carlo L. Bottasso

Wind Energy Institute, Technische Universität München, 85748 Garching bei München, Germany

Correspondence: Carlo L. Bottasso (carlo.bottasso@tum.de)

Received: 19 April 2020 – Discussion started: 19 May 2020

Revised: 27 July 2020 – Accepted: 19 August 2020 – Published: 8 October 2020

Abstract. The performance of an open-loop wake-steering controller is investigated with a new unique set of wind tunnel experiments. A cluster of three scaled wind turbines, placed on a large turntable, is exposed to a turbulent inflow and dynamically changing wind directions, resulting in dynamically varying wake interactions. The changes in wind direction were sourced and scaled from a field-measured time history and mirrored onto the movement of the turntable.

Exploiting the known, repeatable, and controllable conditions of the wind tunnel, this study investigates the following effects: fidelity of the model used for synthesizing the controller, assumption of steady-state vs. dynamic plant behavior, wind direction uncertainty, the robustness of the formulation in regard to this uncertainty, and a finite yaw rate. The results were analyzed for power production of the cluster, fatigue loads, and yaw actuator duty cycle.

The study highlights the importance of using a robust formulation and plant flow models of appropriate fidelity and the existence of possible margins for improvement by the use of dynamic controllers.

1 Introduction

Wakes produced by upstream wind turbines have a profound influence on the performance of downstream machines. Compared to clean isolated conditions, waked turbines produce less power, approaching a 50 % reduction for full-wake interaction (Mechali et al., 2006), and they experience increased loading (Madjidian et al., 2011; Bustamante et al., 2015; Vera-Tudela and Kühn, 2017). The impact in terms of both lost production and increased loading is significant and has cascading effects on operation and maintenance (O&M) and lifetime. Probably one of the most direct indications of the impact of wakes outside of the scientific literature is given by the press announcement issued by Ørsted (formerly DONG) in October 2019. In this announcement, Ørsted, the largest offshore wind energy developer in the world, warned investors that it will not be able to meet its long-term financial targets. Next to market issues, “...the negative impact of two effects across our asset portfolio, i.e., the blockage effect and the wake effect” was listed as the main reason. In addition, Ørsted stated that “...underestimation of

blockage and wake effects is likely to be an industry-wide issue” (Ørsted, 2019).

Wind farm control is widely recognized as one of the main solutions to mitigate wake effects (Gebraad et al., 2016; Fleming et al., 2016; Vali et al., 2017; Fleming et al., 2017; Raach et al., 2018; Fleming et al., 2019). In wind farm control, the turbines in a wind farm operate in a coordinated, collaborative fashion. This stands in direct contrast to the standard, locally greedy approach in which each machine works independently from the others to maximize its own power output – even if this is detrimental to the output of its neighboring turbines. A number of wind farm control strategies are currently being investigated, including static and dynamic induction control (Frederik et al., 2020) and wake steering (Knudsen et al., 2015; Fleming et al., 2016). Among these, wake steering is probably the most promising technique for practical field deployment, and reports of field tests have already been published (Fleming et al., 2017, 2019; Howland et al., 2019). This control technology is also offered as a fea-

ture for offshore wind farms by one of the leading wind turbine manufacturers (Siemens Gamesa, 2019).

Although a field demonstration is clearly the final litmus test for any technology, simulations with high-fidelity models and scaled testing in wind tunnels offer some unique opportunities to improve knowledge and understanding. Bottasso et al. (2014) pioneered wind tunnel testing beyond pure aerodynamic investigations by developing several experimental applications based on actively controlled scaled wind turbines. Campagnolo et al. (2016c) followed up with an experimental demonstration of closed-loop wake steering. In addition to their own scientific advances, these works provided comprehensive opportunities for the validation of simulation models (Wang et al., 2019).

The present paper follows in these same tracks. Here three scaled turbines are tested in a large boundary layer wind tunnel, where dynamic wind direction changes are generated by using a turntable. The three machines are governed by an open-loop wake-steering controller, while each machine is operated by its own closed-loop yaw, pitch, and torque controller. The known, repeatable, and controllable environment of the wind tunnel offers the opportunity to address some key questions:

- What are the effects of neglecting the dynamics of wake interaction by using a steady-state controller? And what are the additional effects caused by a limited yaw rate and a finite sampling time of the controller?
- What are the effects on performance of the fidelity of the underlying model used for control synthesis? Does it pay off to use a better model, and what are the margins for improvement? Are conclusions different when looking at power, loads, or actuation effort?
- What are the benefits of using a formulation that is robust in the face of uncertainties, as opposed to a naive deterministic approach? And is there a minimum wake interaction threshold below which it might be better not to use a wake-steering controller?

This study is an initial effort to try and answer these questions.

The paper is organized as follows. Section 2 describes the experimental setup, including the scaled turbines, the tunnel sheared and turbulent inflow, and the generation with a turntable of dynamic wind direction changes that mimic actual field measurements. Since the ground truth wind direction is known in the case of the experiment, a filtering approach is described to provide the controller with a tunable level of uncertainty, with the goal of characterizing its effects on performance. Section 3 describes the control formulation and implementation. A model-based robust formulation is used here, which first derives look-up tables (LUTs) by an offline optimization and then interpolates within the LUTs at run-time based on the detected operating conditions.

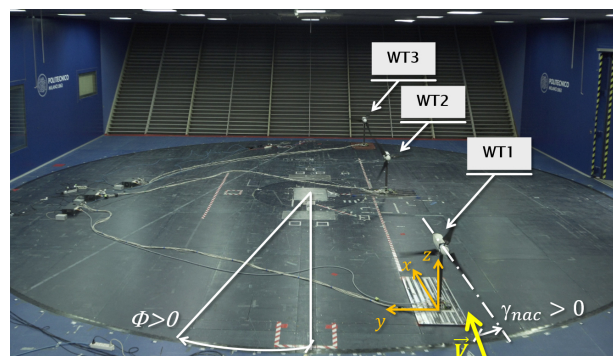


Figure 1. Experimental setup, showing the three model turbines mounted on the wind tunnel turntable. The x - y - z frame is fixed with respect to the tunnel and does not rotate with the turntable.

To explore the effects of varying model fidelity, three different farm flow models are considered. The first is a MATLAB implementation of the FLORIS model developed by TU-Delft (Doekemeijer et al., 2019), which differs from the latest release (NREL, 2020) and lacks the effects of secondary steering and nonuniform inflow. The second is an improved version of the same model based on the learning of correction terms from operational data, termed FLORIS-Augm (Schreiber et al., 2020). The third farm flow model is a purely data-driven model that, based on the accurate measurements that are possible in the wind tunnel, can be considered an exact steady-state representation of the experiment. Section 4 presents an analysis of the experimental results. The non-robust formulation is analyzed first in terms of the effects on performance of uncertainty level, finite yaw rate, neglected dynamics, and model fidelity. Next, the robust formulation is considered and compared to the non-robust one, looking at the metrics of power, fatigue loading, and actuator duty cycle. Section 5 concludes the work and provides some initial answers to the questions posed above.

2 Experimental setup

The experimental setup is shown in Fig. 1: a small cluster composed of three scaled wind turbines is installed on the 13 m diameter turntable of the atmospheric test section of the wind tunnel of the Politecnico di Milano (Bottasso et al., 2014). The turntable can be rotated by the angle Φ to simulate different wind directions. This is achieved by first lifting the turntable with an air cushion by approximately 20 mm and then rotating it by means of a friction wheel. A dedicated controller is used to track the user-prescribed rotation time history. An optical encoder with an accuracy of $\pm 0.1^\circ$ is used as feedback. The turntable was in the lifted position throughout the course of each experiment.

The three turbines are aligned in a row with a longitudinal spacing of five rotor diameters (5D), and they are termed

WT1 (upstream), WT2 (center), and WT3 (downstream). The wind direction Φ is zero when the turbine row is parallel to the wind tunnel centerline. In this position, the row of turbines is located $-1.5D$ to the left of the centerline when looking upstream. Angle Φ is positive for a clockwise rotation of the turntable viewed from the top (see Fig. 1); this means that a positive Φ corresponds to the wind blowing from the left of the row of turbines when looking upstream.

Rotating the turntable does not exactly correspond to a change in wind direction with respect to fixed ground. In fact, the scaled turbines experience a translational movement proportional to the angular speed of the turntable and to their distance from the center of rotation. This generates an additional flow velocity relative to the rotor, on average equal to approximately 0.04 m s^{-1} . In turn, this creates a small extra local wind direction change, quantified to less than 0.5° for the current setup and testing conditions. Other differences with respect to a real wind direction change are caused by the slight horizontal shear present in the wind tunnel flow. The translational movement exposes the turbines to different flow speeds as they move laterally in the tunnel during the turntable rotation. This effect is not negligible, but it can be accounted for if the horizontal shear is known, as discussed later.

2.1 Wind turbine model

Three identical G1 scaled models with a rotor diameter, hub height, and rated rotor speed of 1.1 m, 0.825 m, and 850 rpm, respectively, were used in the experiments. The models, already used in previous research projects (Campagnolo et al., 2016a, c, b), are equipped with active pitch, torque, and yaw control. Strain gauges measure loads on the shaft and at the tower base. Further details about the G1 design, its aerodynamic performance and several of its applications can be found in Bottasso and Campagnolo (2020).

Each wind turbine is controlled with a dedicated real-time Bachmann M1 system, where supervisory control logic, pitch–torque–yaw control algorithms, and all necessary safety, calibration, and data-logging functions are implemented. Demanded reference values for torque, pitch, and yaw are computed by the wind turbine controller and then sent to the actuator control boards, where low-level control functions are executed. The M1 system acquires torque, shaft bending moments, and rotor azimuth position with a sample rate of 2.5 kHz, whereas all other measurements (tower base loads, blade pitch angles, and wind speed and direction) are acquired with a sample rate of 250 Hz.

A standard power controller is implemented based on Bossanyi (2000), with two distinct control regions (Burton et al., 2011). Below rated wind speed (region II), the blade pitch angle is held constant, while the generator torque is a quadratic function of the rotor speed that enforces a constant tip speed ratio (TSR). Above rated wind speed (region III), the generator torque is kept constant, while a proportional-

integral (PI) controller changes the collective pitch of the blades to enforce a constant generated power.

The nacelle orientation γ_{nac} is positive for a counterclockwise rotation when viewed from the top (see Fig. 1) and can be varied at will with respect to the base. The positioning is achieved with a PI controller executed on the control board of the yaw motor. A yaw brake can be engaged once the nacelle reaches the desired position within a tolerance of $\pm 0.2^\circ$. Whenever the reference orientation is changed, the brake and the motor are simultaneously actuated to ensure smooth transitions.

The wind farm controller was implemented on a desktop PC, communicating with the turbine controllers through the MODBUS protocol. This plant-level controller sets a desired misalignment angle γ with respect to the wind for each turbine. A positive γ corresponds to a counterclockwise misalignment looking down onto the model, i.e., the opposite direction of Φ . The relationship between wind direction, nacelle orientation, and yaw misalignment angle is

$$\gamma = \gamma_{\text{nac}} - \Phi. \quad (1)$$

Figure 2 shows the behavior of the G1 rotor thrust coefficient C_T and power coefficient C_P with respect to the rotor-effective wind speed U_{REWS} (top row of the figure) and with respect to the misalignment angle γ (bottom row of the figure).

The behavior of the thrust and power coefficients vs. rotor-effective wind speed was obtained by closed-loop simulations with FAST (Jonkman and Jonkman, 2018), using turbulent flow conditions similar to the ones generated in the wind tunnel in terms of speed and turbulence intensity. The blade aerodynamic model uses Reynolds-dependent airfoil polars tuned as described in Wang et al. (2020). Figure 2b shows that the wind turbine C_P is affected by the Reynolds dependency of its airfoil polars in region II (i.e., for wind speeds lower than approximately 5.7 m s^{-1}). At low winds, and hence at low rotational speeds, the blade airfoil efficiency is reduced because of the low chord-based Reynolds number, resulting in a reduction of C_P . However, the Reynolds number has only a modest effect on the lift coefficient (Wang et al., 2020), thus resulting in an approximately constant C_T (see Fig. 2a).

The behavior of the thrust and power coefficients vs. misalignment angle was characterized with dedicated wind tunnel tests, conducted for $\gamma \in \pm 31^\circ$ with the turbine operating in region II. The results are reported in Fig. 2c, d. The best-fitting cosine-law power-loss exponents equal 2.174 and 1.425 for the power and thrust coefficients, respectively.

2.2 Inflow characteristics

Spire placed at the inlet of the test section passively generate an atmospheric-like boundary layer. The flow was characterized with three-component constant-temperature hot-wire

1276

F. Campagnolo et al.: Wind tunnel testing of wake steering with dynamic wind direction changes

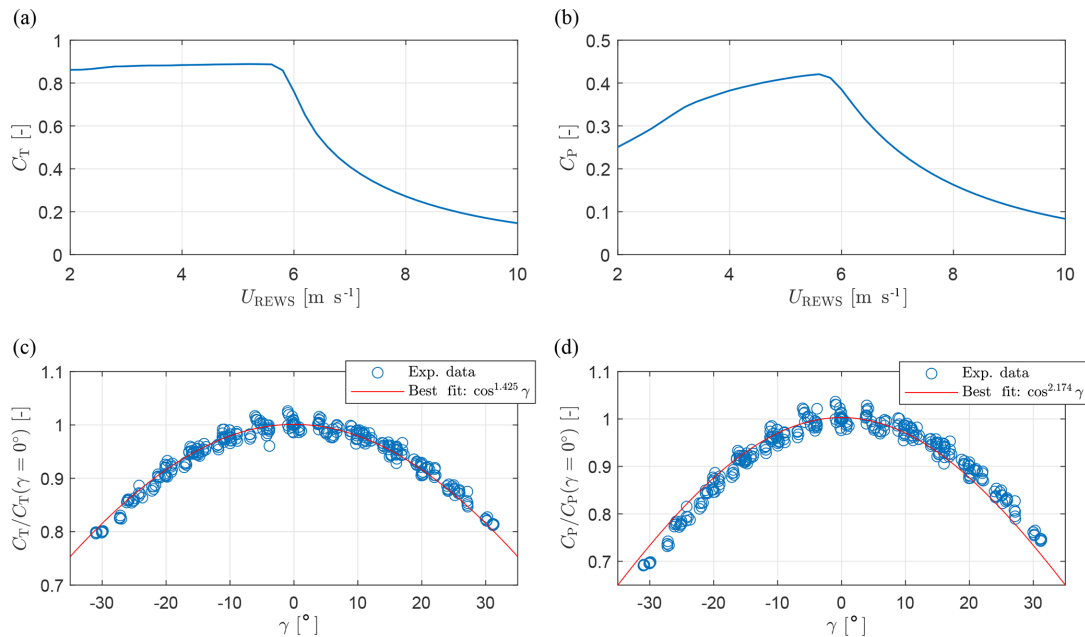


Figure 2. C_T (a) and C_P (b) vs. rotor-equivalent wind speed U_{REWS} . C_T (c) and C_P (d) vs. misalignment angle γ .

probes (CTA), scanning a vertical line 4 D upwind of WT1. The vertical profiles of the longitudinal wind speed U (normalized by the speed at hub height z_H) and the turbulence intensity (TI) are shown in Fig. 3a, b, respectively. The top and bottom points of the rotor are indicated with solid black lines, while a dashed black line indicates hub height. The vertical wind profile within the rotor disk is best-fitted by a power law with an exponent equal to 0.144, while turbulence intensity at z_H is approximately equal to 6 %, mimicking typical neutral, offshore conditions (Hansen et al., 2012).

For a correct interpretation of the wind farm control results, the small lateral nonuniformity of the wind tunnel flow needs to be taken into account (Wang et al., 2017). In fact, as the turntable is rotated, the turbines are also displaced laterally, thereby encountering slightly different ambient conditions. The ambient wind speed was measured by a pitot tube installed at hub height, laterally shifted 1.5 D to the left of the wind tunnel centerline and 3 D upwind of WT1. The pitot tube is, therefore, in front of the turntable and remains fixed with respect to the wind tunnel as the turntable is rotated. This means that the pitot tube is exactly in front of WT1 only for $\Phi = 0$, whereas it is laterally displaced with respect to the front turbine in all other cases. Hence, given the nonuniformity of the wind tunnel boundary layer, when the turntable is rotated the turbines are exposed to a local ambient flow that differs slightly from the one measured by the pitot tube.

To characterize this effect, one G1 was positioned at several different lateral locations y across the wind tunnel (see Fig. 1). The local rotor-effective wind speed U_{REWS} was computed directly from the torque measured on the turbine

for each location. The resulting lateral profile of the wind speed is reported in Fig. 3c. This diagram shows the presence of a horizontal shear with changes in wind speed up to ± 4 %, for both left and right shifts with respect to the pitot tube. These changes will clearly cause significant changes in power, due to its cubic dependency on speed.

2.3 Dynamic wind direction changes

Testing at scale implies not only different physical dimensions of the model, but also a scaling of time with respect to the original system. Specifically, the time speedup factor is defined as $n_t = t_M/t_P$, where t_M is the time of the scaled system and t_P the time of the full-scale system (Bottasso et al., 2014; Canet et al., 2020; Bottasso and Campagnolo, 2020). If $n_l = l_M/l_P$ is the scale factor, i.e., the ratio between the characteristic lengths of the model l_M and of the physical system l_P , then dimensional analysis gives that $t_M = t_P n_l V_P/V_M$, where V_M and V_P are the wind velocities in the two cases. For testing in a boundary layer wind tunnel, $n_l = \mathcal{O}(10^{-1} - 10^{-2})$ and $V_P/V_M = \mathcal{O}(10^0)$, implying that time flows $\mathcal{O}(10^1 - 10^2)$ times faster in the experiment than in the physical full-scale reality. In this specific case, the G1 turbine represents a $n_l = 1/160$ scaled model of an 8 MW full-scale machine (Desmond et al., 2016), while $V_P/V_M = 2$. Therefore, time flows faster by a factor of 80 in the wind tunnel than at full scale. Thus, 1 h of testing in the tunnel corresponds to about 3.3 d in the field, an additional valuable side effect of testing at scale. A simple example of the acceleration of time is provided by the wake advection

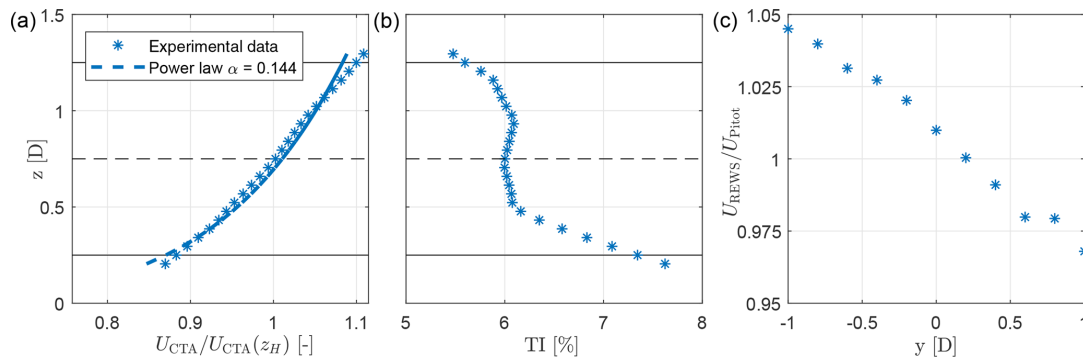


Figure 3. Characteristics of the wind tunnel boundary layer: vertical profiles of wind speed (a) and turbulence intensity (b), measured with CTA probes; lateral profile of the wind speed (c), measured using the rotor as a sensor.

time, which is the time necessary for a flow perturbation to travel from an upstream turbine to a downstream one. As a first approximation, the wake advection time is equal to the ratio of the distance between the two machines and the flow speed. If the wind tunnel and full-scale inflow speeds are in a ratio of 1/2, as in the present case, it is clear that in the wind tunnel the wake advection time is much shorter than at full scale, because the distance between the two turbines is much smaller (by a factor of 160).

In order to obtain results that can be up-scaled, changes in wind direction simulated in the wind tunnel should realistically mimic full-scale variations. To this end, a wind direction time history was measured at 1 Hz at an onshore test site located in northern Germany using a wind vane installed at a height of 89.4 m on a met mast (Bromm et al., 2018). Within the available dataset, 5 d of measurements were selected and scaled by n_t , obtaining a time history used for driving the turntable rotation. The data selection criteria were as follows:

- met mast always fully out of the wakes of neighboring machines;
- wind direction variations within the range $\pm 15^\circ$ as, given the experimental setup, wake interactions within the cluster are expected only for $\Phi \in \pm 15^\circ$;
- enough data to draw statistically meaningful conclusions, using Fleming et al. (2019) as a guideline.

Figure 4a reports the frequency spectrum of the scaled (i.e., sped-up) field-measured wind direction time series Φ_{Met} . The plot also shows the spectrum of the wind direction changes Φ_{CTA} already naturally present (without using the turntable) in the wind tunnel flow due to the generated turbulence, as measured with the CTA probes. The figure shows that there is a very good match at the high frequencies between the real flow and the one in the wind tunnel. On the other hand, it is also evident that the wind tunnel boundary layer completely misses the large-amplitude fluctuations present in the field at scaled frequencies below about

0.66 Hz. Taking into account the time scaling factor, this means that wind direction fluctuations characterized by a period above approximately 2 min are missing from the tunnel flow. Since these are the dominant wind direction changes for wind farm control (Simley et al., 2020), a way is needed to fill the lower band of the spectrum.

With the turntable, these missing low-frequency wind direction fluctuations can be filled in. Unfortunately, an exact reproduction of the complete spectrum is not possible due to hardware limitations. In fact, the rotational acceleration of the turntable is limited by the maximum force that can be exerted with the driving friction wheel. At higher accelerations, inertial effects on the models would also have to be taken into account. To obtain a time series that could be followed by the turntable, piecewise cubic splines were used to best fit a 2 min moving average of the wind direction time history, under the constraints of maximum achievable acceleration and velocity. The resulting time series Φ_{turn} is compared to the sped-up 2 min average of Φ_{Met} in Fig. 4c.

Figure 4b shows the spectrum of the resulting wind directions obtained by combining the natural changes present in the wind tunnel flow with the artificial ones generated by the turntable. A comparison with the field-measured spectrum shows that the two match very well at the lowest and highest frequencies. On the other hand, the combined wind tunnel flow has a gap in the range 0.04–0.66 Hz, which corresponds to direction changes between 2 and 30 min at full scale. Filling this gap would require a modification to the actuation system of the turntable, which was unfortunately not possible within the scope of the present work.

3 Open-loop wake-steering controller

The wind farm control strategy is the open-loop algorithm sketched in Fig. 5. The algorithm consists of a model-based optimization that produces a look-up table (LUT) of discrete set points, followed by an interpolation within the precomputed table at given instantaneous ambient conditions.

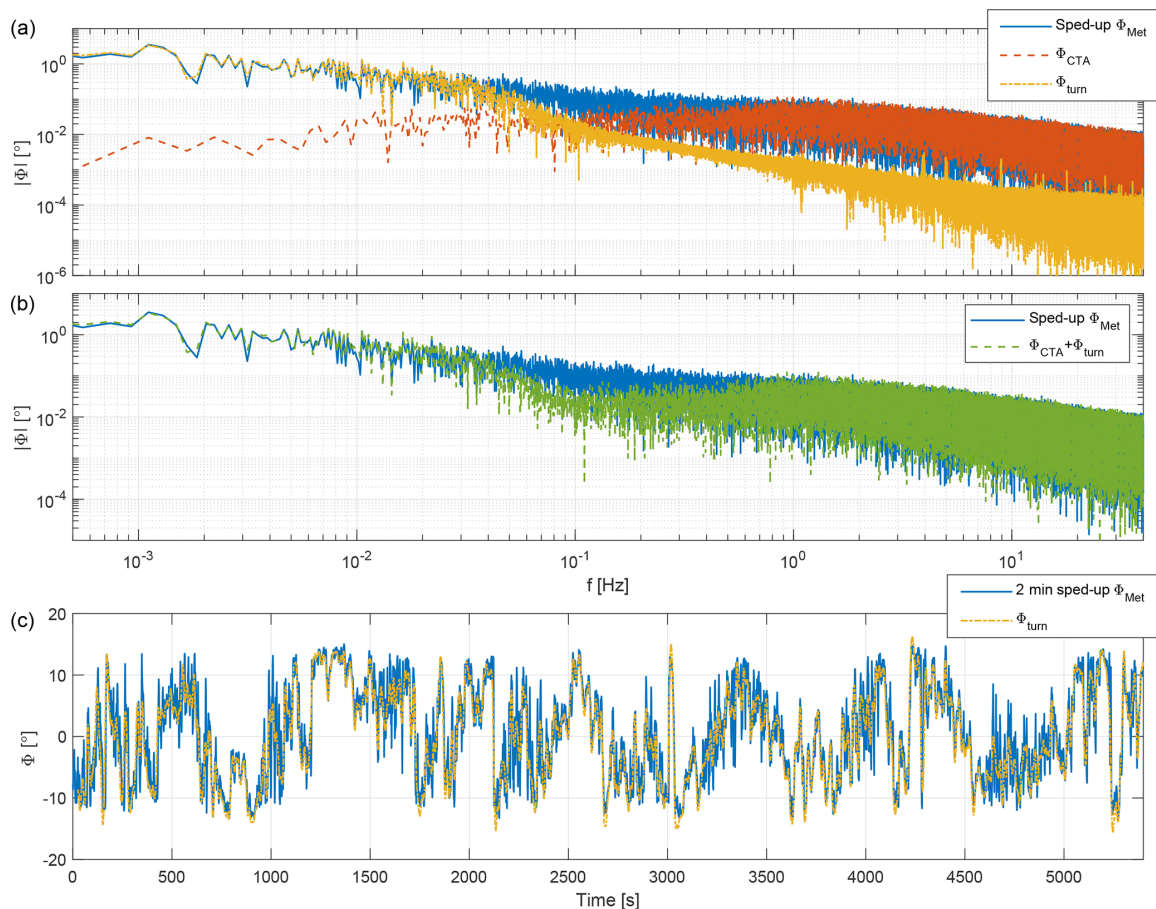


Figure 4. (a) Spectrum of the sped-up field-measured wind direction time series Φ_{Met} (solid blue), the turbulence-induced wind direction changes in the tunnel Φ_{CTA} (dashed red), and the turntable rotation Φ_{turn} (dashed–dotted orange). (b) Spectrum of the sped-up wind direction changes in the field Φ_{Met} (solid blue) and the combined wind direction changes in the wind tunnel $\Phi_{CTA} + \Phi_{turn}$ (dashed green). (c) Time history of the 2 min average of the sped-up field-measured wind direction (blue), compared to the time history used to drive the turntable rotation (dashed–dotted orange).

A wind farm flow model is first calibrated with the use of preexisting data (and possibly retuned online during operation, although the present work did not make use of this possibility). Based on this model, an optimization is performed offline to compute the optimal set points of each machine in the farm that minimize a cost function for given ambient conditions. In this work, the set points consist of yaw offsets of each turbine with respect to the ambient flow direction; a more general implementation could be additionally scheduled in terms of wind speed and turbulence intensity. To understand the effects of model fidelity on the controller performance, LUTs were computed based on the three different flow models described in Sect. 3.1.

During operation, filtered ambient wind conditions are computed, including wind direction, wind speed, and turbulence intensity (because of its effect on wake recovery). These conditions can be estimated from the operational data

of the turbines (Schreiber et al., 2018), or simply by a met mast (Fleming et al., 2019). Based on the ambient wind conditions, the control logic interpolates within the LUT to compute the current set points, which are then dispatched to each individual wind turbine. The process of ambient condition estimation, LUT interpolation, and dispatching is repeated with a desired frequency.

Similar controllers have been recently implemented and tested in the field (Fleming et al., 2019). However, the implementation in a wind tunnel experiment has some specific features, which are discussed next.

The ambient conditions in the experiment are characterized by constant mean wind speed and turbulence intensity but variable low-frequency wind direction changes generated by the turntable. Figure 6a shows the combined wind direction time history $\Phi_{CTA} + \Phi_{turn}$, its 1.5 s moving average, and the turntable rotation Φ_{turn} . In the experiments, the true wind

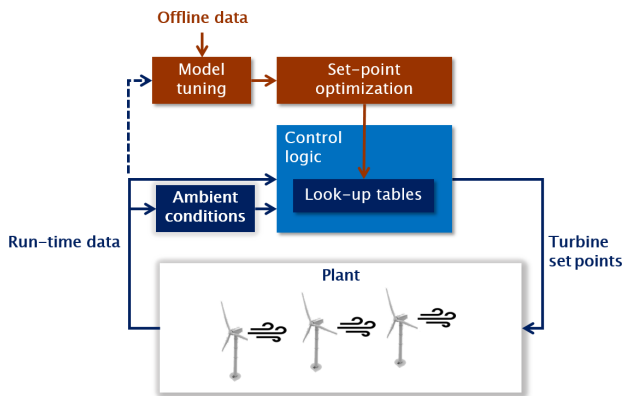


Figure 5. Wind farm control scheme. The option to update the model at runtime to recompile the LUTs (dashed line) was not used in the present work.

direction is therefore known through the turntable encoder with a high accuracy and signal-to-noise ratio, something that is hardly possible in the field.

The turntable signal is filtered and provided as wind direction input to the controller. By filtering this signal, the controller reacts only to low-frequency fluctuations and neglects higher-frequency turbulent changes, which is desirable for yaw-based control (Simley et al., 2020; Fleming et al., 2019). However, increasing the filtering action generates longer delays, which has the effect of changing the wind direction seen by the controller with respect to the true one. This fact was exploited here to generate a variable level of uncertainty and study its effects on the controller performance. To assess the effects of filtering (i.e., uncertainty), three values of the moving average time window were considered and used as input for the controller, namely $T_{MAvg} = 1.5, 7.5, \text{ and } 15 \text{ s}$, which correspond to 2, 10, and 20 min at full scale. The effects of the filter on the wind direction time series are shown in Fig. 6b.

At runtime, the controller outputs the optimal yaw misalignment angle γ_1 for WT1 and γ_2 for WT2 at each time step (equal to 0.75 s, which corresponds to 1 min at full scale), whereas the downstream turbine WT3 adopts a standard wind-tracking yaw strategy with the same time step. To guarantee a more precise yaw misalignment (Bossanyi, 2018), a direct control of the nacelle orientation was preferred to the indirect approach used by Fleming et al. (2017, 2019). In this method, the required absolute nacelle orientation is computed from Eq. (1) as $\gamma_{nac} = \gamma + \Phi_{meas}$, where Φ_{meas} is the measured wind direction (i.e., the filtered turntable encoder signal). The nacelle is then actuated with a maximum yaw rate $\dot{\gamma}_{max} = 10^\circ \text{ s}^{-1}$ ($0.125^\circ \text{ s}^{-1}$ at full scale) to limit gyroscopic loads on the G1. As discussed later, the maximum yaw rate has a significant effect on performance; it should be noted that the value chosen here is lower than the 0.3° s^{-1}

at full scale used in other publications (Bak et al., 2013; Jonkman et al., 2009).

3.1 Wind farm models

Three different wind farm models of different fidelity were used for the synthesis of the LUTs: the lower level of fidelity is provided by the FLORIS model, described in Sect. 3.1.1; the intermediate level by a data-augmented version of FLORIS, described in Sect. 3.1.2; and the higher fidelity level is given by a purely data-driven model, described in Sect. 3.1.3.

For consistency with the wind tunnel experiments, a wind direction change was accounted for in the models as a rotation of the wind farm. A variation in the wind direction is therefore also associated with a slight variation in the ambient speed sensed by each wind turbine, because of the horizontal shear of the inflow shown in Fig. 3. The extra velocity component caused by the motion of the turbine and its effect on the local wind direction were not included in the models because they are negligible.

3.1.1 FLORIS model

Given a set of ambient wind conditions, the FLORIS model computes the steady-state flow within a wind farm and, in turn, the power output of the individual turbines (Doekemeijer et al., 2019). The present results were obtained with the MATLAB implementation available online (Doekemeijer and Storm, 2018), using the *selfSimilar* velocity deficit, the *rans* deflection, the wake model of Bastankhah and Porté-Agel (2016), the *quadraticRotorVelocity* wake combination, and the *crespoHernandez* added turbulence (Crespo and Hernández, 1996). To improve accuracy at the cost of a slightly increased computational effort, the power of a turbine is computed by integrating the flow at the rotor disk using $P = 1/2 \rho \int_A V^3 C_{pd} dA$ (where ρ is air density, V the local wind speed, and A the rotor disk area), instead of the original implementation based on the rotor-average wind speed. The speed dependency of the thrust and power coefficients and the yaw-dependent power losses reported in Fig. 2 were implemented as well. The ambient wind field in the model is horizontally sheared to match the wind tunnel inflow. The model was tuned based on wake measurements of one isolated G1 turbine, as discussed in Campagnolo et al. (2019), obtaining the parameters reported in Table 1; notice that, having been tuned with ad hoc measurements, the values of these parameters differ from the ones provided by Bastankhah and Porté-Agel (2016) and Crespo and Hernández (1996). The wind speed at $y = 0$ was set to 5.25 m s^{-1} , while the turbulence intensity was set to 6.1 %.

1280

F. Campagnolo et al.: Wind tunnel testing of wake steering with dynamic wind direction changes

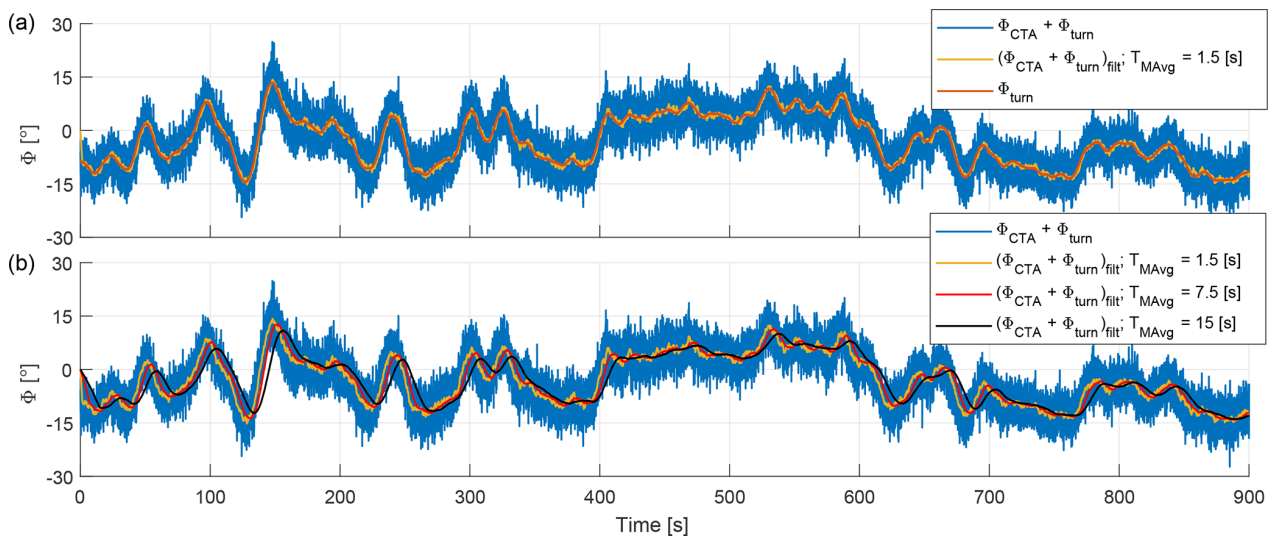


Figure 6. (a) Time history of the combined wind direction changes experienced by the farm (blue), its 1.5 s moving average (orange), and the measured turntable rotation (red). (b) Effect of the increasing time-averaging window T_{MAvg} on the wind direction time series.

Table 1. FLORIS parameters calibrated according to Campagnolo et al. (2019).

α	β	k_a	k_b	TI_a	TI_b	TI_c	TI_d
0.9523	0.2617	0.0892	0.027	0.082	0.608	-0.551	-0.2773

3.1.2 Data-augmented FLORIS model

An improved level of fidelity is obtained by an augmented version of the baseline FLORIS model (termed FLORIS-Augm), following the approach described in Schreiber et al. (2020). The central idea of model augmentation is to surgically insert additional terms into the governing equations to represent expected errors or effects lacking in the model (for example, secondary steering, which is very relevant in the present context and not present in the version of FLORIS used here). The correction terms are expressed in terms of parametric functions that are identified (or learned) from operational data. Since a baseline performance is provided by the underlying FLORIS model, learning is limited to small errors, which somewhat eases the requirements on the data. On the contrary, a purely data-driven approach, which does not use a reference model as a baseline, poses more stringent requirements on the training dataset; indeed, a data-driven model only “knows” what is in the data and nothing else. In practical field applications, it is possibly difficult to generate a rich-enough dataset to identify a model of high quality and wide generality.

The model augmentation method was demonstrated with the use of standard SCADA (supervisory control and data acquisition) data in Schreiber et al. (2020). Here, a similar approach was followed, by adding to FLORIS correction terms for nonuniform inflow and secondary steering (Flem-

ing et al., 2018). The errors were then identified based on the power output of the three turbines in a variety of conditions, including different wind directions and different yaw misalignments, using a subset of the data used for the derivation of the data-driven model described in the following. Further details are given in Schreiber et al. (2020).

Although the FLORIS-Augm model is more accurate than the baseline FLORIS, it is still not perfect. Therefore it is interesting to verify whether an even higher-fidelity model might improve the performance of the wind farm controller. To answer this question, yet another unique ability of wind tunnel testing was exploited here. An extensive, high-quality dataset covering all operating conditions of interest was obtained in the wind tunnel. Based on this dataset, a high-fidelity, purely data-driven model is derived next.

3.1.3 Data-driven model

A dataset was generated by measuring the power output of the three turbines for the 11 wind directions $\Phi = [0, \pm 2.29, \pm 4.58, \pm 6.89, \pm 9.21, \pm 11.54]^\circ$. For each wind direction, the two upstream turbines were operated at various steady misalignment angles γ in the range $\pm 10^\circ$ around the optimal misalignments that, according to the FLORIS model, maximize the total plant power.

The data-driven model was obtained by best-fitting a response surface to the resulting set of data points, using

shape functions inspired by experimental observations and the wake superimposition models used in FLORIS. The formulation of the interpolating shape functions is presented in Appendix A.

3.1.4 Normalized power

The normalized power $P_{n,j}$ of the j th wind turbine is defined as

$$P_{n,j} = \frac{P_j}{1/2\rho AU_j^3}, \quad (2)$$

where U_j is the ambient wind speed at the location of that turbine. Here, the ambient speed is measured by the reference pitot tube and then corrected for the tunnel horizontal shear. The total normalized wind farm power is defined as $P_{n,Wf} = \sum_j P_{n,j}$.

For a turbine operating in undisturbed inflow, normalized power is equal to the standard power coefficient C_p . However, normalized power and the power coefficient differ for a turbine operating in the wake of an upstream machine. Normalized power is preferred to the power coefficient in the present analysis, because it reveals the reduced power extraction of a waked turbine when compared to an unwaked one, a difference that is lost to the classical power coefficient. In fact, two turbines – one in the wake of the other – might be operating in region II at the same power coefficient, although the downstream machine would have a much reduced power output than the front one, which would result in a lower normalized power compared to the upstream turbine.

3.1.5 Comparison of the three models

Figure 7 shows the normalized power of the individual turbines and the whole cluster for the case $\Phi = 0^\circ$ (i.e., with the wind blowing parallel to the row of turbines). Results are plotted versus the misalignment angles γ_1 and γ_2 of the two front turbines WT1 and WT2. Measured data points are indicated with red dots, while smooth surfaces show the predictions of the baseline FLORIS (left), FLORIS-Augm (center), and data-driven (right) models. A quantitative overall measure of the quality of the fits is given by the root-mean-square (rms) errors e_{RMS} , expressed in percent of the available free-stream wind power and included in the legends.

By looking at the plots and at the fitting RMS errors, it appears that the quality of the models degrades when moving downstream along the row of turbines, as expected, considering the increasing role of wake interactions. A comparison of the plots by column reveals the increasing level of fidelity of the models, where FLORIS-Augm is better than FLORIS, and data-driven is better than FLORIS-Augm.

3.2 Look-up table computation

In general, the LUTs for an open-loop wake-steering controller should depend on wind direction, wind speed, and tur-

bulence intensity (because of its effect on wake recovery). However, in the present wind tunnel experiments the last two parameters are kept constant, so that the LUTs were scheduled only with respect to wind direction. A resolution of 0.2° was used for wind directions $\Phi \in \pm 2^\circ$, whereas a lower resolution of 1° was used outside of this range.

For robustness, wind direction and yaw uncertainties should be taken into account in the calculation of the LUTs (Quick et al., 2017; Rott et al., 2018; Simley et al., 2020). Here only uncertainties in wind direction were considered, because yaw uncertainties due to possible sensor errors are negligible for the calibrated G1s.

Steady-state models such as the ones used in this work already include the effects of the higher-frequency wind direction changes of the spectrum. For example, the wake profiles measured by Campagnolo et al. (2019) and used to identify the model parameters of Table 1 represent mean steady values, whereas the actual instantaneous wake undergoes meandering fluctuations. In this sense, it is important to realize that the wake model already contains the effects of the wind direction changes naturally present in the wind tunnel flow, whose spectrum is reported in Fig. 4a in red. However, steady models lack the flow dynamics at the lower frequencies and the delays caused by the advection downstream with a finite travel speed. These models are therefore only capable of predicting slow changes of wind turbine power (Simley et al., 2020). A robust control formulation (Rott et al., 2018) should take into account the uncertain knowledge of the wind direction at these slower timescales.

Here again, wind tunnel testing presents some opportunities that are hardly available when testing in the field. In fact, the actual turntable rotation represents the “ground truth”, while the controller takes as input the filtered signal (shown in Fig. 6b). It follows that wind direction uncertainties are known in this case and are represented by the difference $\Delta\Phi$ between these two quantities. Therefore, one can change the value of the uncertainties (which is challenging in reality at full scale, since the ground truth is typically unknown) by simply changing the filtering of the turntable rotation. This approach was used here to study the effects that uncertainties have on the performance of the controller. Figure 8 reports the distribution of $\Delta\Phi$ for two values of T_{MAvg} equal to 7.5 and 15 s. The fitted Gaussian normal distributions have standard deviations $\sigma_\Phi = 2.01$ and 3.42° , respectively. For $T_{MAvg} = 1.5$ s wind direction uncertainties are negligible.

For each flow model, robust LUTs were computed based on the approach of Rott et al. (2018) for $\sigma_\Phi = [0 : 2 : 6]^\circ$. The MATLAB pattern-search algorithm was used to solve the resulting bounded optimization problem. For each considered wind direction Φ , the optimal yaw misalignments γ_1^* and γ_2^*

1282

F. Campagnolo et al.: Wind tunnel testing of wake steering with dynamic wind direction changes

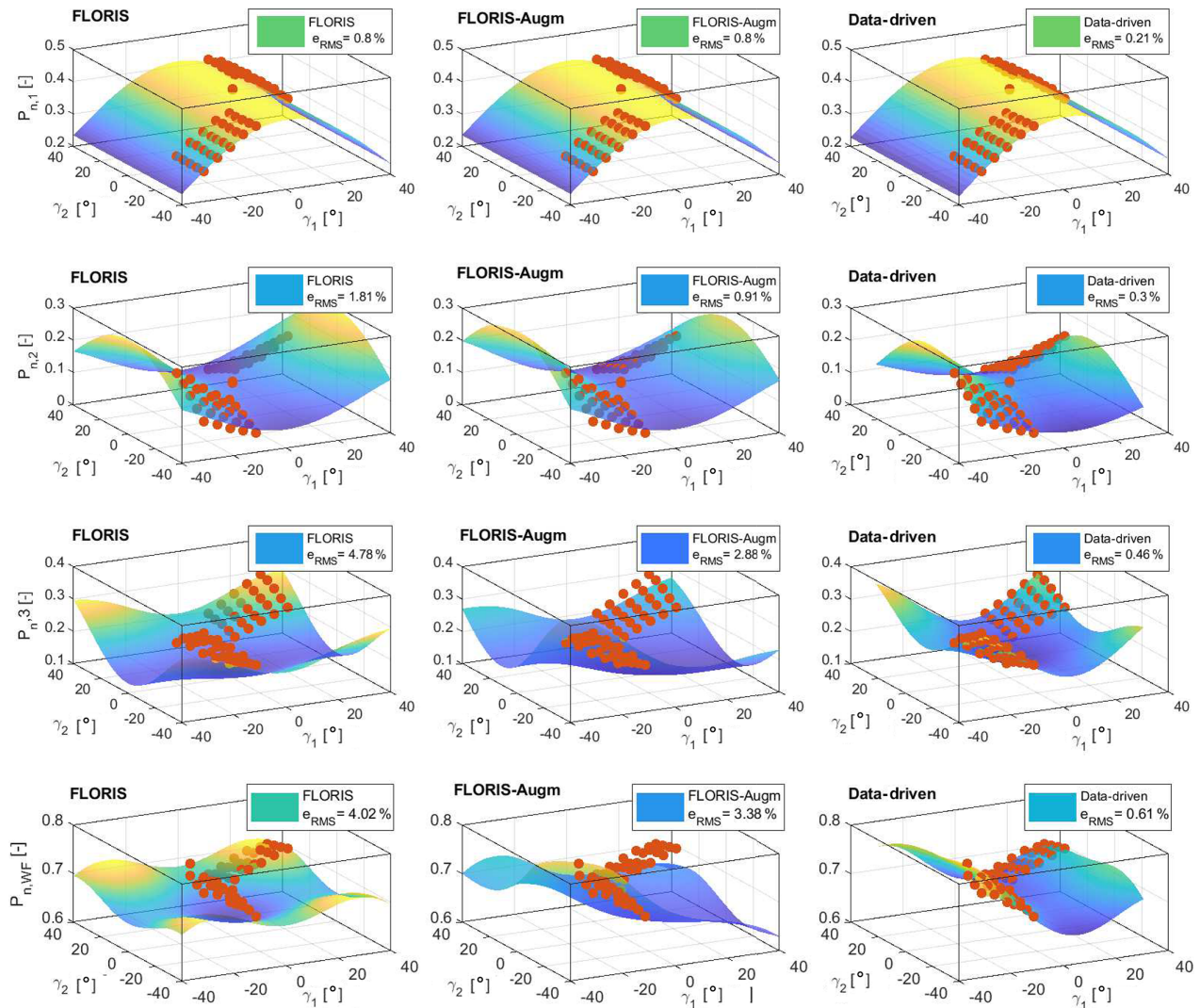


Figure 7. Normalized power of WT1 (first row), WT2 (second row), WT3 (third row), and the wind farm (fourth row), as functions of the misalignment angle γ of the two front turbines WT1 and WT2, for the wind direction $\Phi = 0^\circ$. Red dots: experimental measurements. Smooth surfaces: baseline FLORIS (left), FLORIS-Augm (center), and data-driven (right) models.

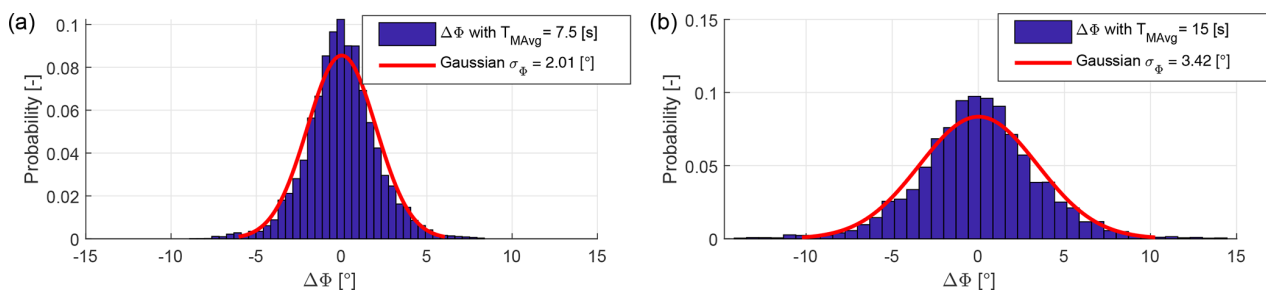


Figure 8. Distribution of wind direction uncertainties, i.e., difference between the actual turntable position and its filtered value (which is the wind direction input to the controller) for $T_{MAvg} = 7.5$ s (a) and $T_{MAvg} = 15$ s (b).

for WT1 and WT2 were computed as

$$[\gamma_1^*(\Phi), \gamma_2^*(\Phi)] = \arg \max_{\gamma_1, \gamma_2} \sum_{k=0}^9 P_M(\Phi + \Delta\Phi_k, \gamma_1 - \Delta\Phi_k, \gamma_2 - \Delta\Phi_k, -\Delta\Phi_k) f(\Delta\Phi_k), \quad (3a)$$

$$\text{such that: } [\gamma_1, \gamma_2] \in \pm 30^\circ, \quad (3b)$$

where $\Delta\Phi_k = (4k/9 - 2)\sigma_\Phi$ is the wind direction uncertainty varying in the range $\pm 2\sigma_\Phi$, $f \sim \mathcal{N}(0, \sigma_\Phi)$ is the Gaussian normal distribution, and $P_M(\Phi, \gamma_1, \gamma_2, \gamma_3)$ is the wind farm power predicted by the wind farm model.

The LUTs obtained with the baseline FLORIS model for different values of σ_Φ are shown in Fig. 9a and b. The effect of an increasing uncertainty is that of generating a smoother transition around $\Phi = 0^\circ$, and in general smaller misalignment of the turbines with respect to the wind.

Figure 9c and d compare the LUTs obtained with the three models for $\sigma_\Phi = 0^\circ$. Considering the front turbine misalignment γ_1 (Fig. 9c), the main difference among the LUTs is in the position of the transition point between positive and negative yaw offset, which is 0, -0.5 , and -0.8° for the baseline FLORIS, FLORIS-Augm, and data-driven models, respectively. The nonzero transition point predicted by two of the models can be ascribed to the nonsymmetric behavior of power for the cluster of turbines, shown in Fig. 10a for the greedy policy, i.e., no wake-steering control. Indeed, the figure shows that the minimum of the wind farm normalized power is at about -0.8° , i.e., for a wind blowing slightly from the right of the row of turbines when looking upstream. This is due to the combined effects of the tunnel horizontal shear and the slight lateral deflection for null yaw misalignment created by the vertically sheared flow.

Looking at the second turbine misalignment γ_2 (Fig. 9d), there is a significant difference among the three models. In fact, the baseline FLORIS does not include secondary steering, which is on the other hand represented to a different level of fidelity by the FLORIS-Augm and data-driven models. This effect leads to smaller misalignments for the second compared to the front machine, in agreement with other recent wind tunnel studies (Campagnolo et al., 2016c; Bastankhah and Porté-Agel, 2019).

4 Results

4.1 Maximum theoretical performance of the controllers

Before considering the behavior of the controllers in the experiments, it is interesting to establish a theoretical upper limit to their performance, neglecting dynamic effects, limited yaw rates, and uncertainties. To this end, the data-driven model was used as plant, being essentially an exact representation (except for measurement errors) of the wind farm behavior for a constant mean wind speed. The wind farm power output was computed using the greedy control policy and the

LUTs for $\sigma_\Phi = 0^\circ$. The total power output of the cluster is shown in Fig. 10a, while panel (b) shows the percent power gain with respect to the greedy policy.

Results indicate that all models lead to positive gains for all investigated wind directions, up to about 25% in the best conditions. The gains for the baseline FLORIS model are only slightly smaller than for the FLORIS-Augm and the data-driven model. This appears to indicate that the cost function of problem (3a) is rather insensitive to the details of the underlying model in the absence of uncertainties. However, these results might be misleading, because uncertainties are indeed present in reality and play a significant role, as shown later.

The results of Fig. 10 can be used to compute the maximum possible performance of the controllers for the wind direction time series used in the experiments and shown in Fig. 4. Under the assumption of an exact knowledge of the wind direction, an instantaneous realization of the required yaw misalignments, and the absence of any flow dynamics, the power gains of the baseline FLORIS, FLORIS-Augm, and data-driven LUTs are respectively equal to 10.73%, 11.41%, and 11.84%. These figures establish a non-achievable maximum theoretical performance of the controllers for this particular farm layout and wind direction time history.

4.2 Impact of different non-robust controller implementations

Next, wind tunnel tests were performed to characterize the effects of the following aspects of open-loop wake steering:

- uncertainty level (which, in the present context, is related to the filtering of the wind direction, i.e., of the turntable rotation);
- effect of a finite yaw rate and of neglected wake dynamics;
- model fidelity, according to the three considered models FLORIS, FLORIS-Augm, and the data-driven model.

The analysis is conducted first for a non-robust controller implementation, i.e., for the formulation expressed by problem (3a) with $\sigma_\Phi = 0^\circ$, while the performance of a robust controller is considered later in the paper.

Dynamic changes in wind direction were obtained by actuating the wind tunnel turntable, as described in Sect. 2.3, in the offshore inflow conditions described in Sect. 2.2. Each test was performed for a total of 90 min divided into nine intervals of 10 min each. This allowed for the periodic calibration of the wind tunnel and the wind turbine sensors, to guarantee the highest possible accuracy of the measurements.

Tests with the greedy control strategy were repeated four times, dispersed over the course of the experimental campaign. The averaged power values for the 90 min wind direction time series were normalized with the results of the first

1284

F. Campagnolo et al.: Wind tunnel testing of wake steering with dynamic wind direction changes

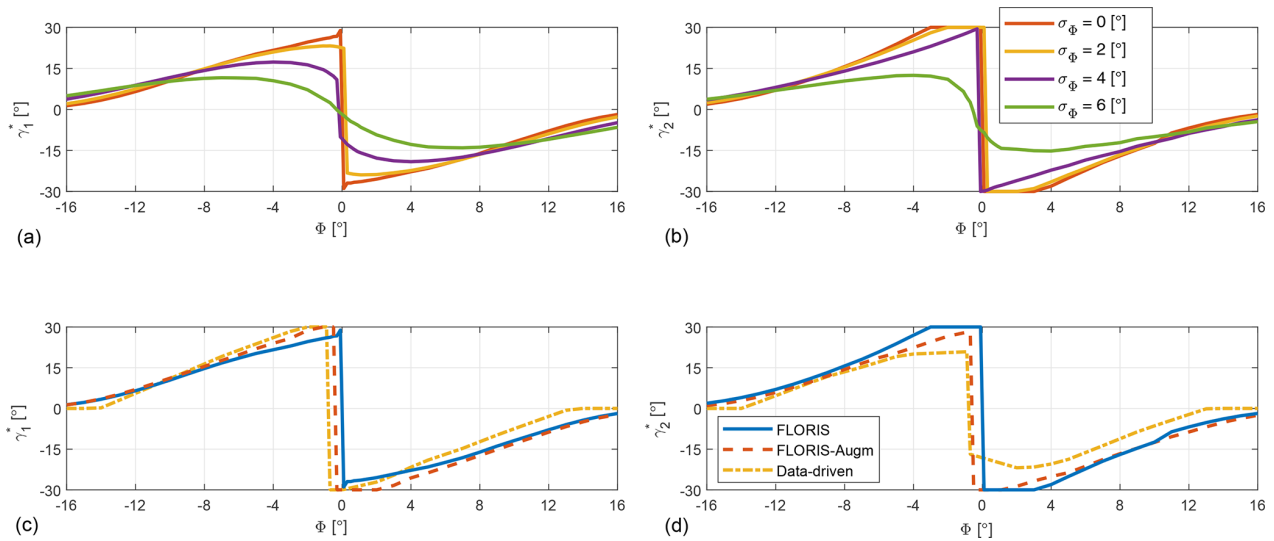


Figure 9. LUTs of optimal misalignment angles γ_1 and γ_2 vs. wind direction Φ . **(a, b)** FLORIS LUTs for different uncertainty levels. γ_1^* for WT1 **(a)**, γ_2^* for WT2 **(b)**. **(c, d)** LUTs for different models and $\sigma_\Phi = 0^\circ$. γ_1^* for WT1 **(c)** and γ_2^* for WT2 **(d)**.

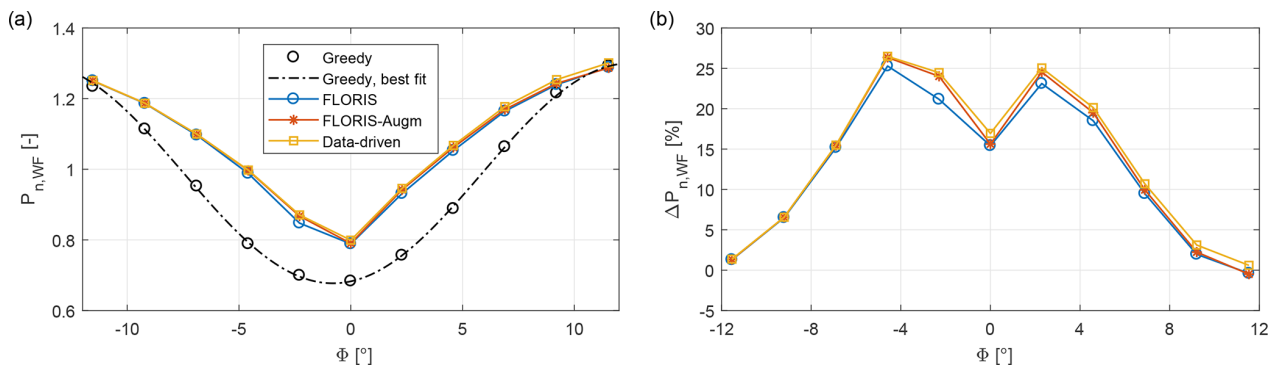


Figure 10. **(a)** Wind farm power output as a function of wind direction for different control policies. **(b)** Maximum theoretical percent power gain with respect to the greedy policy for the three flow models.

test and are shown in Fig. 11 for the whole wind farm and for each wind turbine. The standard deviation of these values across the four repetitions is equal to 0.98 % of the available free-stream wind power for the whole cluster, and to 0.15 %, 0.42 %, and 0.51 % for WT1, WT2, and WT3, respectively. These uncertainties, which can be mainly ascribed to errors of the pitot transducer and shaft torque meter, are acceptable considering the purpose of this analysis and are well below the differences caused by the various effects studied herein.

4.2.1 Effect of wind direction uncertainties

Experimental tests were performed with non-robust LUTs obtained from the baseline FLORIS model for the three filtering values $T_{MAvg} = 1.5$ s ($\sigma_\Phi = 0^\circ$), 7.5 s ($\sigma_\Phi = 2.01^\circ$), and 15 s ($\sigma_\Phi = 3.42^\circ$), which correspond to the three wind direction time histories shown in Fig. 6b.

The power gains with respect to the greedy policy are shown in Fig. 12. Average values aggregated over the whole wind direction time history are shown at wind farm level and for the single turbines. As expected, results indicate a progressive degradation of performance for an increasing level of uncertainty (i.e., for increasing T_{MAvg} and hence σ_Φ). The effects on the front turbine are very limited, whereas they are more pronounced for the second and third turbines due to the effects caused by wake interactions. Indeed, power variations at the front turbine caused by a non-exact alignment with the wind are rather small according to the cosine law shown in Fig. 2d; on the other hand, a non-exact misalignment has a much amplified effect on the location of the wake downstream of the rotor, which may induce large losses on the downstream turbines. Such losses could be even larger for a greater spacing between turbines than the 5 D of the

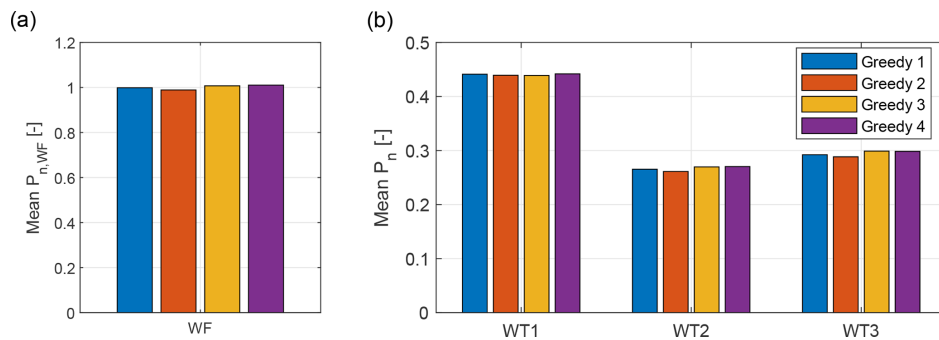


Figure 11. Repeatability of the experiments: averaged, normalized power for the wind farm (a) and the individual wind turbines (b) for four 90 min repetitions with the greedy control strategy.

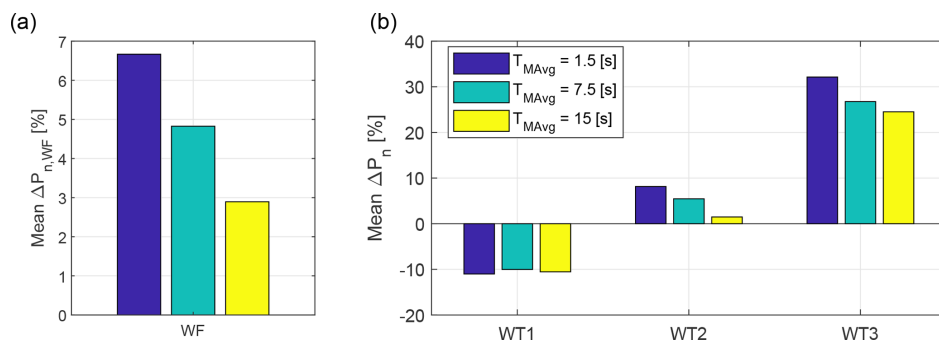


Figure 12. Averaged power gains aggregated over all wind directions for different values of T_{MAvg} (i.e., of wind direction uncertainties σ_Φ).

present experiment. The impact on the overall farm power output is substantial: increasing σ_Φ from 0 to 3.42° cuts the power gain by more than half.

4.2.2 Effect of yaw rate and neglected wake dynamics

Even in the absence of wind direction uncertainties ($T_{MAvg} = 1.5$ s, $\sigma_\Phi = 0^\circ$), the farm-level power gain (about 6.7%, Fig. 12a) is much lower than the established theoretical upper limit (10.73%, Sect. 4.1). This difference is caused by the limited yaw rate of the turbines and by having used a steady model and controller, which implies neglecting the dynamics of wake interaction (including the intrinsic dynamics of the wake, its slow-scale meandering fluctuations, and the advection downstream of any change with a finite travel speed).

Figure 13 establishes the impact of these effects on the performance of the controller. The plot reports plant-level power gains with respect to the greedy policy, as functions of wind direction. To reduce noise in the figure, each point in the plot represents the average power gain for a wind direction bin with a width of 2.5° . The solid orange line with * symbols reports the gains measured in the experiment. The solid blue line with o symbols indicates the theoretical upper limit when using the baseline FLORIS model, obtained by binning the data shown in Fig. 10b. The dashed-dotted

green line with Δ symbols shows the gains computed by a simulation conducted with the data-driven model, using the yaw misalignment angles γ^{Meas} measured in the experiment. Since the data-driven model can be assumed to be an exact steady-state representation of the experiment, the green line of the figure shows the impact of a limited yaw rate on the maximum theoretical performance. Finally, the dashed red line with \square symbols shows the gains when using the yaw misalignment angles γ^* requested by the controller, computed with the data-driven model, i.e., without considering limits in the yaw rate.

These curves allow for the quantification of the following effects:

- The difference between the lower orange curve and the green curve can be attributed to neglected wake dynamics; this non-negligible difference could in principle – at least in part – be regained by using a dynamic controller, instead of the steady-state controller considered here.
- The difference between the green and the red curves is due to a finite yaw actuation rate. This difference indicates that another non-negligible power capture improvement could be gained by a faster actuation, which however would have to be traded against increased load-

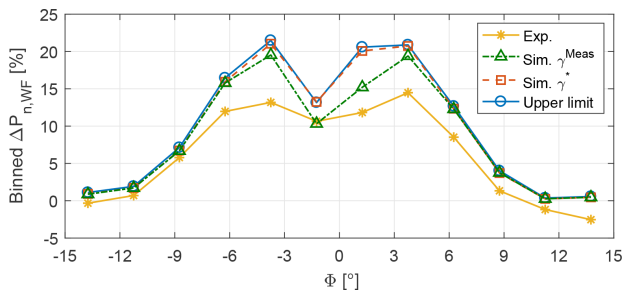


Figure 13. Wind farm power gains with respect to the greedy policy vs. wind direction Φ . Tests were performed with zero wind direction uncertainty ($\sigma_\Phi = 0^\circ$), and LUTs were synthesized from the baseline FLORIS model.

ing and actuator duty cycle (ADC). This gain is limited to relatively small misalignments (about $\Phi \in \pm 6^\circ$ in the figure).

- Finally, the difference between the red and the upper blue curve is due to remaining effects, such as the finite sampling time of the controller. This small difference indicates that these effects are negligible with respect to the others.

4.2.3 Effects of wind farm model fidelity

The influence of wind farm models with an increasing level of fidelity was assessed for the case of negligible wind direction uncertainties ($T_{MAvg} = 1.5$ s, $\sigma_\Phi = 0^\circ$). Figure 14 shows the averaged wind farm power gains aggregated over the whole time history for the three different models. The experimentally measured gains are reported in Fig. 14a, while Fig. 14b shows the gains obtained by simulations with the data-driven model as plant and the misalignment angles γ^{Meas} measured in the experiments. The maximum theoretical power gains of Sect. 4.1 are shown in Fig. 14c. Again, the lower gains of Fig. 14b compared to Fig. 14c can be attributed to the limited yaw rate. The lower power gains of Fig. 14a compared to Fig. 14b can be attributed to neglected dynamics.

The figures show that LUTs synthesized with better wind farm models lead to higher power gains. In fact, for the wind tunnel experiments, employing the FLORIS-Augm and data-driven LUTs increases the power gain by 5.1 % and 16.7 %, respectively, compared to the baseline FLORIS case. The simulation results of Figs. 14b and c show a similar trend. However, the benefits of the highest-fidelity model over the lower-fidelity ones for both simulation cases (10.1 % and 10.4 %) are smaller than in the experiments (16.7 %). This might be due to dynamic effects, which could affect the controller performance in different ways depending on the underlying flow model.

4.3 Robust implementation accounting for wind direction uncertainties

Further experiments were conducted using robust LUTs computed according to problem (3a) for $\sigma_\Phi = [0 : 2 : 6]^\circ$ based on all three models. For all tests, the wind direction (i.e., the turntable encoder signal) was filtered with a moving average with $T_{MAvg} = 7.5$ s. This corresponds to 10 min at full scale, similarly to typical 10 min SCADA data. As shown in Fig. 8, this means that the simulated wind direction uncertainty in the experiments had a standard deviation $\sigma_\Phi = 2.01^\circ$.

Figure 15 reports the power gains with respect to the greedy case for the baseline FLORIS model for varying uncertainty levels σ_Φ in the formulation of the LUTs (i.e., for increasing robustness). To reduce noise, the plot was generated with average values according to wind direction bins with a width of 2.5° . The figure shows that, with an increasing level of uncertainty, power is shifted from the most downstream machine (bottom left plot) to the upstream one (top left plot), whereas the turbine in between is substantially unaffected (top right plot). This makes intuitive sense: with large uncertainties in the wind direction, the power output of downstream machines becomes more uncertain; therefore, the controller tries to lose less power upstream, where changes in wind direction have a more limited impact on the local capture. This clearly comes at a cost, and the total power output at the farm level decreases (bottom right plot). With small uncertainties, the opposite happens: since the location of the wakes is more certain, it pays off to deflect the wake of the front machines in order to try to boost capture downstream.

It should also be noted that wind farm power gains may be negative away from conditions with strong wake interactions. This is indeed the case here for wind directions $\Phi < -10^\circ$ and $\Phi > 8^\circ$. This suggests that wake steering should only be applied in cases where strong enough interactions are expected, and switched off elsewhere.

Figure 16a shows the overall experimental power gains with respect to the greedy case for the various models and for increasing robustness. Additionally, Fig. 16b and c report simulation results with the data-driven model as plant and the effectively realized misalignment angles γ^{Meas} or the demanded misalignment angles γ^* , respectively. The power gain change with respect to the FLORIS LUTs with $\sigma_\Phi = 0^\circ$ is reported above each column. If one looks at the experimental data, shown in Fig. 16a, the power gains are equal to about 4 %–6 %, a range that is considerably lower than the theoretical maximum reported in Fig. 14c. Moreover, gains are higher and less affected by uncertainties for the better-fidelity model. From this point of view, it appears that a higher-fidelity model could provide better and more robust results than a lower-fidelity one.

The situation considered here is indeed much more realistic than the one discussed in Sect. 4.2, and the lower gains

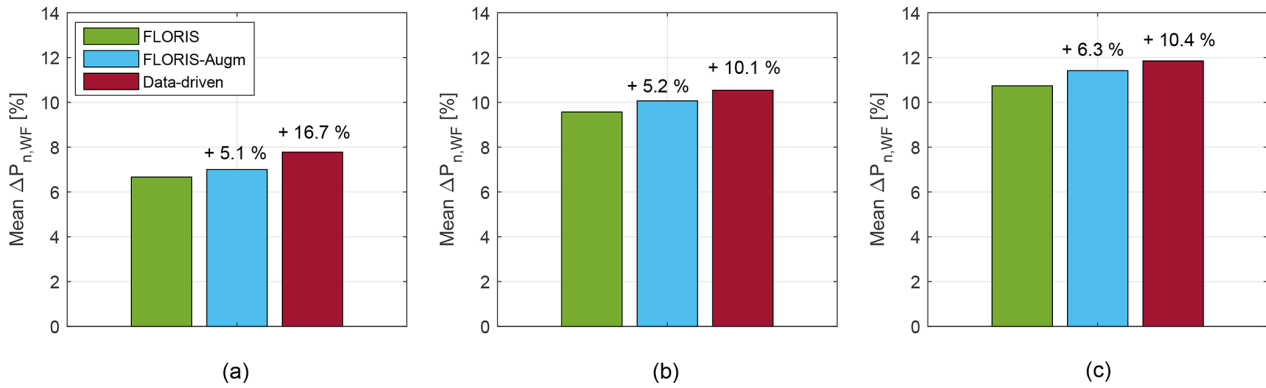


Figure 14. Normalized wind farm power gains for the three models of different fidelity: (a) experimental results, (b) simulations with γ^{Meas} , and (c) maximum theoretical power gain.

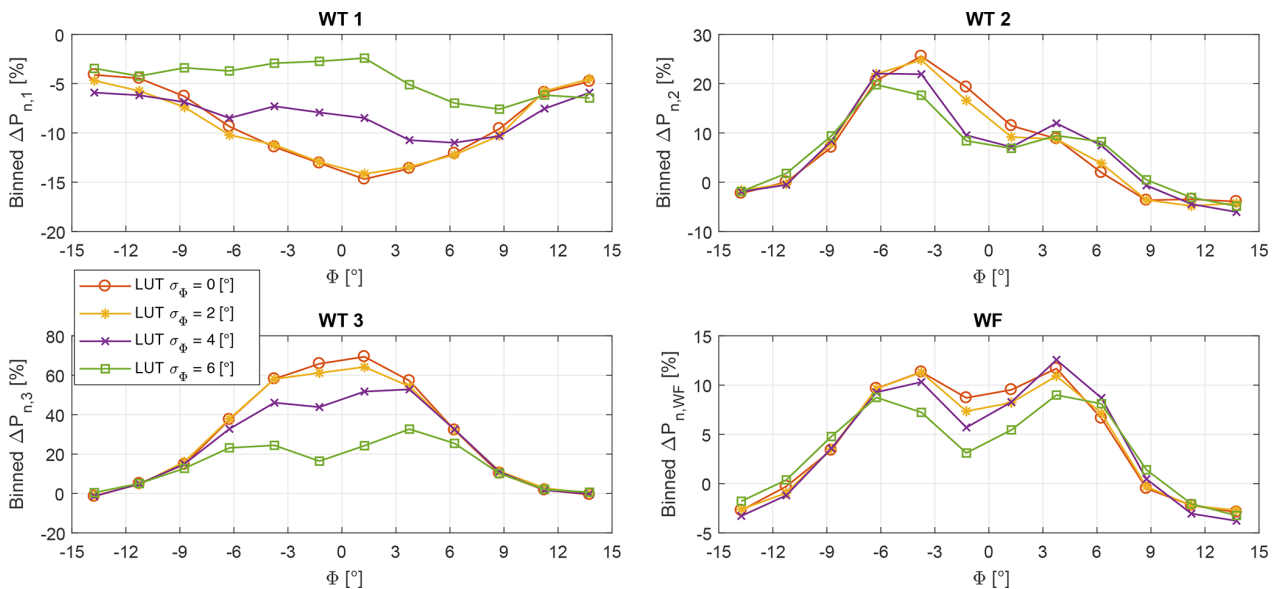


Figure 15. Power gains with respect to the greedy policy vs. wind direction, shown for the baseline FLORIS model and increasing robustness of the LUTs.

observed in this case are due to wind direction uncertainties, limited turbine yaw rate, and wake propagation dynamics. The best performance in the experiments is obtained with the data-driven model for $\sigma_\Phi = 6^\circ$. Additionally, the experimental results of the FLORIS-Augm model are better than the ones of the baseline FLORIS. For both the data-driven and the FLORIS-Augm models, lower gains are obtained when neglecting uncertainties ($\sigma_\Phi = 0^\circ$), which points to the importance of using a robust formulation. Surprisingly, the baseline FLORIS model exhibits just the opposite behavior.

The maximum gains in the experiments are obtained for $\sigma_\Phi = 4$ and 6° for the FLORIS-Augm and data-driven models, respectively. These values are significantly higher than the actual uncertainty in the wind direction signal (equal to $\sigma_\Phi = 2.01^\circ$). This is probably due to the limited yaw rate. In

fact, Fig. 16b shows that with a limited rate even the simulation results yield the best gains for $\sigma_\Phi = 4^\circ$, while Fig. 16c shows that without rate limits the optimal performance is obtained for the effective uncertainty $\sigma_\Phi = 2^\circ$ present in the driving signal. This makes intuitive sense: LUTs computed with a lower uncertainty result in higher gradients of the misalignment angle with respect to wind direction changes, which are less likely to be achieved by a limited yaw rate.

These results allow for some interesting considerations. First, if the model is strongly biased, as in the present baseline FLORIS case, introducing robustness in the formulation may decrease performance. This is in contrast to the results reported by Rott et al. (2018), who, however, did not consider biased models. On the contrary, robustness increases performance if the underlying models have better fidelity, which is

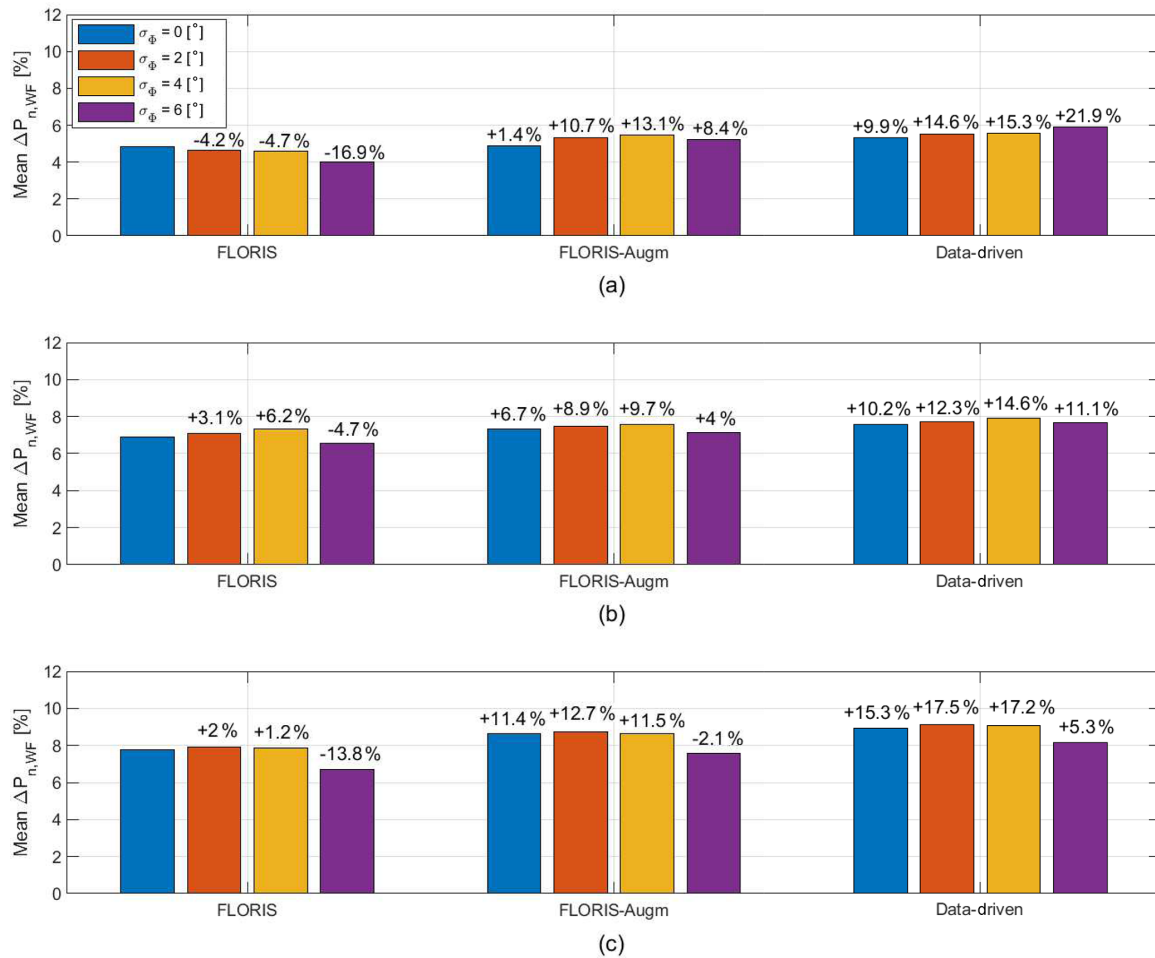


Figure 16. Overall power gains for the three models of different fidelity and increasing robustness of the LUTs: (a) experimental results, (b) simulations with γ^{Meas} , and (c) simulations with γ^* .

the case here for the FLORIS-Augm and data-driven models. Moreover, the impact of a limited yaw rate should certainly be taken into account in the calculation of the LUTs, as proposed by Simley et al. (2020). More importantly, better models and robust LUTs lead to better performance.

4.4 Impact on actuator duty cycle and loads

The wind tunnel experiments were also used to evaluate the impact of wake steering on yaw control effort and fatigue loads.

The average wind farm yaw ADC is defined as

$$ADC_{WF} = \frac{1}{N_{WF}} \sum_{j=1}^{N_{WF}} \frac{1}{T} \int_0^T \frac{|\dot{\gamma}_{nac,j}(t)|}{\dot{\gamma}_{max}} dt, \quad (4)$$

where $\dot{\gamma}_{nac,j}(t)$ is the time rate of change of the orientation of the j th wind turbine, and $N_{WF} = 3$ is the number of turbines.

The average wind farm ADC is an indicator of the usage of the yaw actuators and could therefore be used to quantify the impact of wake-steering control on the maintenance cost of the yaw drives.

Figure 17 shows the increase ΔADC_{WF} with respect to the greedy control policy. The effect of filtering the wind direction signal is shown in Fig. 17a for the non-robust LUT baseline FLORIS formulation. As expected, a longer averaging window smooths the signal, resulting in less yaw activity (but also less power and more fatigue damage, as shown in Figs. 12 and 18a). The increase in ADC with respect to the greedy control case is, however, very substantial.

The results obtained with robust LUTs based on the three models are shown in Fig. 17b, for a wind direction signal filtered with $T_{MAvg} = 7.5$ s. Comparing Fig. 17b with Fig. 17a shows that a robust formulation decreases ADC, as expected by the reduced misalignments prescribed by the controller (see Fig. 9a, b). Increasing robustness has a dramatic ef-

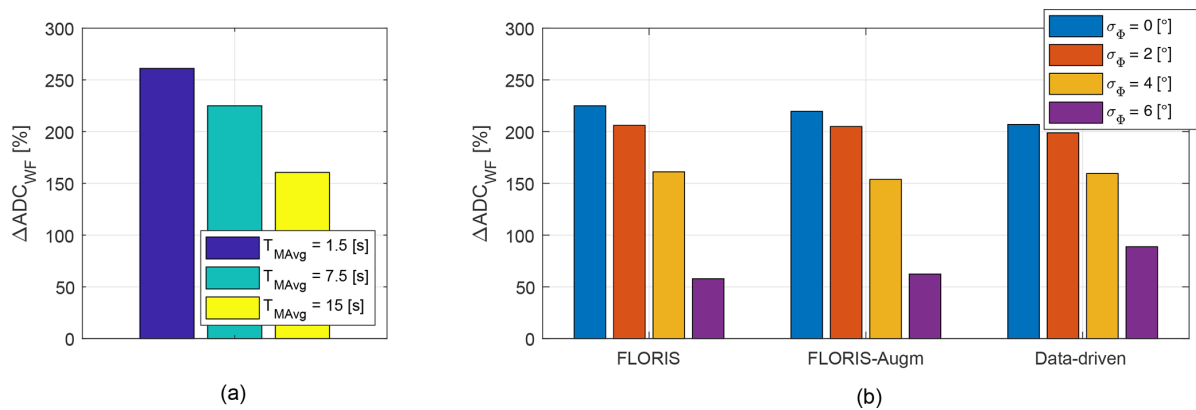


Figure 17. Change in wind farm yaw ADC with respect to the greedy case. (a) Effect of direction uncertainty: non-robust LUT for the baseline FLORIS model and varying T_{MAvg} . (b) Effect of robustness and model fidelity: LUTs for the three models and increasing robustness, for a wind direction signal filtered with $T_{MAvg} = 7.5$ s.

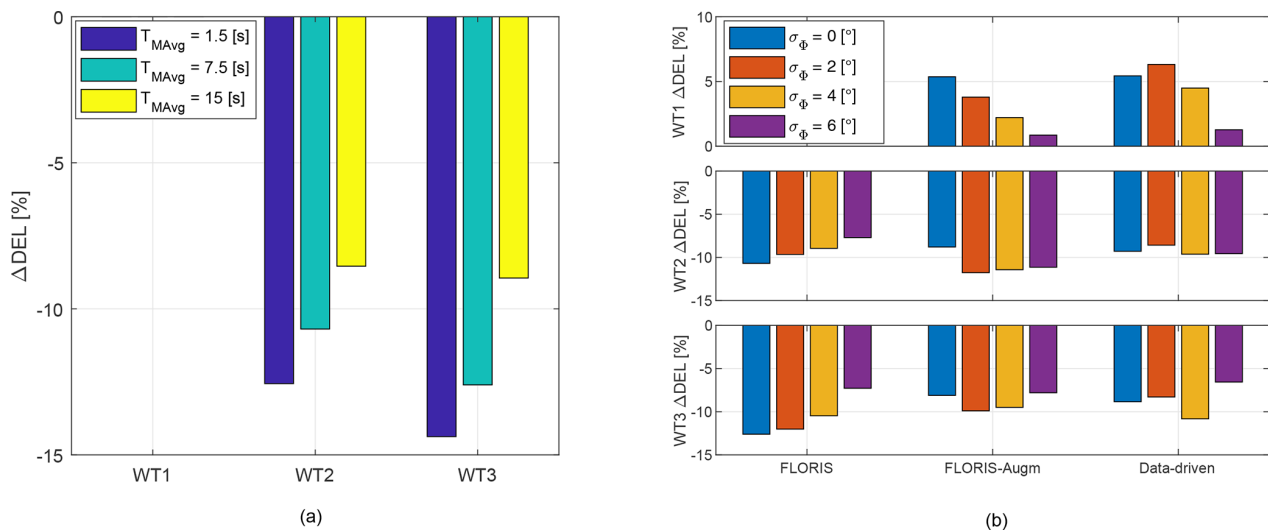


Figure 18. Change in combined rotating shaft DELs with respect to the greedy case. (a) Effect of direction uncertainty: non-robust LUT for the baseline FLORIS model and varying T_{MAvg} . (b) Effect of robustness and model fidelity: LUTs for the three models and increasing robustness, for a wind direction signal filtered with $T_{MAvg} = 7.5$ s.

fect on ADC, which however is still much higher than in the greedy case even for $\sigma_\phi = 6^\circ$. There is a clear tradeoff in wake steering between the benefits of an improved power capture and the detriments caused by an increased ADC. Additionally, the figure also shows that model fidelity has only a relatively minor effect on ADC.

Damage Equivalent Loads (DELs) were computed from bending moments measured on the rotating shaft and at the tower base. Load signals were first filtered above the 6P rotor frequency to remove high-frequency mechanical vibrations. In addition, tower loads were corrected from 1P harmonics generated by the small inertial and aerodynamic imbalance of each rotor. A similar correction was applied to the fixed-

frame hub loads computed from the rotating shaft components. Once cleaned of the 1P component, the fixed-frame loads were projected back onto the shaft frame, obtaining rotating loads corrected for rotor imbalance.

Bending DELs of the rotating shaft are reported in Fig. 18, while tower base bending DELs are given in Fig. 19. In both cases, combined DELs were obtained by projecting the two measured orthogonal bending components on the direction associated with the maximum DEL, and normalizing by the temporal average of $1/2\rho\pi R^3 U_{Pitot}^2$, where R is the rotor radius. The loads for WT1 for varying T_{MAvg} and for the baseline FLORIS cases are not reported in the figure, due to a

1290

F. Campagnolo et al.: Wind tunnel testing of wake steering with dynamic wind direction changes

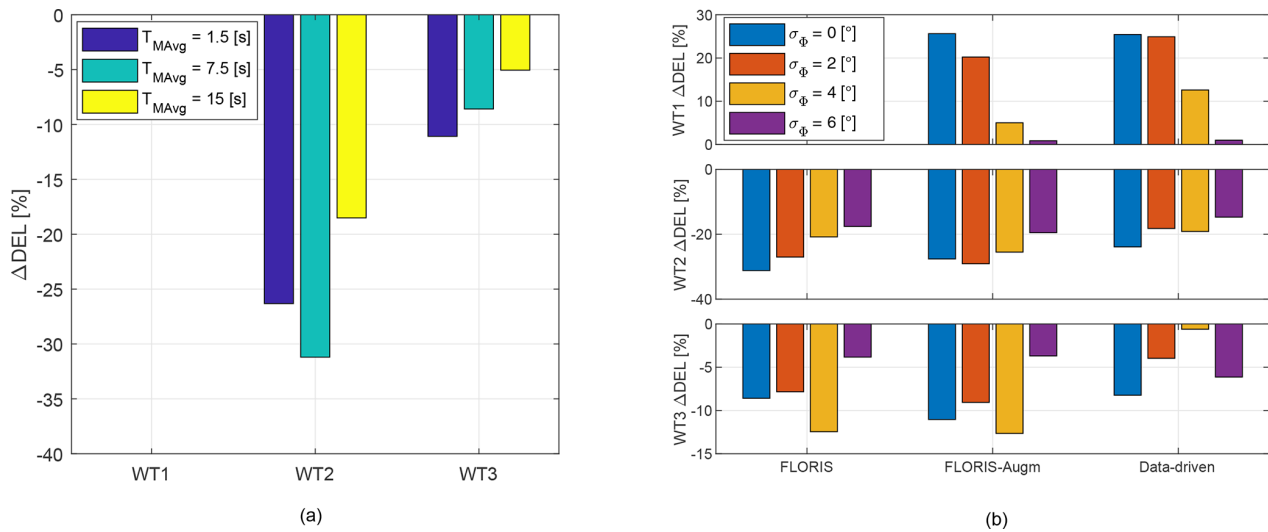


Figure 19. Change in combined tower base DELs with respect to the greedy case. **(a)** Effect of direction uncertainty: non-robust LUT for the baseline FLORIS model and varying T_{MAvg} . **(b)** Effect of robustness and model fidelity: LUTs for the three models and increasing robustness, for a wind direction signal filtered with $T_{MAvg} = 7.5$ s.

problem with the recording of the rotor azimuth of that turbine during these tests.

A few observations can be made from the results for the shaft DELs. First, as expected and as clearly visible in Fig. 18a, load mitigation with non-robust LUTs worsens rapidly for increasing uncertainty (i.e., increasing T_{MAvg}), since more wake interactions are taking place downstream. Second, when using robust LUTs, model fidelity seems to have only a modest effect on DELs, as shown in Fig. 18b. Third, by pointing the rotor away from the wind, the DELs of the front machine have a moderate increase, which is again an expected behavior. However, it is particularly interesting to look at the effect of varying robustness. Indeed, only a marginal increase in DELs is observed for $\sigma_\phi = 6^\circ$, which still corresponds to significant power gains (cf. Fig. 16). Moreover, wake steering is particularly beneficial for the DELs of the second and third turbines, with reductions varying between 7% and 12%, depending on the LUTs. In general, DEL reductions seem to be correlated with power gains: robust LUTs with the largest power gains also generate the maximal load reductions.

Similar conclusions can be drawn from looking at the results for the tower base DELs, despite some differences compared to the shaft loads. Although the absolute loads on the front turbine never exceed those of the downstream ones, the tower DELs of WT1 increase much more significantly with yaw misalignment than the shaft DELs (compare top plot of Fig. 19b with the one of Fig. 18b). Again the increment becomes almost negligible when robust LUTs computed with $\sigma_\phi = 6^\circ$ are used, as shown in Fig. 19b. The tower DELs of the second turbine are significantly reduced, up to about 30% depending again on the LUTs and on the filtering of the wind

direction, whereas the load mitigation on the third turbine is less pronounced and shows a less clear trend.

5 Conclusions

This paper has presented an analysis of the effects of wind direction changes on the performance of an open-loop wake-steering controller.

The study was based on the results of a new unique set of experiments conducted with three scaled turbines operated in a large boundary layer wind tunnel. Wind direction changes were simulated with a turntable, driven by actual measurements performed in the field that were scaled to match the accelerated time of the experiment. The filtered wind direction provided as input to the controller was shown to represent a realistic approximation of the signal that could be acquired by a met mast in the field. Three different models of increasing fidelity were used for the synthesis of the control laws. The control formulation was based on an established robust approach, which includes a naive deterministic optimization as a special case.

The unique possibilities offered by testing in the known, repeatable, and controllable environment of the wind tunnel were exploited here to

- establish a theoretical upper limit to the performance of the controller in the absence of dynamics;
- separate the effects of neglected dynamics, model fidelity, and actuation rate;
- feed to the controller a variable level of uncertainty, in order to quantify its effects on performance.

F. Campagnolo et al.: Wind tunnel testing of wake steering with dynamic wind direction changes

1291

Based on the results of this study, the following conclusions can be drawn:

- Higher-fidelity models lead in general to slightly better results in terms of power capture, whereas the effects of fidelity on actuator usage and fatigue loads are modest. In addition, higher-fidelity models appear to be less susceptible to the effects of uncertainties.
 - The use of a robust formulation is beneficial in terms of power capture but yields even higher payoffs when looking at other metrics. In particular, the overall plant-level ADC and the DELs of the front turbine are greatly reduced when compared to a non-robust formulation.
 - The previous statement is however only true if the underlying flow model is accurate enough. In fact, the use of a robust formulation actually decreased performance for the baseline FLORIS model (which lacks important effects such as secondary steering), in terms of both power capture and load mitigation downstream. This seems to indicate that excessively simplified models should probably be avoided.
 - Increasing the robustness of the controller has the effect of shifting power upstream, as the position of the wakes is affected by larger uncertainties than the ones caused on the front turbine by a non-exact alignment with the wind. This however comes at a cost, as higher wake interactions are allowed to take place for increasing robustness, in turn leading to a lower power capture at the plant level.
 - A robust implementation may lead to power losses in conditions with weak or absent wake interactions. This might suggest the use of wake steering only around conditions where significant wake effects are expected, whereas it should be switched off elsewhere.
- There is a non-negligible margin in power capture performance that may be attributed to dynamic effects. This seems to indicate that dynamic controllers, as opposed to the steady-state ones used here, might lead to a better performance, at the cost of a higher complexity.
 - Yaw rate is an important performance driver, and indeed higher rates achieve better results in terms of power output at the farm level. However, this clearly comes at a large cost in terms of actuator usage and loading. Such tradeoffs can only be quantified by a system-level design study, which is however turbine- and plant-dependent and beyond the scope of this paper.

The present work could benefit from improvements to the experimental setup and the control methods. A relatively straightforward modification to the turntable could allow for higher accelerations, filling a missing band of frequencies in the wind direction spectrum. Instead of using the turntable rotation as an approximation of a met-mast-measured wind direction, the ambient conditions could be estimated directly from the wind turbine operational data (Schreiber et al., 2018). Finally, dynamic closed-loop controllers could be tested to understand and quantify their potential benefits with respect to the present simpler approaches.

Appendix A: Interpolating functions for the data-driven surrogate model

A surrogate model of the behavior of the cluster of three turbines is derived based on experimental measurements of power and wake displacement and on wake superposition principles.

Figure A1a reports, as a function of the wind direction Φ , the measured normalized power $P_{n,dalign}$ (see Sect. 3.1.4) of the downstream turbine in a two-turbine cluster operating below rated wind speed. Both turbines are aligned with the wind, i.e., $\gamma_u = \gamma_d = 0$, where γ_u and γ_d are the yaw misalignments of the upstream and downstream turbines, respectively. The measured data points can be interpolated with the following function:

$$\frac{P_{n,dalign}}{C_P^{\text{II}}} = \begin{cases} 1 - B(1 - \sin(\pi C\Phi - D)), & \text{if } \frac{D-3/2\pi}{\pi C} < \Phi < \frac{D+\pi/2}{\pi C}, \\ 1, & \text{otherwise,} \end{cases} \quad (\text{A1})$$

where C_P^{II} is the power coefficient below rated speed, while $B > 0$, $C > 0$, and D are tunable parameters.

Figure A1b reports the lateral displacement δ_{wc} of the wake of a G1 turbine as a function of the wind misalignment angle γ , measured $5D$ downstream of the rotor. The measured data points can be interpolated with the following function:

$$\delta_{wc} = E \sin(F\gamma), \quad (\text{A2})$$

where $E > 0$ and $F > 0$ are tunable parameters. When the wake of an upstream turbine is deflected, the wake overlap at the downstream machine can be approximated with the overlap that would occur for a wind direction $\Phi + \Delta\Phi$, where

$$\Delta\Phi \approx \sin \Delta\Phi = \frac{\delta_{wc}}{\Delta X} = \frac{E \sin(F\gamma)}{\Delta X}, \quad (\text{A3})$$

and ΔX is the longitudinal distance between the two turbines.

In region II, the power coefficient of a wind-misaligned turbine can be expressed as

$$C_P = C_P^{\text{II}} \cos^n(\gamma + \phi), \quad (\text{A4})$$

where n is the power loss exponent, and ϕ is the phase asymmetry caused by a vertically sheared inflow.

These interpolating functions can be used to express the normalized power $P_{n,d}$ at a misaligned downstream machine as a function of γ_u for a given wind direction Φ_0 . In fact, inserting Eq. (A3) into Eq. (A1), considering Eq. (A4), one gets

$$P_{n,d} = \begin{cases} C_P^{\text{II}} \left(1 - B \left(1 - \sin \left(\pi \hat{C} \sin(F\gamma_u) - \hat{D} \right) \right) \right) \cos^{n_d}(\gamma_d + \phi_d), & \text{if } \frac{\hat{D}-3/2\pi}{\pi \hat{C}} < \sin(F\gamma_u) < \frac{\hat{D}+\pi/2}{\pi \hat{C}}, \\ C_P^{\text{II}} \cos^{n_d}(\gamma_d + \phi_d), & \text{otherwise,} \end{cases} \quad (\text{A5})$$

where $\hat{C} = CE/\Delta X$ and $\hat{D} = D - \pi C\Phi_0$, while n_d and ϕ_d are, respectively, the power loss exponent and phase asymmetry of the downstream turbine. For a three-turbine cluster, such as the one described in Sect. 2, Eq. (A5) can be used to model the normalized power of WT2.

The normalized power at the downstream turbine j affected by the wake released by the upstream turbine i can also be written as

$$P_{n,j} = C_P^{\text{II}} (1 - \delta_i(X_j)A_{i \rightarrow j})^3 \cos^{n_j}(\gamma_j + \phi_j), \quad (\text{A6})$$

where $\delta_i(X_j)$ is the speed deficit of the wake of turbine i at the downstream distance X_j where turbine j is located, and $A_{i \rightarrow j}$ is the fractional overlap area of the rotor of j with the wake of i . Using Eqs. (A5) and (A6), the speed deficits caused by turbine-to-turbine wake interactions can be readily obtained. In fact, the deficit at turbine j caused by the wake released by turbine i is computed as

$$\delta_i(X_j)A_{i \rightarrow j} = \begin{cases} 1 - \left(1 - B_{ij} \left(1 - \sin \left(\pi \hat{C}_{ij} \sin(F_i\gamma_i) - \hat{D}_{ij} \right) \right) \right)^{1/3}, & \text{if } \frac{\hat{D}_{ij}-3/2\pi}{\pi \hat{C}_{ij}} < \sin(F_i\gamma_i) < \frac{\hat{D}_{ij}+\pi/2}{\pi \hat{C}_{ij}}, \\ 0, & \text{otherwise,} \end{cases} \quad (\text{A7})$$

where B_{ij} , \hat{C}_{ij} , \hat{D}_{ij} , and F_j are the corresponding tunable parameters.

Finally, the method of the sum of energy deficits (Renkema, 2007) is used for combining the wakes of the two upstream turbines to get the normalized power of the aligned third machine:

$$P_{n,3} = C_P^{\text{II}} \left(1 - \sqrt{\sum_{j=1}^2 (\delta_j(X_3)A_{j \rightarrow 3})^2} \right)^3. \quad (\text{A8})$$

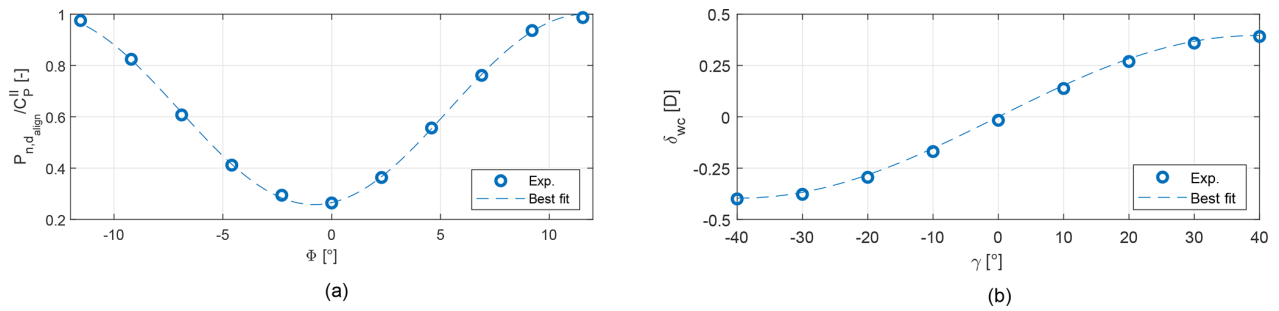


Figure A1. Experimental data points and their best fits for the derivation of the interpolating functions. **(a)** Normalized power of the downstream turbine in a two-turbine cluster vs. Φ for $\gamma_u = \gamma_d = 0$. **(b)** Wake displacement vs. misalignment γ .

1294

F. Campagnolo et al.: Wind tunnel testing of wake steering with dynamic wind direction changes

Data availability. The experimental wind tunnel data can be obtained by contacting the authors.

Author contributions. FC conducted the main research work, developed the data-driven model, was responsible for the execution of the wind tunnel tests, and post-processed the results. CLB conceived the experiments, developed the theory of the FLORIS-Augm model, contributed to the interpretation of the results, and supervised the whole research project. FC and CLB wrote the manuscript. FC and RW conducted the wind tunnel tests. RW was responsible for the operation and maintenance of the scaled turbines and implemented the turbine and farm controllers and associated software. JS implemented the FLORIS-Augm model and the wind farm controller and participated in the wind tunnel tests and in the post-processing and analysis of the results. All authors provided important input to this research work through discussions and feedback and by improving the manuscript.

Competing interests. The authors declare that they have no conflict of interest.

Acknowledgements. The authors acknowledge Stefano Cacciola, Gabriele Campanardi, Alessandro Croce, Donato Grassi, Luca Riccobene, Paolo Schito, and Alberto Zasso of the Politecnico di Milano for their help in the conduction of the wind tunnel experiments.

Financial support. This work has been supported by the CL-WINDCON project, which received funding from the European Union Horizon 2020 research and innovation program (grant agreement no. 727477).

This work was supported by the German Research Foundation (DFG) and the Technical University of Munich (TUM) in the framework of the Open Access Publishing Program.

Review statement. This paper was edited by Horia Hangan and reviewed by two anonymous referees.

References

- Bak, C., Zahle, F., Bitsche, R., Kim, T., Yde, A., Henriksen, L. C., Hansen, M. H., Blasques, J. P. A. A., Gaunaa, M., and Natarajan, A.: The DTU 10-MW reference wind turbine, in: *Danish Wind Power Research 2013*, 2013.
- Bastankhah, M. and Porté-Agel, F.: Experimental and theoretical study of wind turbine wakes in yawed conditions, *J. Fluid Mech.*, 806, 506–541, 2016.
- Bastankhah, M. and Porté-Agel, F.: Wind farm power optimization via yaw angle control: A wind tunnel study, *J. Renew. Sustain. Ener.*, 11, 023301, <https://doi.org/10.1063/1.5077038>, 2019.
- Bossanyi, E.: The Design of Closed Loop Controllers for Wind Turbines, *Wind Energy*, 3, 149–163, 2000.
- Bossanyi, E.: Combining induction control and wake steering for wind farm energy and fatigue loads optimisation, in: *J. Phys. Conf. Ser.*, vol. 1037, 032011, <https://doi.org/10.1088/1742-6596/1037/3/032011>, 2018.
- Bottasso, C. L. and Campagnolo, F.: *Handbook of Wind Energy Aerodynamics*, chap. Wind Tunnel Testing of Wind Turbines and Farms, Springer, Cham, Switzerland, 2020.
- Bottasso, C. L., Campagnolo, F., and Petrović, V.: Wind tunnel testing of scaled wind turbine models: Beyond aerodynamics, *J. Wind Eng. Ind. Aerod.*, 127, 11–28, 2014.
- Bromm, M., Rott, A., Beck, H., Vollmer, L., Steinfeld, G., and Kühn, M.: Field investigation on the influence of yaw misalignment on the propagation of wind turbine wakes, *Wind Energy*, 21, 1011–1028, 2018.
- Burton, T., Jenkins, N., Sharpe, D., and Bossanyi, E.: *Aerodynamics of Horizontal Axis Wind Turbines*, 39–136, John Wiley & Sons, Ltd, New York, USA, 2011.
- Bustamante, A., Vera-Tudela, L., and Kühn, M.: Evaluation of wind farm effects on fatigue loads of an individual wind turbine at the EnBW Baltic 1 offshore wind farm, *J. Phys. Conf. Ser.*, 625, 012020, <https://doi.org/10.1088/1742-6596/625/1/012020>, 2015.
- Campagnolo, F., Petrović, V., Bottasso, C. L., and Croce, A.: Wind tunnel testing of wake control strategies, in: *P. Amer. Contr. Conf.*, Boston, USA, 6–8 July 2016, 513–518, 2016a.
- Campagnolo, F., Petrović, V., Nanos, E. M., Tan, C. W., Bottasso, C. L., Paek, I., Kim, H., and Kim, K.: Wind tunnel testing of power maximization control strategies applied to a multi-turbine floating wind power platform, in: *Proceedings of the The 26th International Ocean and Polar Engineering Conference*, Rhodes, Greece, 26 June–1 July 2016b.
- Campagnolo, F., Petrović, V., Schreiber, J., Nanos, E., Croce, A., and Bottasso, C. L.: Wind tunnel testing of a closed-loop wake deflection controller for wind farm power maximization, *J. Phys. Conf. Ser.*, 753, 032006, <https://doi.org/10.1088/1742-6596/753/3/032006>, 2016c.
- Campagnolo, F., Molder, A., Schreiber, J., and Bottasso, C. L.: Comparison of Analytical Wake Models with Wind Tunnel Data, *J. Phys. Conf. Ser.*, 1256, 012006, <https://doi.org/10.1088/1742-6596/1256/1/012006>, 2019.
- Canet, H., Bortolotti, P., and Bottasso, C. L.: On the scaling of wind turbine rotors, *Wind Energ. Sci. Discuss.*, <https://doi.org/10.5194/wes-2020-66>, in review, 2020.
- Crespo, A. and Hernández, J.: Turbulence characteristics in wind-turbine wakes, *J. Wind Eng. Ind. Aerod.*, 61, 71–85, 1996.
- Desmond, C., Murphy, J., Blonk, L., and Haans, W.: Description of an 8 MW reference wind turbine, in: *J. Phys. Conf. Ser.*, 753, 092013, <https://doi.org/10.1088/1742-6596/753/9/092013>, 2016.
- Doekemeijer, B. M. and Storm, R.: FLORISSE M, available at: https://github.com/TUDELFT-DataDrivenControl/FLORISSE_M/ (last access: 30 July 2019), 2018.
- Doekemeijer, B. M., Fleming, P. A., and van Wingerden, J.-W.: A tutorial on the synthesis and validation of a closed-loop wind farm controller using a steady-state surrogate model, in: *Proceedings of the 2019 American Control Conference (ACC 2019)*, Philadelphia, PA, USA, 10–12 July 2019, 2825–2836, 2019.
- Fleming, P., Aho, J., Gebraad, P., Pao, L., and Zhang, Y.: Computational fluid dynamics simulation study of active power control in wind plants, in: *P. Amer. Contr. Conf.*, Boston, USA, 1413–1420, 2016.

- Fleming, P., Annoni, J., Shah, J. J., Wang, L., Ananthan, S., Zhang, Z., Hutchings, K., Wang, P., Chen, W., and Chen, L.: Field test of wake steering at an offshore wind farm, *Wind Energy Science*, 2, 229–239, 2017.
- Fleming, P., Annoni, J., Shah, J. J., Wang, L., Ananthan, S., Zhang, Z., Hutchings, K., Wang, P., Chen, W., and Chen, L.: Field test of wake steering at an offshore wind farm, *Wind Energ. Sci.*, 2, 229–239, <https://doi.org/10.5194/wes-2-229-2017>, 2017.
- Fleming, P., King, J., Dykes, K., Simley, E., Roadman, J., Scholbrock, A., Murphy, P., Lundquist, J. K., Moriarty, P., Fleming, K., van Dam, J., Bay, C., Mudafort, R., Lopez, H., Skopek, J., Scott, M., Ryan, B., Guernsey, C., and Brake, D.: Initial results from a field campaign of wake steering applied at a commercial wind farm – Part 1, *Wind Energ. Sci.*, 4, 273–285, <https://doi.org/10.5194/wes-4-273-2019>, 2019.
- Frederik, J. A., Weber, R., Cacciola, S., Campagnolo, F., Croce, A., Bottasso, C., and van Wingerden, J.-W.: Periodic dynamic induction control of wind farms: proving the potential in simulations and wind tunnel experiments, *Wind Energ. Sci.*, 5, 245–257, <https://doi.org/10.5194/wes-5-245-2020>, 2020.
- Gebraad, P. M. O., Teeuwisse, F. W., van Wingerden, J. W., Fleming, P. A., Ruben, S. D., Marden, J. R., and Pao, L. Y.: Wind plant power optimization through yaw control using a parametric model for wake effects—a CFD simulation study, *Wind Energy*, 19, 95–114, [we.1822](https://doi.org/10.1016/j.weneng.2016.05.002), 2016.
- Hansen, K. S., Barthelmie, R. J., Jensen, L. E., and Sommer, A.: The impact of turbulence intensity and atmospheric stability on power deficits due to wind turbine wakes at Horns Rev wind farm, *Wind Energy*, 15, 183–196, 2012.
- Howland, M. F., Lele, S. K., and Dabiri, J. O.: Wind farm power optimization through wake steering, *P. Natl. Acad. Sci. USA*, 116, 14495–14500, 2019.
- Jonkman, J. and Jonkman, B.: FAST v8, available at: <https://nwtc.nrel.gov/FAST8> (last access: 20 July 2018), 2018.
- Jonkman, J., Butterfield, S., Musial, W., and Scott, G.: Definition of a 5-MW reference wind turbine for offshore system development, Tech. rep., National Renewable Energy Lab.(NREL), Golden, CO, USA, 2009.
- Knudsen, T., Bak, T., and Svenstrup, M.: Survey of wind farm control—power and fatigue optimization, *Wind Energy*, 18, 1333–1351, <https://doi.org/10.1002/we.1760>, 2015.
- Madjidian, D., Martensson, K., and Rantzer, A.: A distributed power coordination scheme for fatigue load reduction in wind farms, in: Amer. Contr. Conf. Conf., San Francisco, USA, 29 June–1 July 2011, 2011.
- Mechali, M., Jensen, L., and Barthelmie, R.: Wake effects at Horns Rev and their influence on energy production, in: European Wind Energy Conference and Exhibition, Athens, Greece, 27 February–2 March 2006, 1, 10–20, 2006.
- NREL: FLORIS. Version 2.1.1, available at: <https://github.com/NREL/floris> (last access: 26 July 2020), 2020.
- Ørsted: Ørsted presents update on its long-term financial targets, available at: <https://orsted.com/en/Company-Announcement-List/2019/10/1937002> (last access: 15 April 2020), 2019.
- Quick, J., Annoni, J., King, R., Dykes, K., Fleming, P., and Ning, A.: Optimization under uncertainty for wake steering strategies, in: *J. Phys. Conf. Ser.*, 854, 012036, <https://doi.org/10.1088/1742-6596/854/1/012036>, 2017.
- Raach, S., Boersma, S., Doekemeijer, B., van Wingerden, J.-W., and Cheng, P.: Lidar-based closed-loop wake redirection in high-fidelity simulation, *J. Phys. Conf. Ser.*, 1037, 032016, <https://doi.org/10.1088/1742-6596/1037/3/032016>, 2018.
- Renkema, D. J.: Validation of wind turbine wake models, Master of Science Thesis, Delft University of Technology, Delft, the Netherlands, 19, 2007.
- Rott, A., Doekemeijer, B., Seifert, J. K., van Wingerden, J.-W., and Kühn, M.: Robust active wake control in consideration of wind direction variability and uncertainty, *Wind Energ. Sci.*, 3, 869–882, <https://doi.org/10.5194/wes-3-869-2018>, 2018.
- Schreiber, J., Salbert, B., and Bottasso, C. L.: Study of wind farm control potential based on SCADA data, *J. Phys. Conf. Ser.*, 1037, 032012, <https://doi.org/10.1088/1742-6596/1037/3/032012>, 2018.
- Schreiber, J., Bottasso, C. L., Salbert, B., and Campagnolo, F.: Improving wind farm flow models by learning from operational data, *Wind Energ. Sci.*, 5, 647–673, <https://doi.org/10.5194/wes-5-647-2020>, 2020.
- Siemens Gamesa: Siemens Gamesa now able to actively dictate wind flow at offshore wind locations, available at: <https://www.siemensgamesa.com/en-int/newsroom/2019/11/191126-siemens-gamesa-wake-adapt-en> (last access: 15 April 2020), 2019.
- Simley, E., Fleming, P., and King, J.: Design and analysis of a wake steering controller with wind direction variability, *Wind Energ. Sci.*, 5, 451–468, <https://doi.org/10.5194/wes-5-451-2020>, 2020.
- Vali, M., Petrović, V., Boersma, S., van Wingerden, J.-W., and Kühn, M.: Adjoint-based model predictive control of wind farms: Beyond the quasi steady-state power maximization, *IFAC-PapersOnLine*, 50, 4510–4515, 20th IFAC World Congress, Toulouse, France, 9–14 July 2017, 2017.
- Vera-Tudela, L. and Kühn, M.: Analysing wind turbine fatigue load prediction: The impact of wind farm flow conditions, *Renewable Energy*, 107, 352–360, 2017.
- Wang, C., Campagnolo, F., and Bottasso, C. L.: Identification of airfoil polars from uncertain experimental measurements, *Wind Energ. Sci. Discuss.*, <https://doi.org/10.5194/wes-2020-97>, in review, 2020.
- Wang, J., Foley, S., Nanos, E. M., Yu, T., Campagnolo, F., Bottasso, C. L., Zanotti, A., and Croce, A.: Numerical and Experimental Study of Wake Redirection Techniques in a Boundary Layer Wind Tunnel, *J. Phys. Conf. Ser.*, 854, 012048, <https://doi.org/10.1088/1742-6596/854/1/012048>, 2017.
- Wang, J., Wang, C., Campagnolo, F., and Bottasso, C. L.: Wake behavior and control: comparison of LES simulations and wind tunnel measurements, *Wind Energ. Sci.*, 4, 71–88, <https://doi.org/10.5194/wes-4-71-2019>, 2019.

Paper 13: Study of wind farm control potential based on SCADA data

15.1 Summary

Within this work an analytical wind farm model is first validated against SCADA (Supervisory Control And Data Acquisition) data from a typical onshore wind farm consisting of different turbine types installed in an irregular layout. The relevant model inputs as wind speed, direction and turbulence intensity are extracted from standard SCADA measurements that are typically available in every wind farm. Comparisons between model-predicted and measured wake induced power deficits show a good agreement, validating the wind farm model. Secondly the work takes the wind conditions of a full year of operation into account to estimate the total wake losses and the increase of annual energy production that could be achieved by wake steering. Thereby the wind farm model is used to compute for each turbine the optimal yaw misalignment depending on the inflow condition, giving a wind farm control look-up-table as used in the scaled wind farm control experiments in **Paper 12**. For the specific site, an increase in annual power production of almost 2% is estimated, and the wind farm power is expected to increase by more than 10% for specific wind conditions.

15.2 Contribution

Within this peer-reviewed publication, the main research work has been conducted by the author of this dissertation and in equal amount by Bastian Salbert. In details the author of this dissertation initiated the project and closely steered and supervised the research and implementation conducted by Bastian Salbert. All authors provided important input to this research work through discussions, feedback and by writing the paper.

15.3 Reference

J. Schreiber, B. Salbert, and C. L. Bottasso, "Study of wind farm control potential based on SCADA data," *Journal of Physics: Conference Series*, vol. 1037, p. 032012, 2018. doi: 10.1088/1742-6596/1037/3/032012

Study of wind farm control potential based on SCADA data

J Schreiber¹, B Salbert¹, C L Bottasso^{1,2}

¹ Wind Energy Institute, Technische Universität München, Boltzmannstraße 15, D-85748 Garching bei München, Germany

² Dipartimento di Scienze e Tecnologie Aerospaziali, Politecnico di Milano, Via La Masa 34, I-20156 Milano, Italy

E-mail: {johannes.schreiber, bastian.salbert, carlo.bottasso}@tum.de

Abstract. In this work, a control-oriented wind farm model is validated against SCADA data from a typical on-shore wind farm, without additional instrumentation available. The comparison of model-predicted and measured power deficits due to wake impingement shows good agreement. Furthermore, the model is used to compute optimum yaw misalignments for yaw-induced wake steering, leading to an estimated 1.7% increase in annual energy production by mitigation of wake losses. Results show that wake steering based on standard SCADA data, which is usually available in operational wind farms, has promising potential for open-loop model-based wind farm control.

1. Introduction

Wake interactions within wind farms lead to power losses and increased fatigue loading. Wind farm control (WFC) aims at mitigating these wake effects by operating the turbines within a plant in a coordinated manner. This is in contrast with the current greedy policy, where each machine operates individually to maximize its own power capture [1]. Recent approaches focus on increasing plant-level power capture by axial induction or wake redirection control [2, 3]. The latter seems to be a particularly promising approach, and it works by laterally steering wakes through the intentional misalignment of the rotor with respect to the incoming wind vector.

For a computationally efficient prediction of wake behavior and turbine power production, parametric wind farm models have been developed, facilitating WFC design and application [4]. This study validates such a model for baseline operation, and then uses it to investigate the potential increase in annual energy production (AEP) by yaw-induced wake steering.

In a first step, results from the well-known FLORIS (FLOW Redirection and Induction in Steady-state) [5] wake model are compared to historical 10 minute SCADA (Supervisory Control and Data Acquisition) measurements from a typical on-shore wind farm. Ambient wind direction is estimated from calibrated turbine yaw measurements, and undisturbed inflow is established from free-stream reference turbines. The model is able to predict power losses due to wake interactions with good accuracy for all investigated wind directions. In fact, the simulated AEP matches measurements within a 1.4% accuracy.

Finally, the potential increase in AEP is estimated using a model-based wake steering strategy, termed here “advanced sector management”. Thereby, pre-calculated optimum yaw



misalignments are set for the individual turbines as a function of ambient wind conditions. For the investigated cluster of wind turbines, a potential increase in AEP of 1.7% is obtained.

2. Models, methods and power plant

2.1. Wind farm model

The FLORIS wake model [5] together with the Jiménez deflection model [6] are employed within a wind farm framework, which is able to account for arbitrary plant setups with irregular turbine positions, differing hub heights and machine types. The combined velocity reduction of overlapping wakes is derived from the superposition of the energy deficits in the individual wakes, according to the Katic [7] wake interaction model. It was verified that the model implementation gives results identical to the public-domain TU Delft code [8].

The parameter set from Gebraad et al. [4], reported in table 1, is used for all turbines. These parameter values were used “as is”, without any further tuning for the specific site considered here.

Table 1: FLORIS parameters for the NREL 5MW turbine, identified from CFD simulations in a neutral atmospheric boundary layer with $TI = 6\%$ by Gebraad et al. [4]

Power		Wake					
		Deflection		Expansion		Velocity	
p_P	1.88	k_d	0.15	k_e	0.065	$M_{U,1}$	0.5
		a_d	-4.5	$m_{e,1}$	-0.5	$M_{U,2}$	1
		b_d	-0.01	$m_{e,2}$	0.22	$M_{U,3}$	5.5
				$m_{e,3}$	1	a_U	5
				b_U	1.66		

Wind-speed-dependent turbine power and thrust coefficients derived from publicly available power curves are assigned to each turbine in the wind farm. Power down-rating for noise reduction at night can be considered by altering the performance curves accordingly. During simulation, thrust and power coefficients are interpolated [9] and power is calculated for each turbine as function of rotor-averaged wind speed.

Besides the wind farm setup and wake model parametrization, the model inputs are represented by ambient wind speed, direction, shear and air density. A change in ambient turbulence intensity could be considered by adapting the wake expansion parameter for the whole power plant.

2.2. Test wind farm

Windpark Dornum is located in north-western Germany, 5 km away from the North Sea. It is surrounded by flat grassland except for two small villages east- and north-westwards of the wind farm, approximately 1 km away. The region is very populated with wind turbines, ranging from small ~ 100 kW to large multi-MW machines that are owned and operated by different parties. Figure 1 gives a view of the southward wind farm section.

SCADA data of 12 wind turbines was provided by the operator and used for the present study. While this complete set is used for the WFC potential analysis, only a cluster of six identical turbines (E-70, rotor diameter 71 m, hub height 64 m) is utilized for model validation, enabling a direct analysis of wake-caused power deficits, as explained later on more in detail. As shown in figure 2, the investigated turbines are in proximity of several machines of different sizes. Only the wakes of the closest 45 turbines are taken into account in this study, while more than 100 additional turbines further away are not considered, as their influence is expected to be small.



Figure 1: Photograph of Windpark Dornum, taken from PD210 looking towards the south.

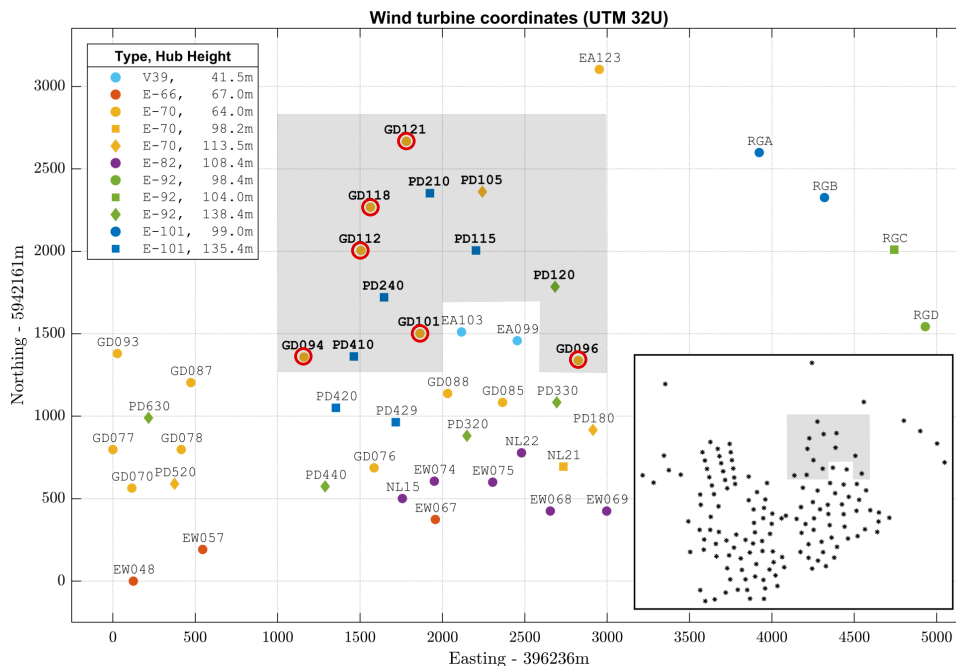


Figure 2: Arrangement of the 45 simulated wind turbines. The grey rectangle encloses the 12 measurement turbines used for optimization; red circles highlight the six E-70 turbines with 64m hub height used for validation. The subplot in the lower right corner shows all surrounding turbines, including the ones not used in the simulation.

A full year of 10 minute averaged SCADA measurements was provided, from which the nacelle anemometer wind speed, measured turbine power (and its extreme values) and yaw orientation are employed. Therefore, the complete data set comprises 52 704 data points for each of the 12 turbines.

The raw data is prepared using a three-step procedure: firstly, data is pre-processed and formatted (conversion of time stamps to UTC+1, removal of duplicate measurements, etc.). Secondly, turbine measurements are discarded in case of

turbine malfunction: turbine status indicating a malfunction,

no power production: power smaller than 5 kW or rotor speed smaller than 1 rpm, or
outliers: anomalous conditions, detected by comparing the anemometer wind speed with power measurements. In case of wind speed above rated and a power production deviating more than 5% from nominal (or night-reduced) rated power, the condition is marked as an outlier. These conditions are believed to mainly originate from unscheduled power curtailments demanded by the grid operator.

The resulting number of discarded data points for the individual turbines is summarized in table 2. Note that one data point can belong to multiple categories at once.

Finally, the remaining data is aggregated into a set of data points, valid for all individual turbines simultaneously. Overall, the data preparation leaves 33 635 ($\approx 64\%$) of “good” data points for further usage.

2.3. Determination of ambient wind conditions

In the absence of additional measuring devices such as meteorological masts or LIDARs, the ambient wind conditions must be estimated from SCADA data alone. A method has been developed that first estimates the ambient wind direction from turbine yaw measurements, and then identifies a set of undisturbed free-stream turbines. In turn, these are used for calculating ambient wind speed, turbulence and vertical wind shear.

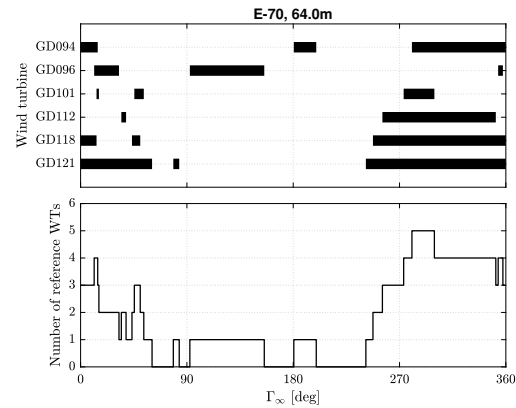
The ambient wind direction can be obtained from the average yaw orientation of all turbines, rather than using wind vane measurements. In fact, on-board wind vane measurements are often not recorded by the SCADA system, which is also the case for the wind farm under consideration. In addition, wind vanes might not always be very accurate, due to their point-wise nature and disturbances from blade passage, rotor wake and nacelle interference effects. Given that the yaw position sensors are usually poorly calibrated (typically, only for rewinding purposes), the average 12-turbine yaw angle is manually corrected by a constant scalar offset to fit the observed power deficit positions to the waking wind directions expected from the wind farm layout. A similar procedure was used by [10, 11, 12], using the yaw signal of only one single reference turbine. In this work, the approach is extended by using the average pointing direction of the entire wind farm. Using multiple yaw signals increases the confidence in the determined ambient wind direction and compensates for turbulent wind direction fluctuations over the area of the wind farm. For larger clusters of wind turbines, more sophisticated models could be employed to also account for large-scale variations of wind direction.

Free-stream turbines are used to determine ambient wind speed, turbulence, shear and reference power, as described later on. The determination of whether a turbine operates in free-stream or not, is here obtained by evaluating the wind farm model with a conservative wake expansion coefficient. A turbine is defined as operating in free-stream if, for a certain wind direction, it does not experience power losses from wake impingement. In the present study, the wakes of all 45 simulated wind turbines are taken into account for the determination of free-stream conditions. The free-stream turbines identified in this way (out of the set of six E-70 turbines) are shown in figure 3 for varying wind directions.

To measure ambient wind speed, it is generally advantageous to use the rotor effective wind speed (REWS) instead of the point-wise measurements provided by the nacelle anemometer. Even though the latter might be partially corrected for turbine induction as well as nacelle and blade induced flow disturbances, the REWS is a better indicator for overall ambient wind speed. There are different methods for REWS estimation discussed in the literature [13, 14]. Most of these methods usually require detailed turbine information, which is however often not available. Therefore, this work estimates REWS simply by using publicly available curves of turbine power versus wind speed. Thereby, given the SCADA measured power, the wind speed is readily obtained from the power curve of the corresponding turbine. Note that, by using such technique, a non-ambiguous REWS determination is only possible between cut-in and rated

Table 2: Number of data points discarded for each turbine.

Turbine ID	Turbine Malfunction	No Power Production	Outliers
GD094	249	5506	394
GD096	850	6337	353
GD101	847	8032	651
GD112	993	8136	651
GD118	898	9208	715
GD121	921	7877	616
PD105	94	5764	723
PD115	272	5628	1384
PD120	280	5290	706
PD210	894	8573	1732
PD240	147	5944	1533
PD410	130	5877	1321

**Figure 3:** Free-stream reference turbines as functions of wind direction by name (top) and resulting number (bottom).

power (control region II, or partial load). In this work, the ambient wind speed is obtained by averaging the REWS of all free-stream turbines. In case that no free-stream turbine exists or can provide a REWS estimate, the ambient wind speed cannot be determined and the data point has to be removed (see next section). As for the ambient wind direction, more sophisticated averaging methods could be used in larger power plants to account for a variation of ambient wind speed throughout the farm.

Note that REWS obtained from power curve lookup is inherently normalized by the constant reference air density of the power curve. If such REWS is used as ambient wind speed in the model simulations, it matches simulated to measured free-stream power exactly, provided that the same constant reference density $\rho_{\text{ref}} = 1.225 \text{ kg/m}^3$ and power curves are used. Remaining power deviations occur only on waked turbines and are caused by inaccurate predictions of the wake model.

A measure for ambient turbulence is derived from turbine power fluctuations in control region II, similarly to the method proposed by Mittelmeier et al. [12]. In the present case, no 10 min power standard deviation is available in the SCADA data, so that the 10 min extreme values P_{min} and P_{max} are used to define the turbulence measure TI_P :

$$TI_P := \frac{P_{\text{max}} - P_{\text{min}}}{P}. \quad (1)$$

The data set was split in two equal parts, according to measurements recorded below or above the median turbulence intensity, herein called *low TI* and *high TI*, respectively.

In case of a wind farm with turbines of different hub height, it is also possible to estimate the vertical wind shear profile. In fact, using simultaneously the free-stream turbine anemometer wind speed measurements at two or more different hub heights, the average power law exponent [15] can be identified. In this work, SCADA measurements of turbines with 64 m and 135.4 m hub height are available, and therefore a yearly average power law exponent of $\alpha \approx 0.3$ could be identified by choosing 64 m as the reference height. This value is used in all model simulations.

3. Results

3.1. Validation

The main purpose of the wind farm flow model is to correctly predict power losses due to wake impingement on downstream turbines. Such wake losses are evaluated with respect to the power

available in the undisturbed inflow, which is here determined from the free-stream turbines. At least one such reference turbine must be available for a given wind direction to enable the determination of power deficits.

To utilize the determined reference power directly—without the need of correcting for turbine type and wind shear (hub height)—, only the set of six identical E-70 turbines with a 64 m hub height is used for validation. For this cluster, due to the large number of surrounding turbines, no free-stream reference turbines are available for 38 % of the data points in the cleaned data set.

Furthermore, measured ambient wind speed and direction must be available to feed the wind farm model. The method presented in section 2.3 does not allow one to infer REWS in control region III (full power). Therefore, the validation has to be limited to conditions in which at least one reference turbine operates below rated wind speed, discarding an additional 0.5 % of the cleaned data points.

The model is simulated for time series of measured ambient wind speed and direction with a constant shear and air density. To increase computational efficiency, the power of all wind turbines is pre-calculated on a grid of discrete wind speeds $V_\infty = [1, 2, \dots, 25 \text{ m s}^{-1}]$ and directions $\Gamma_\infty = [0, 5, \dots, 355^\circ]$. This grid is then used to extract time series of simulated power as function of measured wind speed and direction via linear interpolation.

Time series of both simulated and measured normalized power are then binned over wind directions, thereby inherently considering the statistical distribution of the data points. The power ratio assigned to each 5° -wide wind direction bin is calculated via the median, as this is more robust against outliers in the scattered data. To base the validation on as many data points as possible—and thereby increase the confidence in the results—, no additional restrictions are imposed on the evaluated range of wind speeds.

In figure 4, the measured power over wind direction is shown, both point-wise as well as by the binwise median for each of the six turbines. The latter case is calculated from low and high-turbulent measurements separately, and it is shown by the blue and red solid lines, respectively. The black solid line illustrates the corresponding simulation results, also generated by binning time series of power ratio into 5° -wide wind direction bins. Errorbars visualize the binwise standard deviation of simulated power deficits caused by the described wind speed dependency. Different turbulence levels are not considered in the simulations, as only one fixed set of parameters is used. In the figure, a histogram represents the total time of available measurements for each wind direction bin and turbulence group.

The results show a good overall agreement between model-predicted and measured normalized power. However, for southern and western wind directions, simulated P/P_{ref} tends to be too large, as can be observed very distinctly for GD094 and also by looking at the wind farm efficiency in figure 5. This effect likely originates from upwind turbines that are not considered in the simulation (cf. figure 2), but whose influence is seen in the measurements. Furthermore, non-physical peaks $P/P_{\text{ref}} > 1$ can be noticed in the measurements, for example for GD121 over the entire range of wind directions. In those cases the reference power P_{ref} used for normalization is smaller than the turbine power P , possibly due to noise in the measurements or unmodeled flow effects in the determination of the reference turbines. Generally speaking, normalized power can be affected by inaccurate estimates of reference power, which could in fact be another source for the mentioned deviations with southern and western winds. At these wind directions, low confidence can be placed on the reference power that is determined from only one single free-stream turbine.

The measured low-turbulent power deficits tend to be deeper and narrower due to reduced wake mixing and lower wind direction uncertainty [16]. These effects of turbulence on apparent wake expansion and decay could potentially be modeled by adapting the FLORIS wake expansion parameter k_e . The simulation results correlate slightly better to the low-turbulence

measurements, which is in accordance with the fact that wake parameters were originally identified for low ambient turbulence. Further improvements are to be expected if the model parameters are calibrated explicitly for the specific site and turbines.

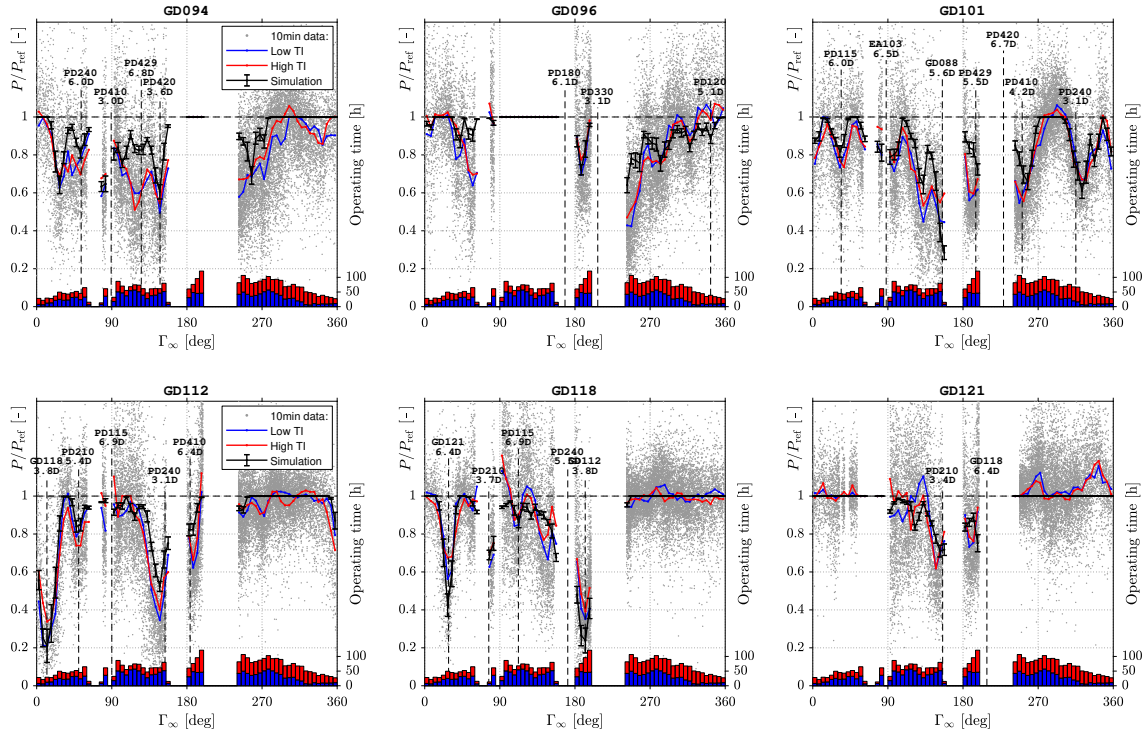


Figure 4: Simulated and measured E-70 power ratio for the year 2016. The 10 min SCADA measurements are given both directly and by their binwise median, which is split according to TI_P . The simulations are given by their binwise medians, vertical bars illustrating the standard deviation due to wind speed dependency within each bin. Vertical lines indicate wakening turbines for normalized distances $< 7D$. The histogram represents the total time of available measurements for each wind direction bin and turbulence group.

As for the individual turbines, the combined power ratio of the six turbines is evaluated in figure 5 in terms of wind farm efficiency η_{WF} , defined as

$$\eta_{WF} = \frac{\sum_{i=1}^{N_T} P_i}{N_T P_{ref}}, \quad (2)$$

where P_i is the power of wind turbine i , P_{ref} is the free-stream reference power, and N_T is the total number of considered wind turbines. As for the individual turbines, the simulated wake losses correspond well with the measurements.

By integrating time series of power over time, the measured and simulated AEP can be computed for the considered turbines, as summarized in table 3. The six turbines together lose circa 11% of the energy available in the ambient inflow due to wake interactions. The wind farm model predicts the actual wind farm AEP with 1.38% accuracy, although deviations of almost 7% occur for the individual machines.

Note that the parameters k_d , related to the wake deflection, and p_p , describing power reduction in yawed operation, could not be validated using the available set of measurements.

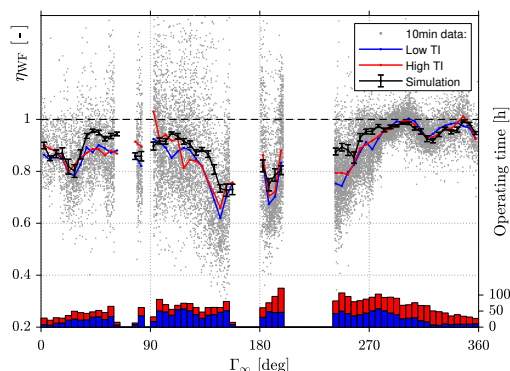


Figure 5: Combined efficiency of the six E-70s, in analogy to figure 4.

Table 3: Measured and simulated wind turbine AEP [GWh].

Turbine ID	AEP meas,ref	AEP meas	AEP sim	Error [%]
GD094	1.27	1.07	1.15	+6.72
GD096	1.27	1.11	1.14	+2.56
GD101	1.27	1.03	1.09	+6.37
GD112	1.27	1.15	1.17	+1.51
GD118	1.27	1.17	1.12	-3.83
GD121	1.27	1.25	1.20	-3.62
Wind farm	7.64	6.77	6.87	+1.38

3.2. Analysis of wake steering potential

Next, the wind farm model is used to estimate the potential increase in power and AEP by wake steering. Therefore, the yaw angles $\vec{\gamma} = (\gamma_1, \gamma_2, \dots, \gamma_{N_T})$ of the $N_T = 12$ considered turbines are optimized to maximize total wind farm power, by solving the following problem:

$$\max_{\vec{\gamma}} \sum_{i=1}^{N_T} P_i(V_\infty, \Gamma_\infty, \vec{\gamma}). \quad (3)$$

The yaw misalignments $\Delta\gamma_i = \gamma_i - \Gamma_\infty$ with respect to the wind direction Γ_∞ are constrained to $\pm 30^\circ$ as in [9].

The optimization problem is solved using the `Matlab` global-optimization patternsearch solver [17]. In contrast to gradient-based optimization algorithms, this direct-search solver can handle the discontinuities in calculated wind farm power originating from the discrete wake velocity profiles.

For an exemplary turbine (GD118) of the wind farm under consideration, figure 6 shows the computed optimum yaw misalignments obtained for discrete combinations of ambient wind directions Γ_∞ and speeds V_∞ . Such look-up tables could be used to control the wind farm in open-loop, providing optimum turbine misalignments based on the ambient wind speed and direction identified from free-stream turbines. Figure 7 shows the relative wind farm power gains $\Delta P/P_{\text{baseline}}$ corresponding to the optimum yaw misalignments.

The results show that, as expected and according to intuition, wake steering is most effective for wind directions with several aligned turbines and for wind speeds in region II of the power curve. In fact, no losses can be mitigated and no power gains are possible if no wake losses occur in the first place. This can be either because no wake interactions take place for certain wind directions, or because wake interactions do not have an effect when the wind speed is sufficiently high for all turbines to operate at rated power. The latter phenomenon occurs towards the typical rated wind speed $V \approx 12 \text{ m s}^{-1}$, when upwind turbines limited to rated power leave more and more power in the flow for downwind machines. The power gains achievable by wake steering diminish, and so do the proposed optimum upwind turbine misalignments. This wind speed dependency emerges solely from the underlying turbine performance curves, and it is not a threshold imposed by the authors. Figure 7 shows that the largest power gain $\Delta P/P_{\text{baseline}} = 1.2 \text{ MW}/7 \text{ MW} \approx 17\%$ occurs at $\Gamma_\infty = 205^\circ$ and $V_\infty = 4 \text{ m s}^{-1}$. The flow field around the 12 optimized turbines before and after optimization is shown in figure 8 for $\Gamma_\infty = 205^\circ$ and $V_\infty = 8 \text{ m s}^{-1}$. The figure clearly illustrates how wakes are steered away from downwind turbines.

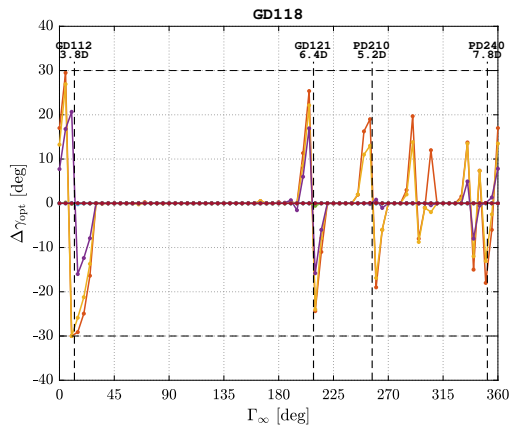


Figure 6: Optimum yaw misalignments $\Delta\gamma_{\text{opt}}$ for an exemplary turbine (GD118) as functions of ambient wind direction Γ_{∞} and speed V_{∞} . Relative directions and distances ($< 9D$) of power-maximized downwind turbines are displayed.

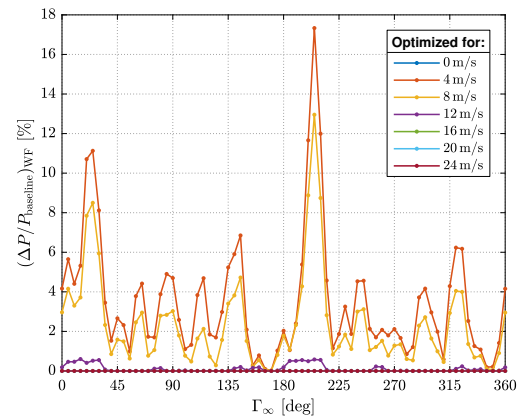


Figure 7: Relative power gain for the 12 measurement turbines as function of ambient wind direction Γ_{∞} and speed V_{∞} .

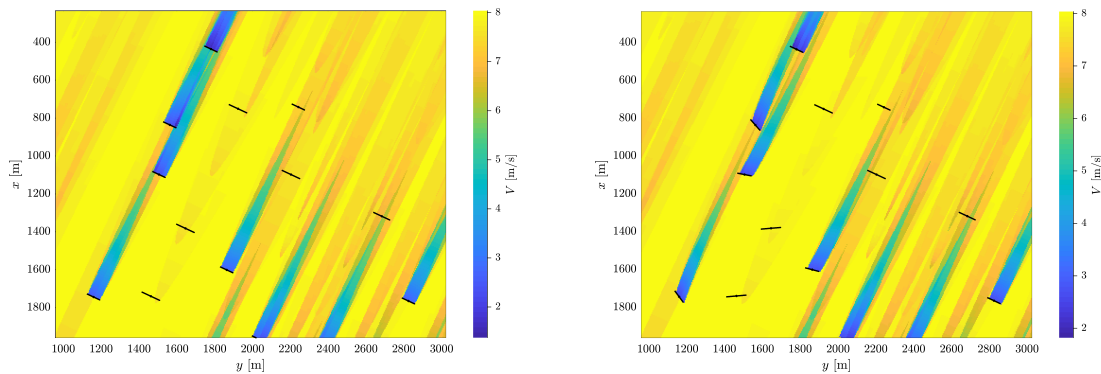


Figure 8: Velocity field around the 12 optimized turbines, before (left) and after (right) optimization for $\Gamma_{\infty} = 205^{\circ}$ and $V_{\infty} = 8 \text{ m/s}$, visualized on a horizontal plane at $z = 64 \text{ m}$. The wakes of some turbines of different hub height are only partially visible. Wakes of surrounding turbines are also visible.

To determine the potential increase in wind farm AEP using the proposed look-up table for advanced sector management, the distributions of ambient wind speed and direction at the given site should be known. As shown in the previous section, for several wind directions all evaluated turbines are waked by upstream turbines for which no data is available. To avoid losing too many measurement points, it was decided to ignore wake effects and compute the yearly wind speed distribution based on all six E-70 nacelle anemometer measurements. Clearly, the average wind speed and therefore the absolute AEP will be underestimated, but the relative increase in AEP should not be significantly affected. The ambient wind direction is obtained as discussed in section 2.3. The resulting wind speed distribution and wind rose are shown in figure 9.

The wind farm efficiency can be determined as a function of wind direction, by evaluating the wind farm model for the identified ambient wind conditions without (baseline) and with (optimized) wake steering, as shown in figure 10. Even though the wind farm efficiency increases over the entire range of wind directions, it is important to note that the surrounding 33 turbines are not optimized. Larger improvements are to be expected by including them into

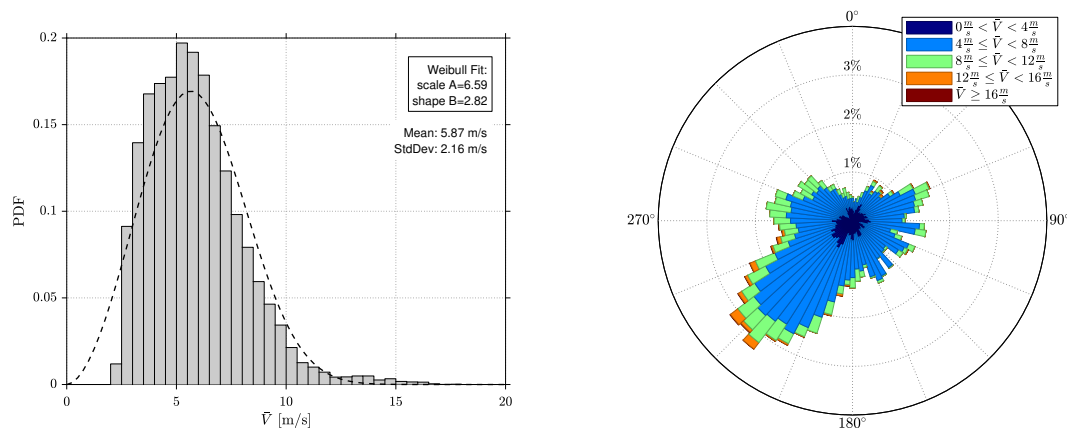


Figure 9: Measured and Weibull-fitted wind speed distribution (left) and wind rose (right) for the year 2016.

the optimization.

Accumulating over all measurements, an AEP increase

$$\Delta AEP / AEP_{\text{baseline}} = 0.64 \text{ GWh} / 38.03 \text{ GWh} \approx 1.7 \%$$

is predicted by the wind farm model when wake steering is implemented on the cluster of 12 turbines.

If the yaw angles are only optimized for the constant site average wind speed, the resulting look-up table is only a function of wind direction and therefore possibly simpler to implement. In such case, the estimated AEP gain decreases to 1.3%. This is less than the stated 1.7% achieved with a wind speed and direction dependent look-up table, as power curve effects are not considered.

The underlying distribution of yaw misalignments shown in figure 11 reveals that, statistically, the majority of the proposed optimum misalignments is rather small, as also observed in [18]. In the present case, almost 80% of the misalignments are smaller than 5° and the misalignment threshold is rarely reached. Therefore, limiting the maximum allowed misalignment angles to the above stated $\pm 30^\circ$ will only have a small influence on the AEP gain as demonstrated by [18], but might increase turbine lifetime by limiting turbine loading [19]. The given distribution of yaw misalignments could be used to trade off the costs associated with wake steering against the energy gains, to ultimately minimize the cost of energy. Employing damage models [20] and performing such an analysis could be the subject of further research beyond the scope of the present work.

4. Conclusions and outlook

This work presented the application of the FLORIS wake model to an operational on-shore wind farm, with two main goals: validating model predictions against SCADA measurements, and estimating the potential of wake steering for a given set of turbines.

Firstly, it was shown that ambient wind direction and free-stream flow properties can be estimated solely from turbine SCADA data, without additional instrumentation.

Secondly, statistical comparisons have shown that the model-predicted wind turbine power deficits and wind farm efficiency are in good agreement with field measurements.

Finally, the wind farm model was employed to find optimum turbine yaw misalignments that maximize wind farm power by yaw-induced wake steering. For each turbine, a look-up table of optimum yaw misalignment as a function of wind direction and speed is obtained that could be

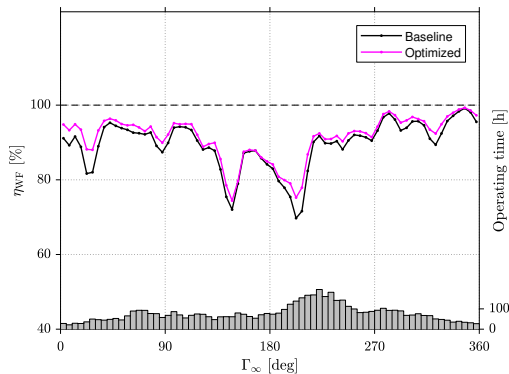


Figure 10: Simulated baseline and optimized wind farm efficiency at measured wind direction and speed. Additionally, the distribution of measured wind directions (operating time) is displayed at the bottom of the plot.

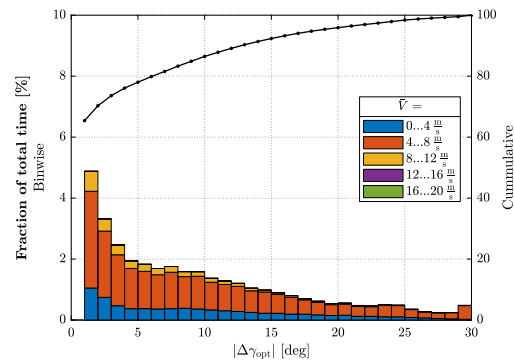


Figure 11: Distribution of the optimum yaw misalignments, shown for $|\Delta\gamma_{\text{opt}}| > 1^\circ$.

used to implement open-loop wake steering in the field. For the studied cluster of 12 turbines, a maximum power gain of 17 % is predicted for southward wind directions at low wind speeds. Based on one year of site-specific wind conditions, a 1.7 % AEP gain can be expected. The necessary yaw misalignments were limited to $\pm 30^\circ$, about 80 % of them being smaller than 5° .

Acknowledgments

The authors thankfully acknowledge Mr. Rik Folkerts and Mr. Thomas Erdmann of Windpark Dornum GmbH for providing measurement data and valuable support. This work has been partially supported by the CL-Windcon project, which receives funding from the European Union Horizon 2020 research and innovation programme under grant agreement No. 727477.

References

- [1] Knudsen T, Bak T and Svenstrup M 2015 *Wind Energy* **18** 1333–1351 ISSN 10954244
- [2] Boersma S, Doekemeijer B M, Gebraad P, Fleming P A, Annoni J, Scholbrock A K, Frederik J A and van Wingerden J W 2017 A tutorial on control-oriented modeling and control of wind farms *American Control Conference 2017* (IEEE) p 1–18 ISBN 978-1-5090-5992-8
- [3] Fleming P, Annoni J, Shah J J, Wang L, Ananthan S, Zhang Z, Hutchings K, Wang P, Chen W and Chen L 2017 *Wind Energy Science* **2**(1) 229–239 ISSN 2366-7451
- [4] Gebraad P M O, Teeuwisse F W, Van Wingerden J W, Fleming P A, Ruben S D, Marden J R and Pao L Y 2016 *Wind Energy* **19** 95–114 ISSN 10954244
- [5] Gebraad P M O, Teeuwisse F W, Van Wingerden J W, Fleming P A, Ruben S D, Marden J R and Pao L Y 2014 A data-driven model for wind plant power optimization by yaw control *American Control Conference (ACC), 2014* (Piscataway, NJ: IEEE) pp 3128–3134 ISBN 978-1-4799-3274-0
- [6] Jiménez A, Crespo A and Migoya E 2010 *Wind Energy* **13** 559–572 ISSN 10954244
- [7] Katic I, Højstrup J and Jensen N O 1986 A simple model for cluster efficiency *European Wind Energy Association Conference and Exhibition* p 407–410
- [8] Storm R and Doekemeijer B An exhaustive matlab implementation of the steady-state floris wind farm model URL https://github.com/TUDELFT-DataDrivenControl/FLORISSE_M
- [9] Gebraad P, Thomas J J, Ning A, Fleming P and Dykes K 2017 *Wind Energy* **20**(1) 97–107 ISSN 10954244
- [10] Hansen K S, Barthelmie R J, Jensen L E and Sommer A 2012 *Wind Energy* **15**(1) 183–196 ISSN 10954244
- [11] Infield D and Zorzi G 2017 *Journal of Physics: Conference Series* **854** 012024 ISSN 1742-6588
- [12] Mittelmeier N, Allin J, Blodau T, Trabucchi D, Steinfeld G, Rott A and Kühn M 2017 *Wind Energy Science Discussions* 1–20 ISSN 2366-7621
- [13] Bottasso C L, Cacciola S and Schreiber J 2018 *Renewable Energy* **116** 155–168
- [14] Soltani M N, Knudsen T, Svenstrup M, Wisniewski R, Brath P, Ortega R and Johnson K 2013 *IEEE Transactions on Control Systems Technology* **21**(4) 1155–1167 ISSN 1063-6536

- [15] James F Manwell J G M and Rogers A L 2009 *Wind energy explained* (Wiley) ISBN 978-0-470-01500-1
- [16] Gaumond M, Réthoré P E, Ott S, Peña A, Bechmann A and Hansen K S 2014 *Wind Energy* **17**(8) 1169–1178 ISSN 10954244
- [17] patternsearch: Find minimum of function using pattern search URL <https://de.mathworks.com/help/gads/patternsearch.html>
- [18] Fleming P A, Ning A, Gebraad P M O and Dykes K 2016 *Wind Energy* **19**(2) 329–344 ISSN 10954244
- [19] Fleming P, Gebraad P M, Lee S, van Wingerden J W, Johnson K, Churchfield M, Michalakes J, Spalart P and Moriarty P 2015 *Wind Energy* **18**(12) 2135–2143 ISSN 10954244
- [20] Damiani R, Dana S, Annoni J, Fleming P, Roadman J, van Dam J and Dykes K 2017 *Wind Energy Science Discussions* 1–25 ISSN 2366-7621

Discussion and Conclusion

This dissertation presents new methods to improve wind condition awareness on turbine and farm level. The new techniques are tested and applied within the field of wind farm control.

First, a novel method to estimate the local wind speed at a turbine rotor is described. The method provides additional information on the wind conditions, which are unknown to most turbines today. Second, it is shown that such information can be used to improve wind farm models and to detect wakes within a wind farm. Last, as one of the many possible applications, the methods are employed for wind farm control. Apart from a significantly increased wind farm power production when using wake steering, it has been also shown that a superior control performance can indeed be reached with improved wind and wake condition awareness.

In this work, numerical simulations have been used to develop, test and improve various methods and models. To confirm and verify the various approaches and their technical feasibility, scaled wind tunnel tests have been performed in a controlled environment. Thereby, a clear highlight of this dissertation has been reached: the successful wind tunnel demonstration of model-based wind farm control. Full-scale tests and real turbine data have been used as much as possible to prove and demonstrate the final application of the developed methods. Results have been shown that include a full-scale test of the wind sensing and wake detection method, as well as the demonstration of model improvements using historical SCADA data of a 43-turbine wind farm.

Four core results are summarized as follows:

- A novel **method to estimate the local wind speed** within the rotor disc of a wind turbine by analysis of blade bending moments, that are available on many modern turbines, has been developed. Different from methods presented in the literature [63, 64, 66], local wind estimates that give estimations for different parts of the rotor disc are obtained. A further advantage is that the method does not rely on an extensive set of measurements for model tuning. Instead a standard numerical turbine model, which is typically already used for turbine certification, is sufficient. The wind sensing method has been successfully tested in field experiments.
- The wind sensing method has been employed to **detect wind turbine wakes** within a wind farm and to improve wind farm flow models. The method developed exploits the distinct fingerprint a wake leaves on a downstream turbine. The information can be exploited to correct wind farm models or to trigger sector management and wind farm control. Solutions for wake detection presented in literature base on remote sensing technologies that rely on additional hardware [20, 21], whereas the newly presented method can be installed as software update on turbines with blade load sensors. The wake detection method has been successfully tested in field experiments.
- **Wind farm models** have been parameterized and improved by learning from historical data. The method developed recognizes that any wind farm model has always only a limited prediction accuracy. Therefore, a baseline model is improved by extra terms designed to correct some of

its presumed specific deficiencies. The method can be seen as an integration of data-driven approaches [74] into state-of-the-art wind farm models [27, 28]. Thereby, the model accuracy is gradually improved by learning from SCADA data. The method also allows the usage and inclusion of dedicated wind sensing. The modeling improvement has been successfully demonstrated and verified in wind tunnel experiments and using historic SCADA data of a full-scale wind farm.

- A model-based **wind farm control** algorithm has been developed with the goal of maximizing the total wind farm power production—also applying the improved wind farm models. Even though a variety of simulation studies [37] and even some first field tests have been executed already [45–47], the first wake deflection control during dynamic wind direction changes within a scaled testing facility has been presented in this thesis, providing additional insight and confidence. Within the successful tests it has been shown that damage equivalent loads can be reduced as a side-product of power maximization. Additionally, an improved model accuracy, obtained by the developed learning method, increases the control performance.

16.1 Outlook

Within this thesis, a load-based wind sensing method has been successfully tested and validated in field experiments. However, additional validations, ideally using a met-mast reaching total turbine height or even high resolution LiDAR inflow measurements, can increase trust in the estimates and bring the method closer to deployment, possibly even as a standard product of turbines that are anyways equipped with load sensors.

In addition to the simple method presented in this work, further and more sophisticated methods, following the rotor-as-a-sensor concept, are currently in development. Those make use of additional load sensors, accelerometers or whatever signals are available to extract additional inflow information, possibly also wind direction and wind veer. However, such sophisticated methods typically rely on training data, which is difficult to obtain in the field. The presented wind sensing method, which shows good results without training, can for example be linked to provide horizontal and vertical shear information. Thereby less sophisticated installations would be necessary to acquire the remaining training data.

The main application for wind sensing presented in this work is wake detection and wind farm control. For wake detection, a rather simple application is sector management. Here, the wake detection can trigger the turbine shutdown as soon as the wake impinges on the turbine rotor. Thereby, large energy losses, which are often faced when using conservative wind direction sectors, can be reduced without the risk of operating within the damage causing wake for a long period.

For wind farm control, a compulsory next step is a solid field demonstration of wake steering control for increased energy capture. Thereby, the wake detection methods presented can help to verify proper wake steering and can finally be used for closing the control loop. Also, the development of models and methods to quantify the atmospheric stability as well as turbulence intensity, employing the rotor-effective shear and turbulence estimates, can help in reducing uncertainties in wind farm control. In addition, the wind farm model improvements and the learning method based on SCADA data can be used to ensure a very accurate model prediction, which is of crucial importance for a successful deployment.

The use of wind sensing goes beyond wind farm control. If turbine loads have been recorded, it is possible to reconstruct detailed historic wind condition time series. Those can be compared to turbine design wind conditions and used, for example, to assess consumed and estimate remaining turbine lifetime, which is of great interest today as many turbines reach the end of their design lifetime. Even more, for new installations the knowledge of wind conditions allows for example the development of

digital twins of wind turbines and farms. Thereby new possibilities are created, including prediction and optimization capabilities, predictive maintenance as well as risk mitigation strategies.

BIBLIOGRAPHY

- [1] Intergovernmental Panel on Climate Change (IPCC), “Summary for policymakers: SPM,” in *Climate Change 2013: The Physical Science Basis. Contribution of Working Group I to the Fifth Assessment Report of the Intergovernmental Panel on Climate Change*, T. F. Stocker, D. Qin, G.-K. Plattner, M. Tignor, S. K. Allen, J. Boschung, A. Nauels, Y. Xia, V. Bex, and P. Midgley, Eds. Cambridge, United Kingdom and New York, NY, USA: Cambridge University Press, 2013, pp. 1–30. ISBN 978-1-107-66182-0. [Online]. Available: http://www.climatechange2013.org/images/report/WG1AR5_SPM_FINAL.pdf
- [2] United Nations, “7. d Paris Agreement,” 2015, accessed: 2020-Oct-08. [Online]. Available: https://treaties.un.org/Pages/ViewDetails.aspx?src=TREATY&mtdsg_no=XXVII-7-d&chapter=27&clang=_en
- [3] Intergovernmental Panel on Climate Change (IPCC), “Technology-specific cost and performance parameters,” in *Climate Change 2014 Mitigation of Climate Change*, IPCC, Ed. Cambridge, United Kingdom and New York, NY, USA: Cambridge University Press, 2014, pp. 1329–1356. ISBN 9781107415416. [Online]. Available: https://www.ipcc.ch/site/assets/uploads/2018/02/ipcc_wg3_ar5_annex-iii.pdf
- [4] International Energy Association (IEA), *Key World Energy Statistics 2020*. OECD, 2020. ISBN 9789264840935. [Online]. Available: <https://www.iea.org/reports/key-world-energy-statistics-2020>
- [5] B. Burger, “Net public electricity generation in Germany in 2019,” Fraunhofer Institute for Solar Energy Systems ISE, 2020, accessed: 2020-Oct-08. [Online]. Available: https://www.energy-charts.info/downloads/Stromerzeugung_2019_3.pdf
- [6] Global Wind Energy Council (GWEC), “Global Wind Report 2018,” 2019, accessed: 2020-Oct-08. [Online]. Available: <https://gwec.net/wp-content/uploads/2019/04/GWEC-Global-Wind-Report-2018.pdf>
- [7] International Energy Association (IEA), “World Energy Outlook 2019,” 2019, accessed: 2020-Oct-08. [Online]. Available: <https://www.iea.org/reports/world-energy-outlook-2019>
- [8] Internationales Wirtschaftsforum Regenerative Energien (IWR), “Windenergie-Markt Deutschland,” 2019, accessed: 2020-Oct-08. [Online]. Available: <https://www.windbranche.de/windenergie-ausbau/deutschland>
- [9] Bundesverband WindEnergie (BWE), “Zahlen und Fakten: Die deutschen Bundesländer im Vergleich,” 2019, accessed: 2020-Oct-08. [Online]. Available: <https://www.wind-energie.de/themen/zahlen-und-fakten/bundeslaender/>
- [10] G. van Kuik and J. Peinke, Eds., *Long-term research challenges in wind energy: A research agenda by the European Academy of Wind Energy*, ser. Research Topics in Wind Energy. Cham and

- s.l.: Springer International Publishing, 2016, vol. 6. ISBN 978-3-319-46919-5. [Online]. Available: <http://dx.doi.org/10.1007/978-3-319-46919-5>
- [11] J. Lange, J. Mann, J. Berg, D. Parvu, R. Kilpatrick, A. Costache, J. Chowdhury, K. Siddiqui, and H. Hangan, "For wind turbines in complex terrain, the devil is in the detail," *Environmental Research Letters*, vol. 12, no. 9, p. 094020, 2017. doi: 10.1088/1748-9326/aa81db
- [12] A. Peña, K. Schaldemose Hansen, S. Ott, and M. P. van der Laan, "On wake modeling, wind-farm gradients, and AEP predictions at the Anholt wind farm," *Wind Energy Science*, vol. 3, no. 1, pp. 191–202, 2018. doi: 10.5194/wes-3-191-2018
- [13] K. Z. Østergaard, P. Brath, and J. Stoustrup, "Estimation of effective wind speed," *Journal of Physics: Conference Series*, vol. 75, p. 012082, 2007. doi: 10.1088/1742-6596/75/1/012082
- [14] L. Ziegler and M. Muskulus, "Fatigue reassessment for lifetime extension of offshore wind monopile substructures," *Journal of Physics: Conference Series*, vol. 753, p. 092010, 2016. doi: 10.1088/1742-6596/753/9/092010
- [15] L. Vollmer, G. Steinfeld, D. Heinemann, and M. Kühn, "Estimating the wake deflection downstream of a wind turbine in different atmospheric stabilities: An LES study," *Wind Energy Science*, vol. 1, no. 2, pp. 129–141, 2016. doi: 10.5194/wes-1-129-2016
- [16] K. Thomsen and P. Sørensen, "Fatigue loads for wind turbines operating in wakes," *Journal of Wind Engineering and Industrial Aerodynamics*, vol. 80, no. 1-2, pp. 121–136, 1999. doi: 10.1016/S0167-6105(98)00194-9
- [17] P. McKay, R. Carriveau, and D. S.-K. Ting, "Wake impacts on downstream wind turbine performance and yaw alignment," *Wind Energy*, vol. 16, no. 2, pp. 221–234, 2013. doi: 10.1002/we.544
- [18] Z. Yang, Y. Li, and J. Seem, "Individual pitch control for wind turbine load reduction including wake interaction," in *American Control Conference (ACC)*, Washington, DC, USA, June 2011, pp. 5207–5212. doi: 10.1109/acc.2011.5991022
- [19] H. Wang and R. J. Barthelmie, "Wind turbine wake detection with a single doppler wind lidar," *Journal of Physics: Conference Series*, vol. 625, p. 012017, 2015. doi: 10.1088/1742-6596/625/1/012017
- [20] S. Raach, D. Schlipf, and P. W. Cheng, "Lidar-based wake tracking for closed-loop wind farm control," *Journal of Physics: Conference Series*, vol. 753, p. 052009, 2016. doi: 10.1088/1742-6596/753/5/052009
- [21] D. P. Held, A. Larvol, and J. Mann, "Detecting wind turbine wakes with nacelle lidars," *Journal of Physics: Conference Series*, vol. 854, p. 012020, 2017. doi: 10.1088/1742-6596/854/1/012020
- [22] P. A. Fleming, P. M. Gbraad, S. Lee, J.-W. van Wingerden, K. Johnson, M. Churchfield, J. Michalakes, P. Spalart, and P. Moriarty, "Evaluating techniques for redirecting turbine wakes using SOWFA," *Renewable Energy*, vol. 70, pp. 211 – 218, 2014, special issue on aerodynamics of offshore wind energy systems and wakes. doi: 10.1016/j.renene.2014.02.015
- [23] S.-P. Breton, J. Sumner, J. N. Sørensen, K. S. Hansen, S. Sarmast, and S. Ivanell, "A survey of modelling methods for high-fidelity wind farm simulations using large eddy simulation," *Philosophical transactions. Series A, Mathematical, physical, and engineering sciences*, vol. 375, no. 2091, 2017. doi: 10.1098/rsta.2016.0097

- [24] S. Boersma, B. Doekemeijer, M. Vali, J. Meyers, and J.-W. van Wingerden, "A control-oriented dynamic wind farm model: WFSim," *Wind Energy Science*, vol. 3, no. 1, pp. 75–95, 2018. doi: 10.5194/wes-3-75-2018
- [25] D. Bastine, B. Witha, M. Wächter, and J. Peinke, "Pod analysis of a wind turbine wake in a turbulent atmospheric boundary layer," *Journal of Physics: Conference Series*, vol. 524, p. 012153, 2014. doi: 10.1088/1742-6596/524/1/012153
- [26] S. Frandsen, R. Barthelmie, S. Pryor, O. Rathmann, S. Larsen, J. Højstrup, and M. Thøgersen, "Analytical modelling of wind speed deficit in large offshore wind farms," *Wind energy*, vol. 9, no. 1-2, pp. 39–53, 2006. doi: 10.1002/we.189
- [27] P. M. O. Gebraad, F. W. Teeuwisse, J. W. Van Wingerden, P. A. Fleming, S. D. Ruben, J. R. Marden, and L. Y. Pao, "A data-driven model for wind plant power optimization by yaw control," in *American Control Conference (ACC), 2014*. Piscataway, NJ: IEEE, 2014, pp. 3128–3134. doi: 10.1109/ACC.2014.6859118
- [28] M. Bastankhah and F. Porté-Agel, "Experimental and theoretical study of wind turbine wakes in yawed conditions," *Journal of Fluid Mechanics*, vol. 806, pp. 506–541, 2016. doi: 10.1017/jfm.2016.595
- [29] A. K. Scholbrock, "Optimizing wind farm control strategies to minimize wake loss effects," Master's thesis, University of Colorado at Boulder, 2011. [Online]. Available: https://scholar.colorado.edu/concern/graduate_thesis_or_dissertations/6d56zw954
- [30] M. J. Churchfield, "A review of wind turbine wake models and future directions," in *2013 North American Wind Energy Academy (NAWEA) Symposium*, Aug. 2013. [Online]. Available: <https://www.nrel.gov/docs/fy14osti/60208.pdf>
- [31] P. Fleming, J. Annoni, M. Churchfield, L. A. Martinez-Tossas, K. Gruchalla, M. Lawson, and P. Moriarty, "A simulation study demonstrating the importance of large-scale trailing vortices in wake steering," *Wind Energy Science*, vol. 3, no. 1, pp. 243–255, 2018. doi: 10.5194/wes-3-243-2018
- [32] A. Keane, P. E. O. Aguirre, H. Ferchland, P. Clive, and D. Gallacher, "An analytical model for a full wind turbine wake," in *Journal of Physics: Conference Series*, vol. 753, no. 3. IOP Publishing, 2016, p. 032039. doi: 10.1088/1742-6596/753/3/032039
- [33] N. O. Jensen, "A note on wind generator interaction," *Risø National Laboratory Roskilde*, 1983. [Online]. Available: https://backend.orbit.dtu.dk/ws/portalfiles/portal/55857682/ris_m_2411.pdf
- [34] I. Katic, J. Højstrup, and N. O. Jensen, "A simple model for cluster efficiency," in *European wind energy association conference and exhibition*, 1986, pp. 407–410. [Online]. Available: https://backend.orbit.dtu.dk/ws/files/106427419/A_Simple_Model_for_Cluster_Efficiency_EWEC_86_.pdf
- [35] M. Bastankhah and F. Porté-Agel, "A new analytical model for wind-turbine wakes," *Renewable Energy*, vol. 70, pp. 116–123, 2014. doi: 10.1016/j.renene.2014.01.002
- [36] DNV GL, "Standard DNVGL-ST-0437: Loads and site conditions for wind turbines," 2016, accessed: 2020-Oct-08. [Online]. Available: <https://rules.dnvgl.com/docs/pdf/DNVGL/ST/2016-11/DNVGL-ST-0437.pdf>
- [37] T. Knudsen, T. Bak, and M. Svenstrup, "Survey of wind farm control-power and fatigue optimization," *Wind Energy*, vol. 18, no. 8, pp. 1333–1351, 2015. doi: 10.1002/we.1760

- [38] A. Jiménez, A. Crespo, and E. Migoya, “Application of a LES technique to characterize the wake deflection of a wind turbine in yaw,” *Wind Energy*, vol. 13, no. 6, pp. 559–572, 2010. doi: 10.1002/we.380
- [39] F. Campagnolo, V. Petrovic, C. L. Bottasso, and A. Croce, “Wind tunnel testing of wake control strategies,” in *2016 American Control Conference (ACC)*. IEEE, 2016, pp. 513–518. doi: 10.1109/ACC.2016.7524965
- [40] S. Boersma, B. M. Doekemeijer, P. Gebraad, P. A. Fleming, J. Annoni, A. K. Scholbrock, J. A. Frederik, and J.-W. van Wingerden, “A tutorial on control-oriented modeling and control of wind farms,” in *2017 American Control Conference (ACC)*. IEEE, 2017, pp. 1–18. doi: 10.23919/ACC.2017.7962923
- [41] P. M. O. Gebraad, F. C. van Dam, and J.-W. van Wingerden, “A model-free distributed approach for wind plant control,” in *American Control Conference (ACC)*, Washington, DC, USA, June 2013, pp. 628–633. doi: 10.1109/acc.2013.6579907
- [42] J. Annoni, P. M. O. Gebraad, A. K. Scholbrock, P. A. Fleming, and J.-W. van Wingerden, “Analysis of axial-induction-based wind plant control using an engineering and a high-order wind plant model,” *Wind Energy*, 2015, doi:10.1002/we.1891.
- [43] A. Rott, B. Doekemeijer, J. K. Seifert, J.-W. van Wingerden, and M. Kühn, “Robust active wake control in consideration of wind direction variability and uncertainty,” *Wind Energy Science*, vol. 3, no. 2, pp. 869–882, 2018. doi: 10.5194/wes-3-869-2018
- [44] B. M. Doekemeijer, J. Van Wingerden, and P. A. Fleming, “A tutorial on the synthesis and validation of a closed-loop wind farm controller using a steady-state surrogate model,” in *2019 American Control Conference (ACC)*, 2019, pp. 2825–2836.
- [45] P. Fleming, J. Annoni, J. J. Shah, L. Wang, S. Ananthan, Z. Zhang, K. Hutchings, P. Wang, W. Chen, and L. Chen, “Field test of wake steering at an offshore wind farm,” *Wind Energy Science*, vol. 2, no. 1, pp. 229–239, 2017. doi: 10.5194/wes-2-229-2017
- [46] P. Fleming, J. King, K. Dykes, E. Simley, J. Roadman, A. Scholbrock, P. Murphy, J. K. Lundquist, P. Moriarty, K. Fleming, J. van Dam, C. Bay, R. Mudafort, H. Lopez, J. Skopek, M. Scott, B. Ryan, C. Guernsey, and D. Brake, “Initial results from a field campaign of wake steering applied at a commercial wind farm – part 1,” *Wind Energy Science*, vol. 4, no. 2, pp. 273–285, 2019. doi: 10.5194/wes-4-273-2019
- [47] P. Fleming, J. King, E. Simley, J. Roadman, A. Scholbrock, P. Murphy, J. K. Lundquist, P. Moriarty, K. Fleming, J. van Dam, C. Bay, R. Mudafort, D. Jager, J. Skopek, M. Scott, B. Ryan, C. Guernsey, and D. Brake, “Continued results from a field campaign of wake steering applied at a commercial wind farm: Part 2,” *Wind Energy Science*, 2020. doi: 10.5194/wes-2019-104
- [48] Bayerisches Staatsministerium für Wirtschaft, Landesentwicklung und Energie, “Bayerischer Energiepreis, Kategorie: Energieforschung,” 2016, accessed: 2020-Oct-08. [Online]. Available: <https://www.bayerischer-energiepreis.de/preistraeger/preistraeger-2016>
- [49] C. L. Bottasso, S. Cacciola, and J. Schreiber, “Local wind speed estimation, with application to wake impingement detection,” *Renewable Energy*, vol. 116, pp. 155–168, 2018. doi: 10.1016/j.renene.2017.09.044
- [50] C. L. Bottasso, S. Cacciola, F. Campagnolo, and J. Schreiber, “Wake detection for wind farm control – formulation and validation,” *34th Wind Energy Symposium, AIAA SciTech Forum*, 2016. doi: 10.2514/6.2016-1741

- [51] J. Schreiber, C. L. Bottasso, and M. Bertelè, “Field testing of a local wind inflow estimator and wake detector,” *Wind Energy Science*, vol. 5, no. 3, pp. 867–884, 2020. doi: 10.5194/wes-5-867-2020
- [52] J. Schreiber, A. Balbaa, and C. L. Bottasso, “Brief communication: A double-gaussian wake model,” *Wind Energy Science*, vol. 5, no. 1, pp. 237–244, 2020. doi: 10.5194/wes-5-237-2020
- [53] J. Schreiber, E. M. Nanos, F. Campagnolo, and C. L. Bottasso, “Verification and calibration of a reduced order wind farm model by wind tunnel experiments,” *Journal of Physics: Conference Series*, vol. 854, p. 012041, 2017. doi: 10.1088/1742-6596/854/1/012041
- [54] J. Schreiber, S. Cacciola, F. Campagnolo, V. Petrović, D. Mourembles, and C. L. Bottasso, “Wind shear estimation and wake detection by rotor loads — first wind tunnel verification,” *Journal of Physics: Conference Series*, vol. 753, p. 032027, 2016. doi: 10.1088/1742-6596/753/3/032027
- [55] J. Schreiber, C. L. Bottasso, B. Salbert, and F. Campagnolo, “Improving wind farm flow models by learning from operational data,” *Wind Energy Science*, vol. 5, no. 2, pp. 647–673, 2020. doi: 10.5194/wes-5-647-2020
- [56] C. L. Bottasso and J. Schreiber, “Online model updating by a wake detector for wind farm control,” in *2018 Annual American Control Conference (ACC)*. IEEE, 2018, pp. 676–681. doi: 10.23919/ACC.2018.8431626
- [57] J. Schreiber, B. Salbert, and C. L. Bottasso, “Study of wind farm control potential based on SCADA data,” *Journal of Physics: Conference Series*, vol. 1037, p. 032012, 2018. doi: 10.1088/1742-6596/1037/3/032012
- [58] F. Campagnolo, J. Schreiber, A. M. Garcia, and C. L. Bottasso, “Wind tunnel validation of a wind observer for wind farm control,” *Proceedings of the International Offshore and Polar Engineering Conference*, 2017. [Online]. Available: <https://www.onepetro.org/conference-paper/ISOPE-I-17-410>
- [59] F. Campagnolo, A. Molder, J. Schreiber, and C. L. Bottasso, “Comparison of analytical wake models with wind tunnel data,” *Journal of Physics: Conference Series*, vol. 1256, p. 012006, 2019. doi: 10.1088/1742-6596/1256/1/012006
- [60] F. Campagnolo, V. Petrović, J. Schreiber, E. M. Nanos, A. Croce, and C. L. Bottasso, “Wind tunnel testing of a closed-loop wake deflection controller for wind farm power maximization,” *Journal of Physics: Conference Series*, vol. 753, p. 032006, 2016. doi: 10.1088/1742-6596/753/3/032006
- [61] F. Campagnolo, R. Weber, J. Schreiber, and C. L. Bottasso, “Wind tunnel testing of wake steering with dynamic wind direction changes,” *Wind Energy Science*, vol. 5, no. 4, pp. 1273–1295, 2020. doi: 10.5194/wes-5-1273-2020
- [62] C. L. Bottasso, A. Croce, and C. Riboldi, “Spatial estimation of wind states from the aeroelastic response of a wind turbine,” in *TORQUE*, EAWE, Ed., 2010. [Online]. Available: https://www.academia.edu/31359978/Spatial_estimation_of_wind_states_from_the_aeroelastic_response_of_a_wind_turbine
- [63] E. Simley and L. Y. Pao, “Evaluation of a wind speed estimator for effective hub-height and shear components,” *Wind Energy*, vol. 19, no. 1, pp. 167–184, 2016. doi: 10.1002/we.1817
- [64] M. Bertelè, C. L. Bottasso, S. Cacciola, F. Daher Adegas, and S. Delpont, “Wind inflow observation from load harmonics,” *Wind Energy Science*, vol. 2, no. 2, pp. 615–640, 2017. doi: 10.5194/wes-2-615-2017

- [65] X. Ma, N. Poulsen, and H. Bindner, *Estimation of Wind Speed in Connection to a Wind Turbine*. Informatics and Mathematical Modelling, Technical University of Denmark, DTU, 1995. [Online]. Available: <https://orbit.dtu.dk/en/publications/estimation-of-wind-speed-in-connection-to-a-wind-turbine>
- [66] M. N. Soltani, T. Knudsen, M. Svenstrup, R. Wisniewski, P. Brath, R. Ortega, and K. Johnson, "Estimation of rotor effective wind speed: A comparison," *IEEE Transactions on Control Systems Technology*, vol. 21, no. 4, pp. 1155–1167, 2013. doi: 10.1109/TCST.2013.2260751
- [67] J. Jonkman and B. Jonkman, "FAST v7," 2018, accessed: 2020-Oct-08. [Online]. Available: <https://nwtc.nrel.gov/FAST7>
- [68] A. Crespo and J. Hernández, "Turbulence characteristics in wind-turbine wakes," *Journal of Wind Engineering and Industrial Aerodynamics*, vol. 61, no. 1, pp. 71–85, 1996. doi: 10.1016/0167-6105(95)00033-X
- [69] B. M. Doekemeijer and R. Storm. (2019) FLORISSE M. Accessed: 2020-Oct-08. [Online]. Available: https://github.com/TUdelft-DataDrivenControl/FLORISSE_M/tree/ed2885107ca2600d0616f86cab3b3d59c5f0cb38
- [70] NREL, "FLORIS. Version 2.2.0," 2020, accessed: 2020-Oct-08. [Online]. Available: <https://github.com/NREL/floris>
- [71] C. L. Bottasso, S. Cacciola, and X. Iriarte, "Calibration of wind turbine lifting line models from rotor loads," *Journal of Wind Engineering and Industrial Aerodynamics*, vol. 124, pp. 29–45, 2014. doi: 10.1016/j.jweia.2013.11.003
- [72] J. Schreiber and F. Campagnolo, "Wind farm control strategies based on wake-redirection by yawing with model augmentation (CL-Windcon Deliverable Report D2.3, Control methodology for induction based control and for wake redirection control, Final Draft)," 2019, accessed: 2020-Oct-08. [Online]. Available: <http://www.clwindcon.eu/wp-content/uploads/2019/09/CL-Windcon-D2.3-DraftFinal.pdf>
- [73] E. Simley, P. Fleming, and J. King, "Design and analysis of a wake steering controller with wind direction variability," *Wind Energy Sci.*, vol. 2019, pp. 1–26, 2019. doi: 10.5194/wes-2019-35
- [74] T. Göçmen and G. Giebel, "Data-driven wake modelling for reduced uncertainties in short-term possible power estimation," *Journal of Physics: Conference Series*, vol. 1037, p. 072002, 2018. doi: 10.1088/1742-6596/1037/7/072002